Uncertainty and Sensitivity in Human Motion Dynamics Simulations

TECHNISCHE
UNIVERSITÄT
DARMSTADT

Am Fachbereich Informatik der
Technischen Universität Darmstadt
zur Erlangung des akademischen Grades eines
Doktor-Ingenieurs (Dr.-Ing.)
eingereichte

Dissertation

von

Dipl.-Ing. Janis Wojtusch
(geboren in Frankfurt am Main)

Erstgutachter:	Prof. Dr. Oskar von Stryk
Zweitgutachter:	Prof. Dr. André Seyfarth
Tag der Einreichung:	03.05.2017
Tag der Disputation:	04.07.2017

Darmstadt 2017

Wojtusch, Janis - Uncertainty and Sensitivity in Human Motion Dynamics Simulations
Darmstadt, Technische Universität Darmstadt

Jahr der Disputation: 2017
Jahr der Publikation: 2018
URN: urn:nbn:de:tuda-tuprints-65909
URL: http://tuprints.ulb.tu-darmstadt.de/id/eprint/6590

Contents

List of Figures

List of Tables

List of Symbols

$\boldsymbol{c}$	Coriolis and centrifugal vector
$\boldsymbol{C}$	Gaussian copula
d	Damping constant
E	Expectation
f	Frequency
$\boldsymbol{f}$	External force vector
F	Reference frame
g	Gravitational acceleration
$\boldsymbol{g}$	Gravitation vector
$\boldsymbol{G}$	Ground reaction force vector
$\boldsymbol{I}_s$	Body segment inertia tensor
$\boldsymbol{J}$	Manipulator Jacobian matrix
k	Spring constant
K_d	Derivative control gain
K_f	Kalman filter gain
K_p	Proportional control gain
K_s	Kalman smoother gain
l_r	Resting length
l_s	Body segment length
m_b	Bone mass
m_s	Body segment mass
m_t	Total body mass
m_w	Wobbling mass
$\boldsymbol{M}$	Mass matrix
$\boldsymbol{o}_s$	Body segment center of mass vector
p_j	Johnson probability density function
P_j	Johnson cumulative distribution function
$\boldsymbol{q}$	Joint position vector
$\dot{\boldsymbol{q}} = \frac{\mathrm{d}\boldsymbol{q}}{\mathrm{d}t}$	Joint velocity vector
$\ddot{\boldsymbol{q}} = \frac{\mathrm{d}\dot{\boldsymbol{q}}}{\mathrm{d}t}$	Joint acceleration vector
$\dddot{\boldsymbol{q}} = \frac{\mathrm{d}\ddot{\boldsymbol{q}}}{\mathrm{d}t}$	Joint jerk vector
r_m	Wobbling mass ratio
$\boldsymbol{r}$	Translation vector
$\boldsymbol{R}$	Rotation matrix
S	Sensitivity index
S^F	First-order sensitivity index
S^T	Total-effect sensitivity index
t	Time

$\boldsymbol{T}$	Homogeneous transformation matrix
u	Standard uncertainty
u_c	Combined standard uncertainty
v	Speed
V	Variance
α	Linear regression value
$\boldsymbol{\alpha}$	Linear regression vector
β	Angular regression value
γ_d	Skewness of a probability distribution
γ_j	Shape parameter of a Johnson distribution
Γ	Free moment
δ_j	Shape parameter of a Johnson distribution
ϵ	Deviation
$\boldsymbol{\zeta}$	Center of pressure vector
$\boldsymbol{\theta}$	Marker position vector
κ_d	Kurtosis of a probability distribution
λ_j	Scale parameter of a Johnson distribution
μ_d	Mean of a probability distribution
ν_d	Median of a probability distribution
ξ_j	Location parameter of a Johnson distribution
σ_d	Standard deviation of a probability distribution
σ_d^2	Variance of a probability distribution
σ_p	Principal standard deviation
$\boldsymbol{\Sigma}_c$	Copula covariance matrix
$\boldsymbol{\Sigma}_v$	Measurement covariance matrix
$\boldsymbol{\Sigma}_w$	Process covariance matrix
$\boldsymbol{\tau}$	Joint torque or force vector
Φ	Univariate Gaussian cumulative distribution function
$\boldsymbol{\Phi}$	Multivariate Gaussian cumulative distribution function
χ	Damping coefficient
ω	Natural frequency
$\square_L$, $\square_R$	Symbol or abbreviation referred to the left or right body side
$\square_X$, $\square_Y$, $\square_Z$	Symbol or abbreviation referred to x-, y- or z-axis

The applied symbols are selected in conformity with the usage and definition in literature and are measured in base or derived units of the International System of Units. Regular typeface indicates scalar quantities, while matrices and vectors are printed in bold typeface. Uppercase symbols denote matrices and lowercase symbols indicate vectors or scalars. The subscript index labels identical symbols with different meaning and can be extended by comma separated abbreviations to allow a further distinction.

List of Abbreviations

2D	Two-dimensional space
3D	Three-dimensional space
ABA	Articulated-body algorithm
ABD	Abdomen body segment
ACR	Acromion landmark
AJ	Ankle joint center
ALI	Anatomic landmark identification sensitivities
AM	Anchor model
ANP	Anthropometric parameter sensitivities
ASIS	Anterior-superior iliac spine landmark
BCF	Biceps femoris muscle
BH	Body height
BJ	Base joint center
BM	Body mass
BOM	Body measurement sensitivities
C1-C7	Vertebrae of the cervical spine
C7	Seventh cervical vertebra landmark
CAL	Calcaneus landmark
CDF	Cumulative probability function
COM	Center of mass
COV	Center of volume
CRBA	Composite-rigid-body algorithm
EJ	Elbow joint center
FAST	Fourier amplitude sensitivity test
FBM	Full body model
FIB	Fibulare landmark
FOO	Foot body segment
FOM	Force measurement sensitivities
FRM	Free moment
GLA	Glabella landmark
GLS	Gastrocnemius lateralis muscle
GLX	Gluteus maximus muscle
GRF	Ground reaction force
GTR	Greater trochanter landmark
GUM	Guide to the Expression of Uncertainty in Measurement
hABA	Hybrid articulated-body algorithm
HAL	Hallux landmark
HAN	Hand body segment

HEA	Head body segment
HJ	Hip joint center
ISB	International Society of Biomechanics
ISO	International Organization for Standardization
JCGM	Joint Committee for Guides in Metrology
JOC	Joint center sensitivities
KJ	Knee joint center
L1-L5	Vertebrae of the lumbar spine
LBM	Lower body model
LFC	Lateral femoral epicondyle landmark
LHC	Lateral humeral epicondyle landmark
LLJ	Lower lumbar joint center
LM	Lateral malleolus landmark
LNJ	Lower neck joint center
LOA	Lower arm body segment
LOAH	Combined body segment consisting of lower arm and hand segment
MC	Motion capture
MC2	Second metacarpale landmark
MC5	Fifth metacarpale landmark
MFC	Medial femoral epicondyle landmark
MH1	First metatarsal head landmark denoting a point medial of the metatarsal head
MH5	Fifth metatarsal head landmark denoting a point lateral of the metatarsal head
MHC	Medial humeral epicondyle landmark
MM	Medial malleolus landmark
MOI	Moment of inertia
MT2	Second metatarsal head landmark denoting a point above the metatarsal head
MT5	Fifth metatarsal head landmark denoting a point above the metatarsal head
OLE	Olecranon landmark
PDF	Probability function
PEL	Pelvis body segment
POI	Product of inertia
PS	Pubic symphysis landmark
PSIS	Posterior-superior iliac spine landmark
RAD	Radiale landmark
RBD	Random balance design
RCF	Rectus femoris muscle
RNEA	Recursive Newton-Euler algorithm
ROG	Radius of gyration
RS	Radial styloid landmark
S1-S5	Vertebrae of the sacrum
SB	Bounded distribution type of the Johnson distribution family
SHA	Shank body segment

SJ	Shoulder joint center
SL	Log-normal distribution type of the Johnson distribution family
SN	Normal distribution type of the Johnson distribution family
SOL	Soleus muscle
SPH	Sphyrion landmark
STA	Soft tissue artifact sensitivities
SU	Unbounded distribution type of the Johnson distribution family
SUP	Suprasternale landmark
T1-T12	Vertebrae of the thoracic spine
T12	Twelfth thoracic vertebra landmark
T8	Eighth thoracic vertebra landmark
THI	Thigh body segment
THO	Thorax body segment
TIA	Tibialis anterior muscle
TIB	Tibiale landmark
TJ	Toe joint center
TM	Template model
TRA	Tragion landmark
ULJ	Upper lumbar joint center
UPA	Upper arm body segment
US	Ulnar styloid landmark
VSL	Vastus lateralis muscle
WJ	Wrist joint center
WOM	Wobbling mass sensitivities
WRI	Wrist landmark

Abstract

Biomechanical dynamics simulations facilitate the investigation of fundamental principles and concepts in human motions. The simulation results help to explain experimentally observed phenomena and reveal underlying mechanisms. Due to unavoidable restrictions in biomechanical measurements and the determination of personalized model parameters, the simulation results always lie within a specific range of possible solutions. Since these uncertainties can have a significant influence on derived scientific conclusions and clinical decisions, this thesis provides a systematic uncertainty and sensitivity analysis of the common inverse dynamics simulation to assess uncertainty propagation and the contribution of individual uncertainty sources in the estimation of joint torques resulting from particular human motions.

The analysis evaluates uncertainties and sensitivities in selected joint torque estimates of the lower limbs for three motion tasks performed by a female and male subject. It follows the procedure of the inverse dynamics simulation including the acquisition of biomechanical measurements, estimation of model parameters and realization of dynamics simulations with a parallel assessment of uncertainty propagation and apportionment. This approach ensures a systematic and consecutive evaluation of uncertainty and sensitivity with respect to the sequential nature of the procedure and existing dependencies between the involved uncertainty sources. The human locomotor system is modeled as a three-dimensional multibody system implemented within an efficient multibody systems library. The analysis employs a global method based on Monte Carlo simulations in combination with a quasi-random sampling strategy in order to explore the whole input space and consider nonlinearities in the biomechanical model. Potential correlations among the uncertain simulation inputs and model parameters are considered.

The biomechanical measurements that form the basis for the uncertainty and sensitivity analysis comprise motion capture data and force plate measurements with an instrumented treadmill for the considered motion tasks. Associated uncertainties caused by variations in anatomic landmark identification, soft tissue artifacts, motion capture and force plate measurements are quantified and modeled by experimental investigations with the actual subjects and measurements systems or by suitable computational models described in literature. The variances in parameters of two comprehensive regression models for joint center estimation and one widely used regression model for anthropometric parameter estimation in female and male subjects are assessed and modeled based on the found uncertainties for biomechanical measurements as well as additional statistical properties from literature. For the anthropometric parameter estimation, a revised set of regression parameters is derived from the obtained results. The impact of the identified uncertainties on estimated anthropometric parameters is investigated in an exemplary sensitivity analysis. With incorporating the previously determined models for the individual uncertainty sources, the uncertainty propagation and apportionment in the actual inverse dynamics simulation are evaluated and discussed for a walking, running and kicking a ball motion performed by both subjects.

The identified uncertainties at the individual levels of the inverse dynamics simulation allow to evaluate the credibility and accuracy in this and similar biomechanical simulations, while the corresponding sensitivities identify uncertainty sources with particularly high influence on the

simulation results. These results give an indication of the expectable validity in biomechanical dynamics simulations, but also allow to enhance the quality of biomechanical studies by specifically approaching the identified problems.

In addition to the uncertainty and sensitivity analysis, complementary research topics regarding a user-centered design methodology for active prosthetic and orthotic devices based on biomechanical simulations of human motions are investigated and presented. A particular focus is put on the analysis and implementation of serial elastic actuator concepts that ensure inherent safety and energy efficiency as well as the development of a personalized audio-visual simulation with respect to relevant psychological factors.

Kurzfassung

Biomechanische Dynamiksimulationen ermöglichen die Untersuchung grundlegender Prinzipien und Konzepte in menschlichen Bewegungen. Die Simulationsergebnisse bilden eine wichtige Grundlage für die Erklärung experimentell beobachteter Phänomene und bei der Aufdeckung fundamentaler Mechanismen. Aufgrund von unvermeidlichen Beschränkungen in biomechanischen Messungen und der Bestimmung von personalisierten Modellparametern sind die erzielten Simulationsergebnisse niemals exakt, sondern liegen immer in einem bestimmten Bereich möglicher Lösungen. Da diese Unsicherheiten signifikanten Einfluss auf abgeleitete wissenschaftliche Schlussfolgerungen und klinische Entscheidungen haben können, wird in dieser Arbeit eine systematische Unsicherheits- und Sensitivitätsanalyse für die weitverbreitete Inversdynamiksimulation durchgeführt. Hierbei wird die Ausbreitung von Unsicherheiten und der Einfluss einzelner Unsicherheitsfaktoren auf die Schätzung von Gelenkmomenten bei bestimmten menschlichen Bewegungen untersucht.

Im Rahmen der Analyse werden ausgewählte Gelenkmomentschätzungen in den unteren Extremitäten für jeweils drei unterschiedliche Bewegungen bei einem weiblichen sowie einem männlichen Probanden ausgewertet. Die Analyse orientiert sich dabei am Ablauf der Inversdynamiksimulation und beinhaltet die Aufnahme biomechanischer Messungen, Schätzung von Modellparametern und Durchführung der Dynamiksimulation mit einer parallelen Auswertung der Unsicherheitsausbreitung und -aufteilung. Dieser Ansatz gewährleistet eine systematische und fortlaufende Untersuchung von Unsicherheiten und Sensitivitäten unter Berücksichtigung des sequenziellen Ablaufs und möglicher Abhängigkeiten zwischen den beteiligten Unsicherheitsfaktoren. Der menschliche Bewegungsapparat wird als dreidimensionales Mehrkörpersystem modelliert und in einer effizienten Mehrkörpersystem-Blibliothek implementiert. Die Analyse nutzt einen globalen Ansatz und basiert auf Monte-Carlo-Simulationen in Verbindung mit einem quasi-zufälligen Stichprobenverfahren, um den gesamten Eingangsvariablenraum abzudecken und Nichtlinearitäten im biomechanischen Modell zu berücksichtigen. Mögliche Korrelationen zwischen den unsicheren Eingangsvariablen und Modellparametern werden dabei ebenfalls beachtet.

Die Ergebnisse der biomechanischen Messungen für die betrachteten Bewegungen bilden die Grundlage für die Unsicherheits- und Sensitivitätsanalyse und beinhalten Daten von einem Bewegungserfassungssystem und in einem Laufband integrierten Kraftmessplatten. Die damit verbundenen Unsicherheiten, verursacht durch Variationen bei der Identifikation anatomischer Leitstrukturen, den Weichteilartefakten, der Bewegungserfassung und der Kraftmessung, werden mittels experimenteller Untersuchungen an den tatsächlich bei den Messungen beteiligten Probanden und Messsystemen sowie geeigneter Berechnungsmodelle aus der Literatur bemessen und modelliert. Die Varianzen in den Parametern von zwei umfassenden Regressionsmodellen zur Schätzung von Gelenkzentren und einem weitverbreiteten Regressionsmodell zur Bestimmung von anthropometrischen Parametern bei weiblichen und männlichen Probanden werden anhand der ermittelten Unsicherheiten in biomechanischen Messungen und zusätzlichen statistischen Daten aus der Literatur ausgewertet und modelliert. Die erhaltenen Ergebnisse ermöglichen die Ableitung eines überarbeiteten Regressionsparametersatzes für die Abschätzung

von anthropometrischen Parametern. Der Einfluss der vorab bestimmten Unsicherheiten auf die Schätzung von anthropometrischen Parametern wird in einer beispielhaften Sensitivitätsanalyse näher untersucht. Unter Einbeziehung der zuvor ermittelten Modelle für die individuellen Unsicherheitsfaktoren werden die Unsicherheitsausbreitung und -aufteilung in der eigentlichen Inversdynamiksimulation für eine Geh-, Renn- und Schussbewegung bei den beiden Probanden analysiert und diskutiert.

Die auf den einzelnen Ebenen der Inversdynamiksimulation bestimmten Unsicherheiten ermöglichen eine Beurteilung der Plausibilität und Genauigkeit dieser und ähnlicher biomechanischer Simulationen, während die entsprechenden Sensitivitäten Unsicherheitsfaktoren mit besonders hohem Einfluss auf die Simulationsergebnisse identifizieren. Diese Ergebnisse geben einen Hinweis auf die erwartbare Aussagekraft von biomechanischen Dynamiksimulationen, erlauben aber ebenso eine Steigerung der Qualität von biomechanischen Studien durch das gezielte Evaluieren der identifizierten Defizite.

Zusätzlich zur Unsicherheits- und Sensitivitätsanalyse werden ergänzende Forschungsthemen bezüglich einer benutzerorientierten Entwurfsmethodik für aktive Prothesen- und Orthesensysteme auf Basis biomechanischer Simulationen menschlicher Bewegungen untersucht und vorgestellt. Ein besonderer Schwerpunkt liegt dabei auf der Analyse und Implementierung seriell-elastischer Antriebskonzepte, die inhärente Sicherheit und Energieeffizienz gewährleisten, sowie auf der Entwicklung einer personalisierten audiovisuellen Simulation unter Einbeziehung relevanter psychologischer Faktoren.

1 Introduction

The human body is able to perform an impressively wide spectrum of motions in an efficient and robust manner. Humans can easily cover long distances by walking or jogging, reach high speeds by running or overcome various obstacles by jumping or climbing with adapting to different types of ground conditions and environments. The capability to manipulate or interact with objects ranges from dexterous handling of small and fragile items like grasping a raw egg to ballistic motions like throwing or kicking a ball. When compared to modern technical systems such as pick-and-place devices or humanoid robots, humans might perform worse at specific motion tasks, but still outperform these systems in overall adaptability, dexterity and robustness. For this reason, the human body is an excellent model for biologically inspired engineering and the development of novel technological solutions in robotics, medicine and rehabilitation.

In terms of biomechanics, voluntary human motions are the result of a complex and well-timed interaction between the nervous system and the locomotor system. The nervous system comprising brain, spinal cord, nerves and ganglia integrates and evaluates sensory information it receives from the organism as well as coordinates and influences the locomotory activity. The locomotor system consisting of bones, joints, skeletal muscles and connective tissue provides form, support and the ability for motion. A precise coordination of all parts is very important for the execution of the desired motion. The Soviet neurophysiologist Nikolai Alexandrovich Bernstein once compared the involved processes in human walking with the collective virtuosity of an orchestra.

> ❝*As in an orchestra, each instrument plays its individual score, so in the act of human walking each joint reproduces its own curve of movements and each center of gravity performs its sequence of accelerations, each muscle produces its melody of efforts, full with regularly changing but stable details. And in like manner, the whole of this ensemble acts in unison with a single and complete rhythm, fusing the whole enormous complexity into clear and harmonic simplicity. The consolidator and manager of this complex entity, the conductor and at the same time the composer of the analyzed score, is of course the central nervous system.* ❞
>
> Nikolai Alexandrovich Bernstein, 1935

Further extending this vivid metaphor, the discord which a single instrument out of tune can bring into the harmony of the entire ensemble well describes the consequences of musculoskeletal or neuromuscular disorders causing subtle and obvious changes in the gait pattern. While small deviations can be compensated by the other musicians, strong disharmonies will interrupt the whole performance. As nowadays technical orchestral enhancement is used to modify and augment the sound of an orchestra or even replace missing instruments, so technical assistive devices like orthoses or prostheses allow humans to improve and recover impaired locomotory abilities.

Understanding the fundamental principles and concepts in human motion is an important foundation for a wide range of applications in medicine, rehabilitation, robotics and sports. Conventional experiment-based approaches help to find general descriptions but are often limited

in providing causal explanations because many crucial variables like joint forces and torques or muscle forces cannot be measured directly and many biomechanical interventions are impossible or unethical [11, 33]. Provided an adequate computational model of the locomotor system, simulation-based approaches have the potential to close these gaps and enable the study of complex interdependencies with arbitrary interventions. The development of advanced numerical methods for modeling, simulation and optimization in the recent decades facilitates the use of computational models in scientific research and clinical applications. Biomechanical simulations of human motions based on musculoskeletal models help to explain experimentally observed phenomena and reveal fundamental mechanisms [239, 242]. Current research topics and clinical applications comprise

- human gait analysis, e.g., [3, 14, 137],
- study and diagnosis of musculoskeletal disorders, e.g., [13, 64, 171],
- design and optimization of assistive devices, e.g., [28, 82, 95],
- control of assistive devices, e.g., [16, 81, 94],
- control of humanoid robots, e.g., [75, 198, 201],
- planning of surgeries and rehabilitation processes, e.g., [76, 117, 132],
- sports performance analysis, e.g., [78, 110, 154].

Furthermore, biomechanical simulations are also deployed in the context of personalized medicine and integrative biomechanics that aim at tailoring therapies to individual patients or patient groups based on predicted treatment response or injury risk [15]. An essential requirement of these approaches is the availability of accurate and personalized musculoskeletal models in order to provide individual physiological characteristics and to customize treatment modalities.

A very relevant and common type of biomechanical simulations is the inverse dynamics simulation that is used to estimate joint forces and torques resulting from a particular human motion. The typical procedure of an inverse dynamics simulation is illustrated in the upper half of Figure 1.1. In a first step, the considered motion task is performed by a human subject and recorded by applying a motion capture system to measure the kinematics of the individual body segments as well as force plates to quantify ground reaction forces or other external forces from the environment. Additionally, electromyography can be applied to measure the electrical activity of selected skeletal muscles that are involved in the recorded motion. In a second step, joint center locations representing idealized centers of rotation in human joints are estimated based on the captured motion data. These joint center estimates allow to derive the length of each individual body segment as well as the joint trajectories including linear or angular joint positions, velocities and accelerations. Together with the body mass of the subject which can be computed from the force plate measurements, the segment lengths are used in a third step to estimate relevant anthropometric model parameters like the mass, center of mass and moment of inertia of the individual body segments. Dependent on the considered motion task and model structure, the determination of additional model parameters such as wobbling masses or joint constraints might be required. All these model parameters are incorporated into a personalized computational model that approximates the involved kinematic and dynamic properties of the human body of the respective subject. In a final step, the joint trajectories and external forces

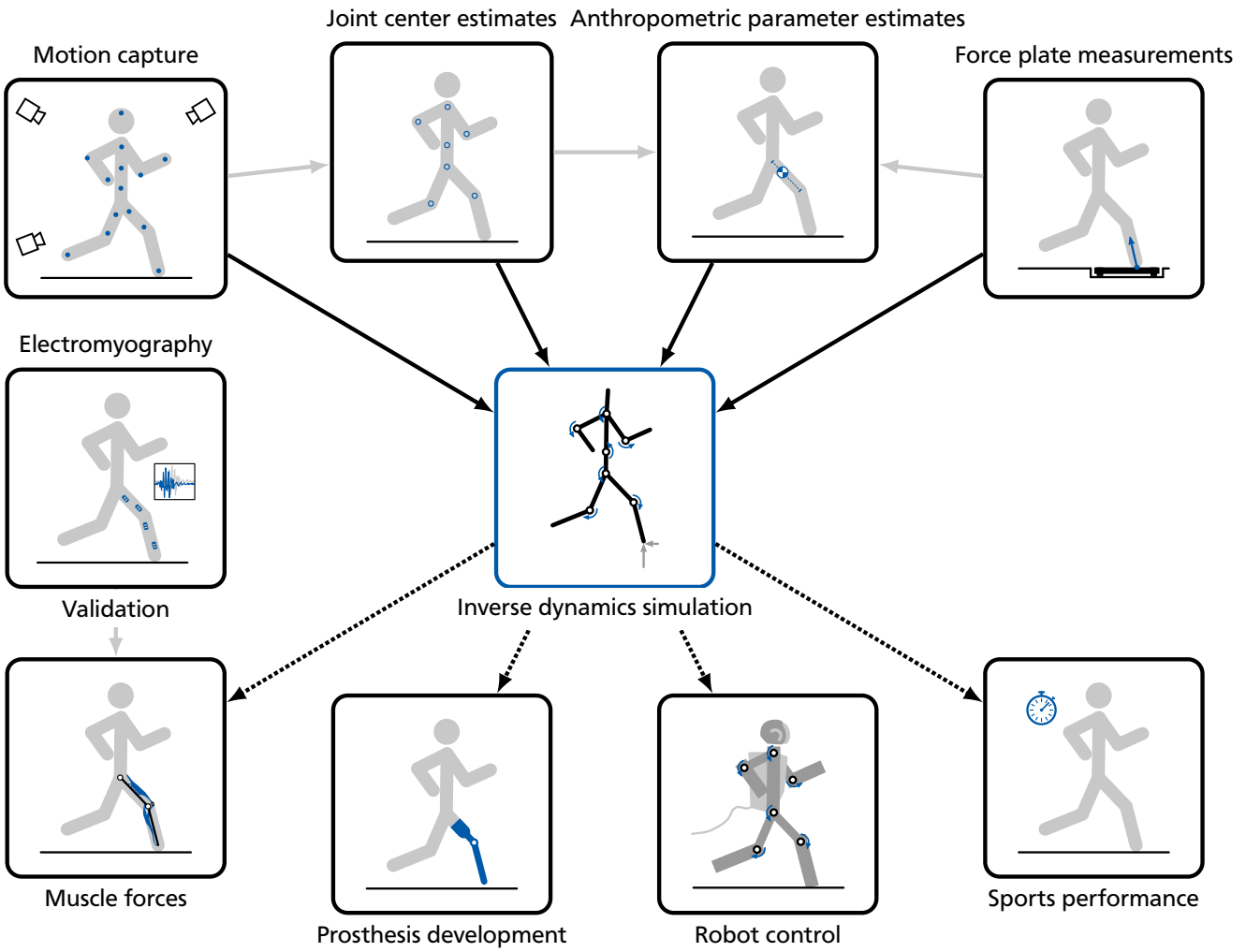

Figure 1.1.: Typical procedure and exemplary applications of an inverse dynamics simulation for estimating joint forces and torques in human motions.

are applied to the computational model in order to perform the inverse dynamics simulation. The simulation results provide the joint forces and torques with regard to the measured spatial motion and external forces as well as the estimated model parameters and applied model structure.

The obtained joint forces and torques may be evaluated directly or establish a basis for subsequent studies. Some exemplary applications are shown in the lower half of Figure 1.1. The estimation of muscle forces, e.g., [228], can be an essential part of a biomechanical or medical analysis. Because of the muscular redundancy originating from the multiple mono- and biarticular skeletal muscles that actuate a single joint, it is necessary to use an optimization-based approach for the estimation. Typically, a static optimization in combination with macroscopic muscle models is applied which searches for muscle forces that reproduce the computed joint forces and torques with minimizing the effort of the associated skeletal muscles. Electrical activities of selected skeletal muscles recorded by electromyography can serve as a reference for validating the optimization results. Joint forces and torques for typical human motions are also of interest in the development of assistive devices like prostheses, e.g., [35]. Characteristic limit values and transient behavior are used to design constructive elements or develop suitable actu-

ation concepts. Actuation concepts for active and mobile assistive devices are usually optimized for small power consumption and high wear comfort, for example by integrating series elastic and parallel elastic elements tuned to computed joint forces and torques, e.g., [93]. Inverse dynamics simulation results are likewise used to design control approaches for robotic devices like the neuromuscular model control for humanoid robots or assistive devices, e.g., [225]. This approach allows to mimic human whole-body motions with integrating biologically inspired reflex models which is intended to improve disturbance reaction and balance recovery. In sports performance studies, joint forces and torques can reveal motion-specific efficiency potentials or injury risks, e.g., [70]. This knowledge helps to adapt or develop training programs and recovery plans.

1.1 Motivation

The growing use of biomechanical simulations in scientific research and clinical applications has the potential to facilitate advancements in many aspects of medicine, rehabilitation, robotics and sports but also raises issues of credibility and accuracy [11, 106]. Before a biomechanical simulation can be expected to provide valid and reliable information, consistency and plausibility have to be checked by applying an appropriate validation scheme. Common error sources in modeling and simulation studies comprise modeling errors, approximation and rounding errors as well as programming and implementation errors. General validation schemes used in computational engineering utilize carefully selected plausibility checks to systematically analyze the simulation model, computing methods and computational implementation. These plausibility checks typically examine the consistency of model assumptions, the suitability of the model structure and parameters as well as the influence of approximation and rounding errors. Furthermore, testing special cases of the considered problem and reviewing the syntactical and numerical correctness of the implementation are common practice. Unfortunately, fundamental restrictions in biomechanical measurements like the difficult or even impossible determination of accurate model parameters or the limitation to indirect experimental measurements for many crucial variables confine the validation process for biomechanical simulations. Besides testing the software implementation and comparing the simulation results with independently reported simulations or experiments, the evaluation of robustness towards uncertainties in model parameters as well as simulation inputs is a central step in recent recommendations for the validation of biomechanical studies [106].

Many studies published in the last years investigated the influence of various uncertainty sources and found considerable impacts on simulation results. Riemer et al. [181] for example found variations of up to 232.0 % in joint torques for a walking motion, while Myers et al. [153] identified an upper bound of 19.7 % for deviations in derived muscle forces. Uncertainties of these magnitudes substantially affect the results of biomechanical and medical investigations but can also lead to an inappropriate dimensioning of critical components in assistive devices. For this reason, a systematic evaluation of uncertainties and sensitivities as proposed in this thesis is very important. Relevant uncertainty sources include variations in personalized model parameters like

- anthropometrical parameter estimates, e.g., [175],
- joint center estimates, e.g. [178],

- wobbling masses, e.g., [163],

as well as inaccuracies in biomechanical measurements like

- kinematic motion data and resultant derivatives, e.g., [185],
- ground reaction forces, e.g., [166],
- soft tissue artifacts, e.g., [214],
- anatomic landmark identification, e.g., [162].

Uncertainties in biomechanical measurements mostly depend on the applied measuring equipment or subsequent data processing but are also affected by hardly predictable effects resulting from soft tissue deformation and irregular bone surfaces. The accurate determination of personalized model parameters gets even more complicated by highly individual body segment proportions and tissue distributions. Individual anthropometric parameters and joint center locations can, in principle, be measured by using medical imaging technologies such as magnetic resonance imaging, e.g. [213], or dual-energy X-ray, e.g. [71]. But these methods are quite expensive and time-consuming or expose human subjects to harmful radiations and are therefore not applicable in most studies. Commonly, personalized model parameters are estimated with regression models, e.g., [66], or with scaling methods, e.g., [62]. Such statistical estimators approximate anthropometric parameters and joint center locations based on averaged data obtained from a limited population of subjects and a small number of individual measurements like body mass, segment lengths and gender or specific anatomical landmark positions. These restrictions can introduce substantial uncertainties and impair the kinematic and dynamic accuracy of the computational model.

Knowing the overall uncertainty of the simulation results and understanding the influences of the involved uncertainty sources are essential requirements in order to draw scientific conclusions and inform clinical decisions. Specialized probabilistic methods allow to study uncertainty propagation through the computational model which is also known as uncertainty analysis and reveal the contribution of individual uncertainty sources to the overall uncertainty of the simulation results which is also referred to as sensitivity analysis. This information helps to identify critical uncertainty sources and allows to evaluate simulation results regarding credibility and accuracy. Previous studies mainly investigated uncertainties and sensitivities in walking motions performed by male subjects, e.g. [153, 227, 237]. A comparison between the results is difficult because each investigation considered a different set of uncertainty sources and applied different assumptions for the uncertainties of simulation inputs which also led to partially inconsistent conclusions. In some studies, local methods for sensitivity analysis were used that are computationally efficient but cannot explore the whole input space. Studies that applied global methods for sensitivity analysis largely simplified the uncertainties of simulation inputs by presuming uniform or Gaussian distributions and neglecting possible correlations. These limitations potentially reduce validity and applicability for the validation of biomechanical simulations. In addition, uncertainties and sensitivities for female, young, elderly and disabled subjects as well as other motion tasks might differ considerably from the core findings obtained for walking with adult male subjects.

1.2 Contribution

This thesis contributes to the field of human biomechanics with a focus on uncertainty and sensitivity analysis in human motion dynamics simulations by providing comprehensive biomechanical measurements for both genders and different motion tasks accompanied by a detailed evaluation of the associated uncertainty propagation and apportionment.

With regard to the important class of inverse dynamics simulations, the impact of common uncertainty sources is systematically investigated for selected joint torques of the lower limbs in three motion tasks performed by an adult female and male subject. Besides the two repetitive motions walking and running, kicking a ball is considered exemplary for a ballistic motion. These motion tasks cover a relevant range of natural human whole-body motions and allow to study uncertainty and sensitivity for varying motion speeds and sequences. By providing results for a female and male subject, gender-specific physiological differences can be considered in the investigation. The uncertainty and sensitivity analysis is oriented towards the procedure of an inverse dynamics simulation including the acquisition of biomechanical measurements, estimation of model parameters and realization of dynamics simulations with a parallel assessment of uncertainty propagation and apportionment. This approach ensures a systematic and consecutive evaluation of uncertainty and sensitivity regarding the sequential nature of the procedure and existing dependencies between the involved uncertainty sources.

The biomechanical properties of the human locomotor system are modeled as a three-dimensional multibody system with thirty degrees of freedom and fourteen body segments implemented within an efficient multibody systems library for modeling and simulation. A global uncertainty and sensitivity analysis based on Monte Carlo simulations in combination with a quasi-random sampling strategy is applied in order to explore the whole input space and consider nonlinearities in the computational model. Uncertainties are modeled using the parametric Johnson distribution system that covers the entire permissible skewness-kurtosis region. A Gaussian copula approach is applied to model potential correlations among uncertain simulation inputs and model parameters. Sensitivities are estimated with a variance-based method for problems with correlated input variables. This comprehensive computational framework provides a capable modeling and simulation environment and ensures an adequate statistical treatment of the evaluated uncertainties and sensitivities. The biomechanical measurement data and anthropometric model parameters used in this thesis as well as the source code of the applied computational scripts and multibody systems library are published and provided under an open-source license.

The results comprise a set of high-quality biomechanical measurements, personalized anthropometric parameter and joint center estimates as well as selected joint torques for the considered motion tasks and both subjects accompanied by the associated uncertainties and sensitivities. In addition, uncertainties of commonly used regression models for joint center and anthropometric parameter estimation are investigated and revised regression parameters are presented based on the obtained results. The identified uncertainties at all levels of the inverse dynamics simulation allow to evaluate the credibility and accuracy in these and similar biomechanical simulations. The corresponding sensitivities enable to recognize uncertainty sources with particularly high influence on the simulation results. This information provides novel insights to improve the

quality of biomechanical measurements and model parameter estimation and facilitates the validation of biomechanical simulations.

Regarding a user-centered design methodology for active assistive devices based on biomechanical simulations of human motions, a number of complementary research topics have been investigated in addition to the uncertainty and sensitivity analysis. Due to the limited space, only a summary of the applied approaches and obtained research results is provided and discussed.

1.3 Structure

The structure of this thesis follows the procedure of an inverse dynamics simulation. Subsequent to this introduction, Chapter 2 provides a brief overview of human biomechanics with presenting the relevant terminology as well as fundamental properties of the human locomotor system and the used measurement equipment. A detailed description of the applied biomechanical model of the human locomotor system and the simulation framework is given in Chapter 3. Different approaches in biomechanical modeling and simulation as well as the estimation of model parameters are presented and discussed with regard to the intended purpose. Chapter 4 introduces existing approaches in uncertainty and sensitivity analysis and discusses the applicability for biomechanical simulations. The applied analysis framework and strategy are described in detail and put in context with the considered inverse dynamics simulation.

Chapter 5 presents the first step of the inverse dynamics simulation procedure and describes the acquisition of the biomechanical measurements used for the uncertainty and sensitivity analysis. Details on the applied measurement protocol and data processing approaches are given and the relevant reference frames are defined. The associated uncertainties comprising variations in anatomic landmark identification, soft tissue artifacts, motion capture and force plate measurements are systematically evaluated in Chapter 6. Statistical models are derived from experimental investigations with the actual subjects and measurements systems or from suitable computational models described in literature.

In Chapter 7, the second step of the inverse dynamics simulation procedure is presented and two comprehensive regression models for the estimation of personalized joint center locations that cover all relevant joints for a biomechanical simulation of human locomotion are described. Statistical models for the uncertainty of the involved regression parameters are obtained by exploiting statistical properties of adjacent anatomical landmarks provided in literature.

Chapter 8 addresses the third step of the inverse dynamics simulation procedure and presents a comprehensive regression model for personalized anthropometric parameter estimation that includes all relevant body segments for a biomechanical simulation of human locomotion. Based on statistical properties reported in literature as well as the obtained results for the uncertainties in biomechanical measurements and joint center estimation, statistical models for the uncertainty of the involved regression parameters are derived. Furthermore, the impact of the identified uncertainties on estimated anthropometric parameters is investigated in an exemplary sensitivity analysis.

The fourth and final step of the inverse dynamics simulation procedure is described in Chapter 9. With incorporating the statistical models for the individual uncertainty sources obtained in the previous investigations, uncertainty propagation and apportionment for selected joint torques

are evaluated in a walking, running and kicking a ball motion performed by a female and a male subject. The found uncertainties and sensitivities are discussed with regard to the expectable credibility and accuracy in human motion dynamics simulations.

The design of active prosthetic and orthotic devices is a prominent application example for biomechanical simulations. Simulation studies like the inverse dynamics simulation provide valuable design parameters such as realistic torque characteristics or acceleration profiles for different motion tasks that facilitate an efficient development based on user's needs. In addition, dynamics simulations of human motions with existing or developed assistive devices enable a first evaluation of novel design approaches and technological improvements. An overview of complementary research topics and study results regarding a user-centered design methodology for active assistive devices is given in Chapter 10.

The thesis closes with a summarizing conclusion and brief outlook in Chapter 11.

2 Background

As the term biomechanics combines biology and mechanics, biomechanical studies primarily involve the investigation of fundamental principles and concepts of biological systems using methods of mechanical engineering but also integrate knowledge of other fields like anatomy, physiology and neuroscience [242]. Nigg and Herzog define biomechanics as "the science that examines forces acting upon and within a biological structure and effects produced by such forces" [156]. For the investigation of human motion dynamics, the biological structure is the human locomotor system while the acting forces are internal muscle and joint forces as well as external reaction forces. This scenario allows to derive different biomechanical problems depending on the actual focus of research. From a mechanical engineering point of view, the relation between relative motions of body segments and the acting forces is of particular interest, whereas the examination of effects caused by locally acting forces on living tissue is closely connected with biology. Functional interdependencies of specific bone and joint geometries are within the scope of anatomy as the study of form and structure, while fundamental processes involved in muscle force generation are associated with physiology as the study of function. The investigation of the cooperative interaction between the nervous system and the locomotor system as an important aspect of motor control is strongly related to neuroscience and psychology. The biomechanical simulations evaluated in this thesis focus on the estimation of internal joint forces and torques resulting from specific human motions and therefore mainly address methods of mechanical engineering. Nevertheless, the results are also relevant for other biomechanical research questions, since internal joint forces and torques are a common basis for the estimation of muscle activities and the examination of functional interdependencies in the musculoskeletal system.

2.1 Terminology

In human biomechanics, anatomical terms of location and direction are used to describe the relationships between different body parts and segments. The following explanations adopt the definitions given by Whittle [239] and Faller and Schünke [77]. Figure 2.1 illustrates a set of frequently used anatomical terms. Three principal planes are defined to divide the body. The sagittal plane, shown in red, is any plane that splits the body into a left and right part corresponding to a full section in side view. The transverse plane, shown in green, is perpendicular to the sagittal plane and is any plane that runs transversely across the body being equivalent to a full section in top view. The frontal plane, shown in blue, is perpendicular to the sagittal and transverse planes and is any plane that separates the body into front and back portions being comparable to a full section in front view. Six principal directions are defined relative to the center of the body. Superior points up towards the head, whereas inferior points down towards the feet. Anterior refers to the front side, while posterior refers to the back side. Left and right are self-evident. To describe directions in body extremities, four additional directional terms are defined. Medial points towards the midline and lateral points away from the midline. Proximal means towards the rest of the body and distal indicates away from the rest of the body.

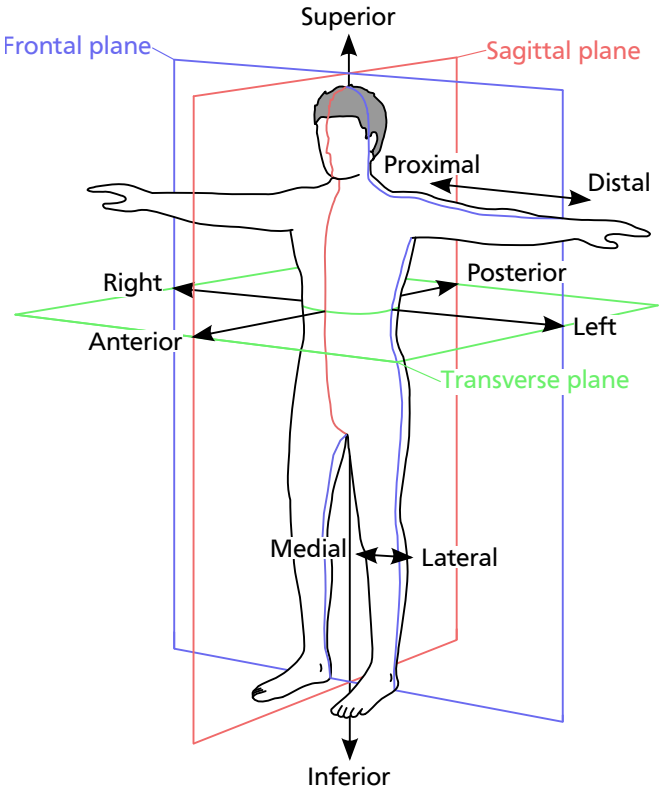

Figure 2.1.: Anatomical terms of location and direction in human biomechanics adapted from Faller and Schünke [77].

The directions of joint motions are specified in relation to the associated principal plane in an upright standing position with legs together and arms at the side also known as the anatomical position. Motions in the sagittal plane are called flexion and extension, where flexion corresponds to squatting down or decreasing the body silhouette, while extension is equivalent to standing up or increasing the body silhouette. The only exception is the motion in the ankle joints which is called dorsiflexion instead of flexion and plantarflexion instead of extension. For many human motions, the joint motions in sagittal plane have by far the largest amplitudes and are therefore considered exclusively in many biomechanical studies [239]. Motions in the frontal plane are called abduction when moving away from the midline and adduction when moving towards the midline. Internal and external rotation describe motions in the transverse plane.

2.2 Human Locomotor System

The human locomotor system consists of bones, joints, skeletal muscles and connective tissue and provides stability, form, support and the ability to move. The active locomotor system comprises the skeletal muscles and tendons, while the passive locomotor system includes the skeleton composed of bony and cartilaginous elements and the joints connected by connective tissue. These elements form the organs of locomotion. The following brief descriptions follow the outline given by Faller and Schünke [77] and focus on the mechanical properties of the locomotor system.

2.2.1 Skeleton

Bones are organs made up of two types of bone tissue, bone marrow, blood vessels and nerves. Cortical bone tissue constitutes the hard outer shell of bones and is dense, strong and stiff. It gives form and support as well as protection for inner organs. Cancellous bone tissue fills the internal bone structure between the outer shell and bone marrow. It is less dense and strong but more flexible and forms a meshed framework aligned towards the mechanical load distribution that the bone experiences.

The human skeleton is composed of about two hundred distinguishable bones of various shapes and structures. The bony shape is an individual genetic characteristic but the bony structure depends on the type and extent of the acting mechanical loads. Most bones in the body extremities are long bones with a shaft and rounded ends called epiphysis. In addition to form and support, these bones and associated joints also provide levers for the muscles during locomotion and are therefore subject to large mechanical loads. Bones and muscles are connected through tendons that grow into the bone at the insertion points creating a strong but flexible connection. Some bones like the kneecap are embedded in tendons and further increase the leverage exerted on the connected bones.

In biomechanical simulations used for the investigation of human whole-body motions, human bones are mostly treated as rigid elements which do not deform under external forces, e.g. [239, 242, 260].

2.2.2 Joints

Joints are connections between bones that enable relative motions of individual body segments. The most common and movable joints in the human body are synovial joints. These joints are enclosed by a joint capsule and the joint surfaces that are separated by a joint space are covered by a resilient and elastic cartilage tissue. A viscous synovial fluid in the joint space serves as a lubricant to reduce friction between the joint surfaces.

The shape of the joint surfaces as well as the arrangement of muscles and ligaments determine the degrees of freedom and direction of motion in a joint. Ligaments are bands of relatively inelastic tissue that stabilize the joints and connect the bones. Muscular forces ensure the integrity of the joints that move along or about specific movement axes. The extent of motion is restricted by geometry, muscles, ligaments and soft tissues. The complex shape of joint surfaces and interactions between ligaments and muscles generally lead to a concatenation of motions in different degrees of freedom and a combination of rotation and translation. The knee joint, for example, is the largest joint of the human body and plays an essential role in carrying the body weight during walking and running. It is a combined joint that permits flexion and extension as well as slight internal and external rotation involving the femur bone in the thigh, the tibia bone in the shank and the kneecap. When the knee joint is flexed, flexion is preceded by an internal rotation of the tibia bone, while the femur bone executes a combined rolling and gliding motion as presented in Figure 2.2. In extended position, the contact point, shown in red, is located centrally. The femur bone performs posterior rolling in early flexion superimposed by

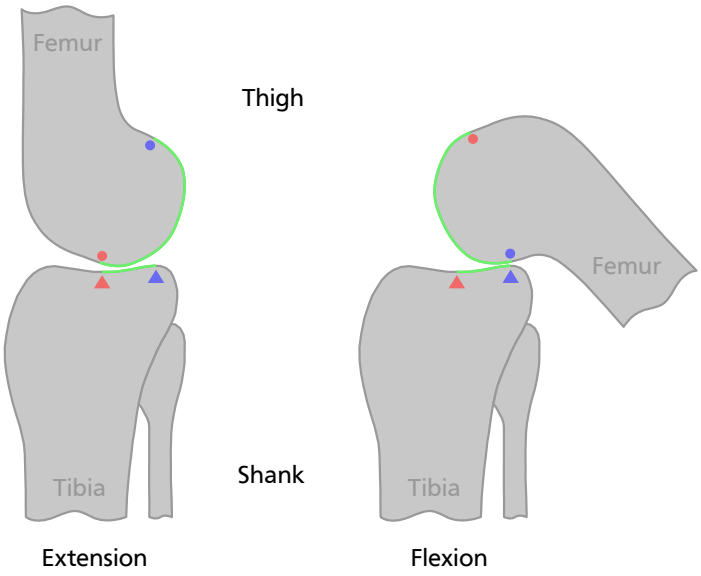

Figure 2.2.: Rolling and gliding mechanism in flexion and extension of the knee joint adapted from Klein and Sommerfeld [125].

an anterior gliding in deep flexion. In flexed position, the contact point, shown in blue, is located posteriorly. The resulting shift of the contact point on both bones is indicated by the green lines. The different lengths of these lines illustrate the ratio of rolling to gliding. The combined rotation and translation in the knee joint cause a constantly changing center of rotation which is also known as polycentric rotation.

A common classification of joints in the human body distinguishes shape and configuration of idealized joint surfaces with reduced complexity and neglected interactions between the different degrees of freedom. Figure 2.3 shows a selection of typical idealized joint types with the corresponding movement axes indicated in red. Ball joints have a ball-shaped head and a concave socket providing three rotational degrees of freedom about three perpendicular movement axes. Examples for ball-like joints include hip and shoulder joints. Condyloid joints consist of an ovoid head that is received into an elliptical cavity enabling two rotational degrees of freedom about two perpendicular movement axes. The wrist joint is an example of a condyloid-like joint. Hinge joints have a cylindrical head and a gutter-like socket which permit only one rotational degree of freedom about a single movement axis. The elbow joint is an example of a hinge-like joint. Additional joint types found in the human body are pivot joints that consist of a cylindrical head fitted into a corresponding hollow socket, saddle joints which have two concave curved surfaces and plane joints that allow gliding motions of plane joint surfaces.

The flexibility of the vertebral column plays an important role in many human motions. It consists of twenty-four articulated vertebrae which support head, neck and trunk. Above and below each vertebra are facet joints that guide and limit the spinal motion. The facet joints are aligned in a way to allow flexion and extension but limiting rotation in order to protect the spinal nerves. The vertebral column is divided into the cervical spine (C1-C7), thoracic spine (T1-T12) and lumbar spine (L1–L5) as well as the fused sacrum (S1-S5).

Biomechanical simulations that consider human whole-body motions largely use idealized joint types such as ball and hinge joints with single point joint centers for the modeling of human

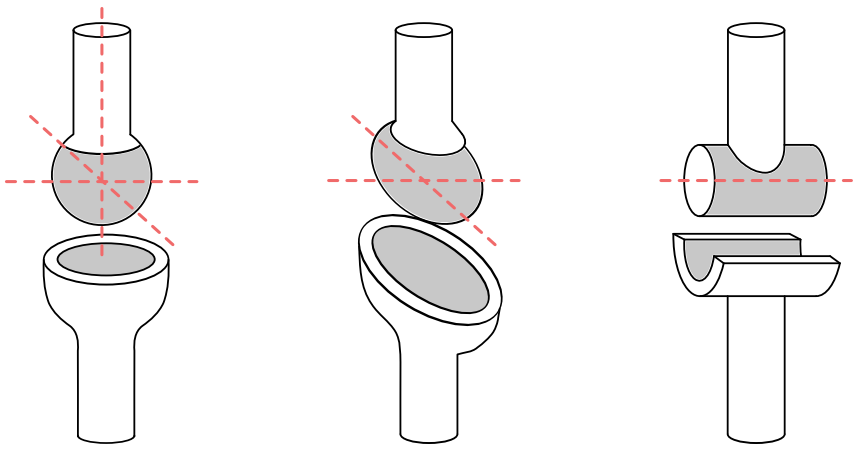

Figure 2.3.: Selection of typical idealized joint types in the human body with indicated movement axes (red) adapted from Faller and Schünke [77].

joints, e.g. [239, 242, 260]. The vertebral column mostly is either approximated by a small number of idealized joints or assumed to be rigid. More detailed models of joint geometries, e.g., [131, 252], are mainly applied for the selective investigation of particular characteristics in specific human joints.

2.2.3 Muscles

Muscles are the actuating elements of the human body and permit locomotion, maintain posture as well as control a number of physiological processes in the body. Involuntary contracting cardiac and smooth muscles are found in organs and the heart, while skeletal muscles that contract voluntarily upon command are attached to bones and effect skeletal motion.

The human body comprises more than six hundred skeletal muscles which consist of a muscle belly with several parallel muscle fibers and markedly thinner tendons. Muscle fibers are composed of sarcomeres and perform a coordinated contraction upon activation by shortening each sarcomere up to a certain minimum length. Muscle activation is triggered by neural control and results from depolarization and repolarization processes in the muscle fibers which produce an electrical activity [126]. The smallest functional unit to describe this neural control is also known as a motor unit. The length of the muscle fibers determines the maximum shortening length and maximum contraction velocity, whereas the maximum muscle force is proportional to the physiologic cross-sectional area which describes the number of parallel muscle fibers. Tendons are elastic bundles of collagen fibers with a great tensile strength and transmit the muscle forces produced by muscle fiber contraction to the skeleton. Because muscle fibers can only actively exert translational pulling forces, muscles act antagonistically on each joint with at least one muscle for each direction. A single joint can be actuated by several monoarticular and polyarticular muscles resulting in a high level of muscular redundancy. Monoarticular muscles act on a single joint, while polyarticular muscles span and affect multiple joints. The effect of an individual muscle on a joint depends on the direction of force exertion defined by the muscle path and the lever arm given by the perpendicular distance of its insertion point to the

movement axis of the joint. Besides the active pulling forces, muscles also apply passive forces that originate from passive structures of tendons, ligaments and connective tissue. A detailed explanation of the muscle contraction mechanism based on muscle proteins that slide past each other to generate movement is given by the sliding filament theory [114].

There are two prevalent types of biomechanical muscle models. The Hill-type muscle model based on experimentally determined force-length and force-velocity relations is a descriptive lumped parameter model and focuses on macroscopic processes in the muscle [107]. It consists of a contractile element that represents the active force generating properties as well as series and parallel elastic elements to model the passive muscle structures. The Huxley-type muscle model describes muscle dynamics on the level of muscle proteins and provides the individual forces in each muscle fiber [113]. It models microscopic processes in the muscle and is suitable for the study of muscle force transitions. Due to the accurate description of the relation between muscle force and muscle state including length, velocity and activation as well as a high computational efficiency, Hill-type muscle models are mostly applied in biomechanical simulations of the human locomotor system, e.g., [12, 34, 91]. The inverse dynamics simulation investigated in this thesis does not depend on biomechanical muscle models but provides joint forces and torques that can be used for the subsequent model-based estimation of muscle forces and activities.

2.2.4 Soft Tissue

Soft tissue is a collective term that includes compliant tissues which connect, support or surround other structures of the body such as skin, fat, muscles, connective tissue or body fluids. During human motions, these tissues act like wobbling masses that can move or wobble relatively to the rigid skeleton and exert characteristic passive forces on the locomotor system. The biomechanical impact of wobbling masses depends on the actual motion task which determines the mechanical excitation of the soft tissue as well as the stiffness of strained and unstrained muscles.

In dynamics simulations of the human locomotor system, wobbling masses, if considered relevant, are commonly modeled as point masses attached to related body segments by linear or nonlinear spring-damper elements, e.g., [8, 98, 258].

2.3 Motion Sequences

Most human motions follow a characteristic sequence of events and phases. This applies to repetitive motions like walking and running but also extends to ballistic motions like kicking a ball. In human motion analysis, the gait cycle is defined as the time interval between two successive occurrences of a repetitive event and is a common description of such a characteristic motion sequence [239]. The gait cycle typically starts with the heel strike as the moment of initial contact and ends with the next heel strike of the same foot. In between, the leg goes through different events that can be divided into a stance phase in which the foot is in contact with the ground and a swing phase that describes the motion of the foot forward through the air. The other leg undergoes exactly the same series of events but is displaced in time by half a cycle.

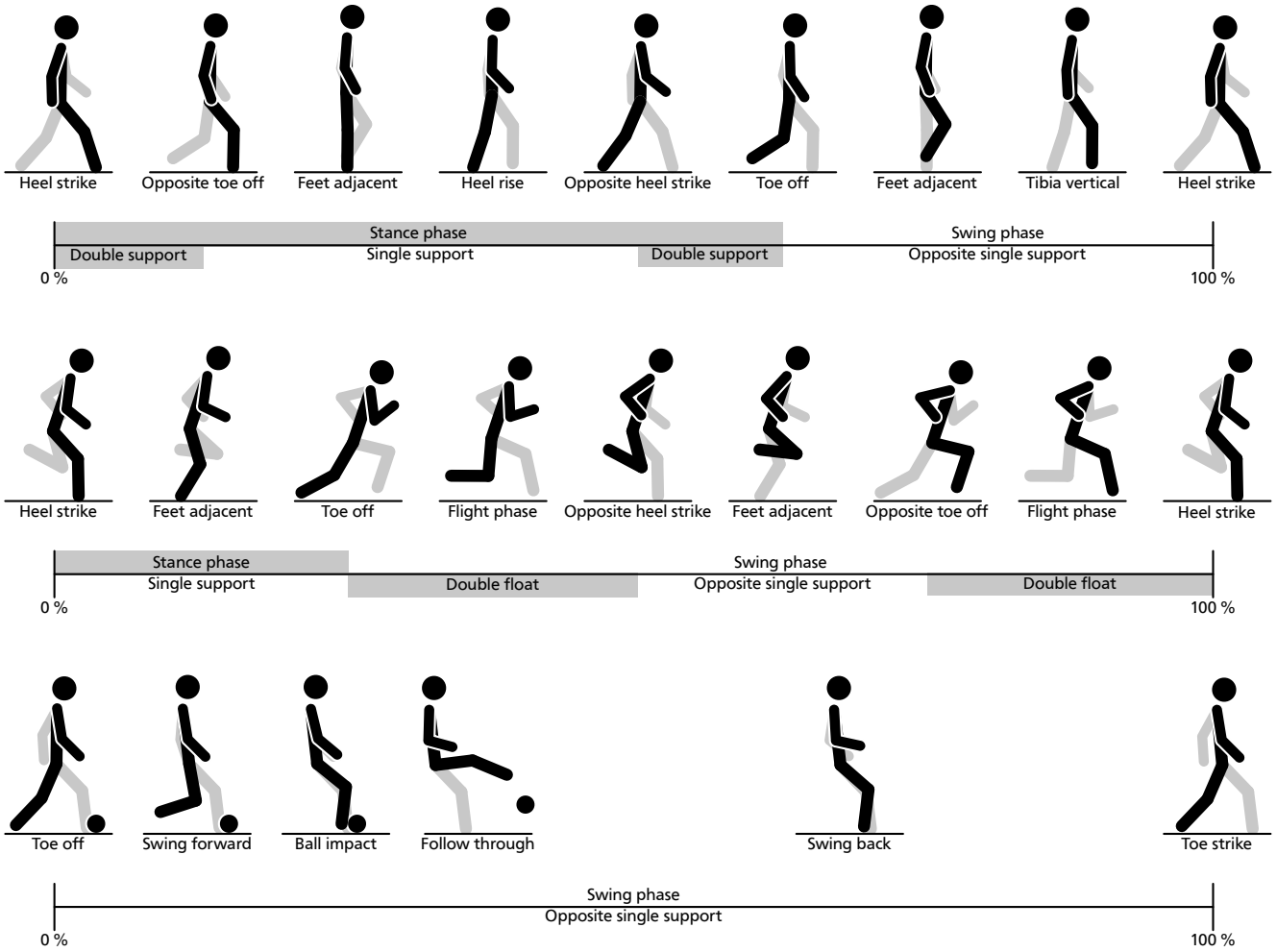

Figure 2.4.: Motion sequences and characteristic events of walking (top), running (middle) and kicking a ball (bottom) partially adapted from Novacheck [158] and Whittle [239].

Similar descriptions can be defined for other motion tasks. Figure 2.4 presents a visualization of the characteristic motion sequences for walking, running and kicking a ball.

Walking follows the sequence of the common gait cycle with a stance phase and a swing phase. The stance phase of a leg starts with the heel strike, passes through the moment when both feet are adjacent as well as the heel rise and ends with the toe off. A phase of double support occurs when both feet have contact with the ground which is initialized by the actual or opposite heel strike and terminated by the actual or opposite toe off. Each walking sequence comprises two periods of double support and two periods of single support. The swing phase starts with the toe off, contains the occasion when both feet are adjacent and the tibia of the shank is vertical and ends with the next heel strike. The stance phase usually lasts about 60 % of the gait cycle with approximately 10 % for each double support phase, while the swing phase takes about 40 % of the gait cycle [239]. With increasing walking speed, the swing phase becomes longer and the stance phase becomes shorter until the double support phase finally disappears and a double float phase occurs marking the transition from walking to running [152].

In running, the stance phase is initialized with the heel strike, goes through the moment when both feet are adjacent and is terminated by the toe off. The toe off happens before the opposite heel strike which results in a double float phase where no foot is in contact with the ground.

Each running sequence contains two periods of single support and two periods of double float that start with the actual or opposite toe off and end with the actual or opposite heel strike. The swing phase includes both double float phases and the occasion when both feet are adjacent. The stance phase generally takes about 30 to 40 % of the gait cycle and the swing phase lasts for the remaining 60 to 70 % of the gait cycle [158].

The characteristic motion sequence of kicking a ball is defined by the initializing toe off, the fast and powerful swing forward ensued by the ball impact and follow through as well as the rather slow swing back which is terminated by the final toe strike. The ball impact occurs at about 20 % of the motion sequence. An approach motion or explicit backswing are not considered in the motion task. The kicking motion can be regarded as a single swing phase with single support provided by the opposite foot.

2.4 Measurement Systems

Conventional biomechanical measurements are bounded to reversible measurement methods and measurands that are accessible without invasive techniques [150]. Hence, a direct measurement of many crucial variables in biomechanical investigations like joint forces and torques or muscle forces is impossible or unethical. Biomechanical simulations allow to estimate these variables based on a computational model of the human locomotor system and a series of feasible and relevant biomechanical measurements. In the study of human motion dynamics, the relevant measurands comprise external reaction forces as well as spatial motions of the individual body segments which allow to derive segment lengths and joint trajectories including linear or angular joint positions, velocities and accelerations. Spatial motions of body segments are typically recorded with motion capture techniques that allow to track the temporal sequence of spatial points, while external reaction forces are quantified with multi-axis force sensors usually installed in force plates. Additionally, electromyography can be used to measure the electrical activity of selected skeletal muscles in order to identify neuromuscular disorders or validate simulation results.

2.4.1 Motion Capture

Modern motion capture systems with high spatial and temporal resolution mostly apply optical marker-based tracking techniques to determine the three-dimensional motion of relevant body segments. Special markers attached to the considered body parts are triangulated at frequencies of 50 to 500 Hz by utilizing data captured from multiple infrared cameras that are calibrated to provide overlapping projections of the recorded human motion. This procedure measures the three-dimensional position of each marker center which is treated as a spatial point without any rotational information. The spatial orientation of body segments has to be inferred from the relative position of three or more markers. In passive systems, optically coated markers reflect infrared light that is generated externally near the camera lenses, while active systems use powered markers with an internal infrared light source. Passive markers have a low weight and do not require any cabling which reduces a possible impairment of the human motion. Due to an independent light control and powerful light sources, active markers can be identified individually and have a higher signal-to-noise ratio that facilitates data processing and increases

measurement accuracy. The restriction to infrared light makes the motion capture system robust against changes in visible light and allows to apply powerful light sources without distracting the human subject. The applied light sources typically generate short light pulses at defined frequencies in order to freeze the scene and reduce motion blur [242].

The markers can be attached directly to the skin of the subject or fixed as marker clusters mounted on rigid structures [239]. The marker clusters provide a defined marker configuration but suffer from additional weight and might lag behind the body segment during fast motions. Another approach uses a predefined marker set that is integrated into a close-fitting suit. In order to achieve an accurate tracking of the body segments and the underlying rigid skeleton, the markers are placed above prominent anatomical landmarks. These anatomical landmarks are internal or subcutaneous bony structures that are identified by specific manual palpation techniques. Local reference frames defined by at least three markers per body segment allow to derive spatial orientation and relative motions between body parts.

A typical problem in motion capture is marker occlusion which occurs when one or multiple markers are covered by a limb during the motion task or are hidden behind a structure of the experimental setup. In this case, the affected markers are not visible for the cameras and cannot be tracked. The problem can be solved by a careful selection of camera locations and additional data processing. The most relevant uncertainty sources in motion capture comprise soft tissue artifacts, anatomical landmark misplacement and instrumental error. All these uncertainties affect the tracking of the body segments. Soft tissue artifacts result from soft tissue deformations that cause relative marker movements with respect to the underlying bones [98]. A misplacement of markers as a consequence of an incorrect identification of anatomical landmarks can impair the location and orientation of local reference frames [60]. Instrumental error arises from intrinsic error sources, camera calibration or data processing. A comprehensive series of reviews on the theoretical background and important uncertainty sources in motion capture is provided by Cappozzo et al. [39, 47, 61, 130].

2.4.2 Force Plates

In the investigation of human motion dynamics, the most common force acting on the human body is the ground reaction force generated by the body standing on or moving across the ground [242]. The ground reaction force is a three-dimensional force vector that acts on each foot in contact with the ground and results from the body weight, dynamical effects during locomotion and interactions with objects or the environment. The force vector for each foot is specified by a vertical component, two perpendicular shear components which act parallel to the ground surface and a point of application also known as the center of pressure. In addition to the force vector, the free moment vector describes the reaction to the force couple exerted by the foot on the ground acting about the vertical axis in the center of pressure [6]. The force and free moment vectors represent the net effect of the actual pressure distribution on the contact surface between foot and ground.

Force plates typically consist of a rigid base plate that is supported by four multi-axis force sensors in each corner to determine the ground reaction force for a single foot. Available force sensors either apply strain gauges or use the piezoelectric, piezoresistive, capacitive or Hall effect to measure forces. Each force sensor produces an electrical signal per axis proportional to

the corresponding component of the applied force that is amplified and sampled at a frequency of about 1000 Hz. Considering the dimensions of the base plate and the relative locations of the force sensors, the three-dimensional ground reaction force and free moment vectors as well as the two-dimensional coordinates of the center of pressure can be calculated from the individual force measurements [156].

General problems of force plates in human motion analysis are the need for long walkways and the restriction to a single step per measuring run. Instrumented treadmills eliminate these limitations by providing a treadmill with integrated force plates for each foot. This allows to measure ground reaction forces in walking or running motions over long time series and at various speeds. Potential disadvantages of instrumented treadmills are an inadequate replication of the overground environment and an increased vulnerability to measurement errors due to the larger and more compliant structure [210]. One reason for possible deviations between treadmill and overground is the change in the belt speed as the foot decelerates it at initial contact and accelerates it at push off which effectively stores energy in the treadmill motor [239]. This effect can be minimized by using a large treadmill with a powerful actuation. A number of studies that compared treadmill and overground gait of healthy subjects obtained inconsistent results. Riley et al. for example reported no relevant differences in motion sequence or joint torques [182], while Alton et al. found significant changes in hip movements [9].

The most relevant uncertainty source in ground reaction force measurements is instrumental error caused by accuracy, nonlinearity, hysteresis and crosstalk of the force sensors and amplifiers as well as signal drift and noise depending on the sensor type [156]. Instrumented treadmills are additionally prone to interferences caused by structural compliance and belt friction, variability of belt speed as well as instrumental errors introduced by insufficient installation and calibration of force sensor [172, 210]. An extensive discussion of different force sensors and measurement methods for reaction forces is provided by Nigg and Herzog [156].

2.4.3 Electromyography

Electrical activity in skeletal muscles is the preliminary condition for any force development [126]. Electromyography is an electrophysiological measurement technique that allows to record this electrical activity produced by contracting muscles. In biomechanical measurements of human motions, surface electromyography with electrode patches is generally applied [239]. The measured signals can be used to validate simulation results or to provide a visible and temporal indication of muscle activity. The electrode patches are attached to the skin of the subject over the considered muscles and measure an electrical voltage between two electrodes relative to a reference electrode at a frequency of about 2000 Hz. The measured signal has to be amplified due to the small voltage amplitudes generated within the motor units and the attenuation caused by multiple layers of soft tissue between muscles and electrodes. Because the measured signal represents a superposition of electrical activities from many motor units, it is of random nature. Typical signal processing for an evaluation of muscle activity comprises rectification, low-pass filtering and normalization [126].

Electromyography enables insights into internal muscular processes and provides valuable information on muscle timings but also suffers from certain limitations. The application of surface electrodes restricts the recording to superficial muscles and excludes the investigation of deep

muscles. Variations in depth and conductivity of subcutaneous tissue at the recording site as well as interferences from adjacent muscles affect the measured signal and make it difficult to provide quantitative and repeatable results [239]. Additionally, the relation between the measured signals and resulting muscle forces is ambiguous and still a subject of ongoing research.

Uncertainty in electromyography mainly originates from changing tissue characteristics and muscle geometries during motion as well as crosstalk between nearby muscles and instrumental error in signal amplification. A comprehensive description of the theoretical background, measurement methods and signal processing in electromyography in given by Konrad [126].

3 Biomechanical Modeling and Simulation

According to Shannon, a simulation is “the process of designing a model of a real system and conduction experiments with this model for the purpose either of understanding the behavior of the system and its underlying causes or of evaluating various designs of an artificial system or strategies for operation of the system” [206]. In biomechanical simulations of human motions, both parts of this definition can apply. The first part involves the investigation of fundamental principles and concepts in human motion supplement to experimental studies, while the second part may relate to an integrated development of technical assistive devices like orthoses or prostheses. Typical simulation studies consist of a problem specification, the design, implementation and validation of a model as well as the run of the simulation and an application of the results. The considered problem in biomechanical simulations depends on the actual focus of research. In the case of inverse dynamics simulations, it is defined as the estimation of joint forces and torques from measured body segment motions and ground reaction forces. Biomechanical models in this context are simplified representations of the human locomotor system based on specific knowledge and assumptions [242]. Model parameters specify the dynamic properties of the biomechanical model and have to be personalized to the individual human subject. Due to the high complexity, these models are usually implemented in computational frameworks that facilitate model derivation and mathematical formalization. Within the modeling and simulation process, several common error sources like modeling errors, approximation and rounding errors or implementation and programming errors can affect the simulation results. For this reason, a systematical validation of the computational model is an important step to provide evidence that the biomechanical simulation produces credible and reliable results regarding the considered problem. Recent recommendations for the validation of biomechanical simulations comprise systematic tests of the software implementation, a comparison of simulation results with independently reported simulations or experiments and an evaluation of robustness towards uncertainties in model parameters as well as simulation inputs [106].

The human locomotor system is composed of a rather rigid skeleton framework that can be divided into individual body segments connected by movable joints with different degrees of freedom and ranges of motion actuated by numerous skeletal muscles with specific force characteristics and lever arms. This type of system can be efficiently modeled with tree-structured multibody system dynamics [242, 259, 260]. The concept of multibody system dynamics applies rigid links connected by constrained joints to describe mechanical systems with interconnected bodies that can move relative to each other [80]. Each link represents a body with specific length, mass, center of mass and inertia tensor. The degrees of freedom (DOF) denote the minimum number of variables required to completely define the configuration space of the mechanical system. An unconstrained body in three-dimensional space (3D) has six degrees of freedom, i.e., three translational and three rotational variables, while the same body in two-dimensional space (2D) only has three degrees of freedom, i.e., one rotational and two translational variables. Constraint conditions in joints imply restrictions in the degrees of freedom of one or multiple bodies. Typical constrained joints are the prismatic joint that allows a relative translation along a single axis and restricts all remaining translations and rotations as well as the revolute joint which enables relative rotation about a single axis and restricts all

other rotations and translations. A comprehensive introduction to multibody system dynamics and efficient dynamics algorithms is provided by Featherstone [80].

3.1 Related Work

In literature, there is a large number of biomechanical models of the human locomotor system based on multibody system dynamics. Some of the models apply a conceptional modeling approach focusing on the global behavior and reducing model complexity. The other part of the models uses a representative modeling approach implementing morphological and physiological details in order to provide causal explanations of musculoskeletal mechanisms. In reference to these two different modeling approaches, Full and Koditschek introduced the terms templates regarding conceptional models and anchors regarding representative models [86].

3.1.1 Modeling Approaches

Template models (TM) describe and predict a target behavior with the least possible number of variables and parameters and approximate the human locomotor system with simple and universal modeling elements like springs and point masses, e.g., [4, 32, 92]. The reductive character of these models facilitates the identification of fundamental principles and concepts in human locomotion. The inverted pendulum model introduced by Alexander [4], shown in the left part of Figure 3.1, is an example of a two-dimensional template model used in the investigation of human walking. It consists of a point mass representing the body mass and two stiff legs with point feet that are connected by revolute joints at the hip. Each one-dimensional revolute joint provides one degree of freedom, while the point mass is able to move in two dimensions relative to a fixed base resulting in two additional degrees of freedom. The model can describe passive human-like walking motions on shallow slopes but exhibits some unnatural

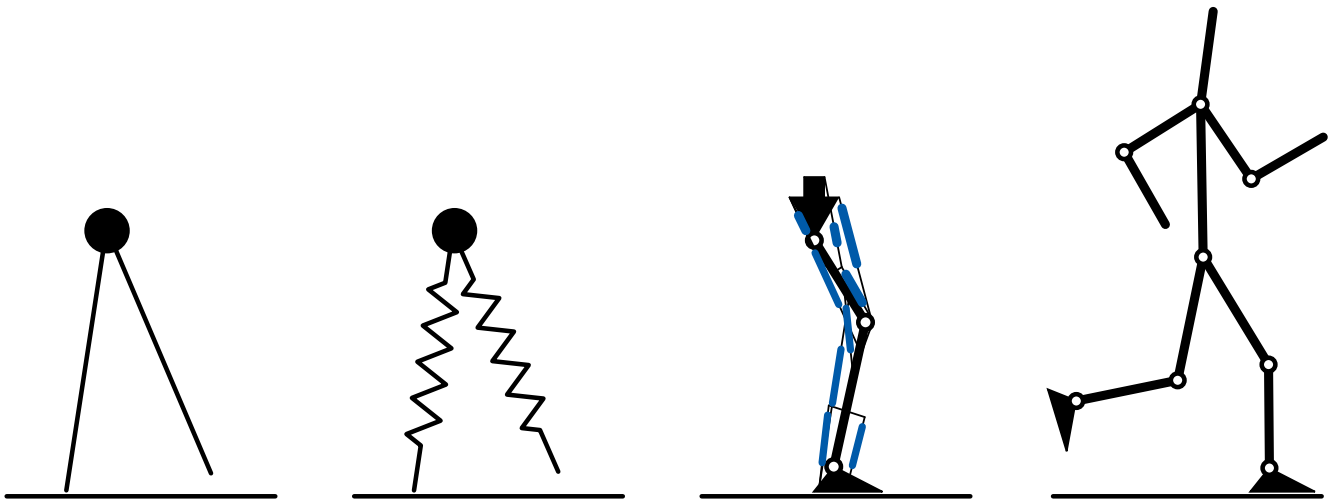

Figure 3.1.: Schematic diagrams of exemplary two-dimensional template models by Alexander [4] (left) as well as Geyer et al. [92] (middle left) and anchor models by Stelzer [222] (middle right) as well as Pàmies-Vilà et al. [167] (right).

discontinuities in reproducing the displacement of the total center of mass. The bipedal spring-loaded inverted pendulum model presented by Geyer et al. [92], depict in the middle left part of Figure 3.1, extends the inverted pendulum model by replacing the two stiff legs with two linear springs. The springs emulate the elastic and energy retrieving characteristics of the human leg and add two degrees of freedom. With this enhancement, the model can reproduce basic dynamics of human walking and running during stance phase like ground reaction forces as well as total center of mass displacement in sagittal plane. Further examples of template models found in literature are listed in the upper part of Table 3.1.

Anchor models (AM) are more elaborate representations of the human locomotor system involving individual body segments, joint geometries or muscle dynamics, e.g., [136, 167, 222]. The detailed model structure allows to investigate particular biomechanical characteristics such as hip joint torques or muscle forces in knee joint flexion. Some of these representative modeling approaches neglect the dynamical influence of the arms because arm swinging in human locomotion primarily is the result of passive dynamics and its impact is mainly limited to a reduction of the free moment in ground reaction forces [54]. In contrast to full body models (FBM) that consider all body segments, e.g., [167, 208], these lower body models (LBM) focus on the lower limbs and simplify the upper body dynamics with a point mass or a single body segment typically combining head, arms and trunk, e.g. [136, 222]. The lower body model for jumping motions used by Stelzer [222] shown in the middle right part of Figure 3.1 is an example for a two-dimensional anchor model with muscle actuation. It describes one leg and comprises four body segments for upper body, thigh, shank and foot connected by three revolute joints and nine muscles based on the Hill-type muscle model indicated in blue. Each body segment has a particular length, mass, center of mass and moment of inertia. The three one-dimensional revolute joints provide three degrees of freedom, whereas the upper body segment is able to translate in two dimensions relative to a fixed base adding two degrees of freedom. The muscles represent individual muscles or muscle groups involved in human jumping. Every muscle has specific attachment points and muscle paths on the body segments spanning one or two joints. The model was mainly applied for forward dynamics optimization where the activation signals of the muscles are optimized with regard to an appropriate objective function minimizing the difference between simulated and measured joint trajectories. The full body model deployed by Pàmies-Vilà et al. [167], presented in the right part of Figure 3.1, is another example for a two-dimensional anchor model. It consists of twelve links representing all major body segments but hands and assuming a rigid trunk segment. Also in this case, each body segment features a specific length, mass, center of mass and moment of inertia. The body segments are connected by eleven one-dimensional revolute joints resulting in eleven degrees of freedom. Additionally, the trunk segment can move in two translational and one rotational dimension relative to a fixed base providing another three degrees of freedom. In contrast to the previous anchor model, this modeling approach does not provide any muscles because it was exclusively used for inverse dynamics simulation to estimate joint torques in human walking which does not require the consideration of muscle dynamics. Further examples of anchor models found in literature are listed in the lower part of Table 3.1. The last three rows describe anchor models provided by the modeling and simulation environments AnyBody [176] and OpenSim [62]. AnyBody is a commercial software package containing functions for musculoskeletal modeling, inverse dynamics simulation and parameter optimization, while OpenSim is a free and open-source software package supporting musculoskeletal modeling, inverse dynam-

Table 3.1.: Selection of biomechanical models for the human locomotor system divided into template models (TM) and anchor models (AM) as well as lower body models (LBM) and full body models (FBM).

Type	Reference	Scope	Properties	Application
TM	Alexander [4]	LBM in 2D	2 joint DOF, 2 base DOF, 1 mass, 2 segments	walking
	Blickhan [32]	LBM in 2D	2 joint DOF, 2 base DOF, 1 mass, 1 passive spring leg	running and hopping
	Geyer et al. [92]	LBM in 2D	4 joint DOF, 2 base DOF, 1 mass, 2 passive spring legs	locomotion
	Häufle et al. [99]	LBM in 2D	1 joint DOF, 1 base DOF, 1 mass, 1 muscle	hopping
AM	Günther [97]	LBM in 2D	10 joint DOF, 3 base DOF, 11 segments, 28 muscles	walking
	Henze [104]	LBM in 3D	16 joint DOF, 6 base DOF, 15 segments, 16 torque drives	walking
	Silva et al. [208]	FBM in 3D	38 joint DOF, 6 base DOF, 16 segments, 38 torque drives	walking
	Stelzer [222]	LBM in 2D	2 joint DOF, 0 base DOF, 2 segments, 5 muscles	kicking
	Stelzer [222]	LBM in 2D	3 joint DOF, 2 base DOF, 3 segments, 9 muscles	jumping
	Ackermann [1]	LBM in 3D	21 joint DOF, 6 base DOF, 8 segments, 21 torque drives	walking
	Ackermann [1]	LBM in 2D	3 joint DOF, 2 base DOF, 5 segments, 8 muscles	disturbed walking
	Alnu'man [7]	LBM in 2D	5 joint DOF, 3 base DOF, 7 segments, 5 torque drives	walking with prosthesis
	Geyer and Herr [91]	LBM in 2D	6 joint DOF, 3 base DOF, 7 segments, 14 muscles	walking
	Lipfert [136]	LBM in 2D	6 joint DOF, 2 base DOF, 7 segments, 6 torque drives	walking and running
	Pàmies-Vilà et al. [167]	FBM in 2D	11 joint DOF, 3 base DOF, 12 segments, 11 torque drives	walking
	AnyBody[1] [176]	LBM in 3D	14 joint DOF, 6 base DOF, 7 segments, 110 muscles	locomotion
	OpenSim[2] [62]	LBM in 3D	23 joint DOF, 6 base DOF, 12 segments, 76 muscles	locomotion
	OpenSim[3] [62]	FBM in 3D	29 joint DOF, 6 base DOF, 12 segments, 76 muscles	locomotion

[1] refers to 'LegTLEM' model in AnyBody [2] refers to 'Gait2392' model in OpenSim [3] refers to 'Full Body Running Model' in OpenSim

ics simulation as well as forward dynamics simulation based on measured joint trajectories. Both software packages offer generic human body models and are getting more and more common in biomechanical investigations of human motion dynamics as well as biomechanical uncertainty and sensitivity analysis, e.g., [3, 153, 227].

The application of two-dimensional models is primarily motivated by the large amplitudes of joint motions in sagittal plane for many human motions. These models reduce the modeling and computation effort but withhold some characteristic patterns in human motions such as pelvic rotation, pelvic obliquity and lateral body displacement [239]. Although a two-dimensional modeling approach can be considered as appropriate for walking [5], the neglect of frontal and transverse plane motions can affect the estimation of joint torques in other motion tasks.

3.1.2 Model Parameters

The application of subject-specific biomechanical measurements obtained from motion capture and force plates in biomechanical simulations of human motions necessitates the adaptation of model parameters in order to personalize the biomechanical model to the subject that performed the considered motion task. This also includes the implementation of gender-specific physiological differences. Number and type of model parameters depend on the actual model structure and complexity. In anchor models used for inverse dynamics simulations, the required model parameters most likely contain anthropometric parameters like length, mass, center of mass and inertia tensor of individual body segments, joint center locations as well as wobbling mass parameters. Personalized anthropometric parameters and joint center locations are commonly estimated with scaling methods or regression models.

Scaling methods are based on a generic biomechanical model that is adjusted in order to match the anthropometry of an individual subject [62]. The scaling procedure applies scaling factors derived from subject-specific motion capture data and body mass to adapt the model parameters including segment lengths and joint center locations as well as inertial parameters comprising the masses, centers of mass and inertia tensors of the individual body segments. In addition, other length-based model parameters such as muscle lengths or lever arms can be matched. Uncertainties in the obtained model parameters originate from variances in the body mass measurement and motion capture data as well as the quality and applicability of the generic model. Available generic models typically represent a healthy adult male subject obtained from different measurements on limited populations of Caucasian subjects, e.g., [40, 174]. The modeling and simulation environments AnyBody and OpenSim rely on scaling methods for the estimation of personalized anthropometric parameters [40, 62]. Regression models apply statistical relations between the unknown model parameters and easy to measure variables. Most regression models are based on linear regression equations for the estimation of anthropometric parameters, e.g., [58, 66] or joint center locations, e.g. [102, 177]. These linear models determine personalized model parameters by multiplying subject-specific measurements such as body mass, segment lengths or anatomical landmark positions with constant regression parameters. Three common collections of regression equations for the estimation of anthropometric parameters in adult subjects have been published by Winter [242], de Leva [58] and Dumas et al. [66, 67, 68]. The particular regression parameters were calculated from measurements on rather small populations of Caucasian subjects. While the model by Winter is restricted to male subjects, the other

two models provide individual parameters for both genders. Due to specific assumptions in the derivation of the parameters, the models by Winter and de Leva restrict the center of mass to the proximal-distal axis and presume a diagonal inertia tensor. The model by Dumas et al. does not restrain the center of mass location and inertia tensor orientation. Uncertainties in the obtained model parameters result from variations in the body mass measurement and motion capture data as well as the quality of the applied regression model. Further details on available methods for the estimation of subject-specific joint center locations and anthropometric parameters are provided in Chapter 7 and 8.

The estimation of personalized wobbling mass parameters is complicated by the ambiguous definition of the term wobbling mass which also leads to various modeling approaches in literature. Typically, the mass of a body segment is separated into a bone mass and a wobbling mass whereas the wobbling mass is assumed to be a point mass. Both masses are connected by linear spring-damper elements, e.g., [8, 139, 258] or nonlinear spring-damper elements, e.g. [98, 96, 163] that enable a relative movement. Most wobbling mass models restrict these relative movements to translational motions, while a few modeling approaches additionally allow rotational motions, e.g., [96]. Published model parameters describing the ratio between bone and wobbling mass as well as stiffness and damping constants are generally obtained from experimental estimations and therefore specified for a single human subject or motion task. Alonso et al. compared simulated ground reaction forces produced by two versions of a two-dimensional lower body anchor model with measured ground reaction forces for walking, running and drop jumping motions performed by five healthy subjects [8]. The first version of the biomechanical model had three wobbling masses connected to trunk, thigh and shank segments, while the second version of the biomechanical model only had one wobbling mass connected to the trunk segment. All wobbling masses represented half of the corresponding segment masses and were modeled as point masses coupled to the center of mass by linear spring-damper elements as shown in Figure 3.2. The relative movement of the wobbling masses was restricted to the proximal-distal axis of the body segment. The authors applied an optimization approach to find the optimal natural frequencies and damping coefficients with minimizing the deviations between simulated and measured vertical ground reaction forces. The evaluation

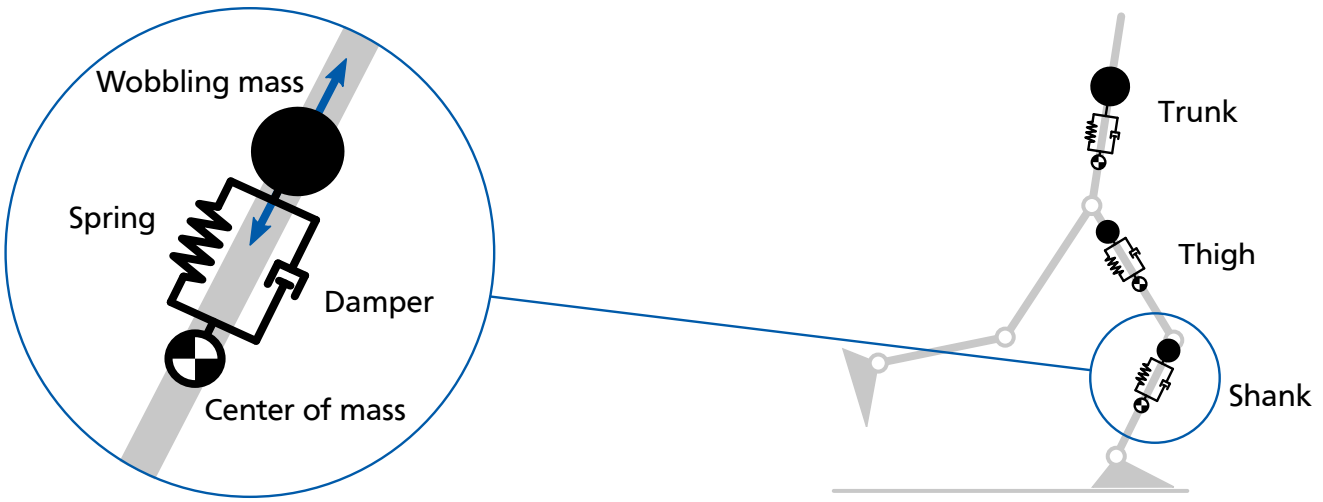

Figure 3.2.: Schematic diagram of an exemplary wobbling mass model with linear spring-damper elements attached to trunk, thigh and shank adapted from Alonso et al. [8].

of the results revealed that the wobbling masses in thigh and shank had no relevant influence on the simulated ground reaction forces in all motion tasks, while the wobbling mass in the trunk significantly reduced deviations in drop jumps but had almost no impact in the other motion tasks. For this reason, wobbling masses are mainly considered in the investigation of jerky motions like running and jumping. Uncertainties in wobbling mass parameters are difficult to quantify and can potentially become quite high, due to the variable soft tissue behavior under mechanical excitation in different motion tasks.

A general problem in biomechanical modeling and simulation of human motions is dynamic inconsistency due to accumulated errors in biomechanical measurements and model parameter estimation. Dynamic inconsistency leads to differences between the measured ground reaction forces and simulated ground reaction forces predicted by the personalized biomechanical model in combination with the measured joint trajectories. In inverse dynamics simulations, these residual forces can be compensated by the base joints that connect the biomechanical model with a fixed base but nevertheless are an indication for measurement and parameter uncertainty. An approach to handle dynamic inconsistency is to modify the most uncertain simulation inputs and model parameters in order to reduce or eliminate the residual forces and provide a consistent set of model parameters and biomechanical measurements. Related algorithms found in literature differ in the assessment of simulation input and model parameter uncertainty. The residual reduction algorithm applied by Delp et al. [62] utilizes static optimization to adapt joint trajectories and the center of mass in the torso segment, while the corrected force plate sharing algorithm presented by Pàmies-Vilà [164] assumes uncertain force plate measurements and adjusts the measured ground reaction forces in stance phase. Both approaches are able to reduce the residual forces but modify essential measurands based on assumed uncertainties. A systematic evaluation of uncertainty sources in biomechanical measurements can help to select the actual most uncertain measurand and reduce the negative impact of corrective signal processing.

3.2 Contribution

The modeling and simulation framework applied in this thesis provides a detailed three-dimensional biomechanical model of the human locomotor system and efficient algorithms for the evaluation of the inverse dynamics procedure. The biomechanical model reflects the current state of research in representative modeling approaches for the determination and investigation of joint torques in human whole-body motions. Due to the application of a comprehensive and recently updated regression model for anthropometric parameters [69], the biomechanical model can be easily personalized to young adult female and male subjects. The model parameters cover the relevant three-dimensional dynamic properties and do not apply restrictive assumptions on the center of mass position or inertia tensor orientation in the individual body segments. The effect of soft tissue dynamics is considered by the integration of a wobbling mass model that was developed for the assessment of walking, running and jumping motions. For the implementation of the biomechanical model and the inverse dynamics procedure, a modular software design based on an efficient and validated multibody systems library [246] is applied.

3.3 Methods

For the inverse dynamics simulation considered in this thesis, a three-dimensional full body anchor model based on tree-structured multibody system dynamics is applied to model the human locomotor system for walking, running and kicking a ball. This approach allows to investigate the impact of uncertainties in model parameters and simulation inputs of lower and upper limbs on the examined joint torques comprising hip, knee and ankle torques of the right leg in sagittal plane. The following assumptions are made in the modeling process:

A1 Each body segment is a rigid link with a constant length, mass, center of mass and inertia tensor during the motion sequence [242].

A2 All joints of the human locomotor system are either ball, condyloid or hinge joints with three, two or one degrees of freedom and single point joint centers [242].

A3 Other modeling elements than rigid links such as joints, springs or dampers are massless [80].

A4 Wobbling masses in the trunk are sufficient to model the dynamics of soft tissues during the motion sequence [8].

A5 Hand motions are negligible for the considered motion tasks.

A6 Foot segments are rigid during the motion sequence.

3.3.1 Biomechanical Model

The structure of the applied biomechanical model, shown in Figure 3.3, consists of fourteen body segments and thirteen rotatory joints with different degrees of freedom. Each leg is modeled with three body segments representing thigh, shank and foot. These body segments are connected by the ankle joint (AJ) with three degrees of freedom, the knee joint (KJ) with one degree of freedom and the hip joint (HJ) with three degrees of freedom. Each arm is modeled with two body segments representing upper and lower arm as well as the elbow joint (EJ) with one degree of freedom and the shoulder joint (SJ) with three degrees of freedom. The hands are considered as not actuated point masses attached to the distal ends of the lower arm segments. Head, thorax, abdomen and pelvis are individual body segments that are connected by the lower neck joint (LNJ) corresponding to the facet joint C7/T1, the upper lumbar joint (ULJ) corresponding to the facet joint T12/L1 and the lower lumbar joint (LLJ) corresponding to the facet joint L5/S1. Lower neck joint and lower lumbar joint each have three degrees of freedom, while the upper lumbar joint has two degrees of freedom and restricts rotations about the superior-inferior axis. In total, the biomechanical model has thirty degrees of freedom.

In addition to the rotatory joints that link the individual body segments, a base joint (BJ) with six degrees of freedom connects the biomechanical model at the lower lumbar joint with a fixed base that provides the global reference frame. The base joint consists of three translational and three rotatory degrees of freedom and allows an unconstrained relative motion between biomechanical model and fixed base. In contrast to the rotatory joints, the base joint should not

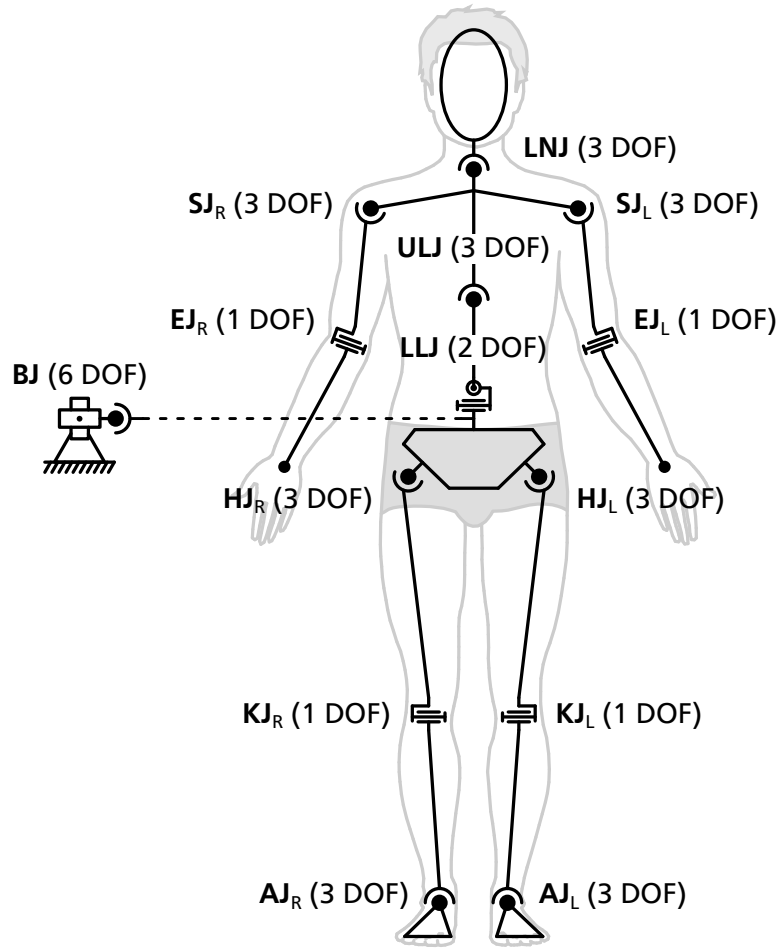

Figure 3.3.: Schematic diagram of the biomechanical model with fourteen body segments and thirteen rotatory joints plus one base joint

be directly controlled by measured joint trajectories derived from motion capture data because the induced forces and torques would cause a dynamical decoupling of lower and upper body at the attachment point. For this reason, a proportional-derivative control approach is used to calculate joint forces and torques $\boldsymbol{\tau}_{BJ} \in \mathbb{R}^6$ in order to compensate any dynamic inconsistency and follow the measured time series of joint positions $\boldsymbol{q}_{BJ} \in \mathbb{R}^6$ and joint velocities $\dot{\boldsymbol{q}}_{BJ} \in \mathbb{R}^6$ at the base joint [167]. The control law is given by

$$\boldsymbol{\tau}_{BJ} = K_p \left(\boldsymbol{q}_{BJ} - \hat{\boldsymbol{q}}_{BJ} \right) + K_d \left(\dot{\boldsymbol{q}}_{BJ} - \hat{\dot{\boldsymbol{q}}}_{BJ} \right)$$

with the proportional control gain K_p, derivative control gain K_d, actual joint positions $\hat{\boldsymbol{q}}_{BJ}$ and actual joint velocities $\hat{\dot{\boldsymbol{q}}}_{BJ}$. The control gains are tuned to enable fast settling times and ensure robust performance with regard to simulation input and model parameter uncertainty.

Personalized model parameters for a healthy female subject (27 yrs, 161 cm, 57 kg) and male subject (32 yrs, 179 cm, 85 kg) are estimated with regression models providing individual regression parameters for both genders based on measurement datasets with subjects of comparable age and stature. The joint center locations are determined from subject-specific anatomical landmark positions measured by motion capture and regression equations provided by Reed et al. [177] and Dumas et al. [66, 68]. The obtained joint center locations enable to derive the

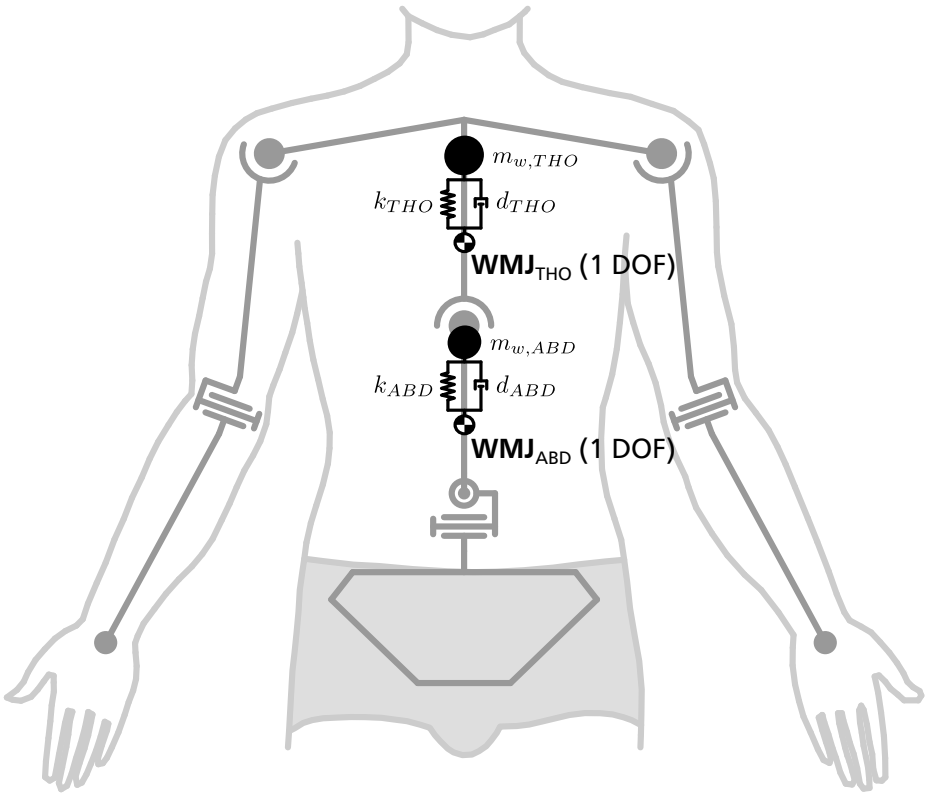

Figure 3.4.: Schematic diagram of the wobbling mass model with linear spring-damper elements attached to thorax and abdomen.

personalized segment lengths. In combination with the subject-specific body mass and body height, these segment lengths are used to estimate the anthropometric parameters for all body segments including mass, center of mass and inertia tensor based on regression equations provided by Dumas et al. [66, 67, 68]. Further details on the estimation of joint center locations and anthropometric parameters are given in Chapter 7 and 8.

In order to incorporate the effect of soft tissue dynamics, wobbling mass models with linear spring-damper elements are attached to the trunk of the biomechanical model following the modeling approach proposed by Alonso et al. [8]. Due to the separation of the trunk into thorax (THO) and abdomen (ABD), two individual wobbling mass models are applied for each trunk segment as illustrated in Figure 3.4. For thorax and abdomen segment, the segment mass m_s is divided by the mass ratio $r_m \in [0, 1.0]$ into a wobbling mass m_w and a bone mass m_b according to

$$m_w = r_m \, m_s,$$
$$m_b = (1.0 - r_m) \, m_s.$$

The bone mass is assigned to the corresponding body segment, while the wobbling mass is assigned to a point mass connected to a translational joint with one degree of freedom (WMJ). The one-dimensional joint enables relative motions between the body segment and the wobbling mass along the proximal-distal axis which coincides with the superior-inferior axis in the trunk. A linear spring-damper element connects the wobbling mass with the segment center of

mass. The spring constant k and damping constant d are derived from an appropriate natural frequency ω and damping coefficient χ. The spring constant can be calculated by

$$\omega = \sqrt{\frac{k}{m_w}},$$
$$k = \omega^2 \, m_w,$$

while the damping constant is determined by

$$\chi = \frac{d}{2 \, m_w \, \omega},$$
$$d = 2 \, m_w \, \omega \, \chi.$$

With the gravitational acceleration g, the resting length l_r of the linear spring is specified as

$$l_r = \frac{m_w \, g}{k}$$

which ensures that the wobbling mass occupies the segment center of mass in stationary upright standing position. All other model parameters of thorax and abdomen segment are kept unchanged. The wobbling mass models are used for all considered motion tasks.

3.3.2 Kinematics Simulation

A linkage of body segments connected by joints is referred to as open kinematic chain if the last or most distal body segment is free to move, while the first or most proximal body segment is constrained to a fixed base [259]. The spatial pose of body segments in an open kinematic chain like the leg is defined by the arrangement of body segments and joints in the kinematic chain and the individual joint positions. In order to place the foot as the most distal body segment at an arbitrary position with an arbitrary orientation in space, the kinematic chain needs to have at least six degrees of freedom. In the human locomotor system, legs and arms typically have more than six degrees of freedom which results in a kinematic redundancy [259]. This redundancy leads to an infinite number of possible joint positions that describe one particular spatial pose of the most distal body segment. Since hand segments and wrist joints are not considered in the applied biomechanical model, only the legs are affected by kinematic redundancy.

The direct kinematics problem calculates the spatial pose of the most distal body segment in a kinematic chain as a function of known joint positions $\boldsymbol{q} \in \mathbb{R}^m$. The spatial pose is defined by a rotation matrix ${}^0\boldsymbol{R}_m \in \mathbb{R}^{3\times3}$ and a translation vector ${}^0\boldsymbol{r}_m \in \mathbb{R}^3$ describing the relative motion between the reference frame of a fixed base F_0 and the reference frame of the most distal body segment F_m. Applying homogeneous transformations ${}^{i-1}\boldsymbol{T}_i(q_i) \in \mathbb{R}^{4\times4}$ with $i = 1 \ldots m$, the direct kinematics problem can be written in a recursive fashion as

$$\begin{aligned} {}^0\boldsymbol{T}_m &= {}^0\boldsymbol{T}_1(q_1) \cdots {}^{m-1}\boldsymbol{T}_m(q_m) \\ &= \left[\begin{array}{ccc|c} & {}^0\boldsymbol{R}_m & & {}^0\boldsymbol{r}_m \\ \hline 0 & 0 & 0 & 1 \end{array}\right], \end{aligned}$$

where m denotes the degrees of freedom in the kinematic chain. The individual homogeneous transformations represent relative motions between the successive reference frames and are functions of single joint positions.

The inverse kinematics problem determines the joint positions corresponding to a known spatial pose of the most distal body segment. This problem is much more complex than the forward kinematics problem because the equations to solve are nonlinear and possible kinematic redundancies might introduce ambiguity [207]. In general, there may exist no, one or multiple solutions to the inverse kinematics problem. An admissible solution is only guaranteed if the spatial pose lies within the achievable workspace of the kinematic chain and the available degrees of freedom can reproduce the particular position and orientation in space. The determination of joint trajectories from motion capture data basically is an inverse kinematics problem. The recorded marker positions specify the poses of the body segments during the motion task which have to be translated to the corresponding time series of joint positions, joint velocities and joint accelerations. In contrast to the classical inverse kinematics problem where only the pose of the most distal body segment is known, the motion capture data also contain spatial information about the other body segments. This additional information significantly facilitates the calculation of the joint trajectories.

3.3.3 Dynamics Simulation

The relationship between joint motions and joint torques as well as possible external forces in a multibody system with potentially multiple kinematic chains and $n \geq m$ degrees of freedom described by generalized coordinates can be deduced from the Lagrange formalism or the Newton-Euler formalism [207]. The inverse dynamics problem calculates the joint torques $\boldsymbol{\tau} \in \mathbb{R}^n$ that are required to generate a known motion specified by joint accelerations $\ddot{\boldsymbol{q}} \in \mathbb{R}^n$, joint velocities $\dot{\boldsymbol{q}} \in \mathbb{R}^n$ and joint positions $\boldsymbol{q} \in \mathbb{R}^n$ considering known external forces $\boldsymbol{f} \in \mathbb{R}^6$. The motion equation for the inverse dynamics problem is given by

$$\boldsymbol{\tau} = \boldsymbol{M}(\boldsymbol{q})\,\ddot{\boldsymbol{q}} + \boldsymbol{c}(\boldsymbol{q},\dot{\boldsymbol{q}}) + \boldsymbol{g}(\boldsymbol{q}) + \boldsymbol{J}^T(\boldsymbol{q})\,\boldsymbol{f} \tag{3.1}$$

with the mass matrix $\boldsymbol{M}(\boldsymbol{q}) \in \mathbb{R}^{n\times n}$, Coriolis and centrifugal vector $\boldsymbol{c}(\boldsymbol{q},\dot{\boldsymbol{q}}) \in \mathbb{R}^n$, gravitation vector $\boldsymbol{g}(\boldsymbol{q}) \in \mathbb{R}^n$ as well as manipulator Jacobian matrix $\boldsymbol{J}(\boldsymbol{q}) \in \mathbb{R}^{6\times n}$. The transposed manipulator Jacobian matrix maps the external forces to the individual joints depending on the pose of the body segments. An example for external forces are the ground reaction forces acting on the foot segments at the center of pressure.

The forward dynamics problem determines the joint accelerations resulting from known joint torques and external forces. Solving Equation (3.1) for the joint acceleration yields the motion equation for the forward dynamics problem defined by

$$\ddot{\boldsymbol{q}} = \boldsymbol{M}^{-1}(\boldsymbol{q})\left[\boldsymbol{\tau} - \boldsymbol{c}(\boldsymbol{q},\dot{\boldsymbol{q}}) - \boldsymbol{g}(\boldsymbol{q}) - \boldsymbol{J}^T(\boldsymbol{q})\,\boldsymbol{f}\right]. \tag{3.2}$$

With given initial joint positions and velocities as well as known time series of joint torques and external forces, Equation (3.2) allows to calculate the sequence of joint positions and velocities by numerical integration.

A mixed computation of forward and inverse dynamics, also referred to as hybrid dynamics [80], allows to perform forward dynamics on some joints with assigned joint torques and inverse dynamics on the remaining joints with assigned joint trajectories. The hybrid dynamics problem therefore includes the forward and inverse dynamics problem. Due to the integration of wobbling masses and force-controlled base joints into the biomechanical model, the inverse dynamics simulation requires the application of hybrid dynamics. While the joint torques of the rotatory joints connecting the individual body segments can be calculated by inverse dynamics from the measured joint trajectories and ground reaction forces, the joint trajectories of the base joints as well as the translational joints describing the wobbling mass motion have to be determined by forward dynamics from the control signal as well as the spring and damper forces.

3.4 Framework

The biomechanical model is implemented with the multibody systems library MBSLIB [84, 246] written in $C++$ that provides efficient algorithms to perform forward kinematics simulations as well as forward and inverse dynamics simulations. MBSLIB is based on the minimal coordinate formulation with relative coordinates which allows to exploit structural properties of multibody systems [233]. In many cases, this exploitation enables to transform a possibly large system of differential algebraic equations into a reduced system of ordinary differential equations with a minimum number of state variables. This reduced problem can be solved numerically in a more robust and efficient manner [222]. For solving inverse dynamics problems, MBSLIB provides an implementation of the recursive Newton-Euler algorithm (RNEA) [140] with a computation complexity of $\mathcal{O}(n)$ for a multibody system with n degrees of freedom. Forward dynamics problems can be solved with implementations of the composite-rigid-body algorithm (CRBA) [234, 80] based on an inertia matrix method and a computational complexity of $\mathcal{O}(n^3)$ or the articulated-body algorithm (ABA) [79, 80] that applies a recursive approach with a computational complexity of $\mathcal{O}(n)$. Both forward dynamics algorithms can be exchanged transparently. Hybrid dynamics problems are supported by providing the hybrid articulated-body algorithm (hABA) [80]. In addition, MBSLIB integrates the automatic differentiation package ADOL-C [235] in tape mode in order to enable the computation of derivatives with respect to system states, control variables and model parameters by operator overloading. The library can be compiled with or without ADOL-C integration. A comprehensive evaluation and validation of MBSLIB are provided by Wojtusch et al. [246].

Tree-structured multibody systems are modeled in a hierarchical model tree which consists of modeling elements like fixed base, fixed translation or rotation, prismatic or revolute joint, rigid link, fork and endpoint. Starting with a fixed base that forms the root node with a single branch, the required modeling elements are added sequentially to the model tree. A fork introduces a new branch. For a valid model tree, all branches need to be terminated by endpoints that represent leaf nodes. Multi-dimensional joints are created by stacking different instances of the one-dimensional prismatic or revolute joints. Forces and torques can be applied to joints and endpoints. Joints allow to set internal force or torque as well as position, velocity and acceleration directly. In addition, generator elements such as linear spring-damper elements allow to apply external forces or torques on joints or endpoints as functions of system states or control

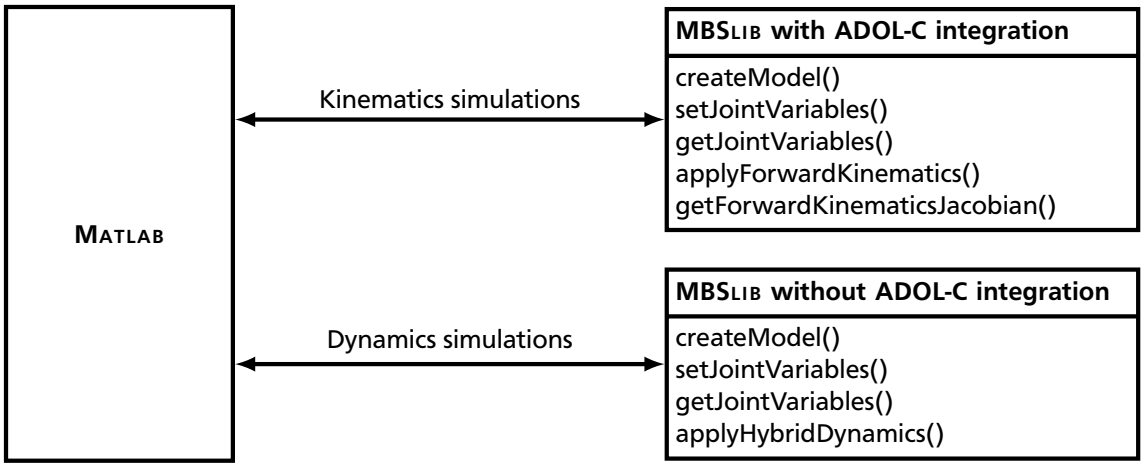

Figure 3.5.: System context diagram of the deployed modeling and simulation framework with MATLAB and two different shared *C* libraries based on MBSLIB.

variables. A schematic diagram of the hierarchical model tree representing the biomechanical model is presented in Appendix A.1.

In contrast to biomechanical modeling and simulation, further data processing such as numerical integration or digital filtering as well as calculations required for uncertainty and sensitivity analysis are implemented in the numerical computing software MATLAB (MathWorks, USA). For this reason, MBSLIB is used to create a shared *C* library that provides a collection of functions which can be dynamically loaded in and directly called from within MATLAB. In the course of the considered inverse dynamics simulation, the required functions comprise the generation of a personalized biomechanical model with subject-specific model parameters, inverse kinematics simulations to determine the joint trajectories from measured motion capture data and hybrid dynamics simulations to compute the joint torques in hip, knee and ankle joint of the right leg. The inverse kinematics problem is solved by applying an extended Kalman smoother approach [57, 257, 256] which uses prior system knowledge in combination with forward kinematics simulations and the derivative Jacobian matrix of the forward kinematics problem to provide smooth estimates for the joint trajectories as well as joint center locations. Although MBSLIB provides efficient algorithms to calculate derivatives by automatic differentiation, operator overloading results in a considerable increase of computational runtime [246]. Therefore, the required functions are distributed among two different shared *C* libraries compiled with ADOL-C integration for kinematics simulations and compiled without ADOL-C integration for dynamics simulations. A system context diagram of the deployed modeling and simulation framework is shown in Figure 3.5. Further details on the extended Kalman smoother approach are given in Chapter 5.

4 Uncertainty and Sensitivity Analysis

The concept of uncertainty describes a state of having limited or imperfect information about a system or process lacking reliability and validity. Uncertainty typically arises in partially observable systems where not all relevant system states are directly accessible and have to be obtained by indirect measurements. These measurands can be mathematically treated as random variables that are characterized by probability distributions. The probability distribution of a measurand describes the probability of its true value lying within an interval of possible values assigned based on available knowledge [119]. Uncertainty can be described as a measure of how well one believes to know the true value of a measurand. In biomechanical simulations of human motions, uncertainty is ubiquitous due to the restricted ascertainability of many input variables and model parameters of the human locomotor system. Apart from regular measurement errors, biomechanical measurements are affected by dispersion because human subjects and motions are not sufficiently reproducible and many crucial variables are difficult or impossible to measure [156]. The uncertainty of simulation results is a combination of individual uncertainty sources in biomechanical measurements and model parameters that propagate through each step of the simulation study. It is necessary to validate that

- the biomechanical model and simulation procedure are implemented correctly,
- the biomechanical model is an accurate representation of the problem and
- an assessment of uncertainty is accounted for in the simulation results

in order to provide evidence that a biomechanical simulation produces credible and reliable results [11, 106]. This thesis mainly focuses on the last point by providing a comprehensive analysis of uncertainty sources and uncertainty propagation in a typical inverse dynamics procedure.

While uncertainty analysis primary quantifies uncertainty in simulation results, sensitivity analysis tries to identify the underlying causes. Saltelli et al. define sensitivity analysis as “the study of how uncertainty in the output of a model (numerical or otherwise) can be apportioned to different sources of uncertainty in the model input” [194]. Uncertainty and sensitivity analysis should ideally be run together in order to obtain an overall impression of uncertainty propagation and apportionment in the considered biomechanical simulation. The quantification of uncertainty in simulation results enables to rate the validity, whereas the identification of critical uncertainty sources allows to improve the biomechanical model and simulation procedure. For this reason, most uncertainty analyses evaluated in this thesis are accompanied by a subsequent sensitivity analysis.

4.1 Related Work

A very powerful and broadly practiced safeguard against overly uncertainty in biomechanical simulations is the application of statistical analysis which uses individual results of multiple subjects or repeated trials to determine an average result, e.g., [34, 54, 136]. If the number

of samples is adequately large, this method ensures valid generalizations that allow to describe fundamental principles and concepts in human motion [156]. Statistical analysis can typically not be applied for unique or pathological motions like kicking a ball or amputee gait because the individual results are highly different and not sufficiently reproducible. Averaging such incomparable results could lead to artificial conclusions without any biomechanical significance. Another common and recommended method to evaluate uncertainty in biomechanical simulations is the comparison of individual results with independently reported simulations or experiments [106]. In practice, these accepted and validated reference standards only exist for a few well-studied motion tasks like walking and running [186] or differences in modeling approaches and variable definitions impede a direct comparison [5]. These limitations restrict the general applicability of both methods and often leave a substantial amount of remaining uncertainty. Therefore, knowing the overall uncertainty of the simulation results and understanding the influences of the involved uncertainty sources are essential requirements in order to draw scientific conclusions and inform clinical decisions.

Existing approaches for uncertainty and sensitivity analysis can be divided into local and global methods [193]. Local analysis investigates how small perturbations of the input variables affect the output variables based on the computation or estimation of derivatives evaluated at a specific sampling point in input space. This derivative-based method is computationally efficient but the results are generally only valid in a narrow range around the selected sampling point. Global analysis assesses how the variance of the output variables is influenced by the variability of the input variables based on a decomposition of the individual variance components. Such variance-based method can become computationally expensive but allows to explore the whole input space and is more informative and robust. In literature, both methods have been used for the investigation of uncertainty and sensitivity in biomechanical simulations. The following classification and remarks adopt the reasoning given by Saltelli at al. [193].

4.1.1 Local Analysis

A simple and common approach to local analysis is the parametric study which involves the variation of one input variable at a time between consecutive simulations [100]. Each input variable takes only two distinct sampling values. By observing the simulation results, any change in the output variable can be directly attributed to the altered input variable. This differential approach assumes uncorrelated input variables and is applicable for linear models or in a small region around the sampling point for nonlinear models. Since it does not consider the simultaneous variation of different input variables, it cannot explore the whole input space and is not able to detect any interactions in the input variables.

More advanced approaches in local analysis use partial derivatives to evaluate uncertainty and sensitivity. A popular derivative-based method is presented in the Guide to the Expression of Uncertainty in Measurement (GUM) published by the Joint Committee for Guides in Metrology (JCGM) [119]. This guide provides general rules for evaluating and expressing uncertainty in measurement and is an internationally accepted and widespread technical specification. A core component of the guidelines is the GUM uncertainty framework that provides a systematic evaluation method to estimate an output variable y and its uncertainty based on given

uncertainties of the n input variables $\boldsymbol{x} \in \mathbb{R}^n$ and a generic model function $y = f(\boldsymbol{x})$. Uncertainties are treated as probability distributions. The input variables are grouped into two categories according to the method used to determine the numerical value. For variables of type A, the probability distributions are explicitly determined using repeated observations or measurements, while the probability distributions for variables of type B are approximately derived from prior knowledge, earlier measurements or information provided by the manufacturer, handbooks or calibration certificates. The uncertainty of both variable types, referred to as standard uncertainty u, is quantified by the standard deviation of the respective probability distribution. The combined standard uncertainty u_c of the output variable is estimated by applying the general law of uncertainty propagation that uses a first-order Taylor series expansion to linearize the model function and assuming that the output variable can be characterized by a Gaussian or Student distribution. For uncorrelated input variables, the combined standard uncertainty is given by

$$u_c(y) = \sqrt{\sum_{i=1}^{n} \left(\frac{\partial f}{\partial x_i} \right)^2 u^2(x_i)}. \tag{4.1}$$

The partial derivatives $\partial f / \partial x_i$ evaluated at the expectation values of the input variables can be interpreted as sensitivity indices and describe how the estimate of the output variable varies with small changes in the input variables. In the case of correlated input variables, the combined standard uncertainty is defined by

$$u_c(y) = \sqrt{\sum_{i=1}^{n} \left(\frac{\partial f}{\partial x_i} \right)^2 u^2(x_i) + 2 \sum_{i=1}^{n-1} \sum_{j=i+1}^{n} \frac{\partial f}{\partial x_i} \frac{\partial f}{\partial x_j} u(x_i, x_j)},$$

where the first term is identical to Equation (4.1) and the second term incorporates the covariances $u(x_i, x_j)$ between the jointly distributed input variables. Supplement documents extend the framework by introducing alternative methods for the propagation of probability distributions through the model function [120] and integrating support for multiple output variables [121]. The approach provides exact results for the estimate of the output variable and the combined uncertainty if the model function is linear and the input variables are normally distributed [120]. In cases where these conditions do not hold including nonlinear model functions, asymmetric probability distributions of the input variables or not normally distributed output variables, the framework gives an approximate solution which might not be satisfactory. In addition, the sensitivity indices are only valid near the sampling point specified by the expectation values of the input variables which does not have to coincide with the actual expectation value of the output variable.

Biomechanical models used for the investigation of human motion dynamics are mainly nonlinear due to the trigonometric relations in the kinematic chains and a Gaussian or Student distribution of the output variables cannot be generally guaranteed. For this reason, the GUM uncertainty framework and other local approaches are generally not suitable for an extensive evaluation of inverse dynamics simulations. The limitation to a single sampling point in input space restricts a quantitative uncertainty and sensitivity analysis by reducing significance and robustness. Nevertheless, the easy implementation and high computational efficiency make local approaches attractive and a number of biomechanical studies used derivative-based methods to determine the effects of uncertainties in anthropometric parameters, joint center locations or biomechanical measurements, e.g., [41, 181, 208].

4.1.2 Global Analysis

A straightforward approach to global analysis inspired by parametric study is the elementary effects method that attempts to explore the whole input space with building a series of input trajectories and averaging a number of local measures, called the elementary effects, to remove the dependency on a single sample point [38, 149]. The input trajectories are constructed by dividing the domain of each input variable into a specific number of subintervals and randomly moving only one input variable at a time while the other input variables remain fixed. The averaged results are used to compute sensitivity indices that characterize the effect of each input variable as negligible, linear, nonlinear or involved in interactions with other input variables. Similar to parametric study, the elementary effect method is computationally simple and assumes uncorrelated input variables. This approach is often used as a screening method to identify important input variables with a small number of consecutive simulations [193].

Other approaches in global analysis focus on the evaluation of variance as a summary measure of uncertainty. Sensitivity is determined by studying how the variance of the output variables specified by the corresponding probability distributions depends on the uncertain input variables. This can be achieved by exploiting the statistical properties of variance and decomposing the output variance into individual variance components. The output variance of a generic model function $y = f(\boldsymbol{x})$ with n input variables $\boldsymbol{x} \in \mathbb{R}^n$ and the output variable y is given by $V(y)$. When fixing one input variable x_i at a particular value, the output variance becomes a conditional variance $V_{\boldsymbol{x}_{\sim i}}(y|x_i)$ taken over all input variables but x_i as denoted by the index $\boldsymbol{x}_{\sim i}$. The difference between the conditional and unconditional output variances can be considered as a measure of the relative importance of the input variable x_i fixed at the selected sample point. This dependency on the sample point is eliminated by taking the average over all possible sample points of the input variable x_i which is given by the expectation $E_{x_i}[V_{\boldsymbol{x}_{\sim i}}(y|x_i)]$. This expectation is always lower or equal to the unconditional output variance, whereby the smaller the expectation the greater the influence of the fixed input variable x_i. Due to the total variance theorem, the unconditional output variance can be decomposed as

$$V(y) = V_{x_i}[E_{\boldsymbol{x}_{\sim i}}(y|x_i)] + E_{x_i}[V_{\boldsymbol{x}_{\sim i}}(y|x_i)]$$

resulting in two variance components designated as first-order effect and residual [193]. The first component acts complementary to the regarded expectation represented by the second component. Normalizing the first component by the unconditional output variance specifies the first-order sensitivity index

$$S_i^F = \frac{V_{x_i}[E_{\boldsymbol{x}_{\sim i}}(y|x_i)]}{V(y)} \tag{4.2}$$

that indicates the average reduction in output variance after fixing the input variable x_i to a specific value. This is a measure of the effect of one input variable alone and therefore cannot incorporate interactions between different input variables. In order to take these interactions into account, the unconditional output variance can be decomposed with reversing the approach and conditioning to all input variables but one. With applying the total variance theorem, the reversed decomposition is given by

$$V(y) = V_{\boldsymbol{x}_{\sim i}}[E_{x_i}(y|\boldsymbol{x}_{\sim i})] + E_{\boldsymbol{x}_{\sim i}}[V_{x_i}(y|\boldsymbol{x}_{\sim i})].$$

The first term can be interpreted as the first-order effect of all input variables but x_i, so that the remaining second term must represent all involvements of the input variable x_i including the interactions with other input variables [192]. Normalizing the second component by the unconditional output variance defines the total-effect sensitivity index

$$S_i^T = \frac{E_{\boldsymbol{x}_{\sim i}}[V_{x_i}(y|\boldsymbol{x}_{\sim i})]}{V(y)} = 1 - \frac{V_{\boldsymbol{x}_{\sim i}}[E_{x_i}(y|\boldsymbol{x}_{\sim i})]}{V(y)} \tag{4.3}$$

that accounts for the total contribution of the input variable x_i to the output variance consisting of the first-order effect and all higher-order effects due to interactions.

The computation of both sensitivity indices specified by Equations (4.2) and (4.3) for all input variables gives a fairly good description of sensitivity at a reasonable computational cost [193]. By definition, the sum of all first-order indices is less or equal to one, while the sum of all total-effect indices is greater or equal to one. If the model function is additive and there are no interactions, both sums equal to one. A total-effect index of zero is a necessary and sufficient condition for rating an input variable as uninfluential which means that it may be fixed anywhere in its probability distribution without affecting the output variance. The first-order indices can be used to rank the importance of input variables according to the reduction in output variance. The difference between both indices measures how much an input variable is involved in interactions with other input variables. A comprehensive discussion of the sensitivity indices is provided by Saltelli et al. [192].

A broad class of numerical procedures for estimating uncertainty and sensitivity with evaluating variance is based on Monte Carlo simulation [147]. This approach uses a large number of random trials to handle problems that are difficult or impossible to solve with other methods. The general pattern of a Monte Carlo simulation includes the following steps:

1. Definition of the model function with specific input and output variables.
2. Definition of domain and probability distribution for each input variable.
3. Generation of many random input variable samples from the specified probability distributions.
4. Computation of output variables based on the generated input variable samples and specified model function.
5. Aggregation of statistical results for uncertainty and sensitivity analysis.

A critical aspect of this procedure is the sampling strategy which has to ensure that the probability distributions of the input variables are well represented by the generated samples. Depending on the complexity of the model function, the required number of samples can vary from a few hundred to many thousands or even millions. This can make the approach computationally demanding, especially if the model function is both expensive to run and rich in input variables. However, this approach is currently the most powerful method for computing uncertainty and sensitivity purely based on model function evaluations [193]. An implementation for uncorrelated input variables is provided by Saltelli [191] and has been broadened to include correlated input variables by Kucherenko et al. [128]. Other suitable methods comprise the Fourier amplitude sensitivity test (FAST) [55] that applies multiple Fourier series expansions or the random balance design (RBD) [224] which is based on Fourier spectrum analysis. These methods can

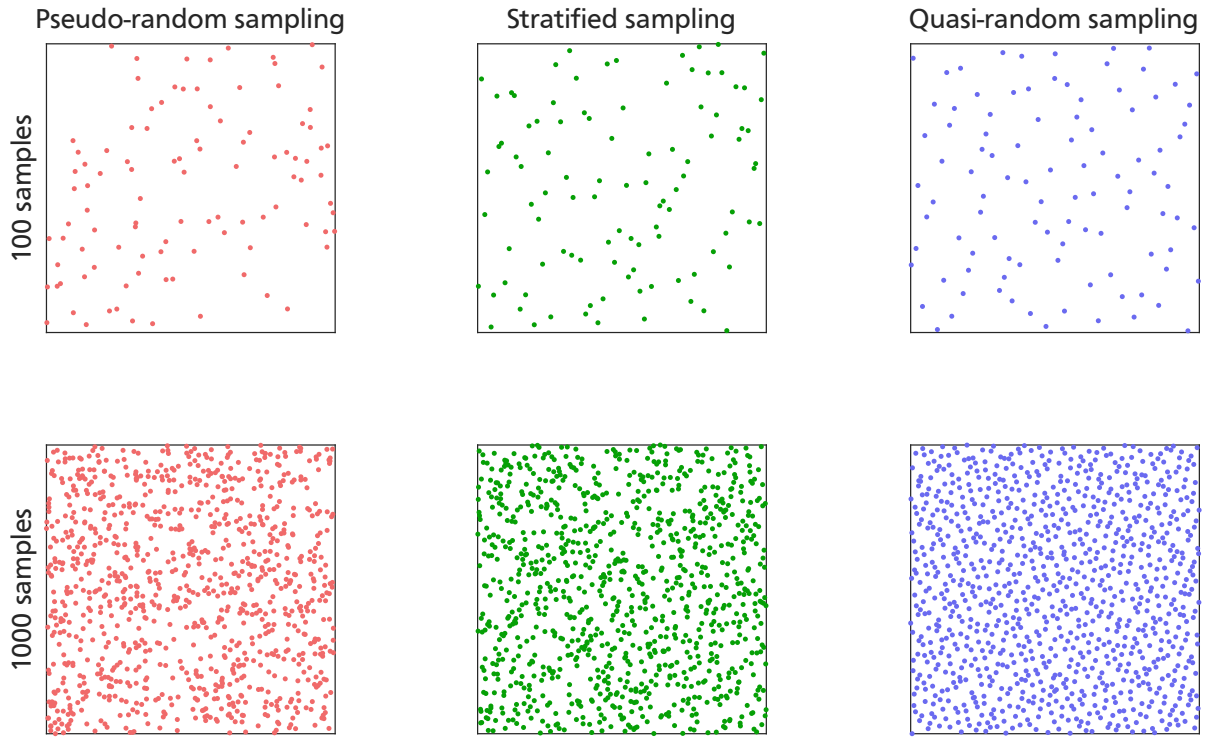

Figure 4.1.: Comparison of pseudo-random, stratified and quasi-random sampling strategies for 100 samples (top) and 1,000 samples (bottom) in the unit square.

become computationally more efficient than Monte Carlo simulation but are usually limited to an estimation of first-order sensitivity indices.

The choice of the sampling strategy can have an essential influence on the numerical convergence of the uncertainty and sensitivity estimation which determines the efficiency of the method. An even sample distribution is desirable in order to equally cover the input space in the statistical evaluation. Classical Monte Carlo simulation approaches use pseudo-random number generators that produce sequences of approximately random samples generated by deterministic algorithms. Generally, pseudo-random samples are not evenly distributed over the considered domain and exhibit notable gaps without any samples as well as clusters with many samples lumped together. This property leads to under- and overemphasized regions in input space and impedes numerical convergence. Stratified sampling strategies such as Latin hypercube sampling [115] improve the coverage by providing a predefined policy for sample generation. The input space is divided into a specific number of subintervals and samples are drawn randomly from selected subintervals according to the given policy. This approach enhances sample distribution but the predefined policy makes it difficult to dynamically generate additional samples in case of iteratively invoked termination criteria. Quasi-random sampling strategies use low-discrepancy sequences like the Sobol sequence [212] to generate nearly random samples which minimize discrepancy as a mathematical measure of lumpiness. To maintain an even spread in input space, quasi-random samples are neither random nor pseudo-random in the sense of being completely unpredictable. If the number of samples is large enough, all low-discrepancy sequences converge to an even distribution. For many problems of various complexity, quasi-random sampling typically outperforms pseudo-random and stratified sampling strategies [127]. Figure 4.1 presents a comparison of the different sampling strategies for

100 samples and 1,000 samples in the unit square. The stratified samples shown in green are based on Latin hypercube sampling, while the quasi-random samples shown in blue are finite subsets of Sobol sequences. All samples were generated with the numerical computing software MATLAB using the corresponding built-in functions.

The model-free sensitivity indices as well as the capability to explore the whole input space considering interactions among the input variables make global approaches very suitable for the evaluation of uncertainty and sensitivity in biomechanical simulations. Several recent biomechanical studies applied variance-based methods to investigate the effects of uncertainties in anthropometric parameters, joint center locations or biomechanical measurements, e.g., [153, 155, 227]. Most of these studies simplify the uncertainty sources by using uniform or Gaussian distributions and assume independent input variables with neglecting possible correlations.

4.2 Contribution

The uncertainty and sensitivity framework applied in this thesis extends existing approaches in biomechanical studies by omitting simplified models for uncertainty sources and considering possible correlations among uncertain simulation inputs and model parameters. It implements a global analysis based on Monte Carlo simulation along with a quasi-random sampling strategy. Uncertainties are modeled using a parametric distribution system that covers the entire permissible skewness-kurtosis region in combination with a copula approach which describes potential correlations. Sensitivities are estimated with a variance-based method for problems with correlated input variables [128]. This approach allows to explore the whole input space and consider nonlinearities in the biomechanical model as well as interactions in the input variables.

The computationally expensive Monte Carlo simulation is implemented as an iterative procedure which considerably decreases the required memory consumption and provides a flexible control over the number of random trials. An adequate trial size is ensured by consistently evaluating the convergence behavior of the numerical estimation. Parallel computing is applied to share the computational load of extensive Monte Carlo simulations among different computer systems and reduce the total computation time.

4.3 Methods

For the evaluation of uncertainty and sensitivity in the inverse dynamics simulation considered in this thesis, a global analysis based on Monte Carlo simulation is applied to estimate the probability distributions of the examined joint torques as well as the corresponding first-order and total-effect sensitivity indices. Possible correlations between input variables that refer to similar model parameters or simulation inputs are identified and incorporated into the uncertainty and sensitivity analysis. This approach allows to investigate uncertainty propagation and apportionment with exploring the whole input space and without neglecting nonlinearities of the biomechanical model and potential relations in input variables. The following assumptions are made in the evaluation process:

A7 All input and output variables are continuous and can be described by unimodal probability distributions.

A8 Similar input variables are correlated, while dissimilar input variables can be treated as independent variables.

A9 Estimation errors for uncertainty and sensitivity converge to zero for a sufficiently large number of samples.

4.3.1 Probability Modeling

The probability distributions used to describe the statistical properties of input and output variables can take very different shapes defined by the aggregation and dispersion of the associated measurement values or simulation results. In descriptive statistics, four statistical moments are typically applied as quantitative measures for the shape of probability distributions. The first moment is the mean μ_d defining the central tendency. The second central moment is the variance σ_d^2 which describes the expectation of the squared deviation from the mean σ_d. The third central moment is the skewness γ_d measuring the asymmetry of the probability distribution about the mean. The fourth central moment is the kurtosis κ_d which characterizes the steepness of the probability distribution. Gaussian distributions for example can take various values for mean and variance but have a skewness of 0 and a kurtosis of 3.0. Figure 4.2 demonstrates the effect on the shape of a probability density function for each of the four statistical moments. The red probability density function represents the standard Gaussian distribution with zero mean and unit standard distribution.

In order to provide a parametric model for the diverse shapes of probability distributions, the Johnson distribution system [118] with four coefficients is applied to describe the probability distributions of input and output variables in the uncertainty and sensitivity analysis. The Johnson distribution system is a family of different unimodal distribution types based on transformations of the Gaussian distribution that allow to model normal (SN), log-normal (SL), bounded (SB) and unbounded (SB) probability distributions in the entire permissible skewness-kurtosis region. Bounded probability distributions can be bounded on the lower end, upper end or both ends and cover Beta and Gamma distributions among others [90]. The four coefficients

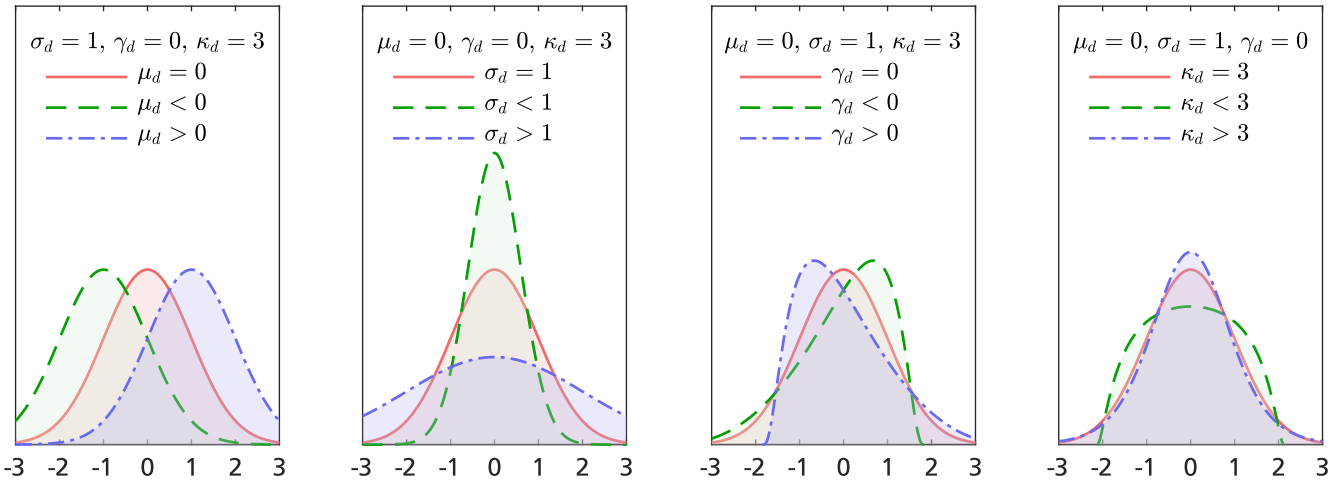

Figure 4.2.: Effects of mean μ_d, variance σ_d^2, skewness γ_d and kurtosis κ_d on the shape of a probability density function.

Table 4.1.: Characteristics of normal (SN), log-normal (SL), bounded (SB) and unbounded (SB) distribution types in the Johnson distribution system.

Type	**Function** $g_1(y)$	**Function** $g_2(y)$	**Support** $\mathbb{H}$
SN	1	y	$(-\infty, +\infty)$
SL	$\frac{1}{y}$	$\ln(y)$	$\left[\xi_j, +\infty\right)$
SB	$\frac{1}{y(1-y)}$	$\ln\left(\frac{y}{1-y}\right)$	$\left[\xi_j, \xi_j + \lambda_j\right]$
SU	$\frac{1}{\sqrt{y^2+1}}$	$\ln\left(y + \sqrt{y^2+1}\right)$	$(-\infty, +\infty)$

consist of two shape parameters γ_j and δ_j, one scale parameter λ_j as well as one location parameter ξ_j. For a random variable $x \in \mathbb{R}$ and the support $\mathbb{H}$, the general probability density function (PDF) p_j is given by

$$p_j\left(x \mid \gamma_j, \delta_j, \lambda_j, \xi_j\right) = \frac{\delta_j}{\sqrt{2\pi}\lambda_j}\, g_1\left(\frac{x-\xi_j}{\lambda_j}\right) \exp\left(-\frac{1}{2}\left[\gamma_j + \delta_j\, g_2\left(\frac{x-\xi_j}{\lambda_j}\right)\right]^2\right)$$

for all $x \in \mathbb{H}$ and with the type-specific functions $g_1(y)$ and $g_2(y)$. All characteristic functions and supports for each distribution type are listed in Table 4.1. The corresponding cumulative distribution functions (CDF) P_j are defined by

$$P_j\left(x \mid \gamma_j, \delta_j, \lambda_j, \xi_j\right) = \int_{-\infty}^{x} p_j\left(t \mid \gamma_j, \delta_j, \lambda_j, \xi_j\right)\, \mathrm{d}t.$$

This parametric model allows to describe the probability distribution of an arbitrary input or output variable with the four coefficients plus a specification of the distribution type. By applying the corresponding inverse cumulative distribution function P_j^{-1}, the uniform samples $u \sim \mathbb{U}(0, 1.0)$ generated from quasi-random sampling can be transformed into random variables $x \sim \mathbb{J}(\gamma_j, \delta_j, \lambda_j, \xi_j)$ following the specified Johnson distribution with

$$x = P_j^{-1}(u).$$

Correlations among input and output variables are modeled by adopting a copula approach [199]. According to Sklar's theorem [209], multivariate joint distributions can be separated into a set of univariate marginal distributions and a copula that describes the dependence structure between the individual marginal distributions. This property enables a straightforward modeling and estimation of correlation by separately quantifying the marginal distributions and the copula. In this thesis, the marginal distributions are described by the four distribution types of the Johnson distribution system, whereby the dependence structure is characterized by a

Gaussian copula. This approach assumes that the correlation can be modeled as a multivariate Gaussian distribution with a mean vector equal to zero and a covariance matrix $\boldsymbol{\Sigma}_c$. With the univariate and multivariate Gaussian cumulative distribution functions Φ and $\boldsymbol{\Phi}$, the Gaussian copula $\boldsymbol{C}$ for the m random variables x_i with $i = 1 \dots m$ can be written as

$$\boldsymbol{C} = \boldsymbol{\Phi}_{\mathbf{0},\boldsymbol{\Sigma}_c}\left(\Phi_{0,1}^{-1}[P_j(x_1)] \dots \Phi_{0,1}^{-1}[P_j(x_m)]\right).$$

Common methods for estimating the type and coefficients of a Johnson distribution from observed samples comprise moment matching [109], quantile matching [238] and maximum likelihood estimation [90]. In moment matching, the probability distribution is parametrized by establishing functional relations between the unknown type and coefficients as well as the statistical moments calculated from the samples. Quantile matching applies a comparable approach with utilizing statistical quantiles fitted to the samples instead of statistical moments. Maximum likelihood estimation calculates the coefficients that maximize the likelihood of drawing the samples given the found coefficients. The estimation based on maximum likelihood provides the best results but requires an iterative approach and can be computationally demanding [90]. Such a procedure can further decrease the computational efficiency of the global analysis and is therefore not considered in this thesis.

In anticipation of Chapter 7 and 8, the histograms of six randomly selected samples taken for uncertainty analysis in joint center and anthropometric parameter estimation are shown in Figure 4.3. Each sample has a size of 1,000,000 values and represents the uncertainty of an individual regression parameter for female or male subjects. All given histograms confirm the

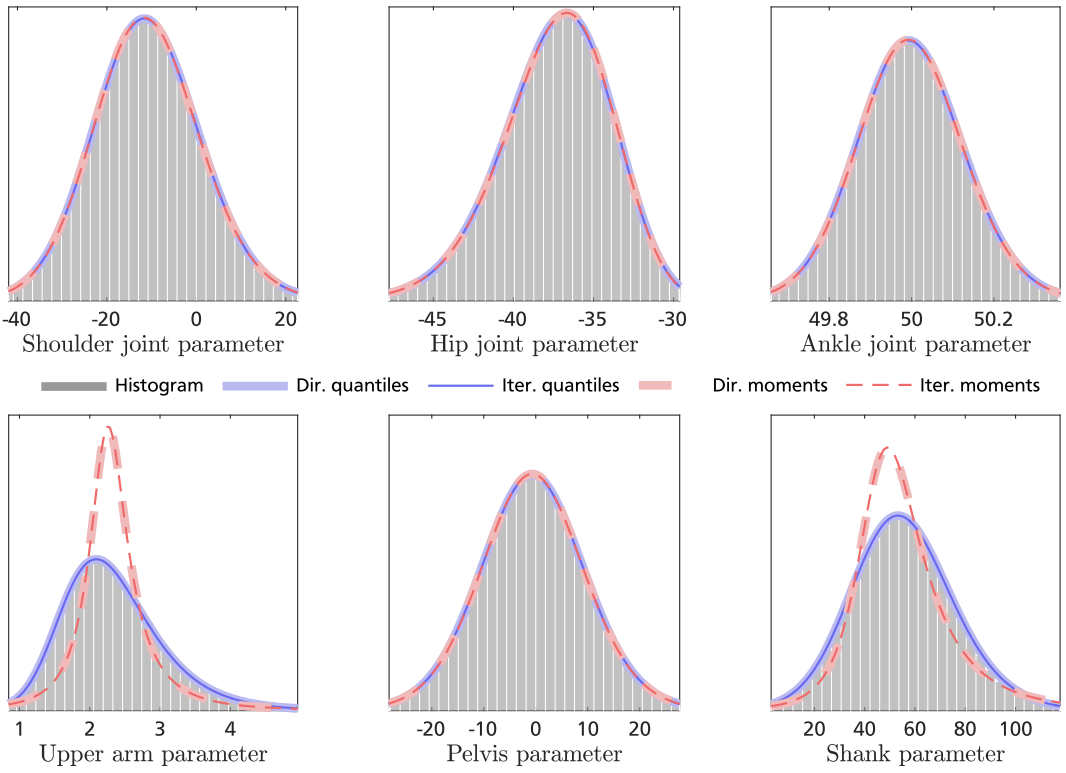

Figure 4.3.: Comparison of Johnson distributions estimated from six randomly selected samples by direct and iterative moment or quantile matching.

assumption of unimodal probability distributions. The red and blue curves represent the Johnson distributions estimated from the samples by moment and quantile matching. In most cases, both approaches achieve an adequate fit but moment matching fails for the upper arm and shank parameters. The reason for this failure is an insufficient determination of the statistical moments from the actual samples. This deficiency in moment matching could substantially affect the results of uncertainty and sensitivity analysis. For this reason, quantile matching is applied for estimating the required coefficients in this thesis. In addition to the results calculated from direct estimation with all samples, the Johnson distributions for an iterative estimation with batches of 10,000 values are given for each approach and sample. A moving average approach is used to merge the results of individual batches with previously obtained results. The results for direct and iterative estimation are congruent in all cases and demonstrate the general applicability of both methods.

4.3.2 Analysis Strategy

Uncertainties of input variables and model parameters propagate through the inverse dynamics procedure and affect joint torque estimation in a variety of ways. Figure 4.4 shows all steps of the procedure from the initial biomechanical measurements to the actual inverse dynamics simulation and illustrates the underlying dependencies and most relevant uncertainty sources. Uncertainties in individual steps result from variations in preceding steps and context-specific uncertainty sources. Anatomical landmark misplacement for example influences joint torque estimation in three different ways. The incorrect identification of anatomical landmarks impairs the location and orientation of markers and local reference frames which define the relative motion between the body segments and directly affect the estimated joint trajectories. In combination with a set of uncertain regression parameters, the misplaced markers are also used to evaluate the joint center locations that specify the kinematic structure of the biomechanical model. These joint center estimates are further applied to estimate the anthropometric parameters based on another set of uncertain regression parameters which define the dynamical properties of the biomechanical model.

All steps that involve kinematics or dynamics simulations with the biomechanical model, i.e., joint trajectory estimation and inverse dynamics simulation, are possibly impaired by model uncertainties which might arise from an inadequate representation of the human locomotor system. An example of such a model uncertainty is the simplified implementation of the knee joint as a one-dimensional revolute joint without regarding the combined rolling and gliding mechanism. A general evaluation for this type of uncertainty is complicated by missing reference data and still an open research problem, e.g., [83]. Therefore, the influence of model uncertainty is minimized by applying generally accepted modeling approaches and not explicitly considered in the uncertainty and sensitivity analysis. Other potential uncertainties like the influence of rounding or truncation errors resulting from floating-point number representations are assumed to be negligible compared to the specified uncertainty sources.

For a comprehensive uncertainty and sensitivity analysis, the individual effects and dependencies of uncertainty propagation have to be identified and considered in the evaluation. In a first phase, uncertainties associated with the biomechanical measurements including anatomical landmark misplacement, soft tissue artifacts and measurement uncertainties are quantified

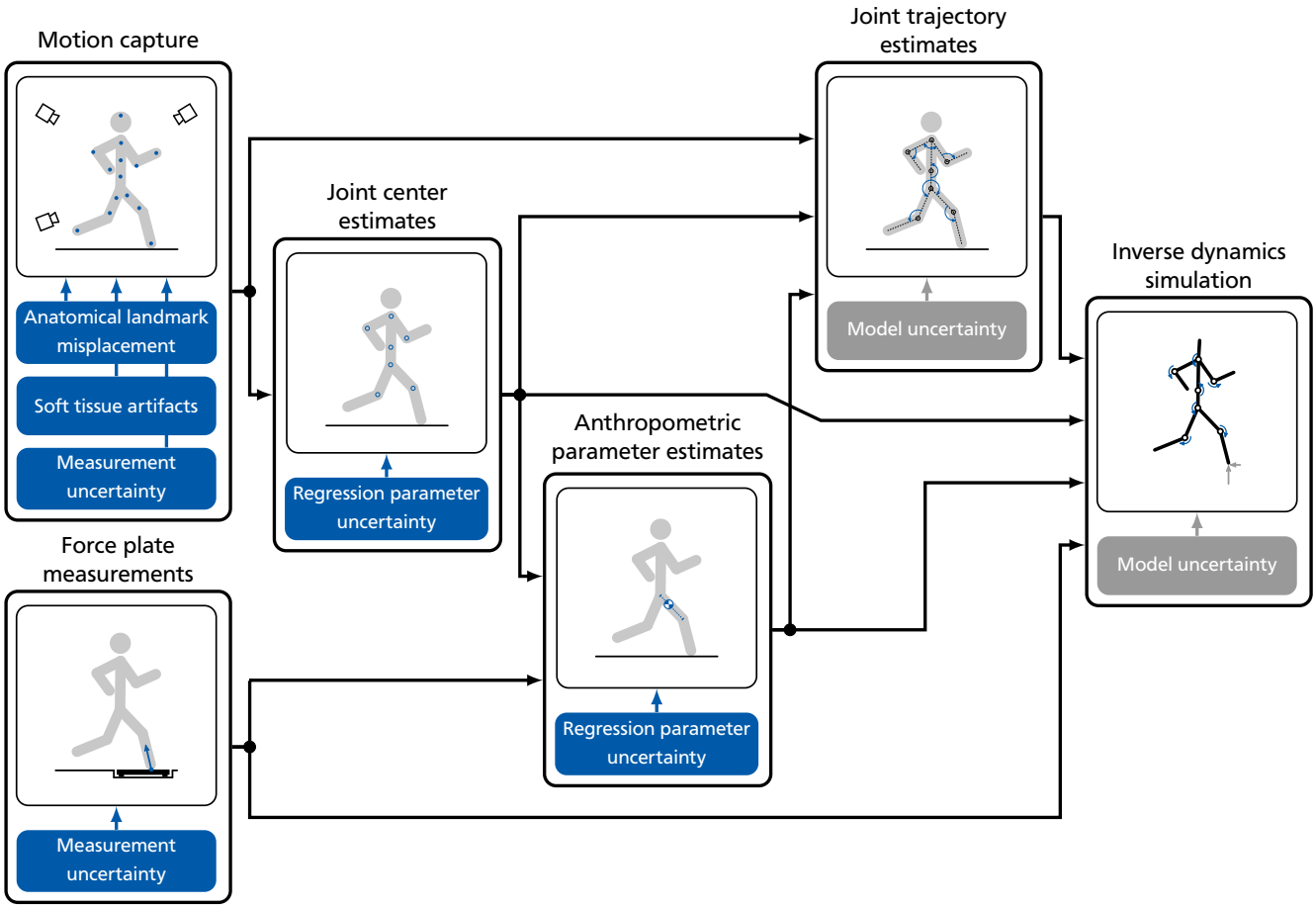

Figure 4.4.: Uncertainty propagation and most relevant uncertainty sources in the inverse dynamics procedure.

by experimental studies as well as reported data from literature. The variability of regression parameters for joint center and anthropometric parameter estimation are analyzed in a second phase by simulation studies with statistical data stated in literature. Based on these results, a preliminary Monte Carlo simulation involving the first four steps of the inverse dynamics procedure is performed to investigate uncertainties and sensitivities in the estimated anthropometric parameters for both subjects. In a third phase, all previously determined uncertainties are incorporated into a concluding Monte Carlo simulation comprising all steps of the inverse dynamics procedure in order to analyze uncertainties and sensitivities in estimated hip, knee and ankle torques for walking, running and kicking a ball performed by both subjects. Details on the applied methods and obtained results for the individual phases are presented and discussed in the Chapters 6 to 9.

4.4 Framework

The framework for uncertainty and sensitivity analysis is implemented in the numerical computing software MATLAB and based on the approach for correlated input variables published by Kucherenko et al. [128]. Sergei Kucherenko kindly provided documented example code that formed the basis for the actual framework. Applied modifications and extensions include an integration of the quasi-random sampling strategy with Sobol sequences as well as support for

the Johnson distribution system and the Gaussian copula approach. The implementation of the quasi-random sampling strategy uses built-in functions to initialize the Sobol sequence and draw the required number of samples. In order to further improve discrepancy of the random samples, a scrambling technique in combination with a static skip and leap are used. The scrambling technique shuffles generated samples by a random linear scramble combined with a random digital shift [143]. Because the initial samples of a Sobol sequence can exhibit undesirable properties that might lead to an unbalanced sampling, the static skip is set to omit the first 1,000 samples. The additional definition of the static leap results in skipping 100 values in the Sobol sequence for each taken sample. Support for the Johnson distribution system is provided by integrating the Johnson Curve Toolbox[1] that ports algorithms by Hill et al. [109, 108]. The toolbox contains functions to fit Johnson distributions with moment or quantile matching and evaluate the relevant probability distribution functions. An extension implemented for this framework enables to calculate statistical characteristics like mean, variance, median and mode for each distribution type.

The Monte Carlo simulation for the numerical estimation of the sensitivity indices requires a large number of random trials. Each of these trials involves multiple evaluations of the model function with different combinations of two independently drawn input variable samples. The model function represents selected or all steps of the inverse dynamics procedure. Because two independent input variable samples are taken for each trial, two sets of output variables are available per trial for uncertainty estimation. The total number of model function evaluations is $N(2\,n+1)$ for n input variables and N trials [128]. The number of input variables is fixed and depends on the considered problem, while the number of trials is variable and determined by the convergence behavior of the numerical estimation. In order to ensure a sufficient trial size, the Monte Carlo simulation is implemented in an iterative manner. Statistical quantiles and the Gaussian copula for modeling uncertainties as well as first-order and total-effect sensitivity indices are calculated for a batch of trials with a predefined size. The results obtained from an individual batch are merged with previously computed results by applying a moving average approach. After each batch, the merged results are tested for convergence by calculating the maximum difference to the previously computed results for all values. Due to the potentially large value range in uncertainty estimation, the maximum differences of the statistical quantiles are normalized to the most recent values. The Monte Carlo simulation is terminated if the maximum difference for all statistical quantiles and sensitivity indices falls below a certain threshold value.

This iterative procedure constitutes an efficient implementation of the computationally demanding Monte Carlo simulation. The moving average approach reduces the required memory consumption by obviating the need to save all intermediate results and sample values, while the consistently invoked termination criterion ensures an adequately but not unnecessarily large trial size. Nevertheless, the needed number of model function evaluations typically grows fast for problems with many input variables. With an increasing complexity of the model function, total computation time for the Monte Carlo simulation can become a critical factor for the applicability of uncertainty and sensitivity analysis. In order to cope with extensive Monte Carlo simulations, parallel computing is applied to share the computational load among different processor cores and computer systems. The iterative procedure supports this approach by allowing

[1] http://www.marine.usf.edu/user/djones/jctm/jctm.html

Table 4.2.: Technical specifications of the computer systems applied for parallel computing.

#	Processor	Cores	Cache	Memory
1	Core-i7-3770K CPU @ 3.50 GHz	4	8 MB L3	32 GB DDR3
2	Core-i7-4790K CPU @ 4.00 GHz	4	8 MB L3	16 GB DDR3
3	Core-i7-4790K CPU @ 4.00 GHz	4	8 MB L3	16 GB DDR3
4	Core-i7-4790K CPU @ 4.00 GHz	4	8 MB L3	16 GB DDR3
5	Core-i7-4790K CPU @ 4.00 GHz	4	8 MB L3	32 GB DDR3
6	Core-i7-4790K CPU @ 4.00 GHz	4	8 MB L3	32 GB DDR3
7	Core-i7-4790K CPU @ 4.00 GHz	4	8 MB L3	32 GB DDR3
8	Core-i7-4790K CPU @ 4.00 GHz	4	8 MB L3	32 GB DDR3
9	Core-i7-6850K CPU @ 3.60 GHz	6	15 MB L3	32 GB DDR4
10	Core-i7-2600 CPU @ 3.40 GHz	4	8 MB L3	16 GB DDR3

a parallel processing of the individual batches. Depending on the complexity of the considered problem, a suitable number of processor cores from a cluster of ten computer systems with multi-core processors and hyper-threading support is used for the Monte Carlo simulation. The computer systems are connected via Gigabit Ethernet and provide sufficient memory for running multiple instances at the same time. Table 4.2 lists the technical specifications of the applied computer systems.

5 Biomechanical Measurements

Biomechanical measurements form the fundamental basis for personalized biomechanical models and biomechanical simulations. For the study of human motion dynamics, the most relevant measurands are spatial motions of the individual body segments recorded by motion capture techniques as well as external reaction forces acting on the human body quantified with force plates. The recorded spatial motions allow to estimate segment lengths, joint center locations and joint trajectories including joint positions, velocities and accelerations. In combination with the force plate measurements, this processed data is used to estimate personalized anthropometric parameters and perform the actual biomechanical simulation. The additional measurement of electrical muscle activities with electromyography can help to identify neuromuscular disorders or validate simulation results. The biomechanical measurements are the first step in the inverse dynamics procedure and therefore of essential importance in the uncertainty and sensitivity analysis.

The biomechanical measurements for the motion tasks considered in this thesis, i.e., walking, running and kicking a ball, were recorded together with measurement data for other human motions and published in the HuMoD database [247]. This database contains raw and processed measurement data from a three-dimensional motion capture system, an instrumented treadmill and an electromyographical measurement system for eight different motion tasks performed by a healthy female and male subject. Along with the measurement data, subject-specific estimates for anthropometric parameters, joint center locations as well as joint trajectories are provided in the database. This data collection and the corresponding data processing lay the foundation for the inverse dynamics simulations investigated in this thesis.

The following descriptions and illustrations are based on a conference paper presented at the IEEE-RAS International Conference on Humanoid Robots [247] and contain verbatim quotes.

5.1 Related Work

The gathering of high-quality biomechanical measurement data usually requires careful preparation, experienced examiners and a gait laboratory with expensive measurement equipment. Subsequent to the measurement, the collected data has to be further processed before it can be used for investigation, modeling and simulation. In order to reduce this preparative effort or in case of no access to a well-equipped gait laboratory, it is possible to resort to one of the several published databases with biomechanical measurement data of various motion tasks performed by human subjects.

The Motion Capture Database[1] and the Multimodal Human Action Database [159] provide spatial motion data acquired with marker-based motion capture systems for locomotion, human interaction, interaction with the environment or physical activities. In addition to spatial motion data, the Motion Capture Database HDM05 [151] includes a personalized kinematic model for each subject that is generated from motion capture data. This kinematic model can be used

[1] http://mocap.cs.cmu.edu

to estimate joint center locations or joint trajectories. The KIT Whole-Body Human Motion Database [142] is an aggregation of multiple data collections with varying extent and contains spatial motion data for several activities of daily living. Some datasets also provide force plate measurements, activity-related information like geometric data of stairs or handrails as well as differently detailed information about the subjects. The SIMTK project[2] is a gathering of small databases containing various biomechanical measurement data for normal and pathological locomotion provided by different researchers and prepared for the modeling and simulation software OPENSIM [62]. The type and extent of included measurement data differ among the individual databases, some of which are related to specific publications. Most of these published databases are not directly suitable for the investigation, modeling and simulation of human motion dynamics due to missing ground reaction forces or detailed anthropometric parameters for the subjects.

5.2 Contribution

The HUMOD database provides a comprehensive and rare combination of biomechanical measurement data and anthropometric parameter estimates for various human motions representing typical repetitive and goal-oriented motions. The included datasets allow to create and validate biomechanical models of the human locomotor system on actuation level and to investigate and simulate human motion dynamics. Besides investigations in biomechanical simulations, the database can be of value especially for the design and development of musculoskeletal humanoid robots and for a better understanding and benchmarking of human-like robot locomotion. The database contains raw and processed biomechanical measurement data for different motion tasks performed by a healthy female and male subject. The biomechanical measurement data, anthropometric parameters and source code of the applied computational scripts as well as a comprehensive documentation of the database are published for download on the HUMOD database website[3]. This open availability of the database enables researchers to use comprehensive, high-resolution and high-quality biomechanical measurement data and promotes the understandability, transparency and quality of the provided data and applied data processing.

5.3 Measurement Protocol

A healthy female subject (27 yrs, 161 cm, 57 kg) and healthy male subject (32 yrs, 179 cm, 85 kg) performed the measurement trials without shoes dressed in underwear. The subjects were given time to become familiar with the measurement setup and equipment before the measurements and to rest between the trials. The measurement procedure was reviewed and approved by the ethical review committee of Friedrich-Schiller-Universität Jena, Germany. The subjects provided informed consent in accordance with the policies of the ethical review committee. All measurements were conducted at the Locomotion Laboratory of André Seyfarth at Technische Universität Darmstadt, Germany.

[2] http://www.simtk.org
[3] http://www.sim.informatik.tu-darmstadt.de/humod

5.3.1 Motion Protocol

The subjects performed eight motion tasks, partially at various speeds or under changed conditions resulting in a total of thirteen different trials for each subject. The motion tasks cover locomotion, interaction with an object and physical activity representing a sample of typical repetitive and goal-oriented motions valuable in biomechanical simulations and humanoid robotics research.

Locomotion trials comprise straight walking at 1.0 m/s, 1.5 m/s and 2.0 m/s, straight running at 2.0 m/s, 3.0 m/s and 4.0 m/s, sideways walking at 1.0 m/s and a transition between standing and straight running at 4.0 m/s. The transition task started with constantly accelerating at 0.1 m/s^2 from 0.0 m/s to 4.0 m/s, continued with holding 4.0 m/s for 20 s and ended with constantly decelerating at -0.1 m/s^2 from 4.0 m/s to 0.0 m/s. Trials including interaction with an object are avoiding a box obstacle (410.0 × 200.0 × 150.0 mm) that was placed lengthwise and crosswise on the treadmill while straight walking at 1.0 m/s and kicking a soft ball (200.0 mm, 160.0 g). Physical activity trials contain continuous squats and jumps with arms akimbo. Squats, kicks and jumps were performed with stopped treadmill. During the first and last 10 s of each trial, the force plates remained unloaded. Before and after performing the particular motion task, the subject stood still on the treadmill for at least 10 s. This idle time was increased to 20 s after fast motion tasks. Details of the individual trials are summarized in Table 5.1.

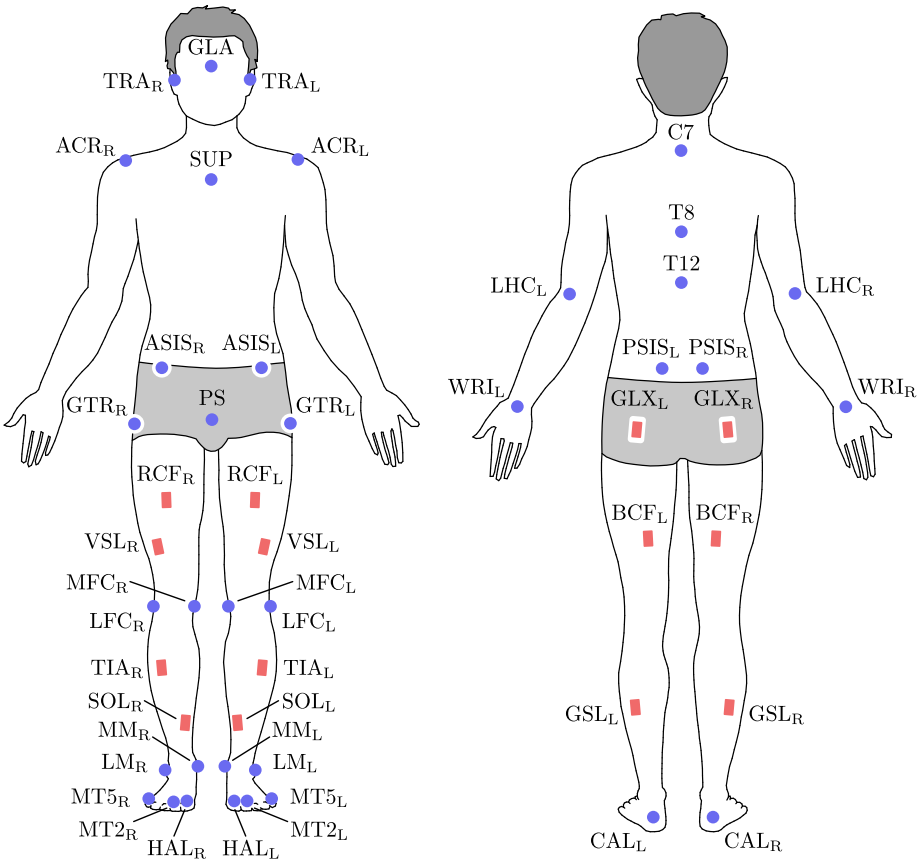

Figure 5.1.: Locations of the thirty-six markers for motion capture (blue circles) and fourteen electrodes for electromyographical measurement (red rectangles).

Table 5.1.: Details of the different motion tasks provided in the HuMoD database covering locomotion, interaction with an object and physical activity.

#	Description	Duration	Events
1.1	Straight walking at 1.0 m/s	60 s	Female: 60 left steps, 60 right steps Male: 54 left steps, 53 right steps
1.2	Straight walking at 1.5 m/s	60 s	Female: 71 left steps, 71 right steps Male: 60 left steps, 60 right steps
1.3	Straight walking at 2.0 m/s	60 s	Female: 81 left steps, 81 right steps Male: 70 left steps, 71 right steps
2.1	Straight running at 2.0 m/s	60 s	Female: 89 left steps, 89 right steps Male: 73 left steps, 73 right steps
2.2	Straight running at 3.0 m/s	60 s	Female: 96 left steps, 97 right steps Male: 79 left steps, 78 right steps
2.3	Straight running at 4.0 m/s	60 s	Female: 105 left steps, 105 right steps Male: 86 left steps, 85 right steps
3	Sideways walking at 0.5 m/s	60 s	Female: 61 left steps, 60 right steps Male: 47 left steps, 46 right steps
4	Transition between standing and straight running at 4.0 m/s	112 s	Female: 150 left steps, 149 right steps Male: 130 left steps, 129 right steps
5.1	Avoiding a long obstacle during straight walking at 1.0 m/s	120 s	Female: 6 obstacles, 119 left steps, 119 right steps Male: 7 obstacles, 105 left steps, 105 right steps
5.2	Avoiding a wide obstacle during straight walking at 1.0 m/s	120 s	Female: 6 obstacles, 120 left steps, 121 right steps Male: 7 obstacles, 106 left steps, 106 right steps
6	Squats with stopped treadmill	40 s	Female: 16 squats / Male: 10 squats
7	Kicking a ball with stopped treadmill	100 s	Female: 8 kicks / Male: 9 kicks
8	Jumps with stopped treadmill	20 s	Female: 35 jumps / Male: 35 jumps

5.3.2 Measurement Setup

The spatial motion of the body segments was recorded with a three-dimensional motion capture system at 500.0 Hz consisting of four Oqus 310+ cameras and six Oqus 300+ cameras (Qualisys, Sweden). After the calibration procedure, a standard deviation of 0.567 mm for the measurement setup of the female subject and 0.660 mm for the measurement setup of the male subject relative to a reference length of 300.2 mm was reported. A set of thirty-five reflective markers with a diameter of 19 mm mounted on thin cardboard was placed on the skin above selected anatomical landmarks. One additional marker was placed on top of the underpants above the pubic symphysis (PS) landmark [177]. The applied marker set reproduces the kinematic structure of the biomechanical model described in Chapter 3 and contains all anatomical landmarks required for joint center estimation. Additional hallux (HAL) landmarks on the large toes which were introduced to measure the relative motion between feet and toe phalanges are not incorporated in the biomechanical model. Every anatomical landmark but the PS landmark was palpated and identified by an experienced examiner, while the PS landmark was palpated through the underpants by each subject under guidance of the examiner due to privacy reasons. Figure 5.1 illustrates the set of thirty-six markers for motion capture. A list of definitions and an index of abbreviations for all anatomical landmarks are provided in Appendix A.2.

The electrical activity of fourteen selected skeletal muscles in the legs was recorded at 2000.0 Hz with an electromyographical measurement system Bagnoli-16 Desktop (Delsys, USA). The measured signals were internally filtered to a bandwidth between 20.0 Hz and 450.0 Hz. For each skeletal muscle, a surface electrode was placed by an experienced examiner according to the guidelines published by the SENIAM project [105]. A reference electrode was fixed near the kneecap. The skeletal muscles were selected with regard to the expected activation during the recorded motion tasks. The locations of the fourteen surface electrodes for electromyographical measurement are depicted in Figure 5.1. An index of abbreviations for the skeletal muscles is given in Appendix A.3.

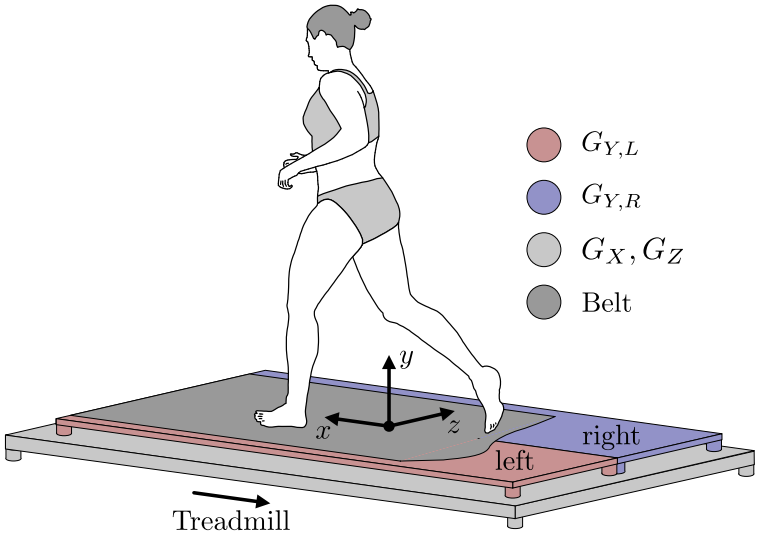

Figure 5.2.: Schematic diagram of the instrumented treadmill with the global reference frame and the single- and multi-axis force sensors.

All trials were performed on an instrumented treadmill ADAL3D-WR (Tecmachine, France). The belt of the treadmill runs over two force plates with four single-axis force sensors (Kistler, Switzerland) that were used to measure the vertical forces G_Y of the left and right foot. The two force plates are mounted on top of four multi-axis force sensors (Kistler, Switzerland) that measured the lateral forces G_X and G_Z. All forces were recorded at 1000.0 Hz. Figure 5.2 shows a schematic diagram of the instrumented treadmill and the single- and multi-axis force sensors.

5.4 Data Processing

The raw measurement data recorded with the motion capture system, instrumented treadmill and electromyographical measurement system was processed with the numerical computing software MATLAB in order to compensate measurement errors and provide additional information for the investigation, modeling and simulation of human motion dynamics. The processed data includes subject-specific estimates for anthropometric parameters, joint center locations as well as joint trajectories.

5.4.1 Spatial Motion Data

Raw spatial motion and ground reaction force data were synchronized by compensating temporal offset and drift as well as transforming the reference frame of the motion capture system into the reference frame of the instrumented treadmill which acts as a global reference frame. Both reference frames were defined with respect to internationally recognized recommendations for biomechanical reference frame notation [249]. Figure 5.2 illustrates the global reference frame where the origin is located at the center of the rectangle spanned by the left and right force plates projected to the top of the belt surface.

Infrequent gaps in raw spatial motion data of up to 300.0 ms resulting from temporarily covered markers were filled by applying locally fitted polynomial approximations. The measured spatial positions of the markers were then shifted to the approximated skin surface. This was achieved by approximating a normal vector perpendicular to the skin surface pointing towards the considered marker from adjacent markers and estimated joint center locations. The normalized normal vector was multiplied by the marker radius and additional support material thickness and subtracted from the measured spatial position. A list of definitions for the normal vectors is given in Appendix A.4. The shifted spatial positions of the markers were then used to estimate the joint center locations for the thirteen joints of the biomechanical model by applying the linear regression equations provided by Reed et al. [177] and Dumas et al. [68].

The motion capture data and therefore also the preliminary joint center estimates are affected by soft tissue artifacts resulting from relative skin to bone motion [130]. An evident indicator for soft tissue artifacts are variations in the segment lengths. The body segments connect the joints and are assumed to be rigid. Figure 5.3 shows the relative variation of the right thigh length for the motion tasks straight walking at 1.5 m/s, straight running at 3.0 m/s and kicking a ball performed by the female subject normalized in time to the motion sequence. Faint lines represent individual thigh length variations for each motion sequence normalized in time, while strong lines indicate the average thigh length variation over all sequences of the particular

Figure 5.3.: Relative length variation in the right thigh of the female subject for straight walking at 1.5 m/s (red), straight running at 3.0 m/s (blue) and kicking a ball with (green) as a result of soft tissue artifacts.

motion task. The relative variation partially exceeds 7 % of the thigh reference length for some of the running cycles. For all other motion tasks, the relative variation is smaller but still notable with absolute peak values of about 3 % and 4 %. The required reference lengths for the body segments were obtained from averaged preliminary joint center estimates taken during idle time at the beginning of each trial with stopped treadmill. In this period, the subjects stood still on the treadmill and the measurements were not affected by soft tissue artifacts.

In order to compensate the influence of soft tissue artifacts and other unpreventable measurement errors, an extended Kalman smoother in combination with the subject-specific kinematics model with thirty degrees of freedom plus six base joints was applied to compute the joint trajectories including joint positions $q_i \in \mathbb{R}$, joint velocities $\dot{q}_i \in \mathbb{R}$, joint accelerations $\ddot{q}_i \in \mathbb{R}$ and joint jerk $\dddot{q}_i \in \mathbb{R}$ with $i = 1 \ldots 36$ as well as smoothed joint center estimates [57, 257, 256]. The extended Kalman smoother estimates the time-dependent joint trajectories

$$\boldsymbol{x}(t) = \left[q_1(t), \dot{q}_1(t), \ddot{q}_1(t), \dddot{q}_1(t) \ldots q_{36}(t), \dot{q}_{36}(t), \ddot{q}_{36}(t), \dddot{q}_{36}(t)\right]^T$$

by combining noisy spatial measurements of the markers $\boldsymbol{z}$ with prior system knowledge and minimizes the estimation error statistically. The prior system knowledge is represented by a process model $f(\boldsymbol{x})$ that characterizes the expected time series of the joint trajectories $\boldsymbol{x}$ and a measurement model $h(\boldsymbol{x})$ that describes the nonlinear relation between the joint trajectories $\boldsymbol{x}$ and noisy measurements of the markers $\boldsymbol{z}$ which is given by the applied kinematics model. Process and measurement noise are modeled as zero-mean Gaussian distributed random variables $\boldsymbol{w} \sim \mathbb{N}(\boldsymbol{0}, \boldsymbol{\Sigma}_w)$, $\boldsymbol{v} \sim \mathbb{N}(\boldsymbol{0}, \boldsymbol{\Sigma}_v)$. The process model is based on the assumption that the joint jerk $\dddot{q}_i$ is constant which results in the linear process model

$$f_i(\boldsymbol{x}_i(t)) = \begin{bmatrix} 1 & \Delta t & \frac{\Delta t^2}{2} & \frac{\Delta t^3}{6} \\ 0 & 1 & \Delta t & \frac{\Delta t^2}{2} \\ 0 & 0 & 1 & \Delta t \\ 0 & 0 & 0 & 1 \end{bmatrix} \boldsymbol{x}_i(t)$$

with the sample time Δt. The extended Kalman smoother applies three successive update steps. First, the process model $f(\boldsymbol{x}(t-1))$ is used for a predictive time update $\hat{\boldsymbol{x}}(t)$. Second, a forward recursion representing the filtering update estimates the joint trajectories $\tilde{\boldsymbol{x}}(t)$ from all measurements $\boldsymbol{z}(t)$ integrating information of past samples with beginning at the first time instant. Third, a backward recursion describing smoothing update uses information of future samples to further improve the joint trajectory estimates $\boldsymbol{x}(t)$ with beginning at the last time instant. The recursive equations of the three update steps are given by

$$\begin{aligned}
\hat{\boldsymbol{x}}(t) &= f\left(\boldsymbol{x}(t-1)\right), \\
\tilde{\boldsymbol{x}}(t) &= \hat{\boldsymbol{x}}(t) + \boldsymbol{K}_f(t)\left[\boldsymbol{z}(t) - h\left(\hat{\boldsymbol{x}}(t)\right)\right], \\
\boldsymbol{x}(t) &= \tilde{\boldsymbol{x}}(t) + \boldsymbol{K}_s(t)\left[\boldsymbol{x}(t+1) - f\left(\tilde{\boldsymbol{x}}(t)\right)\right]
\end{aligned}$$

with the adaptive filter gain $\boldsymbol{K}_f(t)$ and smoother gain $\boldsymbol{K}_s(t)$. A detailed derivation of the Kalman smoother equations is provided by Yu et al. [257, 256]. The kinematic model was implemented with the multibody systems library MBSLIB [84, 246] that provides efficient algorithms to compute the forward kinematics simulation $h(\boldsymbol{x})$ and the Jacobian matrix $\partial \boldsymbol{h}(\boldsymbol{x})/\partial \boldsymbol{x}$ required for updating the adaptive filter gain. The parameters of process and measurement noise were derived from measurement error ratings of the three-dimensional motion capture system and are listed in Appendix A.6. All joint trajectories are given as Tait–Bryan angles in x-y'-z'' convention.

5.4.2 Ground Reaction Forces

The raw ground reaction forces were filtered using a sixth order zero-lag low-pass filter with a cut-off frequency of 50.0 Hz. Individual force sensor offset and drift were compensated with a linear regression based on the measurements of the unloaded force plates during the first and last 10 s of each trial. In order to decompose the measured lateral ground reaction forces G_X and G_Z as well as the measured vertical ground reaction force G_Y for the locomotion trials in the event of mixed force plate contact during double support phase, parametrized transition functions determined using a multiple regression analysis were applied [232]. The shape of the transition functions that approximate the ground reaction force decrease of the foot leaving the ground is specified by force characteristics, the duration of the double support phase and the forward velocity of the subject. This parameterization ensures a smooth transition of the separated forces and allows consideration of step-to-step variability in human locomotion [241]. The ground reaction forces were used to estimate the center of pressure and detect individual events like left and right steps, squats or kicks. The number and type of detected events in each trial are summarized in Table 5.1. In an individual measurement, the body mass of the subjects was determined with the force plates of the instrumented treadmill. This body mass was used in the estimation of the anthropometric parameters.

5.4.3 Muscle Activities

The raw muscle activities were rectified and filtered using a root-mean-square filter with a window size of 300.0 ms [126]. In addition, the filtered muscle activities were normalized to the maximum activity level over all trials of the subject. Each dataset provides filtered and non-normalized as well as filtered and normalized muscle activities.

Table 5.2.: Anthropometric parameters for the female and male subject including segment length l_s, segment mass m_s, segment center of mass $\boldsymbol{o}_s$ and symmetric segment inertia tensor $\boldsymbol{I}_s$.

					$\boldsymbol{o}_s$ in mm			$\boldsymbol{I}_s$ in kg.m^2					
Segment	**Gender**	**Origin**	l_s in mm	m_s in kg	X	Y	Z	XX	YY	ZZ	XY	XZ	YZ
HEA	female	LNJ	275.6	3.8	4.4	158.4	0.3	0.0245	0.0154	0.0262	-0.0005	0	0
	male	LNJ	299.1	5.7	6.0	160.3	0.3	0.0399	0.0224	0.0458	-0.0025	-0.0002	0.0005
THO	female	LNJ	228.1	15.1	4.8	-120.4	0.2	0.1192	0.0853	0.0960	-0.0113	-0.0007	0.0001
	male	LNJ	306.8	25.8	0.0	-170.2	-1.2	0.4280	0.2642	0.3144	-0.0294	0.0002	0.0022
ABD	female	ULJ	179.9	2.3	43.9	-74.7	0.9	0.0341	0.0451	0.0230	0.0030	-0.0001	-0.0002
	male	ULJ	157.1	2.5	27.2	-56.7	-0.5	0.0177	0.0265	0.0097	0.0007	-0.0002	-0.0002
UPA_L	female	SJ_L	239.7	1.2	-17.5	-108.8	6.7	0.0077	0.0021	0.0077	0.0001	0.0002	0.0014
	male	SJ_L	263.1	2.0	4.5	-118.9	6.8	0.0134	0.0027	0.0143	0.0005	-0.0003	-0.0001
UPA_R	female	SJ_R	248.2	1.3	-18.1	-112.7	-6.9	0.0086	0.0023	0.0086	0.0001	-0.0002	-0.0015
	male	SJ_R	267.2	2.1	4.5	-120.8	-6.9	0.0141	0.0029	0.0150	0.0005	0.0004	0.0001
LOA_L	female	EJ_L	225.9	1.0	4.7	-130.9	-4.3	0.0171	0.0007	0.0169	0.0004	-0.0001	0.0006
	male	EJ_L	278.0	1.9	2.8	-158.6	-3.9	0.0479	0.0013	0.0473	0.0001	0	0.0007
LOA_R	female	EJ_R	244.8	1.1	5.1	-139.6	4.7	0.0203	0.0009	0.0201	0.0005	0.0001	-0.0008
	male	EJ_R	284.7	2.0	2.8	-161.6	4.0	0.0505	0.0014	0.0499	0.0001	0	-0.0008
PEL	female	LLJ	124.0	8.4	-1.1	-28.8	0.2	0.1065	0.1286	0.0802	-0.0149	0	0
	male	LLJ	92.1	12.0	2.6	-25.8	-0.6	0.1041	0.1147	0.0921	-0.0064	-0.0015	-0.0007
THI_L	female	HJ_L	381.0	8.4	-29.3	-143.6	-3.4	0.1171	0.0440	0.1248	0.0060	0.0005	0.0060
	male	HJ_L	428.7	10.4	-17.6	-183.9	-14.1	0.1603	0.0429	0.1715	0.0093	0.0008	0.0093
THI_R	female	HJ_R	378.1	8.3	-29.1	-142.6	3.4	0.1145	0.0430	0.1220	0.0058	-0.0005	-0.0058
	male	HJ_R	433.5	10.5	-17.8	-186.0	14.3	0.1658	0.0444	0.1774	0.0097	-0.0008	-0.0097
SHA_L	female	KJ_L	359.3	2.6	-17.6	-145.1	-11.1	0.0261	0.0033	0.0261	0.0001	0	-0.0012
	male	KJ_L	428.9	4.0	-20.6	-175.8	-3.0	0.0582	0.0074	0.0582	-0.0012	0.0003	-0.0019
SHA_R	female	KJ_R	357.7	2.6	-17.5	-144.5	11.1	0.0258	0.0033	0.0258	0.0001	0	0.0012
	male	KJ_R	436.1	4.1	-20.9	-178.8	3.1	0.0612	0.0078	0.0612	-0.0012	-0.0003	0.0020
FOO_L	female	AJ_L	123.6	0.6	52.2	-42.2	-7.5	0.0006	0.0028	0.0027	-0.0002	-0.0001	0
	male	AJ_L	141.4	1.0	80.7	-32.0	-5.5	0.0013	0.0062	0.0060	0.0008	0.0003	0
FOO_R	female	AJ_R	118.8	0.6	51.7	-41.8	7.4	0.0006	0.0027	0.0026	-0.0002	0.0001	0
	male	AJ_R	142.1	1.0	82.6	-32.8	5.6	0.0014	0.0067	0.0064	0.0008	-0.0003	0

5.4.4 Anthropometric Parameters

Personalized anthropometric parameters for all body segments were estimated based on the linear regression equations provided by Dumas et al. [66, 67, 68]. This regression model was derived from measurement datasets with female and male subjects of comparable age and body dimensions and does not apply restrictive assumptions on the center of mass position or inertia tensor orientation. The estimation involved the gender, the body mass obtained from force plate measurements and the individually measured body height as well as the averaged segment lengths determined during idle time at the beginning of each trial.

The segment lengths for upper arm (UPA), thorax (THO), abdomen (ABD), thigh (THI) and shank (SHA) were computed from a straight line connecting the proximal and distal joint center estimates. Because the scalp hair prevented a secure attachment of a marker at the head vertex, the body height and the lower neck joint were used to assess the segment length of the head (HEA). For the lower arms (LOA), the segment length was computed as the distance between the elbow joint and the WRI marker. Hand and lower arm segments were merged by treating the hands as not actuated point masses attached to the WRI markers. The segment length of the pelvis (PEL) was computed from a straight line linking the lower lumbar joint and the midpoint between left and right hip joint. For both foot segments (FOO), the distance between the ankle joint and a reference point specified by the MT2 and MT5 markers was used to compute the segment length. This reference point was defined by adding three-quarters of the distance between the two markers to the location of the MT5 marker in medial direction in order to approximate the lateral-medial forefoot midpoint.

The personalized anthropometric parameters for both subjects and all body segments including segment length $l_s \in \mathbb{R}$, segment mass $m_s \in \mathbb{R}$, segment center of mass $\boldsymbol{o}_s \in \mathbb{R}^3$ and segment inertia tensor $\boldsymbol{I}_s \in \mathbb{R}^{3\times3}$ are listed in Table 5.2. Each inertia tensor is symmetric and can be characterized by three moments of inertia I_{XX}, I_{YY}, I_{ZZ} as well as three products of inertia I_{XY}, I_{XZ}, I_{YZ}. The individual centers of mass and inertia tensors are given relative to local reference frames specified for each body segment in accordance with recommendations published by the International Society of Biomechanics (ISB) [250, 251]. Figure 5.4 exemplary illustrates the origin and orientation of segment reference frames and related anatomical landmarks for trunk and right limbs. In anatomical neutral position, the x-axes, indicated in red, point in anterior direction, the y-axes run from inferior to superior direction and the z-axes show to the right direction. All joint axes coincide with axes of the segment reference frames. Detailed definitions for origin and orientation of all segment reference frames are provided in Appendix A.5.

5.5 Measurement Data

The HuMoD database provides raw and processed biomechanical measurement data of thirteen trials performed by two subjects. There are several data files for each dataset that represents a single trial. The raw measurement data contains unprocessed data from the three-dimensional motion capture system, instrumented treadmill and electromyographical measurement system that is provided in three separate data files per dataset with predefined data structures for each measurement system. The processed spatial motion data includes the synchronized spatial positions of the thirty-six markers, joint center estimates for thirteen joints as well as joint

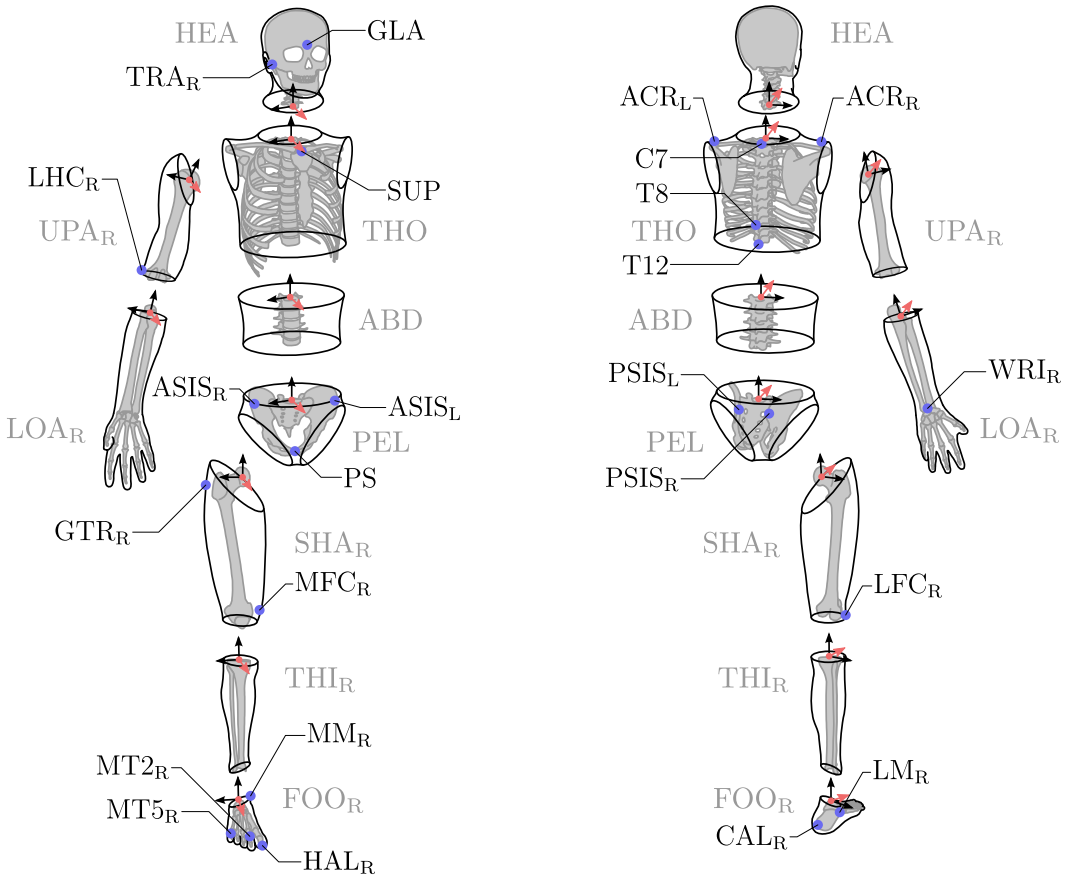

Figure 5.4.: Origin and orientation of local reference frames and related anatomical landmarks for trunk and right limbs with indicated x-axes (red).

trajectories for thirteen joints in arms, trunk, pelvis and legs plus six base joints. The processed ground reaction forces comprise synchronized, filtered and decomposed ground reaction forces and center of pressure estimates. The processed muscle activities contain filtered as well as normalized electrical activities for fourteen selected muscles in the legs. All processed data is combined in a single data file per dataset with individual data structures for each type of measurement and additional information about the trial. Anthropometric parameter estimates and subject information including origin, length, mass, center of mass and inertia tensor for all body segments as well as age, gender, body mass, body height are provided in separate data files for each subject. Positions and lengths are given in millimeters, while all other data is given in base and derived international standard units. In addition to the biomechanical measurement data, the source code of the applied computational scripts for processing the raw measurement data is made available in a revision control system. A comprehensive documentation provides a reference guide on the structure and content of the data files and the computational scripts as well as information about the subjects, motion protocol, measurement setup and data processing. All data files, documents and computational scripts can be downloaded from the HuMoD database website.

For the evaluation of uncertainty and sensitivity in the inverse dynamics simulation considered in this thesis, the motion tasks straight walking at 1.5 m/s, straight running at 3.0 m/s and kicking a ball are chosen. These motion tasks cover repetitive and ballistic whole-body motions at different speeds and with varying motion sequences. The inverse dynamics simulation is applied

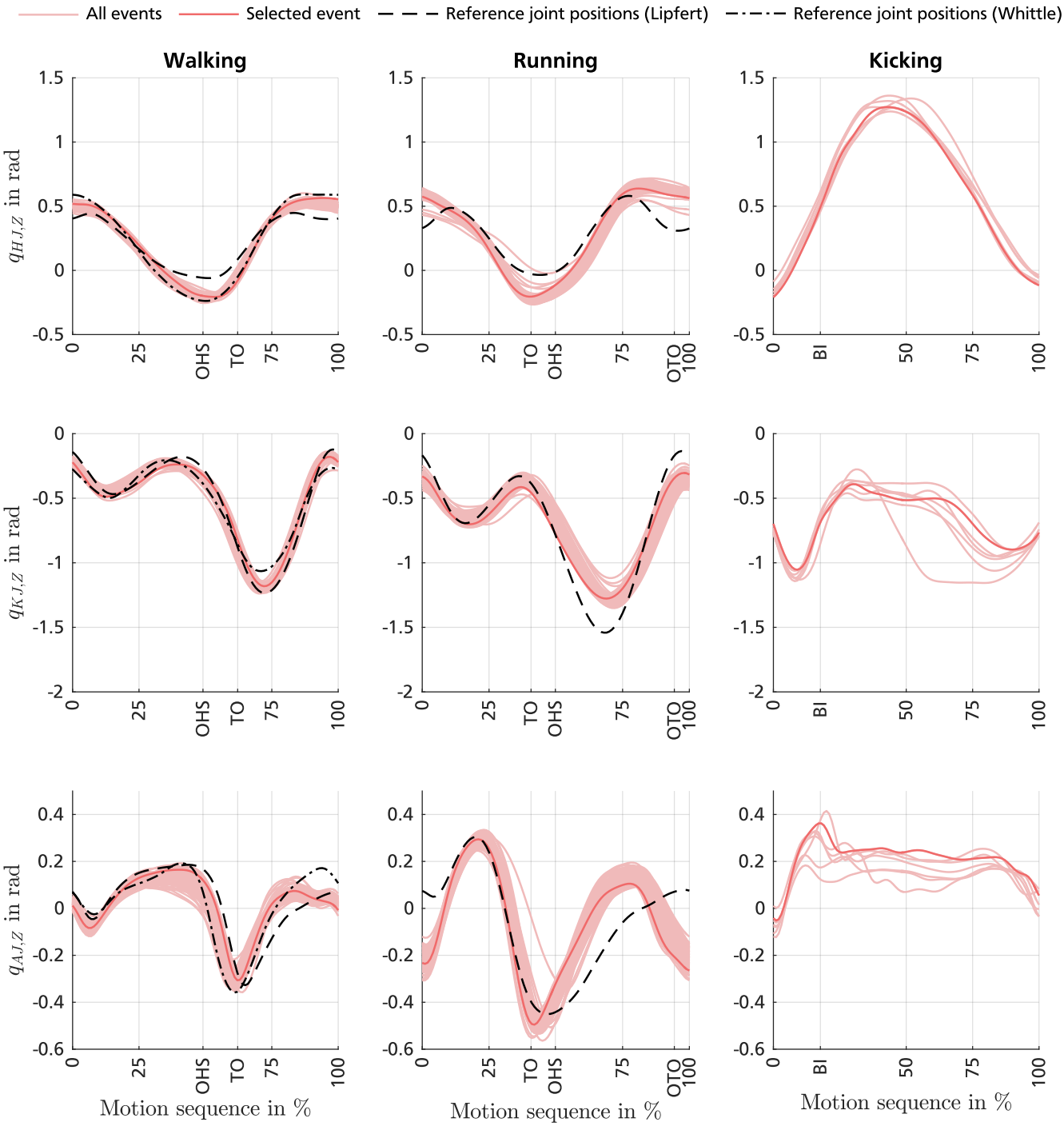

Figure 5.5.: Joint position trajectories for straight walking, straight running and kicking a ball performed by the female subject.

to one arbitrary selected event per motion task. This event is the gait cycle starting with the tenth heel strike of the right foot in the walking and running trials as well as the fifth kick in the kicking a ball trial. The examined joint torques in the inverse dynamics simulation comprise hip, knee and ankle torques about the local z-axes of the right leg. If hip abduction and rotation remain small which is the case for walking and running, leg motions about the local z-axes are approximately congruent with the sagittal plane. Figures 5.5 and 5.6 show the corresponding joint position trajectories in hip joint q_{HJ}, knee joint q_{KJ} and ankle joint q_{AJ} for all motion tasks

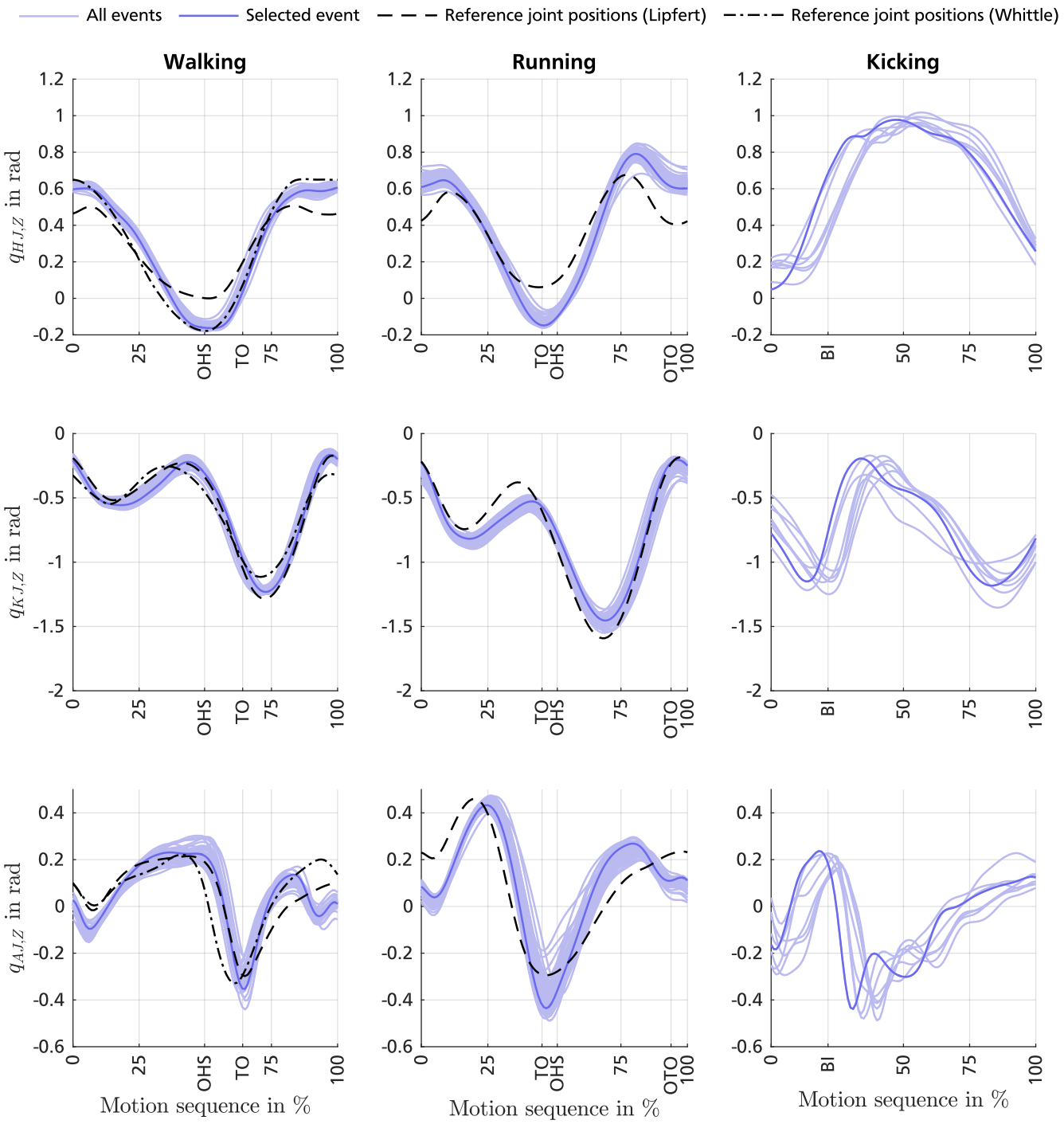

Figure 5.6.: Joint position trajectories for straight walking, straight running and kicking a ball performed by the male subject.

normalized in time to the motion sequence. Faint lines depict all individual events of the trial, while the strong lines denote the selected events. Toe off (TO), opposite heel strike (OHS), opposite toe off (OTO) and ball impact (BI) are indicated for the selected events. The black dashed and dash-dotted lines show reference trajectories taken from Lipfert [136] and Whittle [239] for walking and running in sagittal plane. The data provided by Lipfert incorporates averaged measurements with twenty-one female and male subjects (25.4 yrs, 173.0 cm, 70.9 kg) for walking at 1.6 m/s and running at 2.6 m/s. The data adopted from Whittle represents an individual

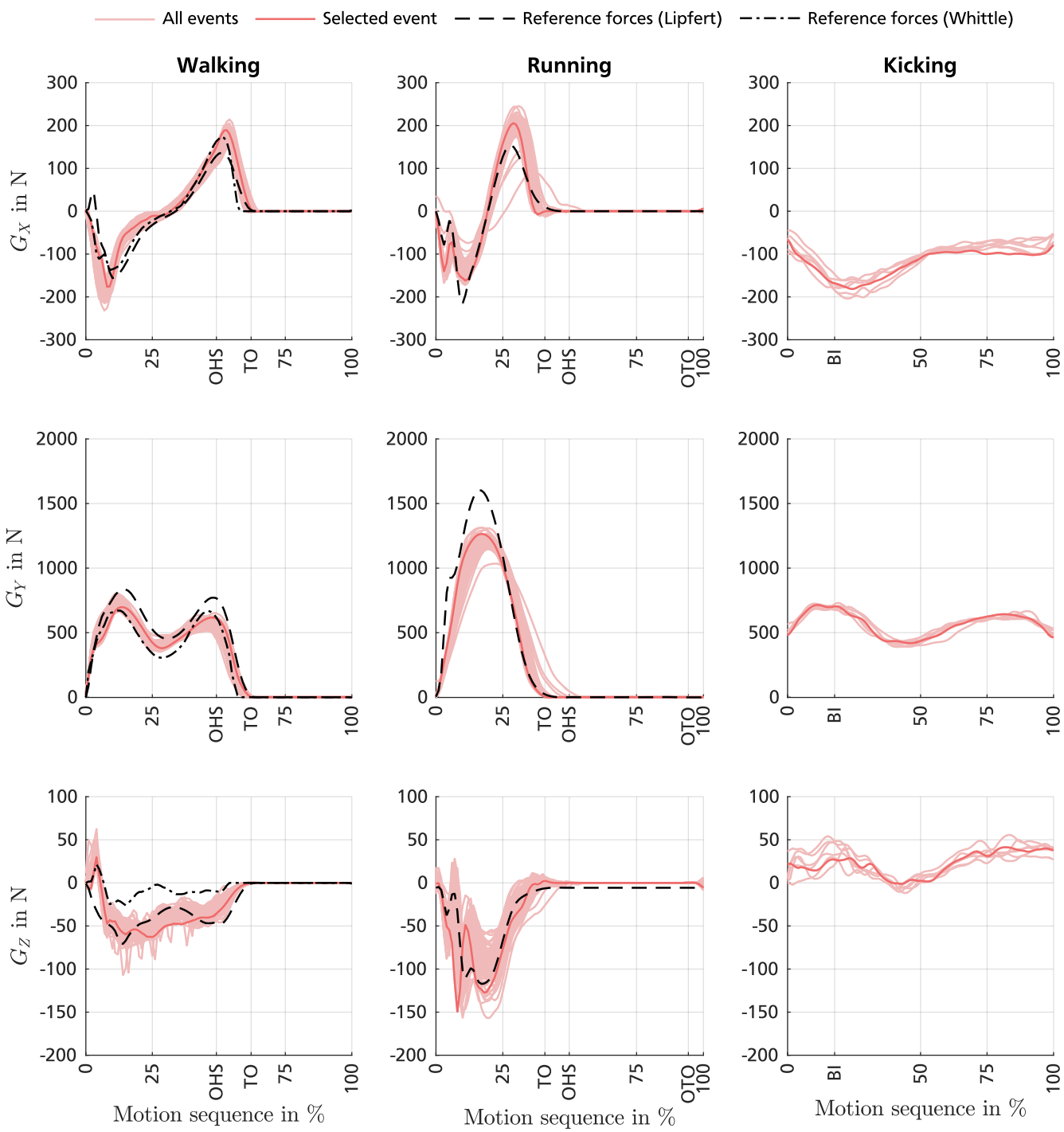

Figure 5.7.: Ground reaction forces for straight walking, straight running and kicking a ball performed by the female subject.

measurement with one female subject (22 yrs, 55 kg) for walking at 1.7 m/s. Differences in joint definitions are compensated by adapting the sign and matching the initial joint positions. In walking, the measured trajectories conform very well with the reference trajectories from literature. Only in the last 20 % of the ankle joint trajectory, some distinctive deviations can be observed for both subjects. Also in running, measured and reference trajectories are basically in agreement. However, some peak values considerably differ in all joints and the beginning and ending in hip and knee joints show some appreciable variations. For kicking a ball, no applicable

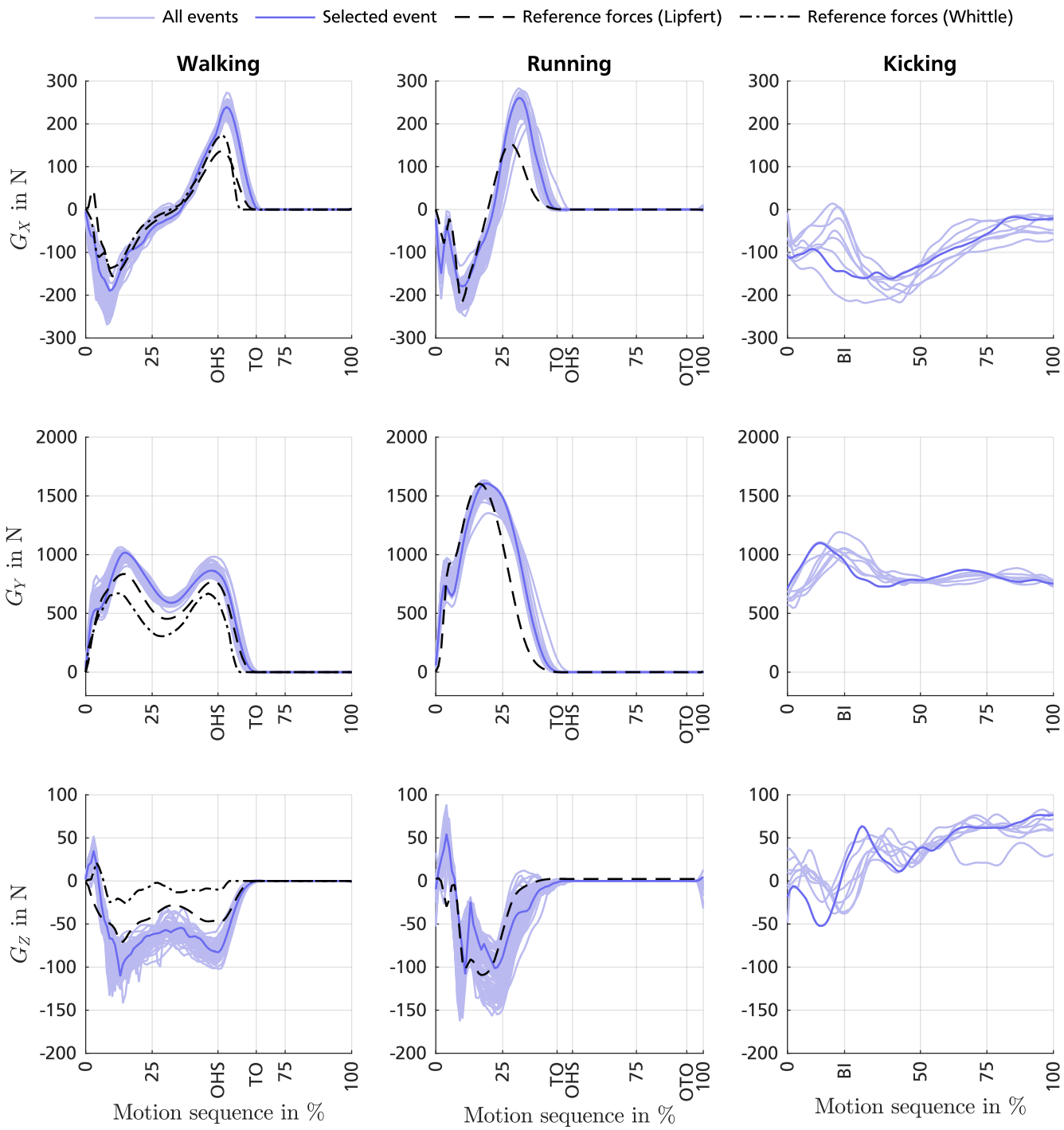

Figure 5.8.: Ground reaction forces for straight walking, straight running and kicking a ball performed by the male subject.

reference trajectories are provided in literature. It is noticeable that the joint position trajectories in knee and ankle joints are very different for both subjects which suggests rather individual kicking techniques. Figures 5.7 and 5.8 depict the measured ground reaction forces G_X, G_Y and G_Z for the right foot in the walking and running trials and the left foot in the kicking a ball trial normalized in time to the motion sequence as well as reference forces taken from Lipfert [136] and Whittle [239]. For additional smoothing, the measured ground reaction forces were filtered once more using a fourth order zero-lag low-pass filter with a cut-off frequency of 20.0 Hz. In

walking and running, measured and reference forces match reasonably well. For walking, the lateral reference force G_Z reported by Whittle is considerably smaller than the measured forces and reference forces provided by Lipfert. For running, the peak values in the lateral force G_X for both subjects and in the vertical force G_Y for the female subject differ noticeably. In addition, a small impact peak in the vertical force G_Y is evident in the measured force of the male subject as well as the reference force but is missing in the measured force of the female subject. This is an indicator for a stronger damping in the female leg dynamics. During the swing phase in walking and running, all forces become zero. Despite the very different joint position trajectories in the kicking a ball trial, the fundamental shapes of the measured ground reactions forces are quite similar for both subjects. The higher amplitudes for the male subject in the vertical force G_Y mainly result from the greater body weight. In principle, the measured joint trajectories and ground reaction forces for walking and running comply with the basic shape of the reported reference trajectories and forces. Possible reasons for the observed deviations include differences in walking or running speed, body proportions, joint definitions and measurement procedures.

5.6 Conclusion

The HuMoD database offers a versatile collection of raw and processed biomechanical measurement data for the investigation, modeling and simulation of human motion dynamics comprising trials for locomotion, interaction with an object and physical activity. Measurements and data processing were conducted based on common recommendations and advanced methods in order to provide accurate and credible measurement results. In the absence of a deterministic model for the unpreventable measurement errors, the application of the extended Kalman smoother is a favorable choice to reduce the influences of instrumental errors, modeling errors and soft tissue artifacts. On one side, deterministic soft tissue artifacts and modeling errors are treated inadequately as stochastic noise. In the case of identical soft tissue artifacts on all markers of one body segment for example, it is impossible to distinguish between body segment motion and soft tissue artifacts [57]. On the other side, all available data and system knowledge is used to eliminate the variation in segment lengths and filter stochastic measurement noise. This ensures smooth joint trajectories and consistent spatial motion data.

The open, free and easy availability of the database enables researchers to use comprehensive and high-quality biomechanical measurement data for biomechanical simulations but also the development of musculoskeletal humanoid robots or the benchmarking of human-like robot locomotion. The provided raw data allows to derive additional biomechanical information or validate the given processed results. The open-source release of the computational scripts in a revision control system helps to improve understandability, transparency and quality of the provided data and applied data processing.

The most relevant uncertainties arising in the acquisition of biomechanical measurements for inverse dynamics simulations are anatomical landmark misplacement [61], soft tissue artifacts [130] and measurement uncertainties in motion capture [47] as well as force plate measurements [172]. The involvement of these uncertainty sources in the inverse dynamics procedure is illustrated in Figure 6.1. Since the biomechanical measurements establish the first step in the estimation of joint torques, high variances in the measurands can have a significant influence on subsequently derived model parameters and simulation results.

Anatomical landmarks are internal or subcutaneous bony structures that serve as important reference points for marker-based motion capture techniques in order to achieve an accurate tracking of the rigid body segments. Examiners usually apply specific manual palpation techniques to identify the bony structures and indicate the identified positions by attaching active or passive markers on the overlying skin surface. In this way, variations in the identification process are mapped to an uncertain area on the skin close to the underlying anatomical landmark. The uncertainty of this identification process depends on the skill and experience of the

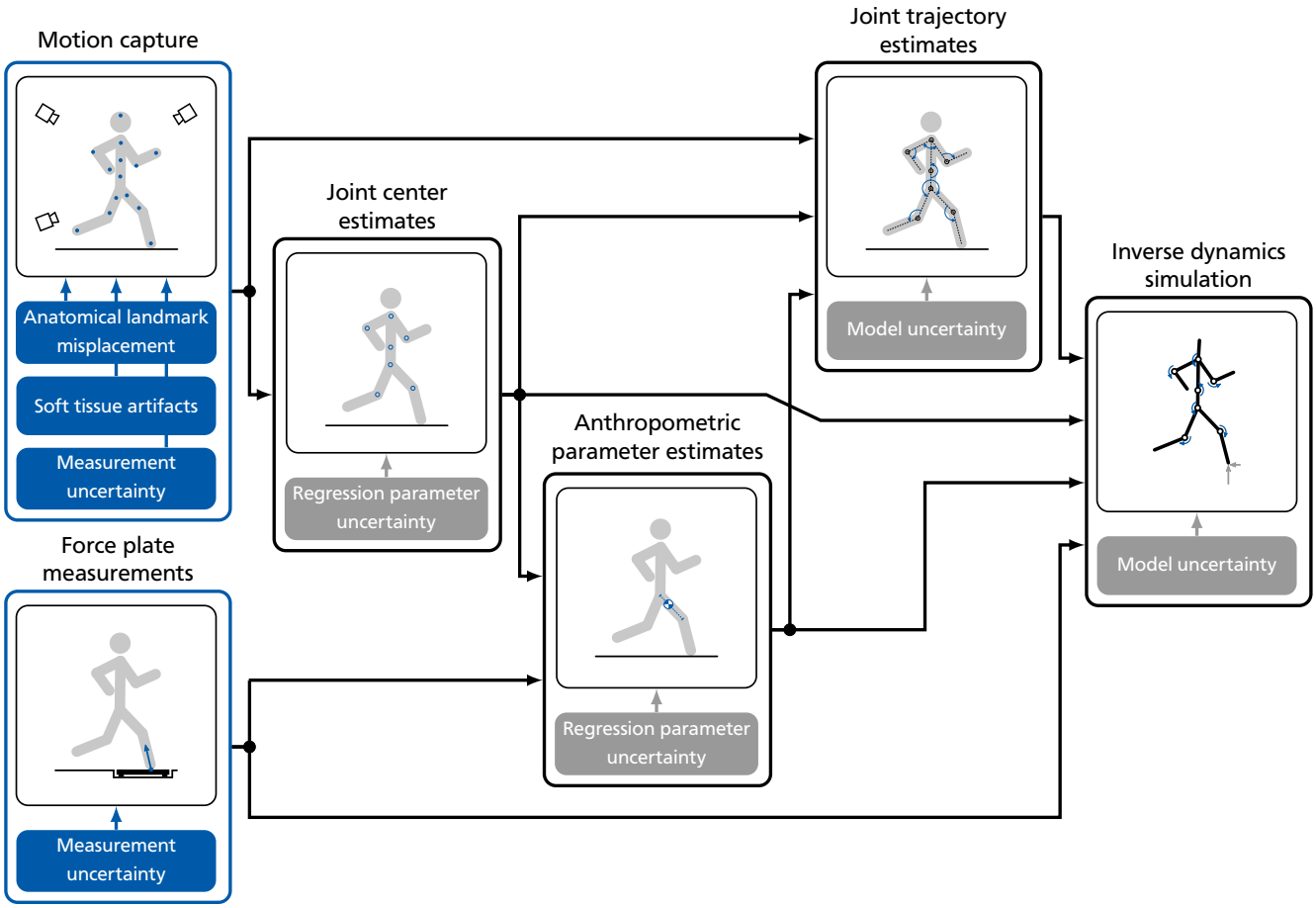

Figure 6.1.: Uncertainty propagation in motion capture and force plate measurements of the instrumented treadmill.

particular examiner and is increased by the fact that most anatomical landmarks are located on bones with relatively large and irregular surfaces and are covered by soft tissue of variable thickness and composition [31, 61].

Soft tissue artifacts are caused by relative movements between the markers attached to the skin surface and the underlying skeleton resulting from deformations of soft tissue during jerky impacts but also regular motions. The extent of the relative movements is associated with the applied marker set and experimental protocol. The deformations lead to a misestimation of the three-dimensional body segment motions and originate from inertial effects, muscle contractions as well as skin compression or sliding particularly occurring in the vicinity of joints [130]. Due to the close relation to the motion sequence, the characteristic frequency components of the artifacts are very similar to the actually performed motion and therefore difficult to distinguish in any filtering approach.

The impact of measurement uncertainties, also known as instrumental errors, highly depends on the quality, setup and calibration of the individual measurement system. The inherent uncertainties consist of random errors that vary in an unpredictable manner for repeated measurements and systematic errors that introduce a constant or proportional offset. In motion capture, measurement uncertainties affect the determination of the spatial marker positions and are mostly influenced by the preceding calibration procedure, the resolution and arrangement of the cameras, the prevailing lighting conditions as well as the involved image processing [47]. In force plate measurements, measurement uncertainties disturb the estimation of the ground reaction forces, free moment and center of pressure and are mainly caused by characteristics of the force sensors and signal amplifiers, imprecise calibration matrices, imperfect mounting of the force sensors as well as signal interference and noise [172]. Instrumented treadmills are furthermore prone to disturbances resulting from structural compliance, belt friction and variations in belt speed [210].

A large number of studies has examined the different uncertainty sources in biomechanical measurements. Experimental investigations of uncertainty quantification for anatomical landmark misplacement and soft tissue artifacts yield principally transferable variance ratings and computational models depending on the applied assumptions and methodology. In contrast, a general quantification of measurement uncertainties for motion capture and force plate measurements is virtually impossible because of the strong dependence on the individual measurement system. For this reason, practical and applicable approaches for a system-specific uncertainty evaluation on site are required, whereas provided variance ratings and experimental results only have exemplary character.

6.1 Contribution

The presented uncertainty quantification comprises a systematic evaluation of important uncertainty sources in biomechanical measurements. Based on a comprehensive literature research, suitable methods for assessing anatomical landmark misplacement, soft tissue artifacts and measurement errors in the applied motion capture system and instrumented treadmill have been derived and used in order to provide appropriate statistical models for the uncertainty and sensitivity analysis of human motion dynamics simulations. For the evaluation of anatomical

landmark misplacement and the measurement errors, experimental investigations with the actual subjects and measurement systems were conducted which guarantees compatibility with the collected biomechanical measurements. In contrast to previous studies, potential correlations between the individual measurands were considered and incorporated into the statistical models. This approach ensures a realistic representation of the analyzed uncertainties and provides novel insights into the relation between the different uncertainty sources. For the assessment of soft tissue artifacts, an exemplary uncertainty analysis based on a computational model presented in literature has been conducted in order to evaluate the influence of relative marker movements in combination with the extended Kalman smoother. The obtained results allow to review the performance of the extended Kalman smoother and rate the potential impact on joint trajectory estimation.

6.2 Anatomical Landmark Misplacement

Experimental and simulative studies showed that anatomical landmark misplacement can have a strong influence on the results of human motion analysis by affecting the orientation of local reference frames or the position of estimated joint centers [60, 148, 153]. Quantifying the accuracy of anatomical landmark identification is therefore an important aspect of the uncertainty and sensitivity analysis for human motion dynamics simulations.

6.2.1 Related Work

According to definitions for general principles in measurement methods of the International Organization for Standardization (ISO), accuracy is a general term and can be described as a combination of trueness and precision where trueness characterizes the closeness between the mean of the measurement results and the actual value, while precision denotes the closeness of agreement between independent measurement results obtained under identical conditions [116]. Precision can be further divided into repeatability that describes intra-examiner precision and reproducibility that denotes inter-examiner precision. In general, trueness and precision are assumed to be equivalent to mean and standard deviation of a Gaussian distribution.

In recent years, several studies in the fields of manual therapy, osteopathy and biomechanics have explored trueness, repeatability and reproducibility of anatomical landmark identification on individual body parts like the knee [170], foot [42], ankle [111], pelvis [111, 123, 124, 161] and spine [31, 87, 88, 101, 123, 189]. Where trueness was evaluated in these studies, identification results obtained by manual palpation methods were compared to identification results derived from two-dimensional radiographs [87, 88, 101, 189] or ultrasound imaging [87, 123]. All of these studies agreed in rating repeatability substantially higher than reproducibility and noticing a considerable impact of variations in anatomical landmark identification. However, besides the restriction on a small number of examined anatomical landmarks, the reported results of these studies are mostly based on nominal or one-dimensional measurements with limited transferability to applications in human motion analysis.

Comparatively few studies have extended the investigation of uncertainty in anatomical landmark identification to multiple body parts or even the whole body. Della Croce et al. evaluated

repeatability and reproducibility of twenty-three anatomical landmarks on the pelvis as well as the left thigh, shank and foot based on manual palpation with six experienced examiners, one healthy female and one healthy male subject [60]. A stereophotogrammetric system with two cameras in combination with reflective markers mounted on a pointer was used to determine the identified positions in three-dimensional space. Trueness and precision of the system were given as 2.5 ± 2.2 mm, 1.5 ± 1.3 mm and 4.0 ± 2.9 mm for the individual axes. Repeatability and reproducibility were reported as root mean square of the multidimensional mean for each axis of the segment reference frames as well as a combined value given by the Euclidean norm. These values can be interpreted as standard deviations and range from 0.7 mm for repeatability in the x-axis of the dorsal aspect of the fifth metatarsal head to 17.9 mm for reproducibility in the z-axis of the antero-medial ridge of the patellar surface groove. Rabuffetti et al. applied a similar method to investigate reproducibility for examiners and repeatability for subjects in a self-marking procedure [173]. Three experienced examiners and three healthy and naive male subjects placed reflective markers on twenty-one anatomical landmarks and three well-defined points that were specified by visual skin characteristics on head and trunk as well as right upper and lower arm and left thigh, shank and foot. For measuring the identified positions, a stereophotogrammetric system with two cameras and an error of less than 1.0 mm was used. Repeatability and reproducibility were reported as combined standard deviations computed with the Euclidean norm of the individual standard deviations for each axis. These values vary within 2.9 mm for reproducibility of a well-defined point on the left thigh and 19.2 mm for reproducibility of the greater trochanter landmark. Moriguchi et al. evaluated repeatability and reproducibility for twenty-three anatomical landmarks symmetrically distributed over the whole body considering the body mass index of the subjects [148]. Thirty healthy male subjects divided into a normal weight and an overweight group and two trained examiners participated in the study. The identified positions obtained by manual palpation were marked with an invisible ultra-violet fluorescent pen and measured by taking photographs in the frontal and sagittal planes under ultra-violet light with a resolution of 1024×768 px. Repeatability and reproducibility for both groups were computed based on two measurements for each anatomical landmark and reported graphically as means and standard deviations pooling measurements of left and right side. The means lie between about 1.5 mm for repeatability of the ulnar styloid process landmark in the normal weight group and about 24.0 mm for reproducibility of the anterior-superior iliac spine landmark in the overweight group. Significant differences between both groups were only found for the anterior-superior iliac spine landmarks. Valente et al. applied a virtual palpation procedure based on a three-dimensional model of a healthy male subject to estimate the precision of anatomical landmark identification on the pelvis as well as right thigh, shank and foot [227]. The three-dimensional model was constructed with data from magnetic resonance imaging. In three trials, five examiners virtually identified twenty-one anatomical landmarks directly on the bone surface of the three-dimensional model. The precision was reported as individual standard deviation for each axis of the segment reference frames. These values are noticeably smaller than previously reported data for repeatability and reproducibility in manual palpation and range from 0 mm for the z-axis of the right inferior plantar aspect of the calcaneus to 3.5 mm for the x-axis of the right lateral tibial condyle landmark. All of these studies cover a comprehensive number of anatomical landmarks and provide relevant measurement results that can be used for the probabilistic modeling of anatomical landmark uncertainty. It is important to note that the limited measurement accuracy in several

studies is close to some of the measured deviations. Also, the negligence of possible correlations between spatial dimensions might affect validity and applicability of the reported data.

6.2.2 Uncertainty Quantification

In order to investigate the effect of anatomical landmark misplacement in the inverse dynamics simulation, appropriate estimates of repeatability and reproducibility for the applied anatomical landmarks are required. However, the confinement to independent spatial dimensions in previous studies can produce misleading precision estimates. The possible impact of neglecting covariances is exemplarily demonstrated in the left and middle diagrams of Figure 6.2. Blue dots denote identified positions for an anatomical landmark found through manual palpation. The black squares mark the multidimensional mean of the identified positions. The light blue oval in the left diagram represents the three-sigma interval of a multivariate Gaussian distribution based on independent variances for each axis with a diagonal covariance matrix, while the light blue oval in the middle diagram represents the three-sigma interval of a multivariate Gaussian distribution with full covariance matrix. Although both distributions were derived from the same set of identified positions, the distribution including covariances gives a better estimate for the actual distribution of the identified positions. The distribution with independent variances covers a larger area and does not regard the spatial orientation of the identified positions. The right diagram of Figure 6.2 illustrates another restriction that arises when probabilistic sampling methods are used to model the uncertainty in anatomical landmark identification mapped to the skin surface. In fact, only two of the three dimensions can be chosen freely, whereas the third dimension is defined by the body shape. Especially on body segments with strong curvature like the hand, upper and lower arm, shank or foot, sampling without allowing for this dependence might result in samples appreciably above or below the actual skin surface. The red triangles illustrate this possible distance. All these limitations can lead to a critical under- or overestimation of precision in anatomical landmark identification and the consequent influences on results of human motion analysis.

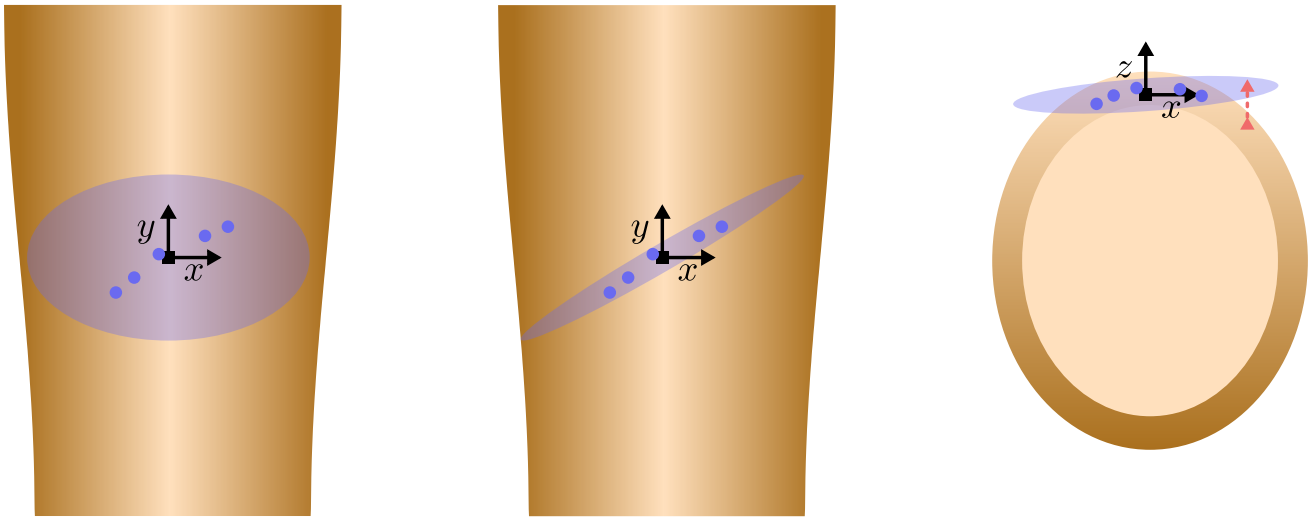

Figure 6.2.: Gaussian distribution with neglecting covariances (left) and with considering covariances (middle) as well as the effect of curvature on probabilistic sampling (right).

To provide an adequate foundation for uncertainty and sensitivity analysis, repeatability and reproducibility of the thirty-six anatomical landmarks utilized in this thesis were investigated experimentally. This included the estimation of full covariance matrices including variances and covariances for each axis of the corresponding segment reference frame as well as three-dimensional sampling points of the surrounding skin surface in order to consider possible correlations of spatial dimensions and allow anatomically correct sampling for probabilistic approaches.

One healthy female subject (28 yrs, 161 cm, 57 kg) and one healthy male subject (33 yrs, 179 cm, 85 kg) as well as five examiners with between two and nine years' experience in scientific human motion analysis including anatomical landmark identification participated in this investigation. The measurement procedure was reviewed and approved by the ethical review committee of Technische Universität Darmstadt, Germany. Subjects and examiners provided informed consent in accordance with the policies of the ethical review committee. Both subjects also participated in the biomechanical measurements for the HuMoD database [247].

Measurement Procedure

The measurement procedure was organized in a single experimental session with three steps and comprised the repeated identification and marking of the thirty-six anatomical landmarks on head, neck, thorax, pelvis as well as left and right upper arms, lower arms, thighs, shanks and feet of both subjects followed by a three-dimensional acquisition of the identified positions. Instead of using active or passive motion capture markers, the examiners indicated the identified positions on the overlying skin surface with special pens. Before the experimental session, the examiners received a booklet with the definitions of the anatomical landmarks as well as supporting graphical illustrations and were given time to read and ask questions. During the experimental session, both subjects wore white underwear that was aligned with skin-compatible and waterproof markings on clothing and surrounding skin and fixed with skin-compatible tape. The correct alignment was checked consistently. All anatomical landmarks but the PS landmark on the pelvis were palpated and marked on skin or clothing by the examiners, while the PS landmark was palpated through and marked on the underpants by the subjects under guidance of the examiners due to privacy reasons. The examiners were free to choose the applied manual palpation technique.

In the first step, all five examiners individually identified and marked each anatomical landmark through manual palpation once in random order first on the female and then on the male subject. Only one examiner was in the room at the same time. The examiners used a blue skin-compatible and waterproof ultra-violet fluorescent pen that is invisible under normal light to mark the identified positions with a small dot of about 2.0 mm in diameter. Hereby, subsequent examiners were not able to see previously placed markings. After each anatomical landmark, the marking was checked with an ultra-violet flashlight and a digital close-up photo of the area was taken under ultra-violet lighting.

For the second step, one of the examiners with eight years' experience was selected. The examiner manually palpated and marked each anatomical landmark five times in random order first on the female and then on the male subject. In this step, a red skin-compatible and waterproof ultra-violet fluorescent pen that is invisible under normal light was used to mark the identified

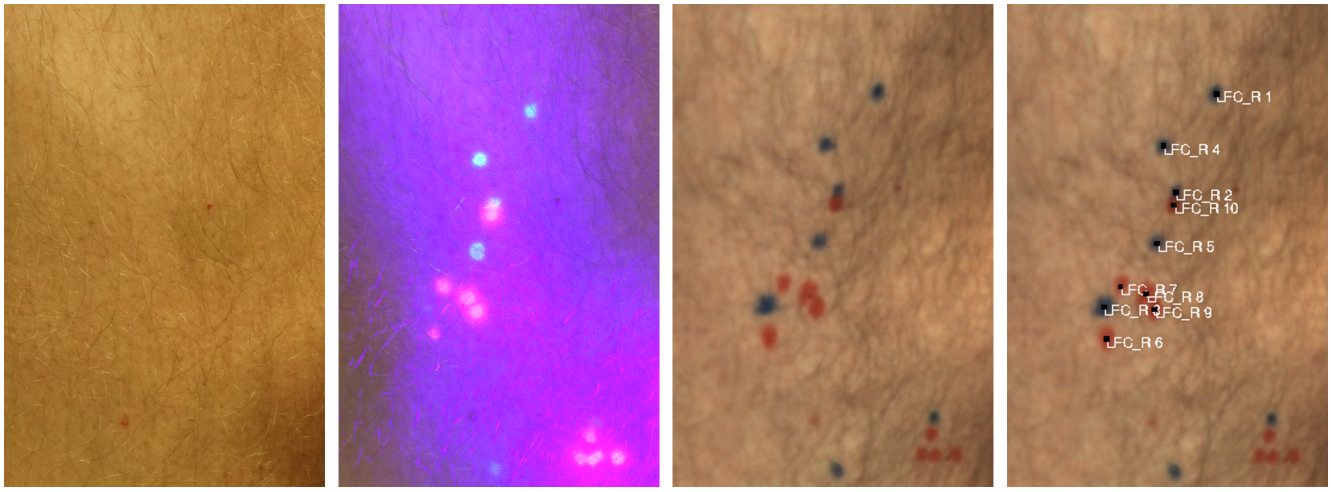

Figure 6.3.: Steps in the measurement procedure for extracting the identified positions from the three-dimensional textured models.

positions. Thereby, the examiner could not see previously placed markings while it was possible to distinguish between markings of the first and the second step. After each anatomical landmark, the marking was checked with an ultra-violet flashlight and a digital close-up photo of the area was taken under ultra-violet lighting.

In the third step, all blue and red markings on skin and underpants of both subjects were carefully traced with regular blue and red skin-compatible waterproof pens under ultra-violet lighting. The hand-held three-dimensional scanner Artec EVA (Artec, Luxembourg) was applied to create a high-resolution whole-body scan of both subjects including three-dimensional mesh and texture information. The scanner is rated with a point accuracy of 0.1 mm, three-dimensional resolution of 0.5 mm and texture resolution of 1.3 MP. Ten independent three-dimensional scans of a rigid reference object with a length of 100.0 mm in different orientations and under changing lighting conditions attested a trueness of -0.122 mm and a precision of 0.104 mm. Both subjects were scanned in upright standing position with the hands placed on the abdomen. This posture was stable and comfortable and did not cover any markings. The software Artec Studio 10 (Artec, Luxembourg) was used to generate and export three-dimensional textured models with 299,998 vertices and 600,000 faces as well as textures with a resolution of 4,096 × 4,096 px.

Data Processing

In further data processing, the blue and red markings were extracted from the three-dimensional textured models, transformed into the corresponding segment reference frames and used to estimate the covariance matrices for each anatomical landmark assuming Gaussian distributions. For this purpose, the textured models were loaded into the mesh processing software Meshlab (ISTI-CNR, Italy). A single examiner placed virtual probes in the centers of all scanned blue and red markings with the assistance of the close-up photos to distinguish overlapping markings. This allowed to determine the three-dimensional positions of the marking centers relative to a global reference frame which was arbitrarily defined during the model export process. Ten independent virtual probe placements at ten randomly chosen anatomical landmarks showed a

mean three-dimensional precision of 0.078 mm, 0.043 mm and 0.003 mm regarding the principal components of the spatial distributions. The measurement procedure is presented exemplary for the right LFC landmark of the male subject in Figure 6.3. The left image shows a close-up photo of the right knee under normal lighting as it was seen by the examiners in the first and second step while the middle left image depicts the area under ultra-violet lighting and exposes some of the blue and red markings placed by the examiners as it was seen in the third step when tracing the markings with regular pens. The middle right image shows the area as a screenshot of the three-dimensional textured model with the traced blue and red markings. The virtual probes used to determine the three-dimensional positions are displayed in the right image.

The statistical evaluation was performed with the numerical computing software MATLAB. Reproducibility and repeatability were evaluated by processing the blue and red marking centers. The multidimensional means of the marking centers for selected anatomical landmarks given in the global reference frame were used to construct the axes of the individual segment reference frames. The vectors $\boldsymbol{v}_X$, $\boldsymbol{v}_Y$ and $\boldsymbol{v}_Z \in \mathbb{R}^3$ containing the three-dimensional marking centers for a particular body segment in the global reference frame were transformed into the appropriate segment reference frame. A shrinkage approach based on the scaled identity matrix was applied to estimate the covariance matrices $\boldsymbol{\Sigma}$ because the maximum likelihood estimator given by

$$\boldsymbol{\Sigma}_{i,j} = \frac{1}{n}\sum_{k=1}^{n}(v_{i,k} - \bar{v}_i)(v_{j,k} - \bar{v}_j),$$

with $i, j \in \{X, Y, Z\}$ is quite unstable for small sample sizes of $n = 5$ [45]. In order to provide more descriptive results and facilitate a comparison to standard deviations reported in previous studies, a principal component analysis based on singular value decomposition was applied to the symmetrical covariance matrices $\boldsymbol{\Sigma}$. This allowed to decompose the correlated covariances into uncorrelated principal variances or standard deviations. The principal standard deviations $\sigma_{p,m}$ can be derived directly from the singular values S_m by

$$\sigma_{p,m} = \sqrt{S_m}$$

with $m \in \{1, 2, 3\}$ where $\sigma_{p,1}$ denotes the largest principal component and $\sigma_{p,3}$ indicates the smallest principal component. The orientation of the principal components is determined by the unitary matrix resulting from singular value decomposition.

The principal standard deviations $\sigma_{p,m}$ were also used for the acquisition of three-dimensional sampling points on the skin surface around each anatomical landmark of both subjects. In combination with appropriate three-dimensional interpolation methods that allow to estimate intermediate points on the skin surface, these sampling points enable anatomically correct sampling for probabilistic approaches. For the acquisition, a two-dimensional rectangular interval that is specified by $\pm 3\,\sigma_{p,1}$ and $\pm 3\,\sigma_{p,2}$ and centered at the multidimensional mean, representing the major principal components and covering at least 99.7 % of a multivariate Gaussian distribution was divided by an equidistant grid of at least two hundred sampling points. Such a grid of sampling points was generated for reproducibility and repeatability and transferred to the corresponding three-dimensional textured model. Samples were taken by computing the intersection of the third principal component axis with the scanned skin surface. Figure 6.4 illustrates the described sampling point distribution for the example given in Figure 6.2. The

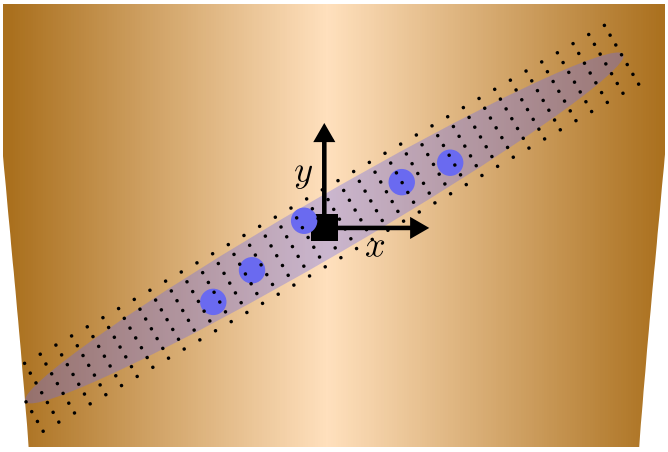

Figure 6.4.: Exemplary sampling point distribution for estimating the skin surface around each anatomical landmark.

small black dots mark the sampling points on the skin surface distributed along the major principal component axes. In the left-most column, some sampling points had to be omitted due to the strong curvature of the body segment.

6.2.3 Results

The principal standard deviations for reproducibility and repeatability of all anatomical landmarks are listed in Table 6.1. The values for reproducibility range from 0.5 mm in the right MT5 landmark of the female subject to 28.1 mm in the right GTR landmark of the male subjects. The values for repeatability start with 0.2 mm for the right HAL landmarks of both subjects as well as the right MM landmark of the female subject and with 17.0 mm for the left PSIS landmark of the male subject. Several anatomical landmarks on thorax, pelvis and thighs exhibit the greatest deviations for both subjects while anatomical landmarks on shanks and feet show rather small variance. In agreement with results from previous investigations, the principal standard deviations for reproducibility are mostly larger than the principal standard deviations for repeatability. For some anatomical landmarks, a substantial difference between left and right side is observable.

The elements of the symmetrical covariance matrices for reproducibility and repeatability of all anatomical landmarks are listed in Appendix A.7. The axes of the covariance matrices are defined by the corresponding segment reference frames. Most anatomical landmarks have fully populated variances and covariances. Due to the large number of individual sample points, the three-dimensional sample grid of the skin surface for reproducibility and repeatability are not reported in this thesis.

6.2.4 Discussion

In this investigation, a high-resolution three-dimensional scanner was used to capture the identified positions of thirty-six anatomical landmarks directly on the skin surface of the subjects. The measurement accuracy was up to thirty times higher than in previous studies and the applied

Table 6.1.: Principal standard deviations for reproducibility and repeatability in both subjects given in millimeters.

	Female						Male					
	Reproducibility			Repeatability			Reproducibility			Repeatability		
	$\sigma_{p,1}$	$\sigma_{p,2}$	$\sigma_{p,3}$	$\sigma_{p,1}$	$\sigma_{p,2}$	$\sigma_{p,3}$	$\sigma_{p,1}$	$\sigma_{p,2}$	$\sigma_{p,3}$	$\sigma_{p,1}$	$\sigma_{p,2}$	$\sigma_{p,3}$
GLA	3.5	1.7	1.4	1.0	0.8	0.5	4.3	1.8	1.6	0.8	0.4	0.3
TRA_L	5.2	2.0	1.9	0.5	0.4	0.3	7.7	4.7	3.5	1.1	0.9	0.6
TRA_R	5.0	2.2	1.9	1.6	0.8	0.6	5.9	3.8	2.8	1.8	1.1	0.8
SUP	3.7	2.1	1.6	1.5	0.8	0.6	3.3	2.1	1.6	2.8	1.3	1.1
ACR_L	15.8	11.3	8.3	2.4	1.3	1.0	14.1	10.3	7.5	3.3	1.9	1.5
ACR_R	14.1	11.5	8.4	2.4	1.4	1.0	14.1	11.6	8.4	3.8	2.5	1.8
C7	5.5	3.2	2.5	1.8	0.6	0.6	3.3	2.3	1.7	7.0	2.6	2.5
T8	14.1	4.9	4.8	2.1	0.9	0.8	22.6	10.1	8.6	1.0	0.8	0.6
T12	25.1	8.7	8.6	8.5	3.2	3.0	14.8	5.5	5.2	5.7	2.1	2.0
LHC_L	3.9	2.1	1.6	1.9	0.9	0.7	7.2	3.1	2.7	2.2	1.3	1.0
LHC_R	7.5	4.0	3.1	1.7	0.8	0.6	10.2	7.4	5.4	2.1	1.9	1.4
WRI_L	4.4	3.0	2.2	0.7	0.5	0.4	5.0	3.5	2.5	1.7	0.8	0.7
WRI_R	3.0	1.8	1.3	1.0	0.5	0.4	3.2	2.2	1.6	1.7	1.6	1.1
$ASIS_L$	5.9	2.1	2.1	2.3	1.0	0.9	6.8	4.0	3.0	2.6	2.4	1.7
$ASIS_R$	6.3	2.3	2.2	1.4	0.8	0.6	7.5	4.1	3.2	3.9	3.4	2.5
$PSIS_L$	20.7	11.7	8.9	2.9	2.1	1.5	16.9	6.8	6.1	17.0	6.6	6.1
$PSIS_R$	15.6	9.7	7.2	4.1	1.6	1.5	15.5	5.7	5.4	16.8	5.9	5.8
PS	2.1	1.3	1.0	1.9	0.9	0.8	3.8	1.5	1.4	4.0	1.5	1.4
GTR_L	22.3	20.2	14.5	6.9	4.2	3.2	10.9	9.5	6.8	5.7	5.0	3.6
GTR_R	14.1	11.0	8.0	7.6	3.0	2.7	28.1	11.7	10.5	6.6	3.7	2.9
LFC_L	14.5	6.3	5.4	2.8	1.7	1.3	8.2	4.3	3.4	10.6	3.9	3.7
LFC_R	16.1	9.6	7.2	3.0	2.5	1.8	14.4	5.6	5.1	8.6	4.1	3.3
MFC_L	6.7	3.3	2.7	4.4	2.4	1.9	14.6	6.0	5.4	3.0	1.3	1.1
MFC_R	5.0	3.1	2.3	2.9	1.7	1.3	9.5	4.0	3.5	2.3	1.9	1.4
LM_L	1.9	1.3	0.9	1.4	0.7	0.6	2.5	1.3	1.0	1.8	1.6	1.2
LM_R	1.8	1.7	1.2	1.6	1.2	0.8	2.2	1.8	1.3	1.8	1.2	0.9
MM_L	1.4	0.8	0.6	1.6	0.6	0.6	2.9	2.4	1.7	3.7	1.8	1.5
MM_R	3.6	1.2	1.2	0.5	0.3	0.2	2.4	1.0	0.9	1.6	1.1	0.8
CAL_L	6.3	2.2	2.2	1.9	0.8	0.7	5.3	3.3	2.5	2.0	0.8	0.7
CAL_R	6.7	2.4	2.3	2.1	0.8	0.8	4.8	3.7	2.7	5.2	1.9	1.8
$MT2_L$	3.5	1.5	1.3	0.8	0.7	0.5	2.8	1.2	1.0	0.9	0.6	0.4
$MT2_R$	3.1	1.2	1.1	1.3	1.0	0.8	4.1	2.2	1.7	0.8	0.5	0.4
$MT5_L$	2.7	1.5	1.1	0.8	0.7	0.5	2.2	1.5	1.1	1.5	0.6	0.5
$MT5_R$	1.5	0.5	0.5	1.4	0.6	0.5	4.3	1.7	1.6	1.4	0.6	0.5
HAL_L	2.0	0.7	0.7	0.6	0.4	0.3	2.0	0.7	0.7	0.7	0.4	0.3
HAL_R	1.6	0.8	0.6	0.5	0.2	0.2	2.2	0.8	0.8	0.4	0.3	0.2

measurement procedure further reduced the risk of introducing additional errors by supplemental measuring instruments. The resulting principal standard deviations exhibit qualitatively comparable results to previous studies. Variability is rated for anatomical landmarks that have not been considered in previous investigations like the T8, T12 or PS landmarks. The reported covariance matrices and sampling points allow to create appropriate probabilistic models and estimate multivariate distributions to further examine the influences on human motion analysis. The structure of the covariance matrices shows that there are substantial correlations in the spatial dimensions of the measurements.

As in most previous studies that examined anatomical landmarks on multiple body parts, the results focus on repeatability and reproducibility of markings on the skin surface and do not include trueness due to missing information about the actual position of the anatomical landmarks. The reported covariance matrices represent the expectation of the squared deviations from the multidimensional mean and therefore only measure the dispersion relative to this distinct reference point. A general description for a true marking on the skin surface is hardly possible since the definitions for the anatomical landmarks exclusively refer to bony structures. A major limitation of this and previous investigations is the small number of subjects and examiners resulting from the large measurement effort. This confinement reduces universal validity and does not allow to generalize characteristics like differences between left and right side or subject gender to other subjects. Furthermore, the applied measurement procedure might have affected the results for some anatomical landmarks. The scanning position with bent arms led to a deformation of the skin surface near the elbow during the scanning process. The self-marking procedure as well as undetected movements of the underpants during the measurements might have impaired the results for PS landmark. Also, the non-random order of the subjects during the identification process could have had an effect on the palpation results because examiners always started with the female subject. Despite these limitations, the obtained data provides repeatability and reproducibility estimates for the applied anatomical landmarks of the female and male subject considering existing correlations between the spatial dimensions of the measurements on the skin surface. The three-dimensional sampling points of the surrounding skin surface allow anatomically correct sampling for probabilistic modeling approaches.

6.3 Soft Tissue Artifacts

For the consideration of soft tissue artifacts in the uncertainty and sensitivity analysis, computational models are required that describe the dynamic deviations of the anatomical landmarks during the different phases of the motion sequence. Because the considered inverse dynamics simulation focuses on the lower limbs, these computational models mainly have to provide reasonable descriptions for soft tissue artifacts in the thigh and shank segments.

6.3.1 Related Work

For the evaluation of soft tissue artifacts, several invasive and noninvasive methods have been applied to measure the relative movement between the skin surface and the underlying skeleton mainly for the lower limbs. Physiologically invasive techniques comprise intra-cortical

pins, e.g. [30], external devices for fracture fixation, e.g. [2], percutaneous skeleton trackers, e.g. [141], or fluoroscopy with implants, e.g. [214]. These methods provide very accurate results but may not be representative of normal human motion due to the musculoskeletal interventions. Noninvasive techniques include acquisition based on medical imaging like X-ray, e.g. [223], ultrasound, e.g. [190] or magnetic resonance imaging, e.g. [195], as well as marker-based approaches, e.g. [89]. While these methods do not involve any physiological impairments, the results are less accurate and some techniques are radiologically invasive or restrict the range of motion. Magnitudes of soft tissue artifacts are reported to exceed 30.0 mm on the thigh segment and reach up to 15.0 mm on the shank segment [169]. In general, the expectable deviations depend on the actual marker location, the performed motion task as well as individual subject characteristics. Comprehensive reviews on different methods applied in the evaluation of soft tissue artifacts as well as detailed discussions of the obtained results are provided by Leardini et al. [130] and Peters et al. [169].

The number of studies that present computational models for describing soft tissue artifacts in simulation is quite small. Based on reported magnitudes and the finding that markers move in a continuous rather than random fashion, Chèze et al. suggested a sinusoidal model for characterizing the dynamic marker deviations on thigh and shank [46]. Each three-dimensional marker position was superimposed with a continuous disturbance trajectory computed from a sinus described by the variable simulation time as well as fixed parameters for amplitude, frequency and phase shift. The parameters were randomly selected from predefined value ranges given by 0 - 10.0 mm for the amplitudes, 0 - 25.0 Hz for the frequencies and 0 - 2π rad for the phase shifts. With these parameters, the disturbed markers had a motion range of up to 20.0 mm and oscillated with up to three times the frequency of average walking. Dumas and Chèze used the same computational model to compare different compensation methods but changed the value range for the amplitudes to 0 - 30.0 mm on the thigh segment and 0 - 15.0 mm on the shank segment [65]. Myers et al. modeled soft tissue artifacts for an uncertainty and sensitivity analysis of a walking motion by uniquely perturbating the three-dimensional marker positions with a constant offset within each phase of the gait cycle [153]. The amplitude of the offset was randomly chosen from a value range of 0 - 15.0 mm. In order to ensure smoothness at the phase transitions, the resulting marker trajectories were subsequently filtered using a fourth-order low-pass filter with a cut-off frequency of 20.0 Hz. Both computational models are based on reported characteristics of soft tissue artifacts but have not been validated against measurement data with human subjects. Although this model uncertainty limits general applicability, the simple modeling approaches in combination with random model parameters within certain ranges provide a reasonable and computationally efficient approximation of the dynamic deviations in a global uncertainty and sensitivity analysis based on Monte Carlo simulation.

6.3.2 Uncertainty Analysis

The computational effort and required number of model evaluations in the Monte Carlo simulation depend on the computation time of the model function as well as the number of input variables. Therefore, these properties of computational models for soft tissue artifacts are critical parameters regarding the performance of the uncertainty and sensitivity analysis. The sinusoidal model proposed by Chèze et al. is based on a random three-dimensional amplitude vector, a random frequency value and a random phase shift for each anatomical landmark [46]. For the

specification of the amplitude vector, a total of four random variables is required which includes three variables for the direction and one variable for the magnitude. Overall, this approach results in six input variables and an almost negligible computation time for the sinus function per anatomical landmark. The offset model introduced by Myers et al. uses one random three-dimensional offset vector for each anatomical landmark and phase of the gait cycle [153]. With the eight gait phases in walking and four random variables per offset vector comprising three variables for the direction and one variable for the magnitude, this approach needs a total of thirty-two input variables. In addition, the modified trajectory has to be low-pass filtered to guarantee smooth transitions. These properties of the offset model lead to a greater computational complexity and higher computation time compared to the sinusoidal model. For this reason, the sinusoidal model is selected for characterizing soft tissue artifacts within the uncertainty and sensitivity analysis considered in this thesis.

As described in Chapter 5, soft tissue artifacts are an important motivation for the application of the extended Kalman smoother together with the subject-specific kinematics model in joint trajectory estimation. Although this filtering approach uses all available data and system knowledge to eliminate measurement uncertainty, it is for example not possible to distinguish between body segment motion and marker uncertainties in the case of identical deviations on all markers of one body segment. In order to evaluate the impact of soft tissue artifacts in combination with the extended Kalman smoother, an exemplary uncertainty analysis for selected joint trajectories of hip, knee and ankle joints in walking has been performed by applying the framework described in Chapter 4. Within this uncertainty analysis, the extended Kalman smoother with constant jerk model and the underlying forward kinematics simulation constituted the model function. The input variables were given by disturbed marker trajectories generated with the sinusoidal model and random model parameters, while the output variables were the resulting joint positions about the local z-axes in hip, knee and ankle joints. Sensitivities were not regarded in this uncertainty analysis that was conducted in two steps.

In the first step, smoothed spatial marker trajectories for all anatomical landmarks on thigh, shank and foot were obtained by applying a forward kinematics simulation based on a reduced subject-specific kinematics model representing the right leg and the corresponding smoothed joint trajectories of the walking motion performed by the female subject. The reduced kinematics model consists of three body segments for thigh, shank and foot that are connected by a knee joint with one degree of freedom and an ankle joint with three degrees of freedom. The thigh segment is attached to a fixed base through a hip joint with three degrees of freedom. This configuration resembles the kinematic structure of the right leg in the full biomechanical model presented in Chapter 3 and reduced the required computational time for the uncertainty analysis. The considered anatomical landmarks comprised the GTR, LFC, MFC, LM, MM, CAL, MT2 and MT5 markers. A spline interpolation was used to normalize each marker trajectory in time relative to the length of the motion sequence. Each normalized marker trajectory contained 101 frames describing the percentage of the motion sequence ranging from 0 % to 100 % with a constant sampling time of 8.2 ms.

The smoothed and normalized marker trajectories formed the basis for the actual uncertainty analysis in the second step. For each trial of the Monte Carlo simulation, the individual frames

of the marker trajectories were superimposed by dynamic marker deviations $\boldsymbol{\epsilon} \in \mathbb{R}^3$ computed with the sinusoidal model given by

$$\boldsymbol{\epsilon}(t) = \frac{x_1}{\sqrt{x_2^2 + x_3^2 + x_4^2}} \begin{bmatrix} x_2 \\ x_3 \\ x_4 \end{bmatrix} \sin(2\pi\, x_5\, t + x_6),$$

where t denotes the simulation time, $x_1 \sim \mathbb{U}(0, 10.0)$ is the random magnitude of the amplitude in millimeters, x_2, x_3, $x_4 \sim \mathbb{U}(0, 1.0)$ specify the random direction of the amplitude, $x_5 \sim \mathbb{U}(0, 25.0)$ is the random frequency in hertz and $x_6 \sim \mathbb{U}(0, 2\pi)$ is the random phase shift in radians. All model parameters are assumed to be uniformly distributed and uncorrelated. The extended Kalman smoother and reduced kinematics model were applied to compute the associated joint trajectories of hip, knee and ankle joints. The parameters for process and measurement noise were adopted from the covariance matrices derived for the full biomechanical model and are listed in Appendix A.6. The uncertainty of the resulting joint positions was described by an appropriate Johnson distribution per joint and frame. The relative threshold limit for convergence was set to 10^{-4} and the individual batches comprised 40,000 trials.

6.3.3 Results

The Monte Carlo simulation was terminated after 25,500,000 trials with reaching the relative threshold limit for all distribution parameters. The results of the uncertainty analysis regarding the joint positions about the local z-axes in hip, knee and ankle joints are presented in Figure 6.5. Following the structure of a box plot, the bold black line shows the median value, whereas the red and light red areas describe probability intervals of 50 % and 95 % for the individual Johnson distributions in each frame. The impact of soft tissue artifacts is fairly consistent over the motion sequence but increases in distal direction with having the greatest magnitudes in the ankle joint. The standard deviations range from 4.6 mrad $\approx 0.265\,^\circ$ to 6.8 mrad $\approx 0.389\,^\circ$ in the hip joint, 6.8 mrad $\approx 0.388\,^\circ$ to 12.0 mrad $\approx 0.685\,^\circ$ in the knee joint and 22.0 mrad $\approx 1.260\,^\circ$ to 43.0 mrad $\approx 2.461\,^\circ$ in the ankle joint. The detailed views magnify the observed dispersion for hip and knee joints at different regions of the motion sequence.

6.3.4 Discussion

The results of the exemplary uncertainty analysis demonstrate that a full compensation of soft tissue artifacts in joint trajectory estimation cannot be guaranteed by the application of an extended Kalman smoother. The dynamic marker deviations had a strong impact on the distal end of the kinematic chain, while the joints closer to the fixed base were affected much less. This effect might at least partially result from the structure of the reduced kinematics model. Due to the kinematic constraints near the fixed base, the range of feasible joint positions for hip and knee joints is considerably restricted. The additional degrees of freedom and body segments in the full biomechanical model applied for the inverse dynamics simulation release some of these kinematic constraints with the consequence that greater variations should be expected in the proximal joints.

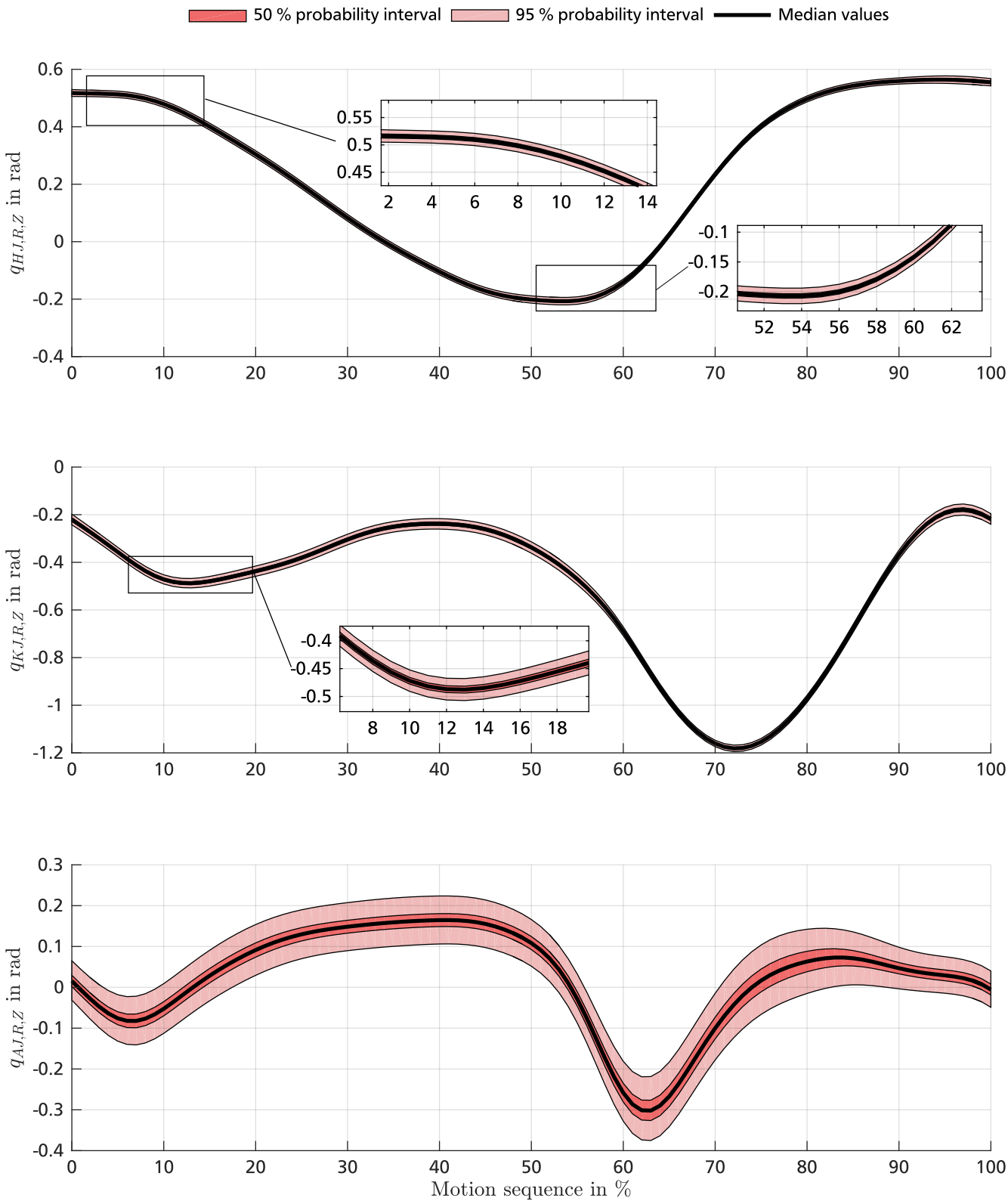

Figure 6.5.: Uncertainty in joint positions due to soft tissue artifacts for walking performed by the female subject.

Particular events of the motion sequence do not seem to have a significant influence on the soft tissue artifacts. The variance on all joints is almost evenly distributed over the motion sequence which implies that the impact of the dynamic marker deviations does not depend on

the magnitude of the joint position. This observation reveals an essential limitation of the applied sinusoidal model with random and uncorrelated model parameters since the existence of a dependency between joint positions and the relative movements of the skin surface becomes intuitively evident. Nevertheless, a probabilistic approach is an expedient choice in the absence of a deterministic model for these correlations. The obtained results show that soft tissue artifacts have to be considered in the uncertainty and sensitivity analysis of human motion dynamics.

6.4 Motion Capture Uncertainty

Manufacturers of motion capture systems typically specify only rough approximations regarding the accuracy of the measurement system because the effective performance strongly depends on the setup and calibration. Hence, a system-specific evaluation on site is required to estimate the actual measurement uncertainty.

6.4.1 Related Work

In recent years, various methods have been presented to evaluate the accuracy of marker-based motion capture systems. Cappozzo et al. proposed a passive pendulum equipped with two markers at known positions that is suspended to swing in two orthogonal planes of the calibrated volume. The motion of the markers was tracked for at least two complete oscillations and the derived time series of distances was then compared to the reference distance [47]. Ehara et al. tested several systems from different manufacturers by determining the distance between two markers attached to the ends of a rigid bar with a length of 900.0 mm [73, 72]. In a first test, a human subject moved the rigid bar within the calibrated volume by following a specific pattern. For a second test, the rigid bar was placed on the floor in order to estimate the standard deviation. The reported results for the diverse systems brought on the market in the mid to late 1990s had a range of 0.9 - 18.4 mm for the mean absolute error and 0.1 - 6.0 mm for the standard deviation. Richards evaluated seven systems from different manufacturers with a mechatronic device that enabled the combined assessment of dynamic and static markers [180]. A rigid bar with six markers arranged in a distinct pattern was actuated by an electric motor and rotated at approximately 60.0 rpm in the horizontal plane. The device was placed in the center of the calibrated volume with one additional marker fixed at the static base. The tests comprised an analysis of the ability to measure the distance between two markers placed 500.0 mm apart which rotated in the calibrated volume, the ability to measure moving markers associated with the static marker, the ability to reconstruct moving markers that were visible to alternating sets of cameras as well as the ability to measure the motion of a marker which moved in close proximity to the static marker. In the assessment of the distance measurement on the rotating rigid bar, the stated root mean square error had a range of 0.6 - 4.9 mm for the tested systems brought on the market in the late 1990s. Della Croce and Cappozzo proposed a test with a rigid rod carrying two markers and multiple target points at fixed and known positions in the calibrated volume [59]. The tip of the rod was placed on the target points and manually rotated in conical motions at the speed of the physical exercise under analysis. A statistical procedure was provided in order to evaluate the measurement accuracy with regard to systematic and random errors. Elliott et al. applied a mechatronic device replicating a human arm with shoulder, elbow

and wrist joints and multiple markers arranged in different marker sets [74]. The shoulder joint was actuated by an electric motor that allowed for representative planar rotation, while movements of the other joints were achieved via manual manipulation. For the assessment of measurement accuracy, the elbow flexion-extension and abduction were derived from the measured marker positions and compared to the reference values. All of these evaluation methods are based on at least one reference value that has to be known or measured to a precision that exceeds the accuracy of the studied system. Modern marker-based motion capture systems can achieve spatial resolutions down to fractions of a millimeter which makes great demands on the applied measuring setup and assessment procedure.

In addition to these general evaluation methods, some special test arrangements for the investigation of small motion magnitudes have been introduced. Liu et al. evaluated the accuracy of a system with a measuring field of 68.2×51.1 mm that used cameras with special lenses for accurate small-scale measurements [138]. Static marker displacement in three orthogonal directions was assessed by moving the markers in seven discrete steps between $0.5\,\mu$m and $20.0\,\mu$m. A wedge comparator with a resolution of $0.25\,\mu$m was applied to determine the reference values. Windolf et al. presented a mechatronic device that had three orthogonally arranged axes with electric motor drives and linear encoders providing an accuracy of $15.0\,\mu$m [240]. This configuration allowed to move a set of markers precisely to predefined grid-points within the operation volume of $180.0 \times 180.0 \times 150.0$ mm. Measurement accuracy was assessed for different camera setups, calibration procedures, maker sizes and lens filters by evaluating the measuring error at several grid-points. These two evaluation methods provide very accurate results but are rather difficult and expensive to extend to applications with larger calibrated volumes like human motion analysis.

6.4.2 Uncertainty Quantification

Uncertainties in motion capture systems lead to measurement errors in all three dimensions of the recorded marker positions and potentially depend on the spatial orientation of the marker motions within the calibrated volume. Also, the speed of the analyzed human motion can have an effect on the measurement uncertainty. In the kicking motion, some markers on the foot segment reach a top translational speed of up to 9.7 m/s. Many evaluation methods presented in literature apply a reference distance between two markers to assess measurement uncertainty. This one-dimensional measure can only provide trueness and precision regarding the relative position of these two markers but is not sufficient to derive individual uncertainties for a single marker in all spatial dimensions during dynamic motions. Supplementary three-dimensional reference measures like predefined target positions in the calibrated volume are difficult to determine with the required accuracy. For this reason, a mechatronic rotor system was used to generate a three-dimensional reference measure in order to estimate measurement uncertainty in all spatial dimensions for different motion speeds and spatial orientations. The rotor system consists of a two-armed rotor with two reflective markers at the rotor ends that is actuated by an electric motor drive. When the rotor spins with constant speed, the markers follow a circular path that is defined by the distance between each marker and the rotation center. With assuming a steady-state rotor motion after a reasonable settling time, the spatial trajectory of this circular path can be used as a three-dimensional reference measure. Deviations between the measured marker positions and an ideal circular path either result from slight unbalances

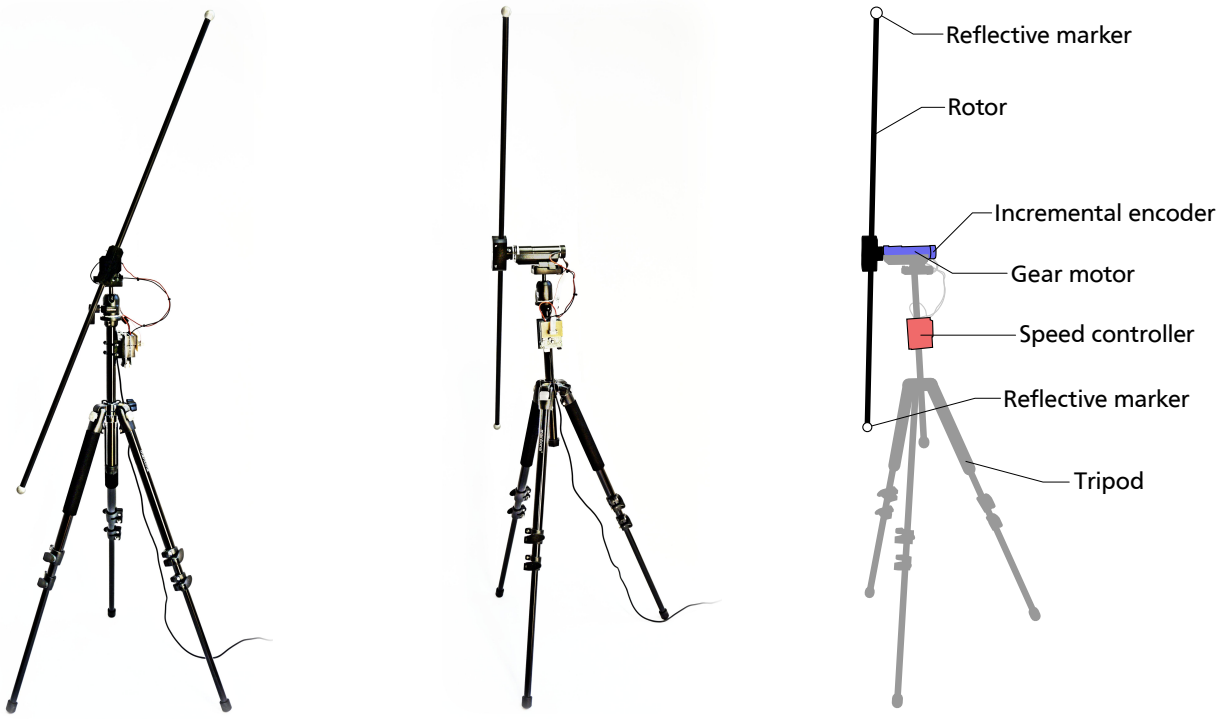

Figure 6.6.: Photographs and schematic diagram of the rotor system speed with two reflective markers and speed controlled motor drive.

in the rotor system that impose low-frequency harmonic oscillations or are caused by high-frequency measurement errors. Based on this relation, the time series of measured marker positions can be used to estimate the measurement uncertainty in all spatial dimensions by isolating high-frequency variations.

Measurement Procedure

The mechatronic rotor system, shown in Figure 6.6, is a custom-build and versatile device for the uncertainty quantification of motion capture systems. The rotor is made of an aluminum tube with a length of 1000.0 mm, a diameter of 12.0 mm and a wall thickness of 1.0 mm. Both reflective markers have a diameter of 20.0 mm and are screwed to the ends of the tube. The rotor is actuated by a direct current motor RE 30 (Maxon, Switzerland) with planetary gear and incremental encoder that is connected to a proportional-integral speed controller. The rotational speed can be adjusted in a range of 0 - 240.0 rpm. The top rotational speed corresponds to a translational speed of about 12.6 m/s and therefore covers the fastest motions observed in the HuMoD database. All components are mounted on a stable tripod (Mantona, Germany) and painted in matte black to reduce reflections.

In the uncertainty quantification, the very same three-dimensional motion capture system with four Oqus 310+ cameras and six Oqus 300+ cameras as used in the acquisition of the HuMoD database was assessed. The evaluation took place in the same room with the instrumented treadmill, where camera setup as well as lighting conditions were reproduced as close as possible. The frame rate was set to 500.0 Hz and a volume of about 2.0 × 2.0 × 1.0 m above the treadmill was calibrated. After the calibration procedure, a standard deviation of 0.680 mm

relative to a reference length of 300.2 mm was reported. The rotor system was applied in three successive measurements to evaluate measurement uncertainties with regard to three different orientations of the rotor plane and nine different rotor speeds. For each measurement, the rotor system was placed in the center of the stopped treadmill and manually aligned to one of the three principal planes comprising sagittal, frontal and transverse plane. It was ensured that the rotation center was always 1.0 m above the top of the belt surface. The measurements started with stopped and perpendicularly aligned rotor for 60 s. The rotor speed was then increased in steps of 30.0 rpm and held for 30 s up to a speed of 240 rpm. In order to reduce vibrations at the speed transitions, a linear ramp approach was applied in the speed controller which reached the set speeds after about 1 s. The rotor was stopped for the last 60 s of the measurements.

Data Processing

For the statistical evaluation of the measurement uncertainty, the numerical computing software MATLAB was used. In a first step, the measured marker position vectors $\boldsymbol{\theta}$ were transformed into a global reference frame in accordance with internationally recognized recommendations for biomechanical reference frame notation [249]. A settling time of 10 s was found to be sufficient for all speed transitions. The different measurements for the individual rotor speeds were processed accordingly by removing the first 10 s as well as the last 2 s to ensure a strict separation. For the initial interval with stopped rotor, the first 10 s and last 32 s were discarded, whereas the final interval with stopped rotor was removed completely. This resulted in a set of three times nine measurement intervals with an equal length of 18 s for sagittal, frontal and transverse plane as well as the rotor speeds from 0 rpm to 240.0 rpm. In a second step, the position of the rotor center as well as the normal vector of the rotor plane were estimated individually for each measurement interval based on the mean vector and the covariance matrix of the measured marker positions. Because changes in rotor speed might have caused different bending in the rotor, the reference lengths of the two rotor arms specified by the averaged distances between the markers and the estimated rotation center were determined separately. In a third step, the measured marker positions were transformed into local reference frames defined by the estimated normal vectors and an arbitrary vector in the rotor planes. Associated local deviations were obtained by subtracting the ideal circular path given by the rotation center and the reference lengths of the rotor arms from the transformed marker positions. Following the made assumptions, periodic low-frequency components of the local deviations were attributed to harmonic oscillations caused by slight unbalances in the rotor system. These low-frequency components were extracted with fitting and subtracting an eighth-order Fourier series expansion h given by

$$h(t) = \frac{a_0}{2} + \sum_{n=1}^{8} a_n \cos(2n\pi f t) + b_n \sin(2n\pi f t),$$

where $\boldsymbol{a} \in \mathbb{R}^9$ and $\boldsymbol{b} \in \mathbb{R}^8$ denote the vectors of Fourier series coefficients and f represents the fundamental frequency. In a fourth step, the extant local deviations for both markers were joined and transformed back into the global reference frame. The resulting global marker deviations $\boldsymbol{\epsilon}_\theta \in \mathbb{R}^3$ were described by appropriate Johnson distributions and a Gaussian copula for each individual measurement interval as well as a dimension-wise combination of all measurement intervals.

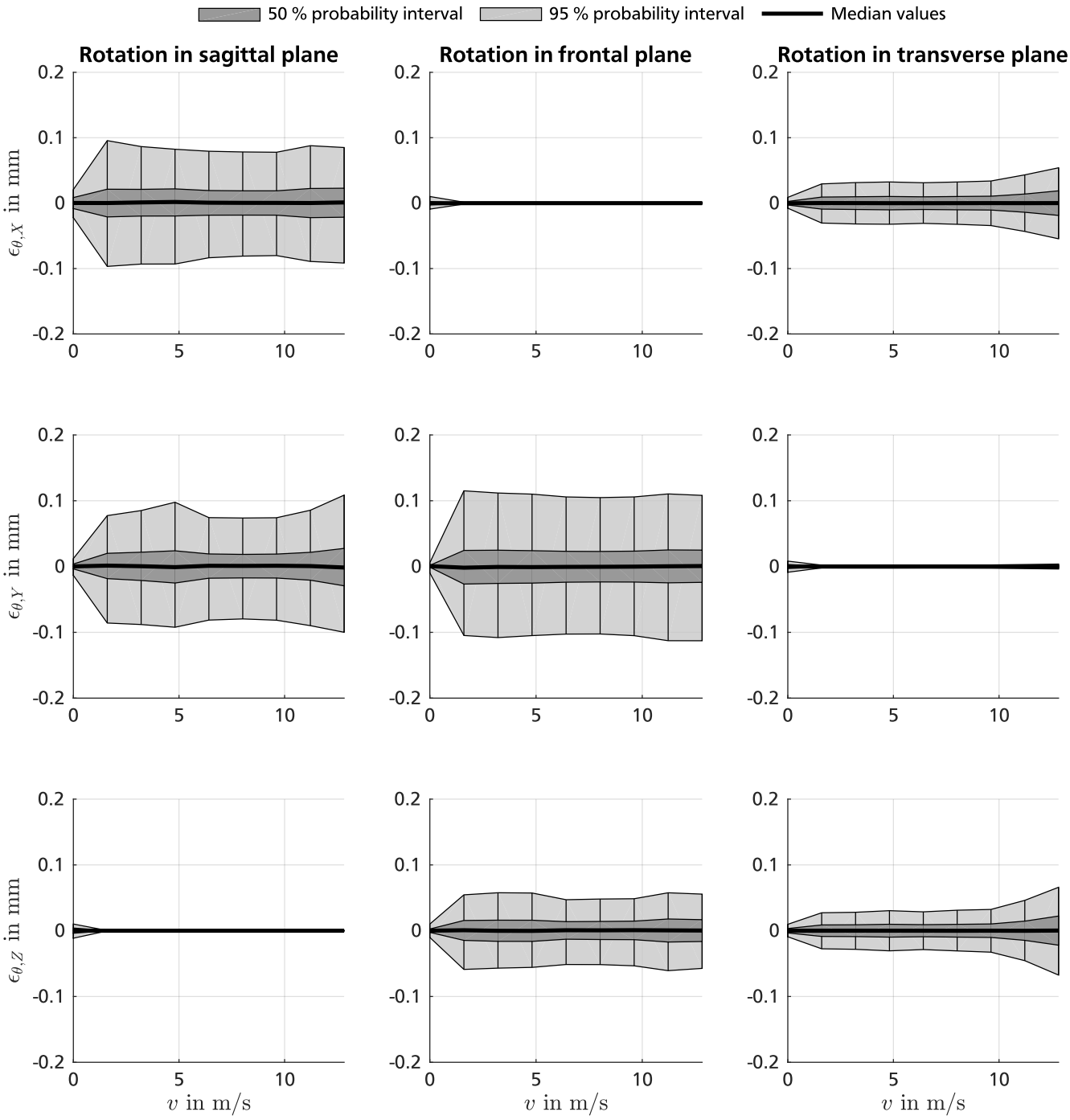

Figure 6.7.: Speed-dependent measurement uncertainty of the motion capture system with regard to different rotor orientations.

6.4.3 Results

The results of the uncertainty quantification for the motion capture system with regard to different rotor orientations and translational speeds are shown in Figure 6.7. Adopting the structure of a box plot, the bold black lines describe the median values, while the gray and light gray areas represent probability intervals of 50 % and 95 % for the individual Johnson distributions at the nine different translational speeds $v \in \mathbb{R}$. Due to the planar rotor motion, the respective dimen-

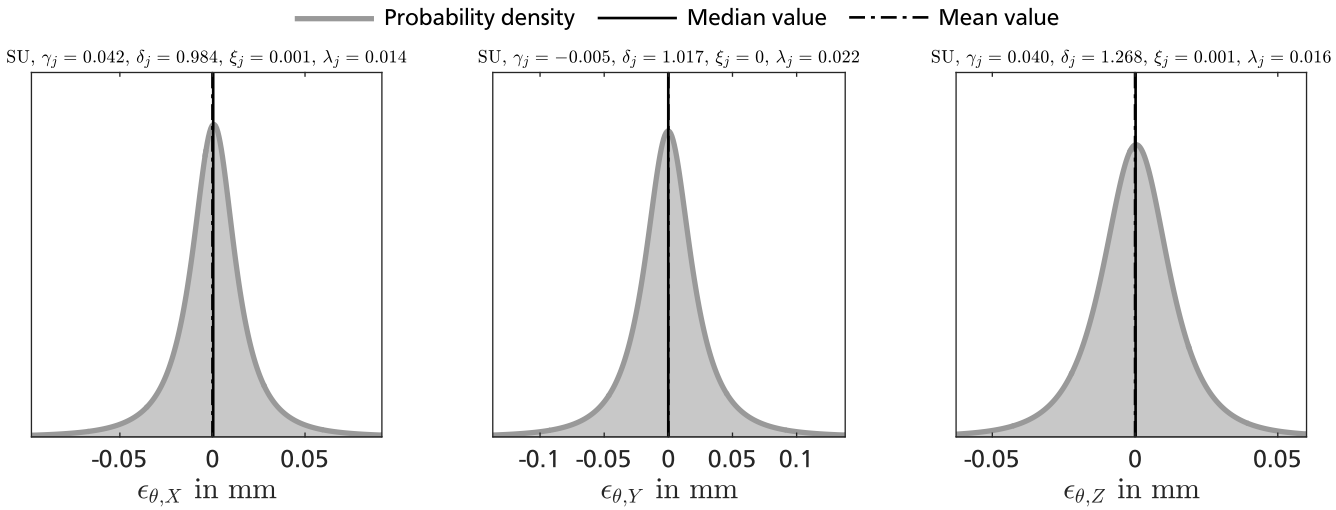

Figure 6.8.: Average measurement uncertainty of the motion capture system with corresponding Johnson distribution types and coefficients.

sions perpendicular to the rotor planes show a much lower measurement uncertainty than the other two dimensions. These ratings do not reflect the actual measurement errors but are concomitants of the applied measurement procedure. Only the two dimensions in the rotor plane provide applicable information for the evaluation of the measurement uncertainty. Besides the difference between static and dynamics measurements, the impact of the measurement uncertainty does not significantly change with the translational speed of the markers. Marker motions in transverse plane have slightly less measurement uncertainty than in the other planes. The standard deviations range from 0.004 mm for the x-axis of a stationary marker in the transverse plane to 0.056 mm for the y-axis of a marker moving with 11.2 m/s in the frontal plane. All 95 % probability intervals are slightly above or even below a deviation of 0.1 mm.

An average rating of the measurement uncertainty is provided by evaluating the dimension-wise combination of all relevant measurement intervals. The overall measurement uncertainty for the motion capture system in each spatial dimension with median and mean values is presented in Figure 6.8. For the individual probability distributions, the corresponding Johnson distribution types and coefficients γ_j, δ_j, λ_j, ξ_j are provided. As in the speed-dependent evaluation of the measurement uncertainty, the median values are very close to zero and the distributions are rather symmetric. This property is also emphasized by the overlapping median and mean values. The standard deviations for the overall measurement uncertainty range from 0.018 mm in the z-axis to 0.038 mm in the y-axis. The copula covariance matrix $\mathbf{\Sigma}_c$ that models the correlation among the individual marginal distributions is given in Table 6.2.

6.4.4 Discussion

The quantification of the measurement uncertainty for the motion capture system shows that the expectable measurement errors are quite small with hardly reaching deviations of 0.1 mm in all spatial dimensions. Despite the low measurement errors, there is an apparent difference between static and dynamic measurements. The static measurements have significantly less measurement uncertainty which justifies the applied practice of estimating the segment lengths

Table 6.2.: Copula covariance matrix of the average measurement uncertainty for the motion capture system.

$\boldsymbol{\Sigma}_c$	$\epsilon_{\theta,X}$	$\epsilon_{\theta,Y}$	$\epsilon_{\theta,Z}$
$\epsilon_{\theta,X}$	0.0630	$*$	$*$
$\epsilon_{\theta,Y}$	-0.0003	0.0491	$*$
$\epsilon_{\theta,Z}$	0.0017	0.0008	0.0598

from still standing subjects. Marker motions along the y-axis exhibit marginally larger measurement errors, whereas horizontal marker motions in the transverse plane have the lowest measurement uncertainty. These differences probably result from the specific camera setup and the dimensions of the calibrated volume. A general dependency on translational marker speed is not evident. The small off-diagonal entries in the copula covariance matrix indicate only a weak correlation among the spatial dimensions.

A possible limitation in the transferability of the uncertainty quantification is the slight inequality in marker size of 1.0 mm between the markers applied in the biomechanical measurements and the uncertainty evaluation. Other potential influence factors that have not been considered in this investigation and might impair the measurement accuracy comprise marker occlusion or discriminability of closely moving markers. Irrespective of these limitations, the obtained results provide an adequate estimate for the measurement uncertainty of the applied motion capture system. Compared to other uncertainty sources like anatomical landmark misplacement or soft tissue artifacts, the measurement uncertainty only has a minor impact on the spatial tracking of the body segments and is therefore neglected in the uncertainty and sensitivity analysis of the inverse dynamics simulation.

6.5 Instrumented Treadmill Uncertainty

Individual ambient conditions, installation sites and calibration procedures as well as a slightly different mounting of the force sensors make each instrumented treadmill a unique measurement system. In order to assess the actual measurement uncertainty, a system-specific evaluation on site is required.

6.5.1 Related Work

Most methods introduced for the evaluation of measurement uncertainty in force plate or instrumented treadmill measurements use high-precision reference sensors to determine the deviations in ground reaction forces, free moment and center of pressure. Cedraro et al. introduced a calibration procedure for force plates based on a measuring device with a three-dimensional load cell that was placed at specific contact points on a force plate defined by a spacing template and loaded through a triangular stage by a human subject [44]. The load cell had a full scale of 500.0 N for shear forces and 1000.0 N for vertical forces, while hysteresis and nonlinearity were specified with 0.06 % and 0.05 % of full scale. In order to assess measurement accuracy,

the measured forces of the load cell and the underlying force plate as well as the coordinates of the predefined contact points and the center of pressure estimates were compared. Hsieh et al. proposed a mechatronic device that consisted of a base secured to the ground, an actuated lever arm with a loading rod and an actuated load carrier with calibration weights that could be moved along the lever arm [112]. All actuated parts were controlled by electric motor drives in combination with linear encoders providing an accuracy of 1.25 μm. For static and dynamics force analysis, the loading rod was positioned at distinct contact points on a force plate and vertical loads ranging from 450.0 N to 1000.0 N were exerted by moving the load carrier and adding different calibration weights. Center of pressure evaluation at higher loads involved an operator that stood on the load carrier and shifted from two-leg to one-leg stance to create greater dynamic forces up to 1400.0 N. Measurement accuracy was evaluated by determining the reference forces based on a moment equilibrium approach and computing the deviations with regard to the measured forces and estimated center of pressure. Several studies applied an instrumented pole operated by a human subject in combination with a motion capture system to evaluate the uncertainty in force plate and instrumented treadmill measurements. Lewis et al. used a pole with three markers incorporated into the body and a three-dimensional load cell on the tip to exert forces in a conical motion to the center and four corners of a force plate [135]. The pole had a length of 1135.0 mm and weight of 1.1 kg. While the load cell recorded the applied forces, the three markers allowed to track the three-dimensional position and orientation of the pole as well as the contact point. The load cell was specified with a full scale of 550.0 N for shear forces and 1100.0 N for vertical forces and had a hysteresis and nonlinearity of 0.2 % and 0.2 % relative to full scale. By transforming the measured forces and contact points into the reference frame of the force plate, it was possible to assess measurement accuracy for ground reaction forces and center of pressure. Collins et al. and Sloot et al. employed a similar approach to test instrumented treadmills [53, 210]. Instead of a three-dimensional load cell, both studies used one-dimensional load cells and loading plates with shallow chamfered holes on both tips of the pole to restrict the applied forces to axial loads. No details about the specifications of the applied load cells were given. Sloot et al. evaluated the measurement uncertainty of two different instrumented treadmills and reported results with a range of 0.4 - 9.8 N for the absolute force errors and 0.8 - 20.0 mm for the absolute center of pressure error. For all of these evaluation methods, a precise knowledge or measurement of the reference forces and reference application points is required in order to provide an accurate estimation of the measurement uncertainty.

6.5.2 Uncertainty Quantification

If a precise tracking is ensured, an instrumented pole is a simple and flexible approach to exert arbitrary force and torque magnitudes at any desired point of the force plate or instrumented treadmill. By using a reference sensor that can measure force and torque in all three dimensions, a comprehensive evaluation of measurement uncertainties for ground reaction forces, free moment and center of pressure is possible. For this reason, an instrumented pole with a high-precision six-dimensional force-torque sensor in combination with the previously assessed motion capture system was applied to analyze the measurement uncertainty of the instrumented treadmill. The uncertainty quantification for the motion capture system attested a measurement accuracy of generally better than 0.1 mm.

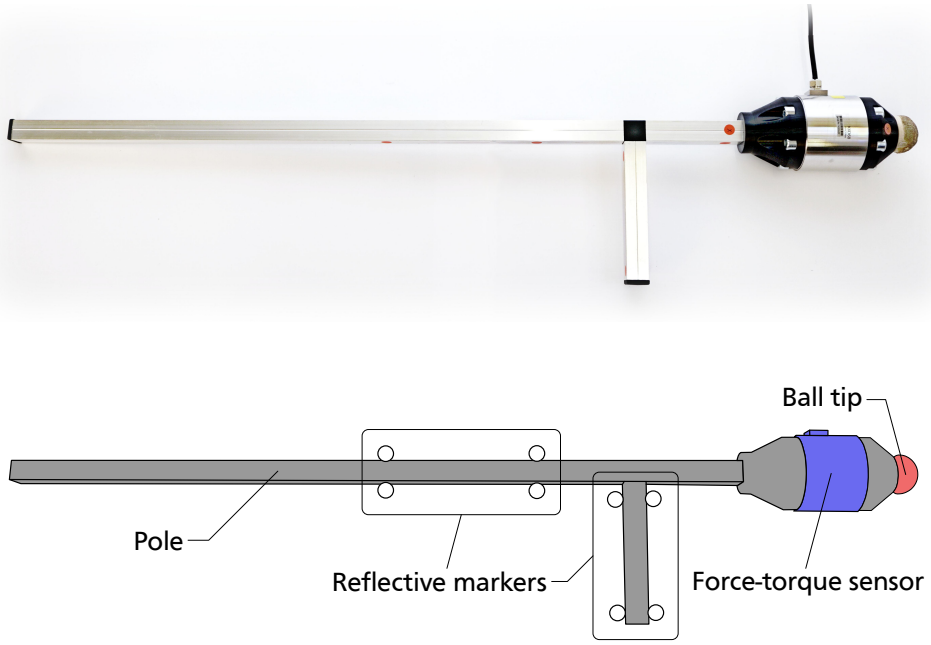

Figure 6.9.: Photograph and schematic diagram of the instrumented pole with eight reflective markers and six-dimensional force-torque sensor.

Measurement Procedure

The instrumented pole, depict in Figure 6.9, is custom-build and consists of square aluminum tube with a side length of 23.5 mm and a wall thickness of 1.5 mm. A calibrated six-dimensional force-torque sensor K6D68 (ME-Meßsysteme, Germany) is mounted between one end of the pole and a ball tip with a diameter of 40.0 mm. Thus, all loads that are applied to the free end of the pole are transmitted to the ball tip and can be simultaneously measured with the incorporated force-torque sensor. The force-torque sensor is specified with a full scale of 1000.0 N for shear forces, 2000.0 N for vertical forces as well as 20.0 Nm for the torques about all three axes. Hysteresis and nonlinearity are rated with 0.1 % and 0.1 % relative to full scale. The force and torque measurements are recorded at 1000.0 Hz with a measuring amplifier GSV-1A8USB (ME-Meßsysteme, Germany). The ball tip is made of hardwood and covered with a mixture of sand and epoxy to increase stiction during the measurements. Eight reflective markers with a diameter of 19.0 mm are placed on the main pole and a side arm with a length of 150.0 mm. This marker configuration allows to define a local reference frame in the centerline of the pole that is aligned to the axes of the force-torque sensor. The location of the markers is only shown in the schematic diagram, while red markings indicate the attachment points in the photograph. The pole has a total length of 1020.0 mm and weights 1.4 kg.

The uncertainty quantification was performed on the very same instrumented treadmill with two force plates for vertical forces and four multi-axis force sensors for the lateral forces that has been used in the acquisition of the HuMoD database. The evaluation took place in the same room but had to utilize a modified setup of the three-dimensional motion capture system due to a limited availability of the cameras. Two Oqus 310+ cameras and four Oqus 300+ cameras with a frame rate of 500.0 Hz were placed around the instrumented treadmill and focused on a calibrated volume of about 2.0 × 1.0 × 1.0 m above the top of the belt surface. After the calibration procedure, a standard deviation of 0.451 mm relative to a reference length

of 300.2 mm was reported. The force sensors of the treadmill were calibrated and set to a frame rate of 1000.0 Hz. The measurement was divided into three parts framed by an idle time of 10 s at the start and end of the recording. In the first part with a duration of 30 s, discrete force and motion impulses were applied to all measurement systems by repetitively dropping the instrumented pole approximately every 5 s from a height of about 20.0 cm onto the belt surface. During the second part with a duration of 240 s, a trained human operator exerted static and dynamic forces and torques at several equally distributed application points on the belt surface in order to produce non-zero and non-uniform reaction forces in all force sensors. The particular forces and torques were held for approximately 10 s followed by an idle time of 5 s before changing the application point. In the third part with a duration of 30 s, the procedure of the first part was repeated.

Data Processing

The measurement data comprised time series of the spatial marker motions, forces recorded by individual force sensors in the treadmill as well forces and torques recorded by the force-torque sensor in the pole. The statistical evaluation of the measurement uncertainty was performed with the numerical computing software MATLAB. In a first step, individual force sensor offset and drift in the instrumented treadmill were compensated with a linear regression based on the measurements of the unloaded force plates during the idle time of 10 s at the start and end of the recording. All measurement systems were synchronized based on the discrete force and motion impulses recorded during the first and third part of the measurement. The measurement data of each measurement system was transformed into a reference frame in accordance with internationally recognized recommendations for biomechanical reference frame notation [249]. The reference frame of the treadmill with the origin in the center of the rectangle spanned by the left and right force plates projected to the top of the belt surface was defined as the global reference frame. In a second step, all force and torque measurements were filtered using a sixth-order zero-lag low-pass filter with a cut-off frequency of 50.0 Hz. A Kalman smoother with constant jerk model was applied to estimate the spatial position and orientation of the pole relative to the global reference frame. In order to account for inertial and gravitational effects introduced by the ball tip and the attached mounting, the corresponding forces and torques were computed and subtracted from the measurements of the force-torque sensor based on estimates for mass, center of mass and inertia tensor of the affected components in combination with the recorded spatial motion trajectories. In a third step, the reference values for the ground reaction forces $\boldsymbol{G} \in \mathbb{R}^3$ in all spatial dimensions, the free moment $\Gamma \in \mathbb{R}$ about the y-axis and the center of pressure $\boldsymbol{\zeta} \in \mathbb{R}^2$ in the ground plane recorded during the second part of the measurement were obtained by transforming the compensated measurements of the force-torque sensor into the global reference frame and determining the positions of the application points from motion capture data as well as a geometric model of the ball tip. The corresponding measurement values of the treadmill were derived from the individual force sensor measurements [230]. In a fourth step, the measurement deviations $\boldsymbol{\epsilon}_G \in \mathbb{R}^3$, $\epsilon_\Gamma \in \mathbb{R}$ and $\boldsymbol{\epsilon}_\zeta \in \mathbb{R}^2$ were computed by subtracting the reference values obtained with the force-torque sensor from the measurement values of the treadmill and described by appropriate Johnson distributions and a Gaussian copula. In addition to this average rating of the measurement uncertainty, a possible dependency on the absolute magnitude of the ground reaction force $\|\boldsymbol{G}\|_2 \in \mathbb{R}$ was considered by dividing the measurement deviations into six classes with a width of 50.0 N and characterizing each indi-

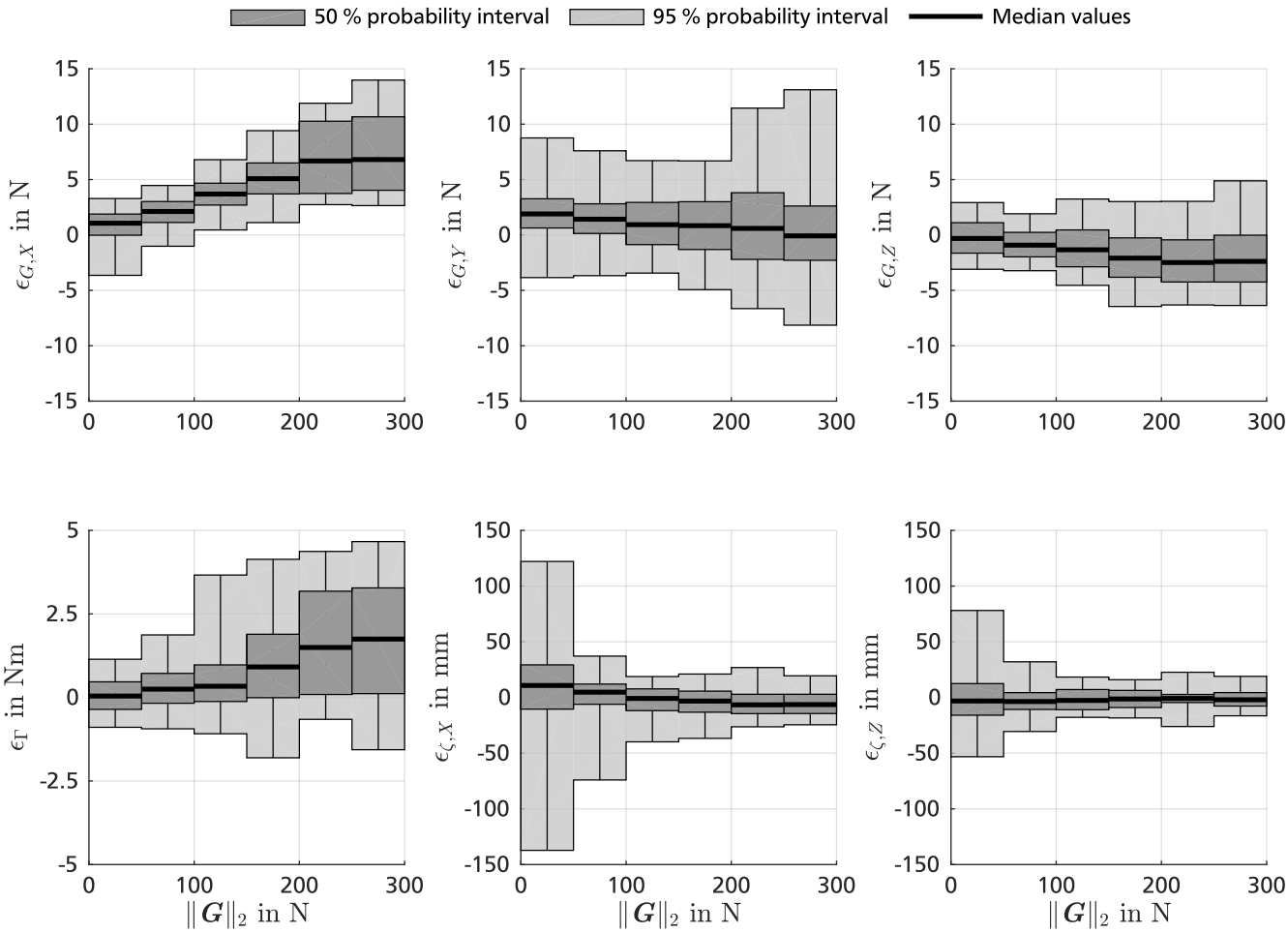

Figure 6.10.: Force-dependent measurement uncertainty of the instrumented treadmill relative to the absolute magnitude of the ground reaction force.

vidual class with suitable Johnson distributions and a Gaussian copula. The sixth class contains all data points with force magnitudes larger than 250.0 N. By this segmentation, it is ensured that each class comprises more than 13,000 data points. During the measurements, the exerted forces reached maximum values of 100.2 N in the x-axis, 447.9 N in the y-axis and 144.6 N in the z-axis, while the applied torque about the y-axis had a maximum value of 0.676 Nm.

6.5.3 Results

The results of the uncertainty quantification for the instrumented treadmill relative to the absolute magnitude of the ground reaction force are shown in Figure 6.10. Adopting the structure of a box plot, the bold black lines represent the median values, whereas the gray and light gray areas represent probability intervals of 50 % and 95 % for the individual Johnson distributions. All ratings imply considerable measurement deviations for the regarded measurands. While the variability of the ground reaction forces and the free moment clearly increases with larger force magnitudes, the center of pressure estimates rather gain precision. The reason for this reciprocal relation is a division by the vertical component of the ground reaction force in the calculation of the center of pressure. With rising values of the vertical component, uncertainties in other involved measurands are of less consequence and the variability of the estimate is reduced. In

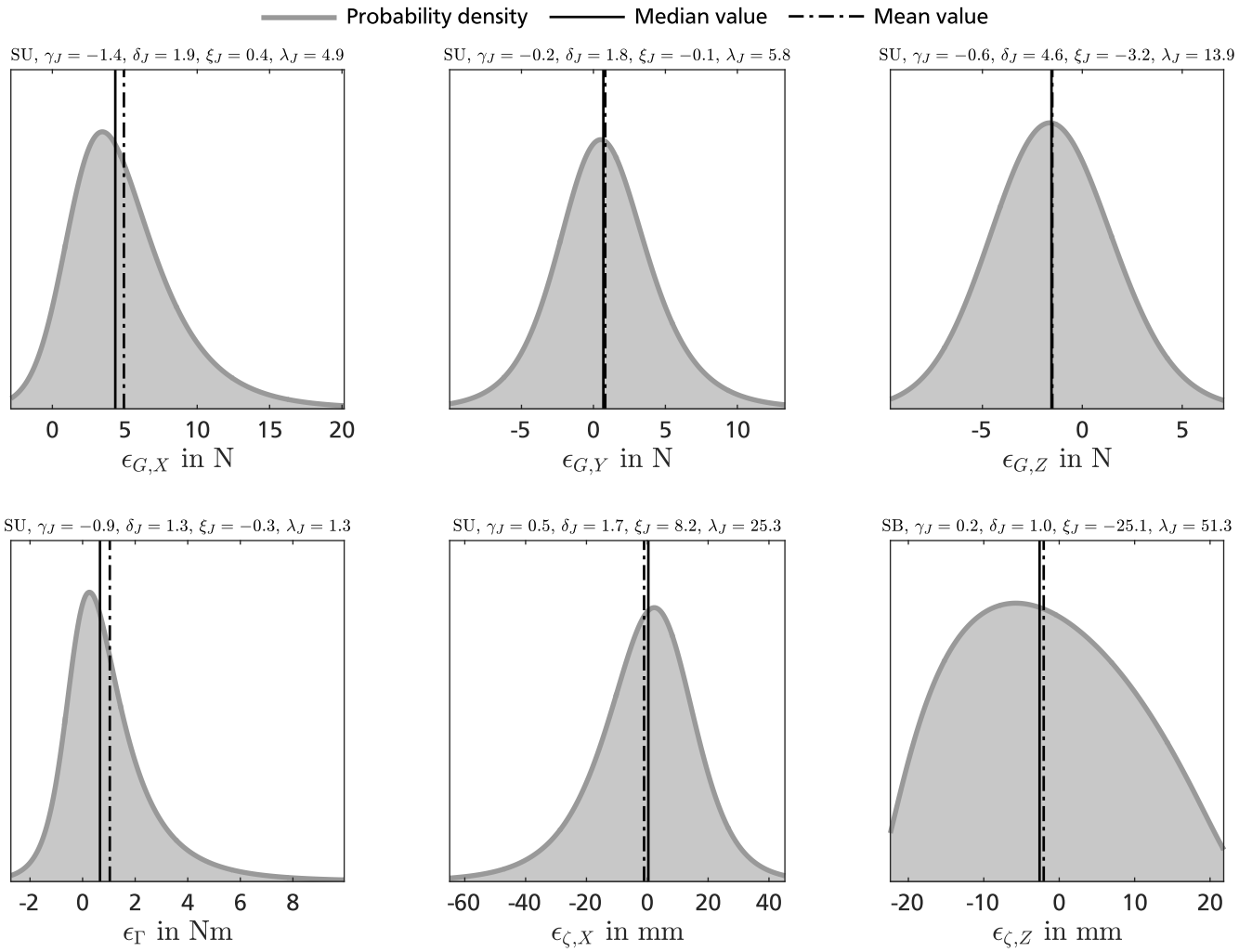

Figure 6.11.: Average measurement uncertainty of the instrumented treadmill with corresponding Johnson distribution types and coefficients.

addition to the changes in precision, the median values as indicators for systematic errors vary over the force magnitudes. Particularly, the lateral ground reaction force in the x-axis and the free moment are affected by increasing median values for ascending force magnitudes. The standard deviations for the ground reaction forces range from 1.407 N in the second class regarding the x-axis to 5.445 N in the sixth class regarding the y-axis. For the free moment, the standard deviations lie between 0.549 Nm in the first class and 1.856 Nm in the sixth class. The standard deviations for the center of pressure alter within 9.098 mm in the sixth class regarding the z-axis and 78.8 mm in the first class regarding the x-axis.

The averaged rating of the measurement uncertainty over all magnitudes of the ground reaction force is presented in Figure 6.11. For the individual probability distributions, the median and mean values as well as the corresponding Johnson distribution types and coefficients γ_j, δ_j, λ_j, ξ_j are provided. Small deviations between the median and mean values exhibit slight asymmetries in the distributions for some measurands. As in the force-dependent evaluation of the measurement uncertainty, the lateral ground reaction force in the x-axis and the free moment have median and mean values that differ substantially from zero. Also, the other measurands but the center of pressure in the x-axis are affected by notable offsets. The standard deviations

Table 6.3.: Copula covariance matrix of the average measurement uncertainty for the instrumented treadmill.

$\boldsymbol{\Sigma}_c$	$\epsilon_{G,X}$	$\epsilon_{G,Y}$	$\epsilon_{G,Z}$	ϵ_{Γ}	$\epsilon_{\zeta,X}$	$\epsilon_{\zeta,Z}$
$\epsilon_{G,X}$	0.0833	$*$	$*$	$*$	$*$	$*$
$\epsilon_{G,Y}$	-0.0154	0.0382	$*$	$*$	$*$	$*$
$\epsilon_{G,Z}$	-0.0244	0.0101	0.0558	$*$	$*$	$*$
ϵ_{Γ}	0.0379	-0.0265	0.0054	0.0712	$*$	$*$
$\epsilon_{\zeta,X}$	-0.0117	0.0014	0.0060	-0.0016	0.00731	$*$
$\epsilon_{\zeta,Z}$	0.0082	0.0149	-0.0276	-0.0275	-0.0062	0.0850

for the ground reaction forces lie between 3.149 N in the z-axis and 3.961 N in x-axis, while the standard deviations for the center of pressure range from 10.8 mm in the z-axis to 18.2 mm in x-axis. The standard deviation of the free moment has a value of 1.976 Nm. The copula covariance matrix $\boldsymbol{\Sigma}_c$ that models the correlation among the individual marginal distributions is given in Table 6.3.

6.5.4 Discussion

The quantification of the measurement uncertainty for the instrumented treadmill reveals significant measurement deviations in ground reaction forces, free moment and center of pressure. The found measurement uncertainties partially exceeded the evaluation results reported by Sloot et al. for two other instrumented treadmills. Whereas the ground reaction forces directly result from adding up the measurement values of the respective force sensors, free moment and center of pressure are calculated in several steps that involve measurement values of multiple force sensors as well as geometric parameters of the treadmill [230]. Therefore, measurement errors in the force sensors affect all measurands but potentially have a larger impact on the estimation of free moment and center of pressure. The reciprocal relation between the magnitude of the ground reaction force and the precision in the center of pressure is a consequence of this interdependency. The considerable off-diagonal entries in the copula covariance matrix are another indicator for the correlation among the individual measurands.

Potential limitations in the applied measurement procedure are the modified setup of the motion capture system as well as rather small force and torque magnitudes compared to the values which can be expected in biomechanical measurements. Due to the changed arrangement with fewer cameras, the good tracking performance that has been found in the corresponding uncertainty quantification cannot be guaranteed for this investigation. Nevertheless, the standard deviation which was reported after the calibration procedure indicated less variance than in the original setup with more cameras and a larger calibrated volume. For this reason, a similar or even better tracking performance can be expected. The limited force and torque magnitudes result from the manual operation of the instrumented pole. For a more comprehensive uncertainty quantification, the mechanical setup could be modified by providing a stage for the human operator in order to use the body weight as a primary source for the applied forces and torques. With the manual operation, the exerted vertical forces were only slightly lower than the

average forces in the walking and kicking motions performed by the female subject but about three times smaller than the maximum forces in the running motion performed by the male subject. Furthermore, the uncertainty quantification focuses on the instrumented treadmill without accounting for additional uncertainty sources like the parametrized transition functions used in the data processing of the biomechanical measurements to decompose the measured lateral ground reaction forces [232]. These transition functions are based on averaged measurements with different subjects and therefore can only approximate the actual subject-specific force characteristics. Despite these limitations, the acquired results provide a proximate but reasonable quantification for the measurement uncertainty of the applied instrumented treadmill. The obtained statistical models allow to consider realistic measurement deviations for ground reaction forces, free moment and center of pressure in the uncertainty and sensitivity analysis of the inverse dynamics simulation.

6.6 Conclusion

High variances in motion capture and force plate measurements substantially affect the tracking of body segments and the estimation of ground reaction forces which can have a significant impact on derived model parameters and simulation results. The presented uncertainty quantification for important uncertainty sources in the acquisition of biomechanical measurements provides an essential foundation for the uncertainty and sensitivity analysis of human motion dynamics simulations. The obtained statistical models for anatomical landmark misplacement, soft tissue artifacts and measurements errors in the applied motion capture system and instrumented treadmill have been derived from experimental investigations with the actual subjects and measurements systems or from suitable computational models described in literature. This approach ensures on one hand good compatibility with the biomechanical measurements used in the inverse dynamics simulation considered in this thesis and gives on the other hand new insights into the relation between the different uncertainty sources in modern measurement systems.

The results of the experimental investigation on anatomic landmark misplacement yield repeatability and reproducibility estimates for thirty-six anatomical landmarks of the female and male subject considering existing correlations between the spatial dimensions. For probabilistic modeling approaches, three-dimensional sampling points of the surrounding skin surface enable an anatomically correct sampling. The exemplary uncertainty analysis of soft tissue artifacts based on a sinusoidal model presented in literature shows that the dynamic marker deviations have a strong impact on joint trajectory estimation and cannot be fully compensated by the application of an extended Kalman smoother. The uncertainty quantification for the applied measurement systems leads to mixed results. While the expectable measurement errors in motion capture are rather negligible compared to the other regarded uncertainty sources, the measurement uncertainty of the instrumented treadmill eminently impairs the determination of ground reaction forces, free moment and center of pressure. With regard to these results, anatomic landmark misplacement, soft tissue artifacts as well as measurement uncertainties of the instrumented treadmill are further considered in the uncertainty and sensitivity analysis of the inverse dynamics simulation.

7 Uncertainty Analysis of Joint Center Estimation

The estimation of joint center locations is an important requirement for the definition of the individual body segments and the kinematic structure of the biomechanical model. Personalized estimates for the considered joints are typically calculated from motion capture data in combination with an appropriate regression model. Uncertainties in the regression parameters therefore influence the derived anthropometric parameters and joint trajectories but also affect the results of the inverse dynamics simulation [178]. Figure 7.1 illustrates the involvement of this uncertainty source in the inverse dynamics procedure.

7.1 Related Work

There are two common approaches for estimating the joint center locations in biomechanical studies. In the functional method, joint center locations are estimated as the pivot point of the three-dimensional relative motion between the adjacent body segments. This approach allows

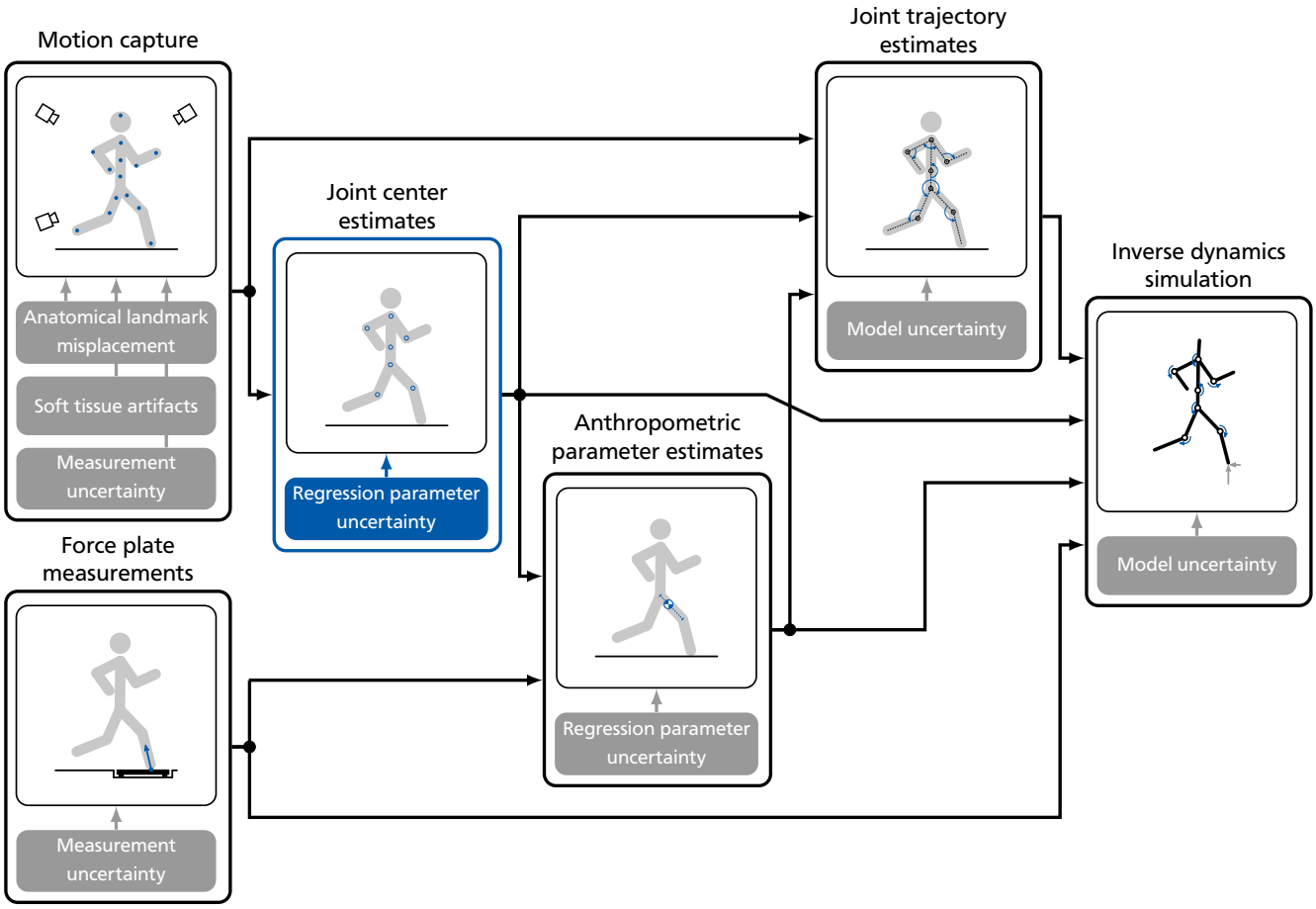

Figure 7.1.: Uncertainty propagation in joint center estimation based on an appropriate regression model.

for accurate and subject-specific estimates but requires an adequate motion range in the considered joints which might exclude elderly or pathological subjects and is often based on persistent exciting trajectories that have to be specifically regarded in the measurement protocol. Leardini et al. [129] and Camomilla et al. [37] for example identified the hip joint center with the functional method, whereas Schwartz and Rozumalski [204] simultaneously estimated the hip and knee joint centers. The predictive method utilizes statistical relations between anatomical landmarks and joint center locations by providing regression equations with particular regression parameters for female and male subjects. Except for the hip joint center, these models typically involve two or three anatomical landmarks and are specified by one or two parameters for each joint. Besides the spatial position of the necessary anatomical landmarks, this approach does not require any additional information or preparation and is therefore widely adopted in biomechanical and medical studies. Dempster conducted the first large-scale effort to provide regression equations for joint center estimation by taking systematic measurements on dissected cadavers of male subjects [63]. Snyder et al. used radiographs of male volunteers to investigate joint center locations in sitting and standing postures as well as the relation between markers on the skin surface and the underlying joints [211]. Based on measurements from preserved specimens of a skeleton collection, Reynolds et al. determined spatial positions of several anatomical landmarks on the pelvis for male and female subjects [179]. Reed et al. published a comprehensive regression model for various joints together with the associated regression parameters for female and male subjects with focusing on typical postures of automobile occupants [177]. The model was derived from measurement data of twenty-five female and male subjects provided by Schneider and Robbins [183, 184, 197] as well as joint center estimates largely based on the findings from Dempster, Snyder et al. and Reynolds et al. In a study about anthropometric parameter estimation, Dumas et al. applied this model for the determination of hip, shoulder, lower neck and lower lumbar joint locations but assumed a coincidence with the midpoint between a lateral and a medial anatomical landmark for all other joints [66]. In a later study, Dumas et al. also included the upper lumbar joint by approximating the spatial position with a Kriging interpolation approach [68]. Several additional studies provide other suitable regression models but rather focus on individual body segments or joints, e.g., [56, 102, 205].

Existing studies on the uncertainty in joint center estimation mainly address the hip joint. Bell et al. compared the hip joint centers estimated by one functional and two predictive methods reported in literature with an orthogonal pair of radiographs on seven male subjects [29]. All of the tested approaches had a deviation of at least 20.0 mm and showed a significant variation in repeated trials. Leardini et al. assessed another set of functional and predictive methods on eleven male subjects by a comparison with results of a Roentgen stereophotogrammetric analysis [129]. The two predictive methods had an average root mean square error of up to 30.0 mm, while the functional method performed much better with an average root mean square error of 13.0 mm. Sangeux et al. used three-dimensional ultrasound as reference for a comparison of two predictive and five functional methods on nineteen subjects of unspecified gender [196]. The results revealed an average absolute error of 15.0 mm for the best functional method and 16.0 mm for the best predictive method. Andersen et al. evaluated three predictive methods including the two methods studied by Sangeux et al. against measurements based on computerized tomography for eighteen female and male subjects with metal-on-metal hip resurfacing arthroplasty [10]. The found deviations for the individual methods ranged from

15.0 mm to 21.0 mm. All these results indicate the expectable variance in hip joint centers but do not give any information about uncertainties in other joints. In order to investigate the impact of joint center uncertainty on the estimation of joint torques in an inverse dynamics simulation, Stagni et al. [215] and Reinbolt et al. [178] performed an uncertainty analysis for walking motions. Stagni et al. used a local analysis and imposed three-dimensional offsets of up to 30.0 mm in the hip joint based on the results provided by Leardini et al., while Reinbolt et al. applied a global analysis with a Monte Carlo simulation and assumed three-dimensional offsets of up to 10.0 mm in hip, knee and ankle joints. Both studies found significant effects on the estimated joint torques in the lower limbs.

7.2 Contribution

The presented uncertainty analysis is, to the best of the author's knowledge, the first extensive evaluation of variances in all parameters of two comprehensive regression models for joint center estimation in female and male subjects. Because of the limited availability of suitable reference data, an indirect approach has been applied that exploits statistical properties of anatomical landmarks reported in literature to derive the expectable uncertainty in the considered regression parameters. The required information has mostly been extracted from the same data collections that were originally used to define the individual regression models. This procedure avoids ambiguous transformations between different reference frames or geometric definitions and ensures the best possible compatibility. In contrast to previous studies, the evaluation is not restricted to a single joint but comprises the most relevant joints for a biomechanical simulation of human locomotion. The obtained statistical models provide appropriate representations of the uncertain regression parameters and enable to assess the impact of variations in joint center estimation within the uncertainty and sensitivity analysis of the inverse dynamics simulation.

7.3 Uncertainty Analysis

Due to the high practical relevance, the focus of the uncertainty analysis was put on the comprehensive regression models provided by Reed et al. and Dumas et al. The model by Reed et al. can be applied with a reduced set of anatomical landmarks and covers all major joints but the wrist joint. The model by Dumas et al. forms an important basis for the estimation of anthropometric parameters and introduces additional relations for joints in arms and legs. In the biomechanical model described in Chapter 3, the definitions given by Dumas et al. have been adopted for almost all joints. Only the definition for the elbow joint is taken from Reed at al., while the wrist joint is not considered.

7.3.1 Model Definition

The definitions for all relevant regression parameters of both models are illustrated in Figure 7.2. The joint center locations are estimated by adding a suitable spatial vector, shown in red, to a given reference point. The magnitude of the vector results from the multiplication of a particular reference length $L_i \in \mathbb{R}$ with $i = 1 \dots 8$ by a corresponding linear parameter $\alpha \in \mathbb{R}$.

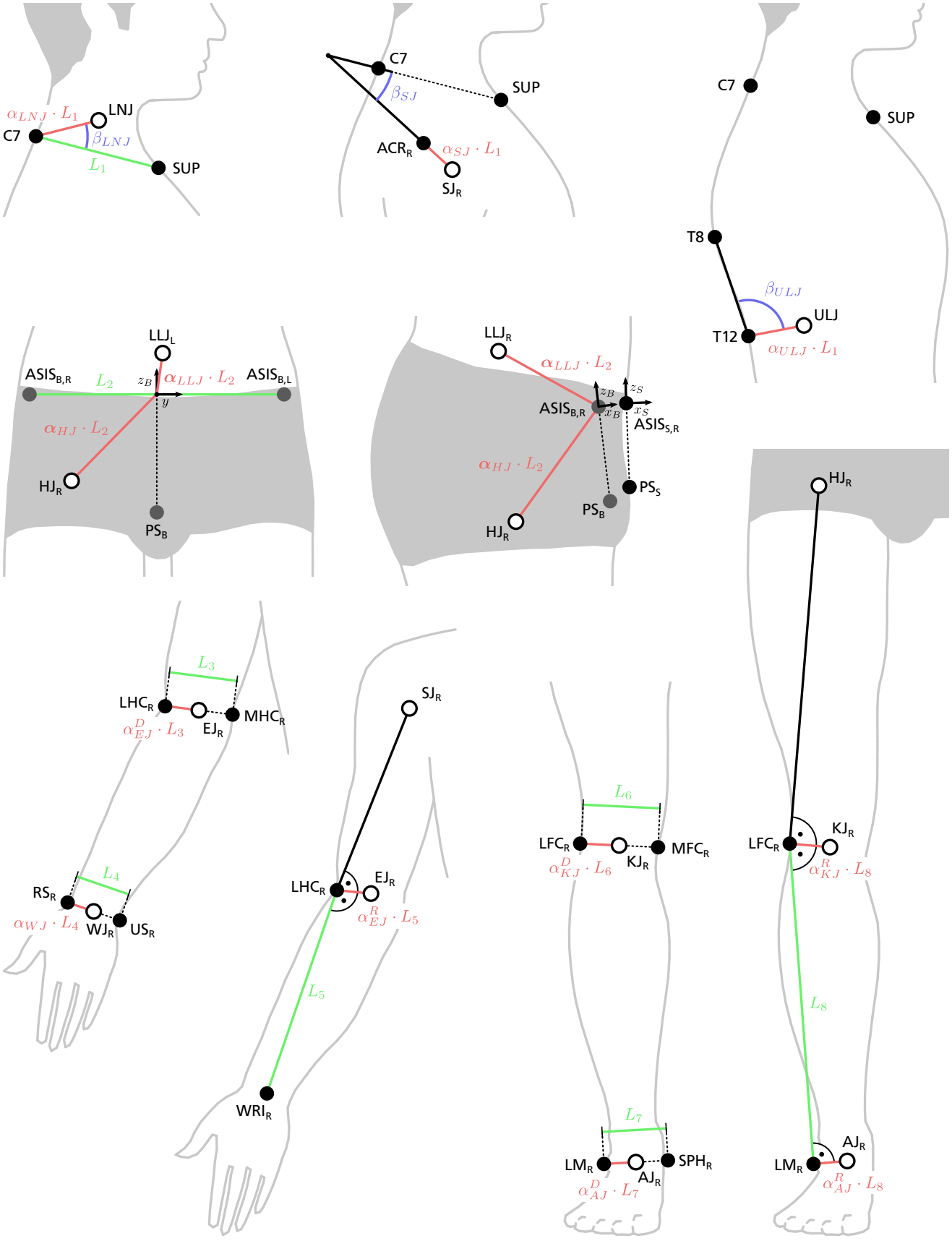

Figure 7.2.: Definitions of regression parameters for joint center estimation in the regression models provided by Reed et al. [177] and Dumas et al. [66, 68].

The reference lengths, indicated in green, are defined by two anatomical landmarks or other joint centers. For three joints, an additional angular parameter $\beta \in \mathbb{R}$, highlighted in blue, is specified that determines the direction. Otherwise, the direction is given by a line connecting two anatomical landmarks or other geometric relations. The lower neck joint for example is determined by the anatomical landmarks C7 and SUP as well as the parameters α_{LNJ} and β_{LNJ}. The spatial position of the joint center is computed by multiplying the reference length L_1 that equals to the distance between C7 and SUP by the parameter α_{LNJ} and rotating the result about an axis perpendicular to the sagittal plane in the reference point C7. In addition to the anatomical landmarks that were applied in the biomechanical measurements described in Chapter 5, Dumas et al. use the radial styloid (RS) landmark and ulnar styloid (US) landmark on the wrist as well as the sphyrion (SPH) landmark on the ankle. A list of definitions and an index of abbreviations for these anatomical landmarks are provided in Appendix A.2. The influence of the spatial difference between the SPH landmark and the MM landmark which is included in the spatial motion data of the biomechanical measurements is assumed to be negligible.

Both regression models utilize identical definitions for the joints in the torso, whereas the definitions for joints in arms and legs vary. A superscript *R* marks parameters that are used exclusively in the model by Reed et al. and a superscript *D* indicates parameters which are only applied by Dumas et al. The reference values for all regression parameters were re-calculated based on definitions and measurement data specified in the respective publications. Disagreements between re-calculated and originally stated values were discussed with Matthew Reed and Raphaël Du-

Table 7.1.: Reference regression parameters for joint center estimation in female and male subjects comprising linear parameters α and angular parameters β.

		α in %			β in deg	
Joint	**Parameter**	female	male	**Parameter**	female	male
LNJ	α_{LNJ}	52.8	54.8	β_{LNJ}	13.7	7.7
SJ	α_{SJ}	35.8	33.4	β_{SJ}	-4.6	-11.3
EJ	α^D_{EJ}	50.0	50.0	-	-	-
	α^R_{EJ}	15.5	14.0	-	-	-
WJ	α_{WJ}	50.0	50.0	-	-	-
ULJ	α_{ULJ}	49.9	51.9	β_{ULJ}	-91.9	-94.2
LLJ	$\alpha_{LLJ,X}$	-26.5	-26.9	-	-	-
	$\alpha_{LLJ,Y}$	0	0	-	-	-
	$\alpha_{LLJ,Z}$	15.8	12.8	-	-	-
HJ	$\alpha_{HJ,X}$	-19.7	-20.9	-	-	-
	$\alpha_{HJ,Y}$	-37.2	-36.1	-	-	-
	$\alpha_{HJ,Z}$	-27.1	-28.3	-	-	-
KJ	α^D_{KJ}	50.0	50.0	-	-	-
	α^R_{KJ}	12.6	11.9	-	-	-
AJ	α^D_{AJ}	50.0	50.0	-	-	-
	α^R_{AJ}	8.7	8.4	-	-	-

mas and have been updated accordingly. The updated reference values are listed in Table 7.1. Side-dependent values are assumed to be symmetric and exemplarily given for the right body side. By changing signs as appropriate, the values can be translated to the left body side.

The definitions for hip and lower lumbar joints slightly differ from the other definitions. The joint center locations are given relative to a reference frame on the bony surface of the pelvis, marked by a subscript B, that is derived from a reference frame on the skin surface, indicated by a subscript S. The common y-axis of both reference frames is specified by the line connecting the ASIS landmarks and points to the left. A projection of the PS landmark onto the y-axis provides the origin of the skin reference frame, where the line connecting this origin with the PS landmark defines the z_S-axis. The x_S-axis is mutually perpendicular to the y- and z_S-axes. In order to determine the bone reference frame, the ASIS and PS landmarks are shifted by flesh margins given in the skin reference frame. Reed et al. state flesh margins of -10.0 mm on the x_S-axis for the ASIS landmarks and -17.7 mm on the x_S and z_S-axes for the PS landmark. With using the shifted anatomical landmarks, the bone reference frame is constructed in the same way as the skin reference frame. The joint center locations for lower lumbar and hip joints are computed by multiplying the reference length L_2 which represents the distance between the ASIS landmarks by the parameter vectors $\boldsymbol{\alpha}_{LLJ} \in \mathbb{R}^3$ and $\boldsymbol{\alpha}_{HJ} \in \mathbb{R}^3$ and adding the resulting vector to the origin of the bone reference frame.

7.3.2 Analysis Procedure

A major limitation in the uncertainty analysis of joint center estimation is the lack of available reference data for actual joint center locations. Data collections with related measurement data, e.g., [183, 184, 197], at most provide the means and standard deviations for the applied anatomical landmarks but do not contain any information about the dispersion of joint center locations. Smaller studies that use medical imaging technology, e.g., [10, 129, 196], usually have not published the measured joint center locations and mostly focus on only a single joint. For this reason, the uncertainty in the presented regression models for joint center estimation has been analyzed based on means and standard deviations for anatomical landmarks reported by Schneider and Robbins [183, 184, 197] as well as Reynolds et al. [179] in combination with a Kriging interpolation approach that has previously been applied for the localization of joint centers by Dumas et al. [68].

The basic assumption in this uncertainty analysis is that the known variations in anatomical landmarks interrelate with the unknown variances of adjacent joint centers. An important requirement for the assessment of this relation is the possibility to properly estimate joint center locations with regard to uncertain samples of anatomical landmarks drawn from the reported means and standard deviations. This can be achieved with Kriging interpolation that originally emerged from natural resources evaluation in geostatistics and provides a linear unbiased estimator for a random function specified by a set of known sampling points [226]. The principle is to compute the parameters of the linear estimator based on two datasets. The first dataset comprises the mean coordinates of relevant anatomical landmarks as well as the coordinates of the considered joint centers estimated with the mean coordinates. The second dataset only contains an uncertain sample of the same anatomical landmarks that is computed by sampling random offsets from the specified standard deviations and adding these offsets to the mean coordinates.

For the sampling, a Gaussian distribution is assumed. The obtained linear estimator now allows to interpolate the unknown joint center locations for the given uncertain samples.

The coordinates of an unknown joint center $\begin{bmatrix}\hat{x}_j & \hat{y}_j & \hat{z}_j\end{bmatrix}^T$ relative to an uncertain sample of anatomical landmarks are estimated from the coordinates of the corresponding joint center

$$\boldsymbol{v}_j = \begin{bmatrix}x_j & y_j & z_j\end{bmatrix}^T$$

given for the mean coordinates of the same anatomical landmarks considering the uncertain coordinates $\begin{bmatrix}\hat{x}_{a,i} & \hat{y}_{a,i} & \hat{z}_{a,i}\end{bmatrix}^T$ and mean coordinates

$$\boldsymbol{v}_{a,i} = \begin{bmatrix}x_{a,i} & y_{a,i} & z_{a,i}\end{bmatrix}^T$$

of n anatomical landmarks. Following the Kriging interpolation approach applied by Dumas et al., the linear estimator consists of a linear polynomial of coordinates plus a weighted average of interpoint distances and is given by

$$\begin{aligned}
\hat{x}_j &= a_{1,X} + a_{2,X}\, x_j + a_{3,X}\, y_j + a_{4,X}\, z_j + \sum_{i=1}^{n} b_{i,X} \|\boldsymbol{v}_j - \boldsymbol{v}_{a,i}\|_2, \\
\hat{y}_j &= a_{1,Y} + a_{2,Y}\, x_j + a_{3,Y}\, y_j + a_{4,Y}\, z_j + \sum_{i=1}^{n} b_{i,Y} \|\boldsymbol{v}_j - \boldsymbol{v}_{a,i}\|_2, \\
\hat{z}_j &= a_{1,Z} + a_{2,Z}\, x_j + a_{3,Z}\, y_j + a_{4,Z}\, z_j + \sum_{i=1}^{n} b_{i,Z} \|\boldsymbol{v}_j - \boldsymbol{v}_{a,i}\|_2.
\end{aligned}$$

The estimator parameters a and b are determined by solving a system of linear equations for the uncertain and mean coordinates of the n anatomical landmarks such that

$$\begin{bmatrix}\hat{\boldsymbol{X}} \\ \boldsymbol{0}\end{bmatrix} = \begin{bmatrix}\boldsymbol{H} & \boldsymbol{X} \\ \boldsymbol{X}^T & \boldsymbol{0}\end{bmatrix} \begin{bmatrix}\boldsymbol{B} \\ \boldsymbol{A}\end{bmatrix}$$

with

$$\boldsymbol{A} = \begin{bmatrix}a_{1,X} & a_{1,Y} & a_{1,Z} \\ a_{2,X} & a_{2,Y} & a_{2,Z} \\ a_{3,X} & a_{3,Y} & a_{3,Z} \\ a_{4,X} & a_{4,Y} & a_{4,Z}\end{bmatrix}, \qquad \boldsymbol{B} = \begin{bmatrix}b_{1,X} & b_{1,Y} & b_{1,Z} \\ \vdots & \vdots & \vdots \\ b_{n,X} & b_{n,Y} & b_{n,Z}\end{bmatrix},$$

$$\boldsymbol{X} = \begin{bmatrix}1 & x_{a,1} & y_{a,1} & z_{a,1} \\ \vdots & \vdots & \vdots & \vdots \\ 1 & x_{a,n} & y_{a,n} & z_{a,n}\end{bmatrix}, \qquad \hat{\boldsymbol{X}} = \begin{bmatrix}\hat{x}_{a,1} & \hat{y}_{a,1} & \hat{z}_{a,1} \\ \vdots & \vdots & \vdots \\ \hat{x}_{a,n} & \hat{y}_{a,n} & \hat{z}_{a,n}\end{bmatrix}.$$

The elements $h_{k,l}$ of the matrix $\boldsymbol{H} \in \mathbb{R}^{n \times n}$ with $k = 1 \ldots n$ and $l = 1 \ldots n$ equal to the interpoint distances $\|\boldsymbol{v}_{a,k} - \boldsymbol{v}_{a,l}\|_2$. A detailed derivation of the Kriging interpolation equations is provided by Trochu [226].

The uncertainty analysis has been performed by applying the framework described in Chapter 4 without regarding sensitivities. Knee and ankle joints as well as shoulder, elbow and wrist

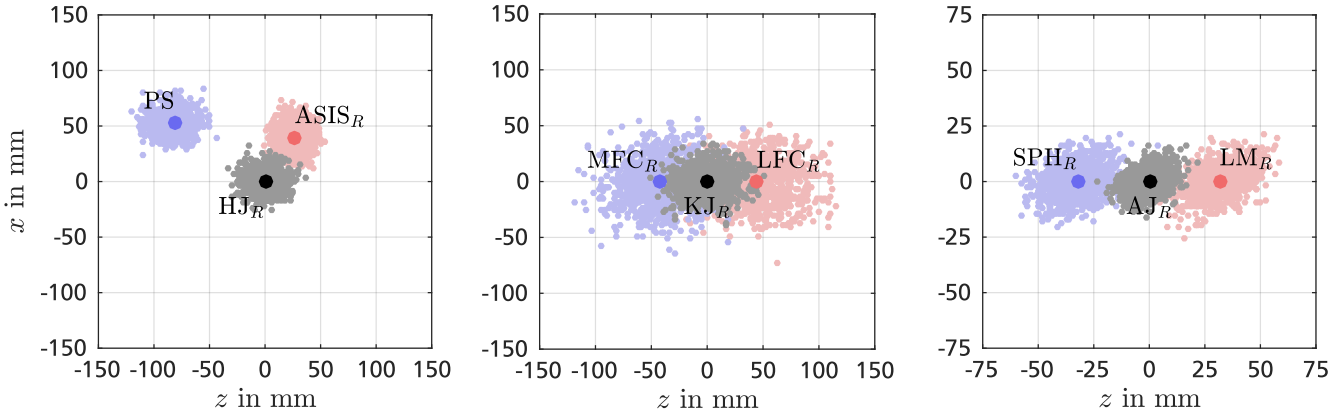

Figure 7.3.: Example for uncertain joint center locations in hip, knee and ankle joints of female subjects based on the Kriging interpolation approach with 1,000 samples.

joints were assessed in groups based on the Gaussian distributions of eight and thirteen relevant anatomical landmarks. The lower neck, upper lumbar, lower lumbar and hip joints were evaluated individually with the Gaussian distributions of seven, ten, four and three relevant anatomical landmarks. In total, twelve Monte Carlo simulations were conducted to analyze the regression parameters for female and male subjects. For the lower lumbar and hip joints, the data for small female and medium male subjects reported by Reynolds et al. was used, while all other joints were assessed based on the data for small female and medium male subjects provided by Schneider and Robbins. In a study about the localization of the pelvis in an automobile seat, Park et al. estimated the variations in the flesh margin for the ASIS landmarks and found standard deviations of 5.6 mm in horizontal direction and 4.7 mm in vertical direction from measurements on ninety female and male subjects which correspond to about 50 % of the reported flesh margin [168]. This result was applied to the considered flesh margins for the ASIS and PS landmarks and a Gaussian distribution with a standard deviation of 50 % relative to the respective absolute values was assumed. Reed et al. defined an offset vector with a length of 10.0 mm to determine the location of the lower lumbar joint from anatomical landmarks in the pelvis. For this offset vector, a Gaussian distribution with a standard deviation of 10 % relative to the length was used.

In each trial of the Monte Carlo simulation, an uncertain sample of the involved anatomical landmarks was drawn from the specified Gaussian distributions and the corresponding joint center locations were estimated with the described Kriging interpolation approach. This process is exemplarily illustrated in Figure 7.3 for 1,000 samples in hip, knee and ankle joints regarding the parameters for female subjects. The uncertain samples of two relevant anatomical landmarks, indicated by the faith red and blue points, as well as the resulting joint centers, marked by the gray points, are shown in transverse plane. The equivalent mean coordinates are represented by the strong red, blue and black points. Based on the estimated joint center locations, the particular regression parameters were derived from the defined relations and the observed variability of each parameter was modeled by an appropriate Johnson distribution. Correlations between associated parameters were described by a Gaussian copula. Unfortunately, the reported statistical properties for the anatomical landmarks do not contain any covariances which implies that all samples have to be treated as independent random variables. This simplification can induce anatomically invalid arrangements of anatomical landmarks and joint center

Table 7.2.: Copula covariance matrix for regression parameters of joint centers in the female leg.

Σ_c	$\alpha_{HJ,X}$	$\alpha_{HJ,Y}$	$\alpha_{HJ,Z}$	α_{KJ}^{D}	α_{KJ}^{R}	α_{AJ}^{D}	α_{AJ}^{R}
$\alpha_{HJ,X}$	0.0000	$*$	$*$	-	-	-	-
$\alpha_{HJ,Y}$	0.0000	0.0829	$*$	-	-	-	-
$\alpha_{HJ,Z}$	0.0000	0.0005	0.0001	-	-	-	-
α_{KJ}^{D}	-	-	-	0.0497	$*$	$*$	$*$
α_{KJ}^{R}	-	-	-	0.0009	0.0323	$*$	$*$
α_{AJ}^{D}	-	-	-	0.0423	-0.0083	0.0798	$*$
α_{AJ}^{R}	-	-	-	0.0040	0.0101	-0.0104	0.0775

locations. For this reason, several plausibility checks have been implemented that examine each drawn sample together with the resulting joint center and discard the respective trials in the case of failure. Most of the plausibility checks validate if the estimated joint center location lies between two bounding points or within a reasonable bounding region defined by adjacent anatomical landmarks. The relative threshold limit for convergence was set to 10^{-4} and the individual batches comprised 40,000 trials. In addition, a minimum limit of 1,000,000 trials was specified.

7.4 Results

The number of trials after which the individual Monte Carlo simulations were terminated ranged from 1,000,000 trials to 2,400,000 trials. The resulting probability distributions for the regression parameters in the legs of female and male subjects are presented in Figure 7.4 and 7.5. Besides the median and mean values, the specified reference values, marked by the dotted black lines, are given for comparison. For each distribution, the corresponding Johnson distribution types and coefficients γ_j, δ_j, λ_j, ξ_j are provided. The copula covariance matrices Σ_c that model the correlation among the individual marginal distributions are given in Table 7.2 and 7.3. Not all entries of the copula covariance matrices are populated because of the individual Monte Carlo simulations for single or grouped joints. The results for all other joints are listed in Appendix A.8.

Table 7.3.: Copula covariance matrix for regression parameters of joint centers in the male leg.

Σ_c	$\alpha_{HJ,X}$	$\alpha_{HJ,Y}$	$\alpha_{HJ,Z}$	α_{KJ}^{D}	α_{KJ}^{R}	α_{AJ}^{D}	α_{AJ}^{R}
$\alpha_{HJ,X}$	0.0827	$*$	$*$	-	-	-	-
$\alpha_{HJ,Y}$	0.0000	0.0000	$*$	-	-	-	-
$\alpha_{HJ,Z}$	0.0036	0.0000	0.0084	-	-	-	-
α_{KJ}^{D}	-	-	-	0.0548	$*$	$*$	$*$
α_{KJ}^{R}	-	-	-	0.0003	0.0829	$*$	$*$
α_{AJ}^{D}	-	-	-	0.0290	-0.0138	0.0340	$*$
α_{AJ}^{R}	-	-	-	0.0005	0.0139	-0.0076	0.0834

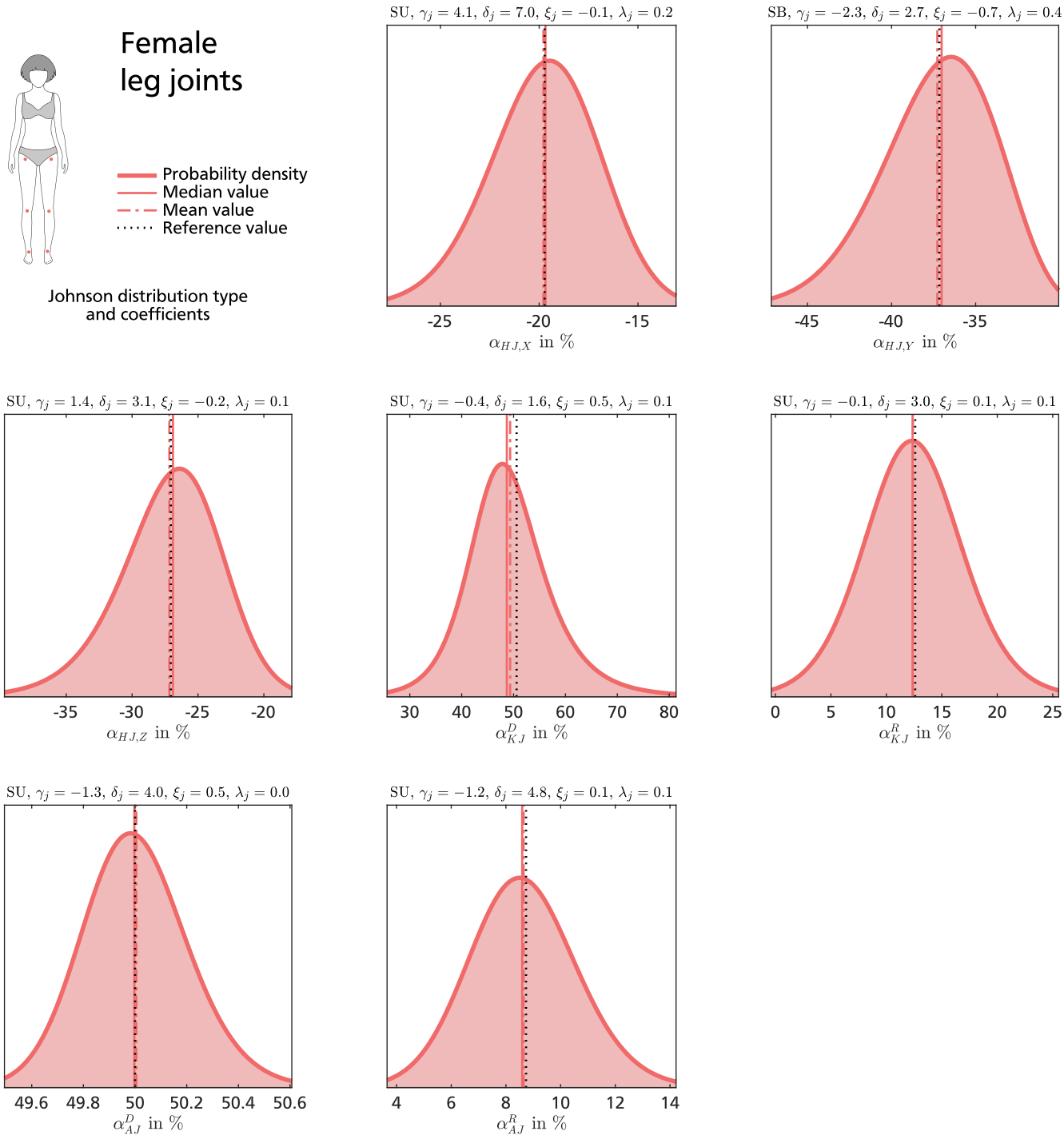

Figure 7.4.: Regression parameter uncertainty for joint centers in the female leg with corresponding Johnson distribution types and coefficients.

In most of the obtained distributions, the median and mean values are very similar which indicates a high symmetry. The only exceptions with slight differences are the linear and angular parameters for the upper lumbar joint as well as the linear parameter for the shoulder joint. Additionally, the median and mean values almost always conform with the specified reference values. This conformity supposes that the reference values which have been calculated from the mean coordinates of the involved anatomical landmarks are good representations for the actual distributions. Small deviations can be found in the linear parameter for the elbow joint used

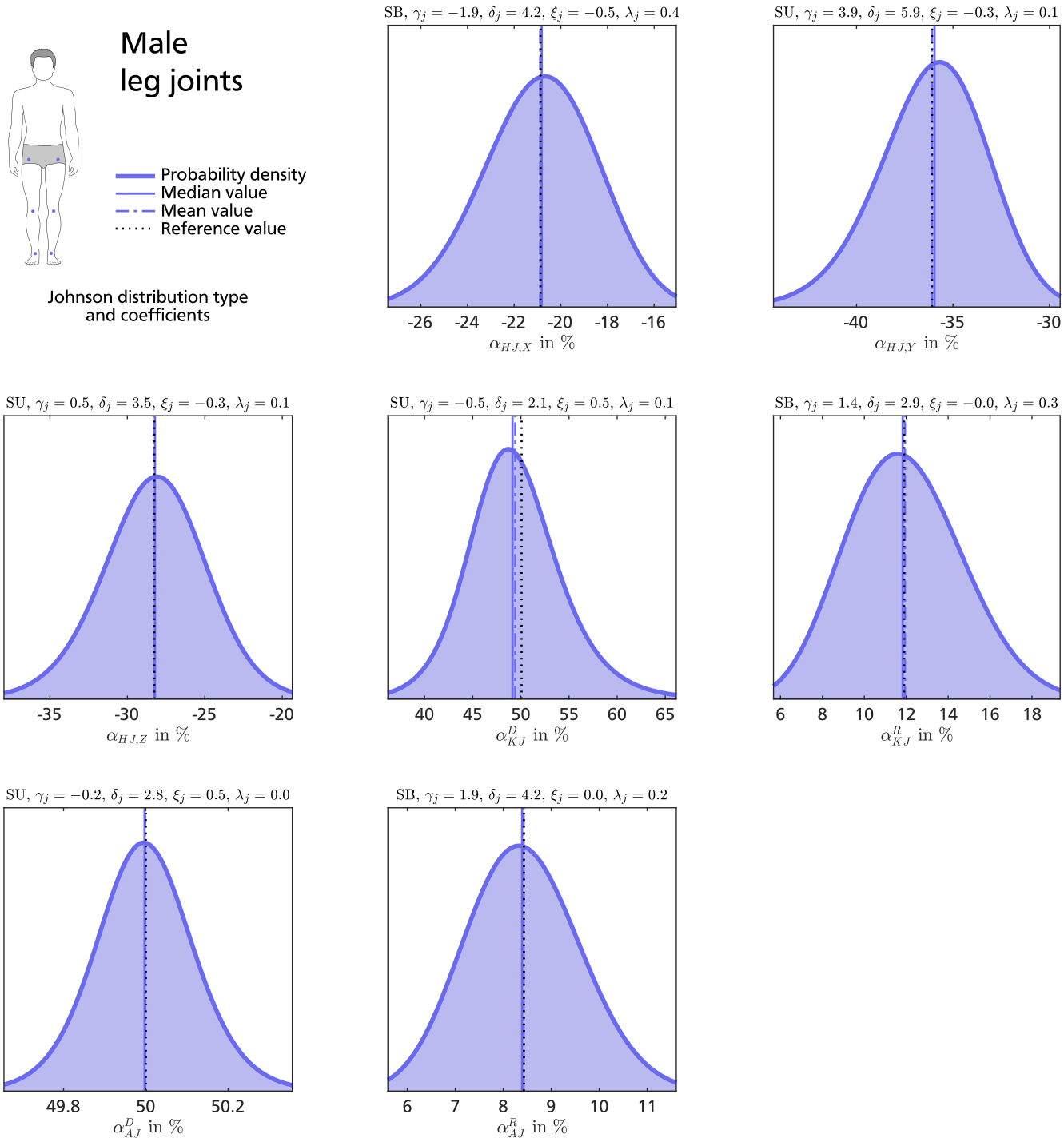

Figure 7.5.: Regression parameter uncertainty for joint centers in the male leg with corresponding Johnson distribution types and coefficients.

by Dumas et al. as well as the linear parameters for the lower lumbar joint in x- and z-axis. The standard deviations for the linear parameters range from 0.113 % in the male wrist joint to 19.8 % in the female upper lumbar joint, while the standard deviations for the angular parameters lie between 10.8 ° in the male lower neck joint and 24.4 ° in the female upper lumbar joint. The relative standard deviations of the regression parameters with respect to the provided non-zero reference values reach up to 296.3 % for female subjects and 140.6 % for male subjects. The relative interquartile range that is defined by the difference between the 75 th percentile

and the 25 th percentile divided by the median value has a minimum of 0.254 % in the male wrist joint and a maximum of 403.5 % in the female shoulder joint. On average, the relative interquartile ranges of the parameters for female subjects are 30.4 % larger than the parameters for the male subjects. The linear parameter of the lower lumbar joint in the y-axis is excluded from this interpretation of the relative interquartile ranges because its median and mean values are very close to zero.

7.5 Discussion

The uncertainty analysis of regression parameters in joint center estimation based on means and standard deviations of anatomical landmark locations reported in literature reveal substantial variances in many of the considered linear and angular parameters. In general, the parameters for female subjects have a higher variability than the parameters for male subjects which is not directly evident from the original standard deviations. The most probable explanation for this effect is that particular anatomical landmarks have a high influence on the obtained joint center estimates and dominate the analysis. Furthermore, angular parameters as well as linear parameters for legs and arms used by Reed et al. exhibit rather large uncertainties. The first finding presumably results from the fact that even small spatial deviations in joint center estimates are amplified by the distance to the rotation center, while the second finding might follow from the reduced set of involved anatomical landmarks.

A validation of the found uncertainties is quite difficult because there is no applicable reference data for most of the considered joints. Only for the hip joint, various studies have investigated the expectable uncertainty of different predictive methods mainly with male subjects. The reported error ratings lie between 16.0 mm and 30.0 mm. The standard deviations of the three linear parameters in the hip joint for male subjects acquired in the uncertainty analysis amount to 2.437 %, 2.841 % and 3.445 % in x-, y- and z-axis. With adopting a value of 230.0 mm for the reference length L_2 of an average male subject from Reynolds et al. and approximately assuming a Gaussian distribution, an absolute error of 11.7 mm for one sigma, 23.4 mm for two sigma and 35.1 mm for three sigma can be deduced. Since the three-sigma interval covers more than 99.7 % of the distribution, the absolute error of 35.1 mm can be regarded as an upper bound which occurs very rarely. These characteristics correspond quite well with the reported error ratings and support the fundamental validity of the uncertainty analysis.

Nevertheless, there are several potential limitations. The restricted availability of reference data enforces an indirect approach. The assumed interrelation between the variability in anatomical landmarks and joint centers might seem plausible but is not fully evidenced by existing studies. The Kriging interpolation approach introduces further uncertainties by applying an efficient but proximate linear estimator for this interrelation. In addition, it is debatable if the implemented plausibility checks are able to compensate the influence of the missing covariances. The underlying measurement data was partially taken from seated subjects and the model by Reed et al. was created with a focus on automobile occupants. With this postural restriction, the estimation results might not be completely transferable to general human motions due to the deformation of the torso segment and the bent legs. Besides the actual variability in anatomical landmarks, the reported standard deviations also contain measurement errors and anatomical landmark misplacement. Though, a rather high accuracy can be expected for the data provided

by Reynolds et al. due to the direct measurements on preserved specimens of pelvis bones. Altogether, the presented results provide an approximate but representative assessment of the uncertainty in a comprehensive set of regression parameters for joint center estimation. The obtained statistical models enable a reasonable consideration of expectable variations in joint center estimates for the uncertainty and sensitivity analysis of human motion dynamics.

7.6 Conclusion

Uncertainties in regression parameters for joint center estimation can have a substantial influence on the results of an inverse dynamics simulation because kinematic and dynamic properties of the biomechanical model depend on the derived joint center locations. The presented uncertainty analysis provides a fundamental and broad evaluation of variations in linear and angular parameters of two comprehensive regression models. Both models cover the most relevant joints for a biomechanical simulation of human locomotion. One of the models can be applied with a reduced set of anatomical landmarks in legs and arms, while the other model requires additional anatomical landmarks but has been used in the definition of an estimation procedure for anthropometric parameters. The obtained statistical models have been calculated based on the assumption that variations in anatomical landmarks interrelate with variances of adjacent joint center locations. This approach allowed to apply statistical properties of anatomical landmarks reported in literature to approximate the uncertainty of individual regression parameters. The results show significant variations in all linear and angular parameters, where the variability of parameters for female subjects is higher on average. These findings form a reasonable basis for the uncertainty and sensitivity analysis of the inverse dynamics simulation but also indicate that further studies are required to refine existing regression models and extend biomechanical data collections by accurate measurements of joint center locations.

8 Uncertainty and Sensitivity Analysis of Anthropometric Parameter Estimation

Anthropometric parameters comprise length, mass, center of mass and inertia tensor of the body segments and define the kinematic and dynamic properties of the biomechanical model. While the segment lengths are defined by the distances between the joint center estimates, the other anthropometric parameters result from the mass distribution of the body segments. Personalized anthropometric parameters are typically estimated from the individual body mass and joint center locations in combination with an appropriate regression model. Uncertainties in the involved regression parameters and body segment lengths potentially affect the derived joint trajectories as well as the results of the inverse dynamics simulation [175]. Figure 8.1 illustrates the involvement of this uncertainty source in the inverse dynamics procedure.

8.1 Related Work

Various methods have been proposed to obtain subject-specific anthropometric parameters. An overview of the applied techniques and the historical background is provided by Nigg and Her-

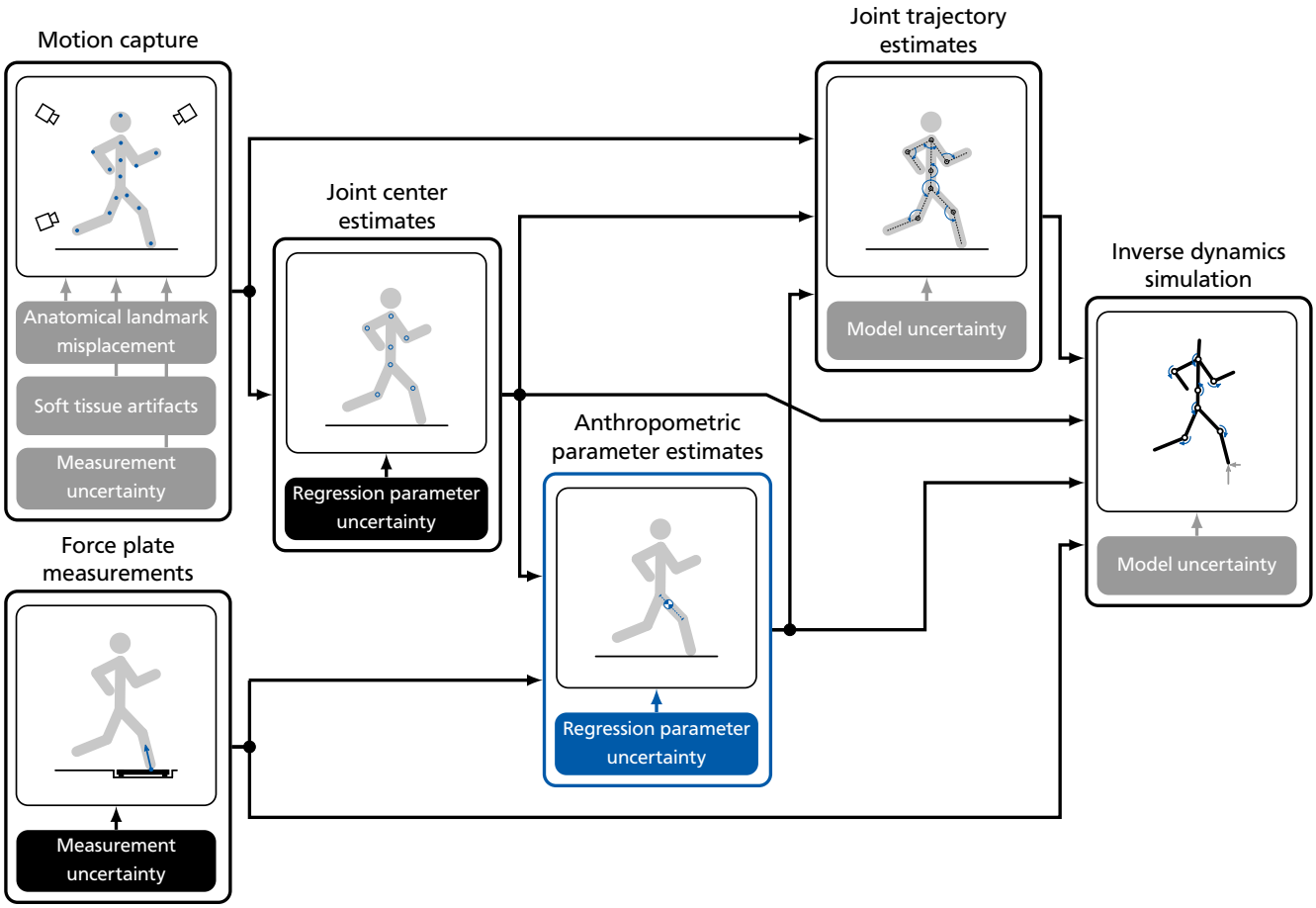

Figure 8.1.: Uncertainty propagation in anthropometric parameter estimation based on an appropriate regression model.

zog [156] as well as Zatsiorsky [260]. In general, anthropometric parameters can be directly measured on cadavers, e.g., [52, 63], and indirectly measured on living subjects through volume measurements together with an approximation of the density distribution, e.g., [145, 255], or medical imaging techniques, e.g., [71, 213]. For biomechanical simulations, typically only indirect measurement approaches can be applied which are rather expensive, time-consuming or expose human subjects to harmful radiations. For this reason, personalized anthropometric parameters are commonly estimated with scaling methods or regression models.

Scaling methods apply a generic biomechanical model that is scaled to match the anthropometry of an individual subject based on the body mass and personalized motion capture data [62]. In a first step, scaling factors are calculated for each body segment with respect to relative distances between pairs of anatomical landmarks evident in the generic model as well as the personalized motion capture data. These scaling factors are used in a second step to adjust model parameters including segment lengths and joint center locations as well as inertial parameters. In addition, it is possible to scale other length-based model parameters such as muscle lengths or lever arms. The application of scaling methods is quite expedient if an appropriate generic model and personalized motion capture data are available. The uncertainty of the obtained anthropometric parameters depends on the quality and applicability of the generic model as well as variances in the body mass measurement and motion capture data. The model parameters of available generic models typically represent an adult male subject derived from different measurements on limited populations of Caucasian subjects, e.g., [40, 174].

Regression models use statistical methods for estimating the relationship between the unknown anthropometric parameters and easy to measure variables. Although there is evidence that nonlinear regression equations yield better approximations of relevant parameters [254], common regression models, e.g., [58, 66], are based on linear regression equations. In these linear models, personalized anthropometric parameters are computed with multiplying subject-specific measurements such as body mass or segment lengths by constant regression parameters. Three comprehensive and widely used regression models for the estimation of anthropometric parameters in adult subjects are the model by Winter [242] obtained from measurements by Dempster [63], the model by de Leva [58] based on measurements by Zatsiorsky et al. [261] as well as the model by Dumas et al. [66, 67, 68] derived from measurements by McConville et al. [145] and Young et al. [255]. Dempster applied equilibrium and pendulum methods to directly measure the anthropometric parameters of eight Caucasian male cadavers (68.5 yrs, 169.0 cm, 59.6 kg. Zatsiorsky et al. indirectly measured the anthropometric parameters of one hundred Caucasian male subjects (23.8 yrs, 174.1 cm, 73.0 kg) and fifteen Caucasian female subjects (19.0 yrs, 173.5 cm, 61.9 kg). Body segment dimensions and inertial parameters were determined by approximating the human body with a set of rectangular cuboids and using density measurements obtained from frontal gamma-ray scans. In each cuboid, the center of mass was assumed to be at the geometrical center and the principal axes of inertia were expected to be aligned with the axes of symmetry. McConville et al. and Young et al. indirectly measured the anthropometric parameters of thirty-one Caucasian male subjects (27.5 yrs, 177.5 cm, 77.3 kg) and forty-six Caucasian female subjects (31.2 yrs, 161.2 cm, 63.0 kg). Shape and volume of individual body segments were obtained from photogrammetric measurements. Inertial parameters were calculated by assuming a constant density of $1.0\,\mathrm{g/cm^3}$. While the models by de Leva and Dumas et al. provide individual parameters for both genders, the model by Winter is restricted to male subjects. Due to the symmetry assumptions in the applied measurement

data, the regression equations by Winter and de Leva are subject to two restrictive presumptions. The center of mass is assumed to be on the proximal-distal axis of the body segment and the inertia tensor is expected to be principal in the axes of the body segment. The regression equations by Dumas et al. do not restrain the center of mass location and inertia tensor orientation. Similar to scaling methods, the application of regression models requires personalized motion capture data to specify the subject-specific segment lengths but does not depend on the predefined structure and configuration of a generic model. The uncertainty of the estimated anthropometric parameters depends on the quality and relevance of the underlying measurement data as well as the variances in the body mass measurement and motion capture data. A further discussion and comparison of the three presented regression models are provided by Dumas and Wojtusch [69].

Scaling methods and regression models assume a fixed relation between anthropometric parameters and body dimensions based on measurements typically taken from limited populations of normal-weighted healthy adults. These fixed relations are supposed to cover numerous anthropometric properties including body segment shape and mass distribution. For this reason, both methods should not be applied for subjects that differ considerably from the populations of the underlying measurement data. Especially, the applicability for pathological subjects like amputees is restricted because the fixed relations obtained from healthy subjects may not be suitable representations of the highly individual anthropometric properties in pathological subjects. Several enhanced approaches have been proposed in order to overcome these restrictions of scaling methods and regression models and to provide more accurate estimates. Parameter identification approaches based on inverse dynamics, e.g., [17, 231], enable a real-time estimation of anthropometric parameters but require the subjects to perform additional persistent exciting trajectories which has to be considered in the measurement protocol and might not be feasible for elderly or pathological subjects. Mathematical approaches to approximate the shape of individual body segments by sets of geometric bodies, e.g. [103, 253], provide accurate results but necessitate the time-consuming recording of numerous anthropometric measurements. These limitations in addition to the expediency and conveniences of scaling methods and regression models have prevented a wide adoption of the enhanced approaches so far.

Several studies have investigated the impact of uncertainties in anthropometric parameters on the results of an inverse dynamics simulation. For example, Rao et al. compared the estimation results of six different regression models with seven female and male subjects and evaluated joint torques computed for walking motions based on the estimated anthropometric parameters [175]. A high sensitivity of the anthropometric parameter estimates to the applied regression models was found which resulted in deviations ranging from 9.7 % to 60.0 %. Peak values of the hip joint torque in sagittal plane during the swing phase varied by up to 20.1 %. Riemer et al. applied a local sensitivity analysis to assess the influence of uncertainties in anthropometric parameters and other uncertainty sources for walking motions with ten female and male subjects [181]. The anthropometric parameters were estimated with the regression model by de Leva and superimposed by a small and large set of relative errors. For the small set, errors of 5.0 % were applied, while the large set included errors between 5.0 % and 47.0 %. Uncertainties in anthropometric parameters were identified as one of the main contributors to the variations in the obtained joint torques which reached up to 232.0 %. Pàmies-Vilà et al. used the regression model by Dumas et al. and assumed that the errors follow a zero-mean Gaussian distribution [165]. Joint torques were computed for a half gait cycle and one thousand samples with

changing the three-sigma interval from 2.0 % to 10.0 % in steps of 2.0 %. The results revealed deviations of up to 14.4 % and a considerable dependence on the joint accelerations. All of these studies suggest that variations in anthropometric parameters have a significant influence on the results of human motion dynamics simulations but do not provide the actual uncertainties of the applied regression models. Knowing this uncertainty would enable to apply more realistic uncertainty and sensitivity analyses and refine inaccurate regression parameters.

8.2 Contribution

The presented uncertainty and sensitivity analysis is, to the best of the author's knowledge, the first extensive investigation of uncertainty propagation and apportionment in all parameters of a comprehensive regression model for anthropometric parameter estimations in female and male subjects as well as personalized anthropometric parameters by taking the example of the thigh segment. For the investigation, statistical properties reported in literature as well as the previously obtained results for the uncertainty quantification in biomechanical measurements and the uncertainty analysis for joint center estimation have been used. The original computational scripts for the determination of the regression parameters were reviewed and found programming and typographical errors have been corrected. Based on the identified uncertainties and sensitivities, revised regression parameters for all body segments are derived and potential limitations of the regression model are discussed. The presented statistical models provide appropriate representations of the uncertain regression parameters and allow to evaluate the influence of variations in anthropometric parameter estimation within the uncertainty and sensitivity analysis of the inverse dynamics simulation.

8.3 Uncertainty and Sensitivity Analysis

In contrast to the regression equations provided by Winter and de Leva, the regression model by Dumas et al. does not apply restrictive assumptions on the center of mass position or inertia tensor orientation. The underlying measurements by McConville et al. and Young et al. offer an almost balanced relation between female and male subjects with similar age and body dimensions to the two subjects that participated in the biomechanical measurements. In addition, the provided measurement data comprises means and standard deviations for most of the recorded measurands. For this reason, the focus of the uncertainty analysis was put on the evaluation of possible variations in the parameters of the comprehensive regression model provided by Dumas et al. In order to rate the impact of the observed uncertainties, an exemplarily uncertainty and sensitivity analysis for the anthropometric parameters in the right thigh segments of the actual subjects has been conducted subsequently.

8.3.1 Model Definition

The extensive collections of measurement data provided by McConville et al. and Young et al. contain means and standard deviations for volume measurements as well as estimates of the three-dimensional center of volume, principal moments of inertia and orientation of the principal axes of inertia with respect to an anatomical reference frame for individual body segments.

Table 8.1.: Definitions of segment length and origin for anthropometric parameter estimation with the regression model provided by Dumas et al. [66, 67, 68].

Segment	Segment length definition	Origin
HEA	LNJ to head vertex	LNJ
THO	LNJ to ULJ	LNJ
ABD	ULJ to LLJ	ULJ
UPA	SJ to EJ	SJ
LOA	EJ to WJ	EJ
HAN	WJ to midpoint between second and fifth metacarpal head	EJ
PEL	LLJ to projection of HJ in sagittal plane	LLJ
THI	HJ to KJ	HJ
SHA	KJ to AJ	KJ
FOO	AJ to midpoint between first and fifth metatarsal head	AJ

Both studies used the same segmentation and defined seventeen body segments including head, neck, thorax, abdomen, pelvis as well as left and right upper arms, lower arms, hands, thighs, shanks and feet. A set of anatomical landmarks was provided for each body segment following the same definitions. The sampled populations of thirty-one male subjects in the study by McConville et al. and forty-six female subjects in the study by Young et al. were chosen to represent the actual body mass and body height distributions of the general United States adult population of the 1970s. The shape and volume of each individual body segment were measured with a stereo-photogrammetric technique which allows a three-dimensional reconstruction of surface points. These points were selected anatomical landmarks or points placed every 7.0 mm on a horizontal cross section, where the interval between each cross section was 13.0 mm in head, abdomen, hands and feet or 25.0 mm in the other body segments. The inertial parameters were derived from the volume and shape measurements with assuming a constant density of $1.0\,\mathrm{g/cm^3}$. A comparison of this indirect measurement approach with direct measurements on six male cadavers exhibited an average error of 5.6 % for the center of volume and 3.5 %, 3.9 % and 5.8 % for the principal moment of inertia in frontal, sagittal and horizontal plane [146].

In a first study, Dumas et al. [66, 67] applied an adjustment procedure to transform the reported means from the given anatomical reference frames into reference frames in accordance with internationally recognized recommendations for biomechanical reference frame notation [250, 251]. This transformation ensures that segment lengths and reference frames are defined by joint center locations which is more convenient and common in human motion analysis. The joint center locations were determined based on the specified anatomical landmarks and the regression model that is described and analyzed in Chapter 7. Because McConville et al. did not always report spatial positions of at least three anatomical landmarks on two adjacent body segments, the required rotation matrices were assumed to be the same as in the study by Young et al. Based on the transformed means, regression parameters for head (HEA), torso, pelvis (PEL) as well as left and right upper arms (UPA), lower arms (LOA), hands (HAN), thighs (THI), shanks (SHA) and feet (FOO) were derived, where the neck was incorporated into the head segment and thorax and abdomen were merged into a single torso segment due to missing

information for the upper lumbar joint estimation. In a second study, Dumas et al. [68] used a Kriging interpolation approach to locate the upper lumbar joint with respect to the given anatomical landmarks and derived supplementary regression parameters for thorax (THO) and abdomen (ABD). The definitions for segment length and origin of each individual body segment are listed in Table 8.1.

The regression model comprises parameters for the estimation of the unknown segment mass, center of mass and inertia tensor from the known body mass and segment lengths. The segment mass m_s results from

$$m_s = \alpha_m \, m_t,$$

where α_m denotes the regression parameter and m_t is the total body mass. The location of the center of mass $\boldsymbol{o}_s$ with respect to the local reference frame of the respective body segment is estimated by

$$\boldsymbol{o}_s = \begin{bmatrix} \alpha_{o,X} \\ \alpha_{o,Y} \\ \alpha_{o,Z} \end{bmatrix} l_s$$

with the three regression parameters $\alpha_{o,X}$, $\alpha_{o,Y}$, $\alpha_{o,Z}$ and the segment length l_s. The inertia tensor $\boldsymbol{I}_s$ including moments and products of inertia with respect to the center of mass and local reference frame is given by

$$\boldsymbol{I}_s = \begin{bmatrix} \alpha_{I,XX}^2 & * & * \\ \alpha_{I,XY}^2 & \alpha_{I,YY}^2 & * \\ \alpha_{I,XZ}^2 & \alpha_{I,YZ}^2 & \alpha_{I,ZZ}^2 \end{bmatrix} m_s \, l_s^2,$$

where the three regression parameters $\alpha_{I,XX}$, $\alpha_{I,YY}$, $\alpha_{I,ZZ}$ define the moments of inertia and represent the radii of gyration divided by the segment length. The three regression parameters $\alpha_{I,XY}$, $\alpha_{I,XZ}$, $\alpha_{I,YZ}$ specify the products of inertia and can take imaginary values if the corresponding product of inertia is negative.

Raphaël Dumas kindly provided the documented source code of the computational scripts written for the numerical computing software MATLAB that were used for the transformation of the original measurement data and the derivation of the regression parameters. A careful code review revealed some programming and typographical errors that were corrected and tested. The modified computational scripts were applied to re-calculate the reference values for all regression parameters based on the specified definitions and measurement data. Disagreements between re-calculated and originally stated values were discussed with Raphaël Dumas and have been updated accordingly. The updated reference values are listed in Table 8.2. Side-dependent values are assumed to be symmetric and exemplarily given for the right body side. By changing signs as appropriate, the values can be translated to the left body side.

8.3.2 Analysis Procedure

The uncertainty and sensitivity analysis has been performed in two steps. In the first step, an uncertainty analysis was applied to investigate possible variations in the parameters of the considered regression model. The second step involved an exemplarily uncertainty and sensitivity

Table 8.2.: Reference regression parameters for anthropometric parameter estimation in female and male subjects including the parameters for the segment mass α_m, center of mass α_o and inertia tensor α_I.

			α_o in %			α_I in %					
Segment	**Gender**	α_m in %	X	Y	Z	XX	YY	ZZ	XY	XZ	YZ
HEA	female	6.7	0.8	55.9	-0.1	30.3	24.2	31.5	4.7i	1.1	0.5i
	male	6.7	2.0	53.4	0.1	28.4	21.2	30.2	7.2i	2.3i	2.8
THO	female	26.3	1.5	-54.2	0.1	37.9	32.0	33.7	11.6i	3.3i	1.3
	male	30.4	0.0	-55.5	-0.4	41.6	33.3	35.9	11.0i	1.4	2.8
ABD	female	4.1	21.9	-41.0	0.3	65.4	77.6	52.2	25.1	2.9i	5.2i
	male	2.9	17.6	-36.1	-3.3	54.2	66.3	40.2	11.0	6.0i	5.3i
UPA	female	2.3	-5.5	-50.0	-3.3	30.0	15.3	29.8	2.6i	4.2i	12.8
	male	2.4	1.8	-48.2	-3.1	29.3	13.2	29.9	5.3	4.5	3.4
LOA	female	1.4	2.1	-41.1	1.9	26.5	14.2	24.7	9.8	3.3	12.6i
	male	1.7	-1.3	-41.7	1.1	27.6	11.0	28.0	8.1	1.5i	1.7
HAN	female	0.5	7.7	-76.8	4.8	63.5	43.2	58.5	29.3	22.7	27.7i
	male	0.6	8.2	-83.9	7.5	61.2	37.8	55.7	21.7	15.5	19.9i
PEL	female	14.7	-7.2	-22.8	0.2	94.6	104.7	82.2	35.0i	3.0i	2.3i
	male	14.2	-0.2	-28.2	-0.6	101.7	106.4	96.2	25.2i	11.8i	7.5i
THI	female	14.6	-7.7	-37.7	0.8	31.0	19.2	31.7	7.3i	2.4	7.4i
	male	12.3	-4.1	-42.9	3.3	29.0	15.3	29.7	6.8	1.8i	7.3i
SHA	female	4.5	-4.9	-40.4	3.1	28.0	10.3	28.0	2.2	0.7	5.7
	male	4.8	-4.8	-41.0	0.7	28.3	9.6	28.1	4.0i	1.7i	4.2
FOO	female	1.0	38.2	-30.9	5.5	24.3	50.5	49.7	14.7i	9.2	5.0i
	male	1.2	50.2	-19.9	3.4	22.0	48.6	47.7	16.8	10.7i	0.3

analysis for the anthropometric parameters in the right thigh segments of the actual subjects in order to evaluate the influence of the observed uncertainties in the regression parameters on the personalized anthropometric parameters. Both steps were conducted by applying the framework described in Chapter 4, where sensitivities were only regarded in the second step.

Uncertainty Analysis

For the first step, the updated computational scripts were used to perform the uncertainty analysis based on the standard deviations reported by McConville et al. and Young et al. as well as the uncertainties in the regression model for joint center estimation presented in Chapter 7. Due to missing covariances in the reported measurement data, all measurands are assumed to follow a Gaussian distribution and are treated as independent variables. Because the head vertex is not specified in the provided measurement data, the length of the head segment was approximated by subtracting the vertical coordinate of the estimated lower neck joint from the given body height. The density was kept constant. Each body segment for female and male subjects was analyzed individually which resulted in a total of twenty Monte Carlo simulations. In each trial of these Monte Carlo simulations, a sample of measurands, regression parameters

for joint center estimation and other related uncertain input variables like flesh margins was drawn from the specified distributions and used to calculate the respective regression parameters for anthropometric parameter estimation. Since the parameters $\alpha_{I,XY}$, $\alpha_{I,XZ}$, $\alpha_{I,YZ}$ that specify the products of inertia can become imaginary, the squared values were used for the uncertainty analysis. The observed variability of each parameter was modeled by an appropriate Johnson distribution in combination with a Gaussian copula to describe potential correlations among the parameters. The relative threshold limit for convergence was set to 10^{-4} and the individual batches comprised 40,000 trials. In addition, a minimum limit of 1,000,000 trials was specified.

Uncertainty and Sensitivity Analysis

For the second step, uncertainty propagation and apportionment in the anthropometric parameters of the thigh segment were evaluated for the actual subjects by conducting an uncertainty and sensitivity analysis based on the biomechanical measurements described in Chapter 5 and the previously identified uncertainties. The computation of the anthropometric parameters requires the segment length and the body mass which involves motion capture data and force plate measurements of the still standing subjects as well as the regression parameters in anthropometric parameter and joint center estimation. Therefore, the found uncertainties for the regression parameters together with the determined uncertainties for anatomical landmark identification and force plate measurements presented in Chapter 6 were incorporated into the evaluation. In accordance with the results of the uncertainty quantification, the uncertainty of the motion capture system was neglected. The spatial positions of the involved anatomical landmarks were calculated by averaging the motion capture data over four seconds during the initial idle time in the walking trial. For anatomical landmark misplacement, the uncertainties obtained in the reproducibility experiments which denote the inter-examiner precision were applied. The three-dimensional sampling points of the surrounding skin surface were not considered in order to reduce the computation time. In each trial of the two Monte Carlo simulations, a sample of measurement uncertainties and regression parameters was drawn from the specified distributions and used to calculate the respective anthropometric parameters. The uncertainty of the resulting parameters was modeled by an appropriate Johnson distribution and sensitivities were rated through the first-order and total-effect sensitivity indices. The relative threshold limit was set to $5 \cdot 10^{-4}$ for uncertainty convergence and $5 \cdot 10^{-3}$ for sensitivity convergence. The individual batches comprised 40,000 trials. In total, the sensitivity analysis had thirty-six input variables and eleven output variables.

8.4 Results

In accordance with the exemplary sensitivity and uncertainty analysis, the results of the uncertainty analysis are presented with a focus on the thigh segment for female and male subjects.

Uncertainty Analysis

For the uncertainty analysis, the individual Monte Carlo simulations were terminated after between 1,000,000 and 5,400,000 trials. The obtained probability distributions for the segment

Table 8.3.: Copula covariance matrix for regression parameters of anthropometric parameters in the female thigh.

Σ_c	α_m	$\alpha_{o,X}$	$\alpha_{o,Y}$	$\alpha_{o,Z}$	$\alpha_{I,XX}$	$\alpha_{I,YY}$	$\alpha_{I,ZZ}$	$\alpha_{I,XY}$	$\alpha_{I,XZ}$	$\alpha_{I,YZ}$
α_m	0.0815	$*$	$*$	$*$	$*$	$*$	$*$	$*$	$*$	$*$
$\alpha_{o,X}$	0.0000	0.0000	$*$	$*$	$*$	$*$	$*$	$*$	$*$	$*$
$\alpha_{o,Y}$	-0.0001	0.0000	0.0004	$*$	$*$	$*$	$*$	$*$	$*$	$*$
$\alpha_{o,Z}$	0.0003	0.0001	0.0003	0.0776	$*$	$*$	$*$	$*$	$*$	$*$
$\alpha_{I,XX}$	-0.0249	0.0000	-0.0016	-0.0247	0.0845	$*$	$*$	$*$	$*$	$*$
$\alpha_{I,YY}$	-0.0206	0.0000	-0.0012	-0.0182	0.0483	0.0700	$*$	$*$	$*$	$*$
$\alpha_{I,ZZ}$	-0.0220	0.0000	-0.0014	-0.0232	0.0579	0.0461	0.0750	$*$	$*$	$*$
$\alpha_{I,XY}$	-0.0016	-0.0001	-0.0001	-0.0101	0.0072	0.0066	0.0060	0.0211	$*$	$*$
$\alpha_{I,XZ}$	-0.0019	0.0000	-0.0002	-0.0032	-0.0025	0.0053	0.0132	-0.0008	0.0288	$*$
$\alpha_{I,YZ}$	-0.0003	0.0000	0.0000	-0.0011	0.0003	0.0001	0.0004	0.0003	0.0003	0.0003

Table 8.4.: Copula covariance matrix for regression parameters of anthropometric parameters in the male thigh.

Σ_c	α_m	$\alpha_{o,X}$	$\alpha_{o,Y}$	$\alpha_{o,Z}$	$\alpha_{I,XX}$	$\alpha_{I,YY}$	$\alpha_{I,ZZ}$	$\alpha_{I,XY}$	$\alpha_{I,XZ}$	$\alpha_{I,YZ}$
α_m	0.0831	$*$	$*$	$*$	$*$	$*$	$*$	$*$	$*$	$*$
$\alpha_{o,X}$	0.0000	0.0000	$*$	$*$	$*$	$*$	$*$	$*$	$*$	$*$
$\alpha_{o,Y}$	-0.0002	0.0000	0.0057	$*$	$*$	$*$	$*$	$*$	$*$	$*$
$\alpha_{o,Z}$	0.0014	0.0000	0.0013	0.0828	$*$	$*$	$*$	$*$	$*$	$*$
$\alpha_{I,XX}$	-0.0234	0.0000	-0.0024	-0.0142	0.0821	$*$	$*$	$*$	$*$	$*$
$\alpha_{I,YY}$	-0.0258	0.0000	-0.0032	-0.0144	0.0485	0.0835	$*$	$*$	$*$	$*$
$\alpha_{I,ZZ}$	-0.0227	0.0000	-0.0024	-0.0160	0.0423	0.0467	0.0776	$*$	$*$	$*$
$\alpha_{I,XY}$	-0.0064	0.0000	-0.0004	-0.0287	0.0400	0.0281	0.0272	0.0814	$*$	$*$
$\alpha_{I,XZ}$	-0.0016	0.0000	-0.0003	-0.0006	0.0139	0.0060	-0.0032	0.0045	0.0244	$*$
$\alpha_{I,YZ}$	0.0000	0.0000	0.0000	0.0000	0.0000	0.0000	0.0000	0.0000	0.0000	0.0000

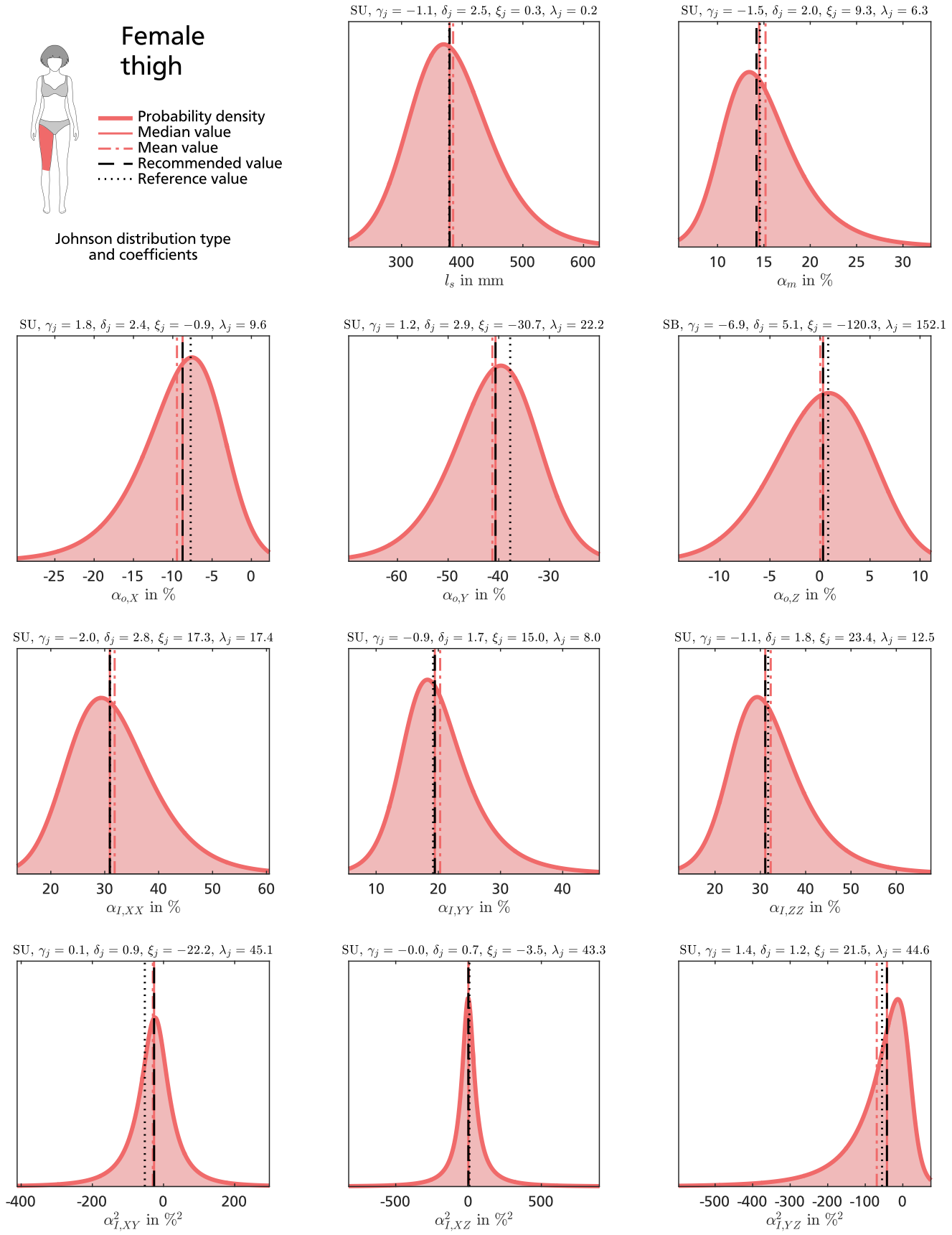

Figure 8.2.: Regression parameter uncertainty for the anthropometric parameters of the female thigh with corresponding Johnson distribution types and coefficients.

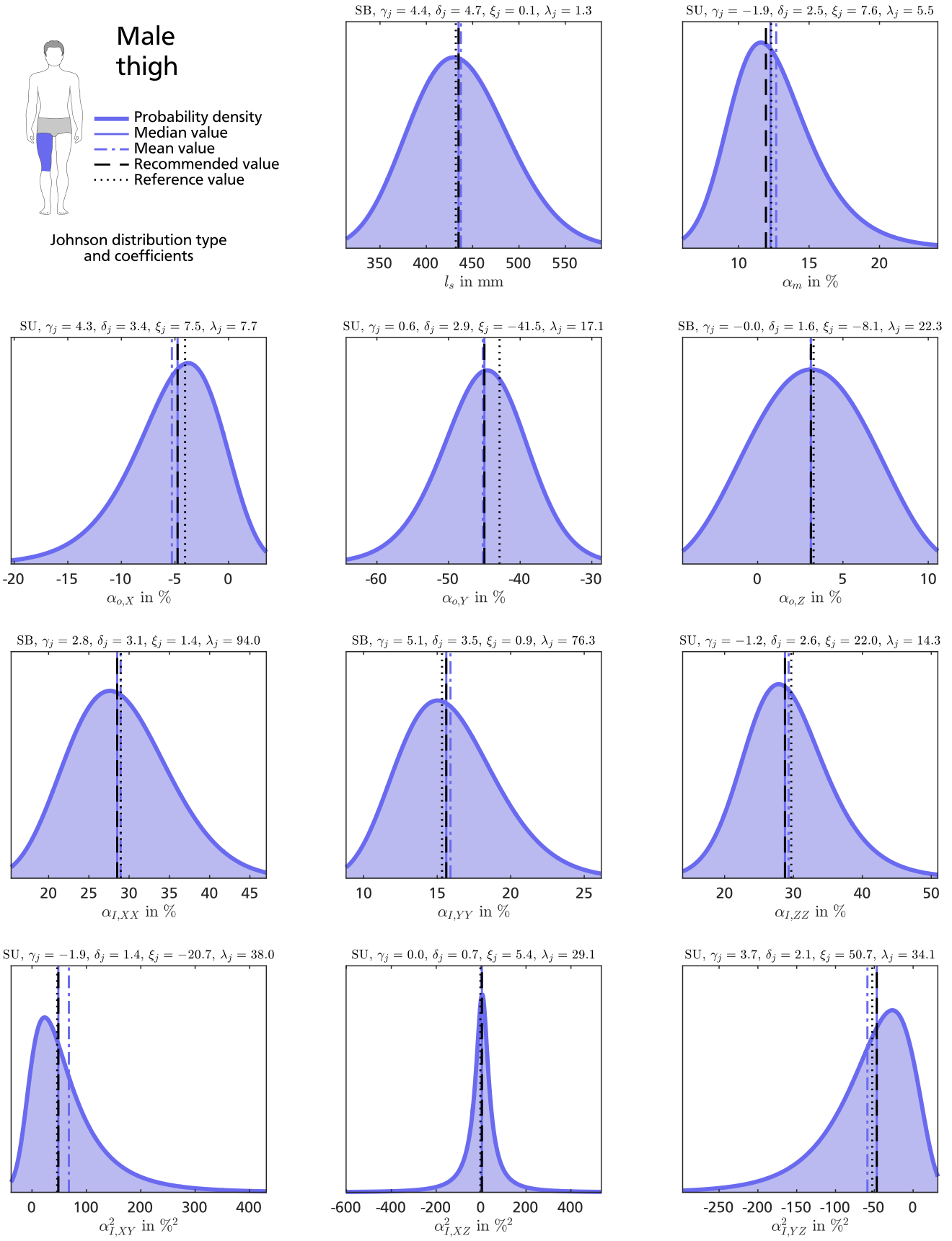

Figure 8.3.: Regression parameter uncertainty for the anthropometric parameters of the male thigh with corresponding Johnson distribution types and coefficients.

length as well as the considered regression parameters of the female and male thigh are presented in Figure 8.2 and 8.3. In addition to the median and mean values, the specified reference values, marked by the dotted black lines, are given for comparison. For each distribution, the corresponding Johnson distribution type and coefficients γ_j, δ_j, λ_j, ξ_j are provided. The standard deviations of the regression parameters range from 4.7 % to 15.3 % for female subjects and from 3.3 % to 12.4 % for male subjects, where the smallest deviation is found in the mass parameter and the greatest deviation is present in the product of inertia parameter with respect to the x- and z-axes for both genders. Due to the squaring, the distributions for the product of inertia parameters have a quite large dispersion compared to the other parameters. The copula covariance matrices $\mathbf{\Sigma}_c$ that model the correlation among the individual marginal distributions are given in Table 8.3 and 8.4. The results for all other body segments are listed in Appendix A.9. The relative standard deviations of the regression parameters with respect to the provided reference value reach up to 4,987.2 % for female subjects and 67,254.9 % for male subjects.

A rather high symmetry is indicated by very similar median and mean values for most of the obtained distributions, while there is a considerable difference between these measures and the specified reference values in some particular cases. Especially, the parameters for the center of mass in thorax, abdomen and leg segments as well as the parameters for the inertia tensor in head, abdomen, arm and shank segments show significant deviations. A rather good conformity is found in pelvis and hand segments. The observed differences suggest that the original reference values which were solely derived from the provided means might not represent the best choice for the regression parameters. One reason for this finding is the fact that the applied transformations involve nonlinear operations and interactions between the uncertain parameters. These interrelations are not fully considered by a single evaluation with the provided means. In contrast, the applied Monte Carlo simulation is able to make allowance for the contained nonlinearities and interactions but also incorporates the statistical properties of the individual uncertainty sources. Therefore, the obtained distributions can be regarded as a more realistic representation of the regression model and the corresponding measures of central tendency like median, mean or mode are good candidates for refined regression parameters. Since the median ν_d is the measure that minimizes the average absolute deviation [236], it is considered as an appropriate choice and a set of revised regression parameters was derived from the respective median values. In order to ensure a correct scaling of the segment masses, the vector of the segment mass parameters $\boldsymbol{\alpha}_m$ was normalized by solving a static optimization problem that enforced a sum of 100 % with maximizing the relative probability density of the individual parameters. The optimization problem has the form

$$\begin{aligned} \underset{\boldsymbol{\alpha_m}}{\text{minimize}} \quad & -\sum_{i}^{10} h_i \, \frac{p(\alpha_{m,i})}{\nu_d(\alpha_{m,i})} \\ \text{subject to} \quad & \sum_{i}^{10} h_i \, \alpha_{m,i} = 100\,\%, \end{aligned}$$

where the factor $h_i \in \{1, 2\}$ accounts for the quantity of the particular body segments. The nonlinear programming solver *fmincon* of the numerical computing software MATLAB that is based on an interior-point algorithm was used to solve the optimization problem with selecting the respective medians as start values. The found recommended values are listed in Table 8.5

Table 8.5.: Recommended regression parameters for anthropometric parameter estimation in female and male subjects including the parameters for the segment mass α_m, center of mass α_o and inertia tensor α_I.

			α_o in %			α_I in %					
Segment	**Gender**	α_m in %	X	Y	Z	XX	YY	ZZ	XY	XZ	YZ
HEA	female	6.3	9.6	52.2	-0.1	28.4	22.6	29.3	3.3i	0.8	0.6
	male	6.5	1.7	57.0	0.1	29.4	18.6	31.7	3.6i	1.6i	2.2
THO	female	27.9	4.0	-46.7	0.1	36.9	32.4	33.2	8.7i	2.6i	1.4
	male	31.9	0.6	-47.7	-0.4	38.8	32.6	34.0	8.6i	1.4	2.0
ABD	female	3.9	4.7	-25.4	0.4	80.7	95.2	66.9	3.1i	1.5	5.1i
	male	2.8	0.5	-19.2	-3.8	65.4	75.9	46.8	15.8i	4.4i	6.4i
UPA	female	2.1	-5.0	-49.8	-3.1	27.2	14.8	26.6	1.9i	1.9i	10.5
	male	2.3	0.9	-48.5	-2.9	27.0	12.6	27.5	5.4	3.1	2.2
LOA	female	1.3	1.8	-39.3	3.6	27.2	16.0	25.1	9.7	4.0	12.8i
	male	1.7	-1.6	-40.0	1.7	27.8	11.9	28.4	7.8	1.6	1.5i
HAN	female	0.5	7.4	-77.4	4.7	62.1	43.7	58.1	27.6	21.3	26.9i
	male	0.6	8.1	-83.9	7.4	60.7	38.1	55.1	20.8	14.6	18.7i
PEL	female	15.6	-5.8	-24.0	0.5	95.9	105.0	81.8	30.6i	3.7i	0.6
	male	14.2	-0.4	-28.3	-0.5	101.9	106.3	95.2	22.6i	9.7i	6.3i
THI	female	14.2	-8.8	-40.6	0.3	30.9	19.4	31.1	5.2i	1.2i	6.5i
	male	11.9	-4.8	-45.0	3.1	28.5	15.6	28.8	7.0	1.9	6.8i
SHA	female	4.2	-4.6	-40.5	4.7	27.8	11.0	27.8	2.0	1.3	2.8
	male	4.6	-5.1	-40.9	2.3	27.9	10.0	27.9	2.1i	0.7i	1.0i
FOO	female	0.9	32.0	-32.0	14.5	25.4	51.9	51.4	14.5i	9.1	2.8i
	male	1.2	45.8	-24.1	8.5	23.5	50.1	49.3	16.6	10.7i	2.9

and indicated in the provided graphs of the distributions by a dashed black line. In average, the absolute difference between the reference and recommended values amounts to 19.6 % in the parameters for female subjects and 41.2 % in the parameters for male subjects. The largest differences can be observed for the product of inertia parameter with respect to the x- and y-axes in the female abdomen with 709.7 % and the center of mass parameter in the x-axis for the male abdomen with 3384.5 %.

To facilitate the comparison of the parameter uncertainties, summaries of the relative interquartile ranges for each parameter class are presented in Figure 8.4 and 8.5. The parameter classes are separated by gray vertical lines and comprise the segment length as well as the parameters for segment mass, center of mass, moments of inertia and products of inertia. The interquartile ranges that are presented in the left part of the diagram and specified by the difference between the 75 th percentile and the 25 th percentile have been divided by the sum of all interquartile ranges in the respective parameter class. The right part of the diagram lists and visualizes the particular share of the involved parameters in the corresponding interquartile range sums. Generally, the dispersion of the regression parameters is larger for female subjects which becomes evident from the mostly higher values for the obtained interquartile range sums. This does not apply to the segment lengths as these are typically greater in male subjects and are not given as

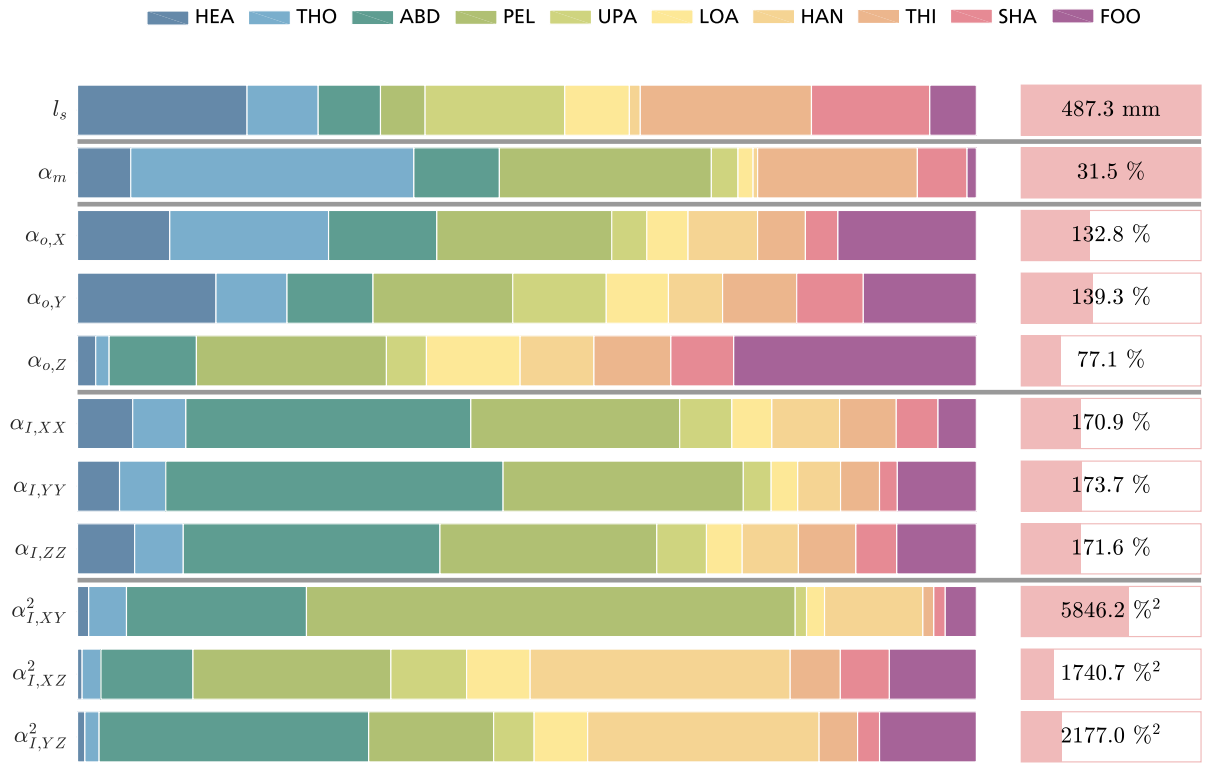

Figure 8.4.: Relative interquartile ranges for female regression parameter uncertainties (left) with respect to the interquartile range sums for each parameter class (right).

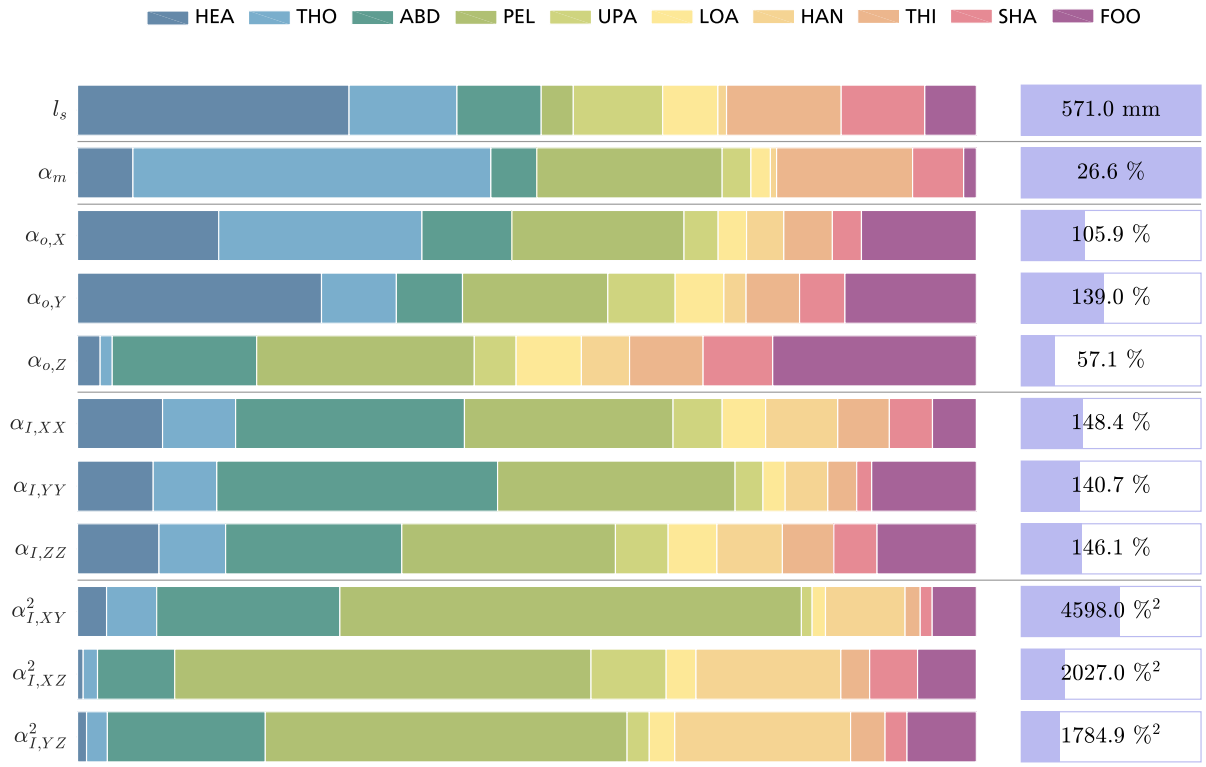

Figure 8.5.: Relative interquartile ranges for male regression parameter uncertainties (left) with respect to the interquartile range sums for each parameter class (right).

a relative regression parameter. For both genders, the center of mass parameters in x- and y-axis as well as the product of inertia parameter with respect to the x- and y-axes have a higher variability than the other parameters in the respective parameter classes, whereas the share of the moment of inertia parameters is rather balanced. The relative interquartile ranges in the left part of the diagram reveal that the head, thorax, abdomen, pelvis and foot segments exhibit the largest uncertainties. This finding is basically valid for both genders. While the pelvis segment considerably varies in all parameters, the other body segments are mainly affected in individual parameter classes. The abdomen segment has a significant variability in the parameters for the inertia tensor but is rather unimpaired in the mass and center of mass parameters. The opposite attribution applies to the head, thorax and foot segments. A rather small uncertainty is evident in the parameters for arms and legs, where only the segment length and mass parameter of the thigh segment vary notably.

The general structure of the copula covariance matrices shows that there are substantial correlations between the individual parameters in all body segments. Particularly, the moment of inertia parameters have internal interdependencies but are also negatively correlated to the parameters for mass and center of mass. This latter relation results from the actual regression equations. The inertia tensor is calculated with a multiplication by the segment mass and the squared segment length. The inertia tensor parameters therefore have to compensate higher or lower values in these parameters in order to ensure a reasonable estimate of the inertia tensor.

Uncertainty and Sensitivity Analysis

For the exemplary uncertainty and sensitivity analysis, the Monte Carlo simulations were terminated after 1,260,000 trials for the female subject and 1,500,000 trials for the male subject with regard to the uncertainty analysis which corresponds to 630,000 and 750,000 trials for the sensitivity analysis. The resulting probability distributions for the uncertainties in the anthropometric parameters of the female and male right thigh are presented in Figure 8.6 and 8.7. Besides the median and mean values, the obtained parameters for the specified reference values and the presented recommended values are indicated by the black dotted and dashed lines. In the female thigh, the standard deviations reach 14.3 mm for the segment length, 2.7 kg for the segment mass and range from 18.8 mm to 35.0 mm for the center of mass as well as from 0.0134 kg.m^2 to 0.0852 kg.m^2 for the inertia tensor. In the male thigh, the standard deviations have a value of 14.4 mm for the segment length, 2.8 kg for the segment mass and range from 13.7 mm to 28.2 mm for the center of mass as well as from 0.0126 kg.m^2 to 0.0804 kg.m^2 for the inertia tensor. These ratings are in agreement with the results of the preceding uncertainty analysis and support a generally higher variability in the anthropometric parameters of the female subject with exception of the segment length and mass. The deviations between the estimated anthropometric parameters for the original reference values and the revised recommended values are very evident for some of the center of mass and product of inertia parameters. The anthropometric parameter estimates determined with the recommended values coincide quite well with the found median values of the distributions, while the center of mass parameter in the y-axis calculated with the reference value for example differs by 10.9 mm for the female subject and 9.0 mm for the male subject.

The results of the sensitivity analysis are presented in Figure 8.8 and 8.9. Each bar represents one anthropometric parameter and is segmented according to the respective uncertainty

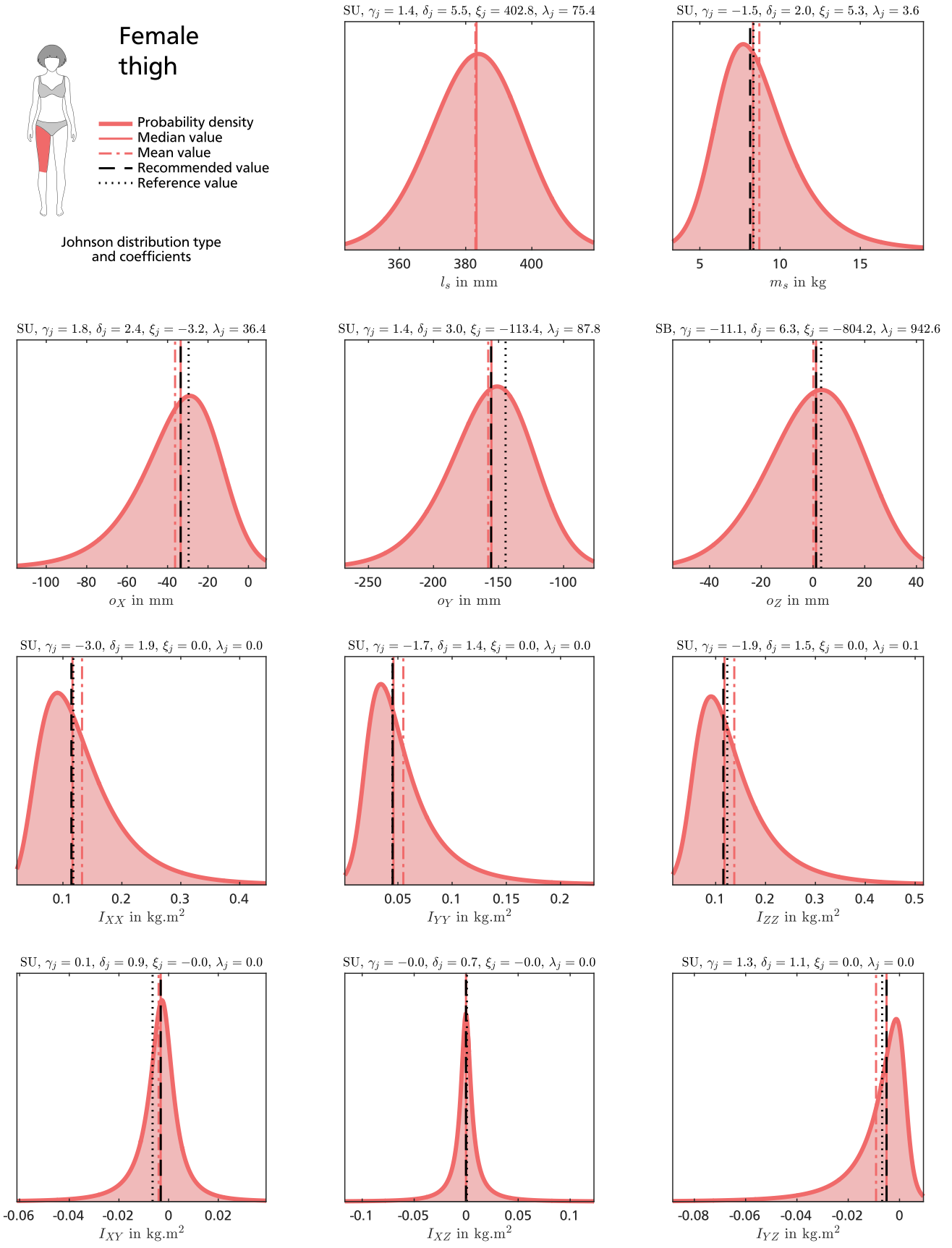

Figure 8.6.: Anthropometric parameter uncertainty for the female thigh with corresponding Johnson distribution types and coefficients.

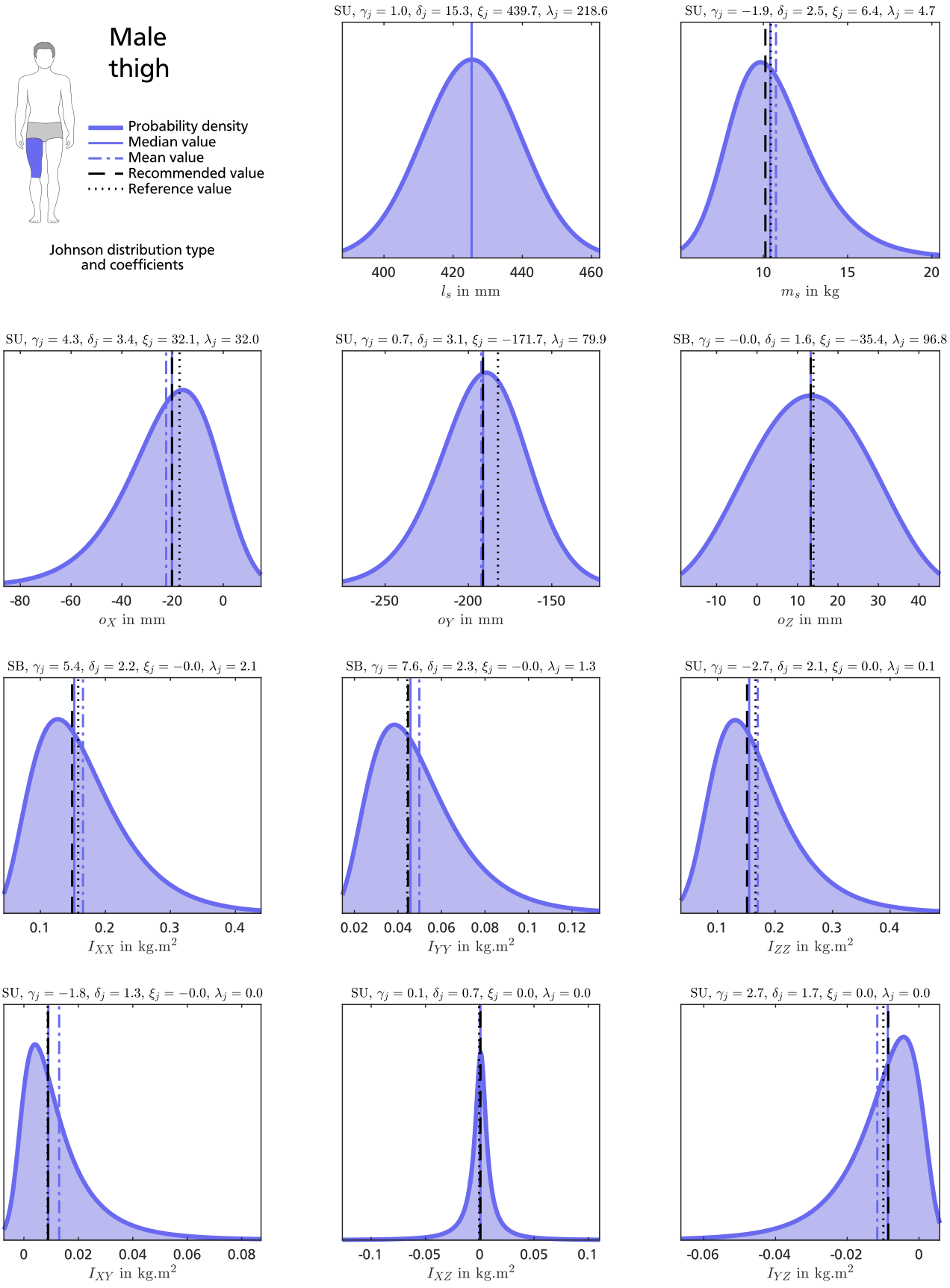

Figure 8.7.: Anthropometric parameter uncertainty for the male thigh with corresponding Johnson distribution types and coefficients.

apportionment with respect to the involved uncertainty sources, i.e., uncertainties in body measurements (BOM), regression parameters for anthropometric parameter estimation (ANP), regression parameters for joint center estimation (JOC) and anatomical landmark identification (ALI). The sensitivity index S equals to the normalized first-order indices, where all first-order indices were set to zero that had a vanishing total-effect index after rounding to four decimal places. The uncertainty in the segment length only depends on the regression parameters for joint center estimation and the anatomic landmark identification. This relation is also observable in the diagram. For the female subject, the uncertainties in the joint center parameters have a considerably higher influence, whereas the impact of the variations in anatomic landmark identification is greater for the male subject. All other anthropometric parameters are almost exclusively affected by the uncertainties in the associated regression parameters. Only the inertia tensor parameters are slightly impaired by the variance of the regression parameter for the segment mass. The propagation of the uncertainties in joint center estimation and anatomic landmark identification through the multiplication with the segment length in the center of mass and inertia tensor parameters is rather negligible. Also, the uncertainties in the body weight measurements with the force plates of the instrumented treadmill are insignificant compared to the effect of the regression parameter for the segment mass.

8.5 Discussion

Both uncertainty analyses reveal significant uncertainties in the regression parameters for anthropometric parameter estimation as well as the personalized anthropometric parameters, where the variations are slightly larger for female subjects. Particularly, the regression parameters for the body segments in the torso, i.e., thorax, abdomen and pelvis, have large variances which implies high uncertainties for estimated segment masses, centers of mass and inertia tensors. The regression parameters for the arm and leg segments show comparatively small variations. The obtained uncertainties in the regression parameters for the thigh segment that has been exemplarily considered are also evident in the corresponding anthropometric parameters. The revised regression parameters that were derived from the median values of the respective distributions achieve slightly better estimation results than the original reference regression parameters with regard to the observed variations. Following from the sensitivity analysis, the uncertainties in the anthropometric parameters are mainly caused by the variations in the associated regression parameters. Although the variances in the segment length are essentially influenced by the variations in joint center estimation and anatomical landmark identification, this uncertainty is not considerably propagated to the other anthropometric parameters.

Besides the described uncertainty sources in regression parameters and measurement data that have been regarded in the uncertainty and sensitivity analysis, there are several influencing factors which are rather difficult to quantify and integrate into the evaluation. McConville et al. and Young at al. assumed a constant density distribution in the individual body segments to estimate the inertial parameters. This presumption is a quite strong simplification of the actual density distribution in the human body, where bones typically have a much larger density than fat or muscle tissue [77]. Nevertheless, existing studies that discussed the impact of the uniform density assumption on the derived anthropometric parameters obtained inconsistent results. Clauser et al. rated the error in center of mass estimation as 2.0 - 3.0 cm [52] and Hatze reported an error magnitude of 4.0 - 7.0 % in principal moment of inertia estimation [103],

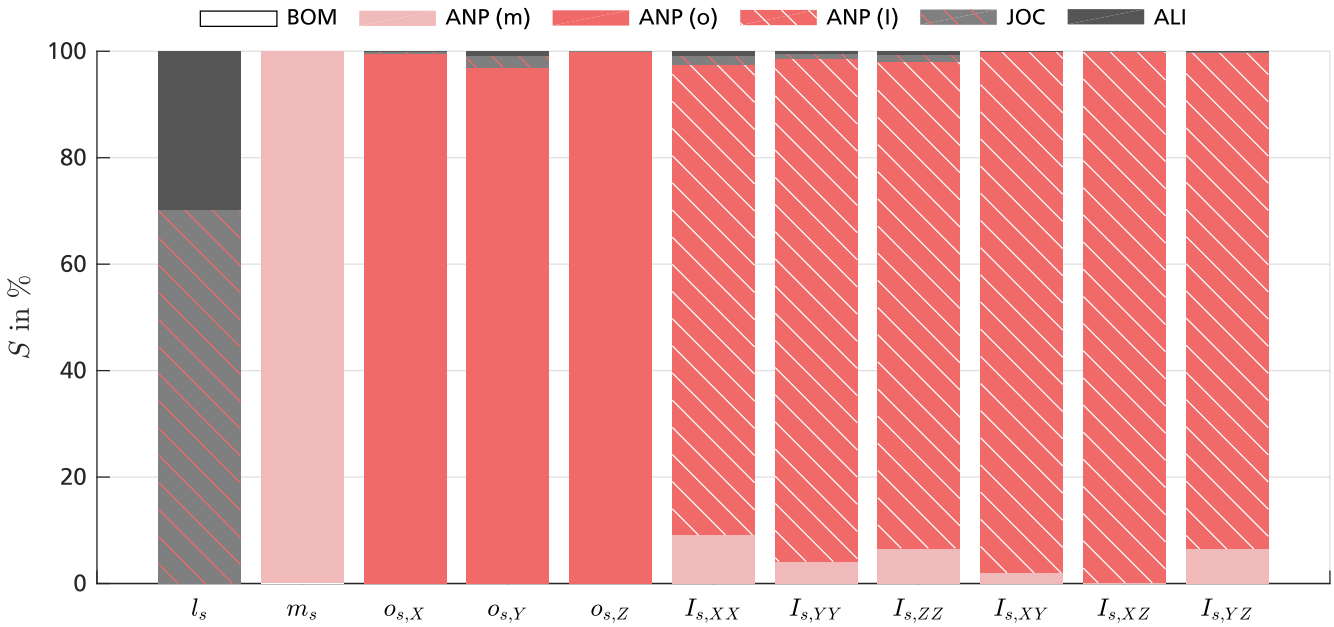

Figure 8.8.: Anthropometric parameter sensitivity of the female thigh with regard to uncertainties in body measurements (BOM), regression parameters for anthropometric parameter estimation (ANP), regression parameters for joint center estimation (JOP) and anatomical landmark identification (ALI).

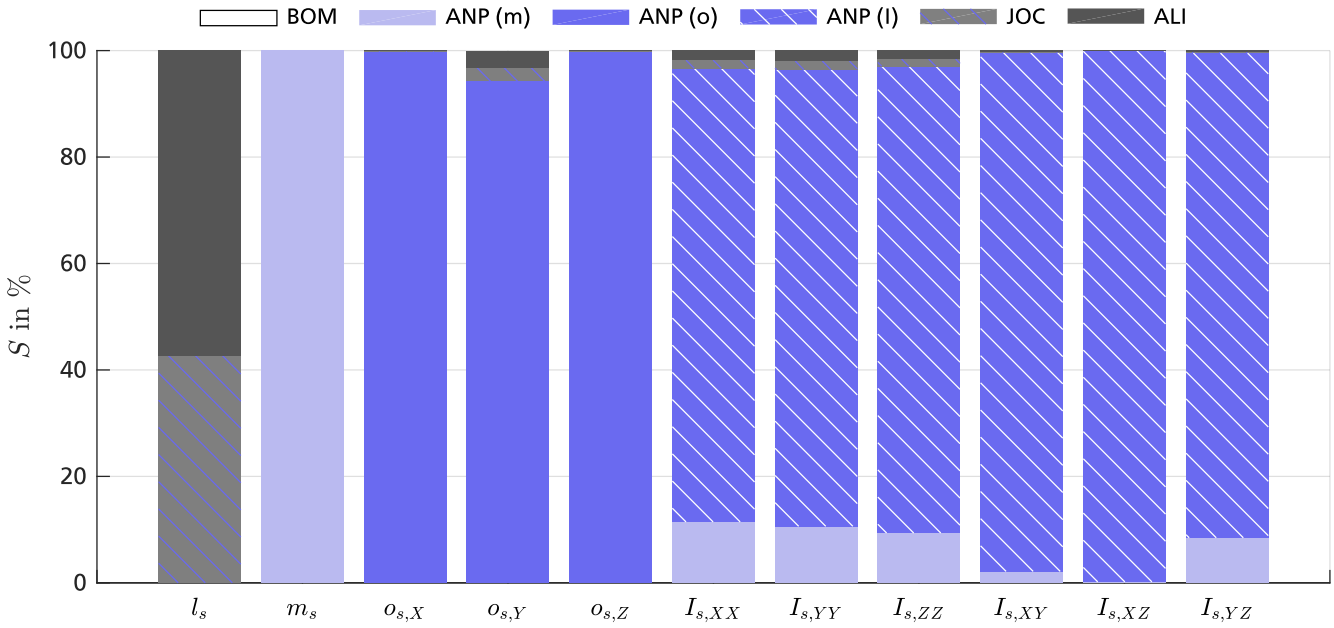

Figure 8.9.: Anthropometric parameter sensitivity of the male thigh with regard to uncertainties in body measurements (BOM), regression parameters for anthropometric parameter estimation (ANP), regression parameters for joint center estimation (JOP) and anatomical landmark identification (ALI).

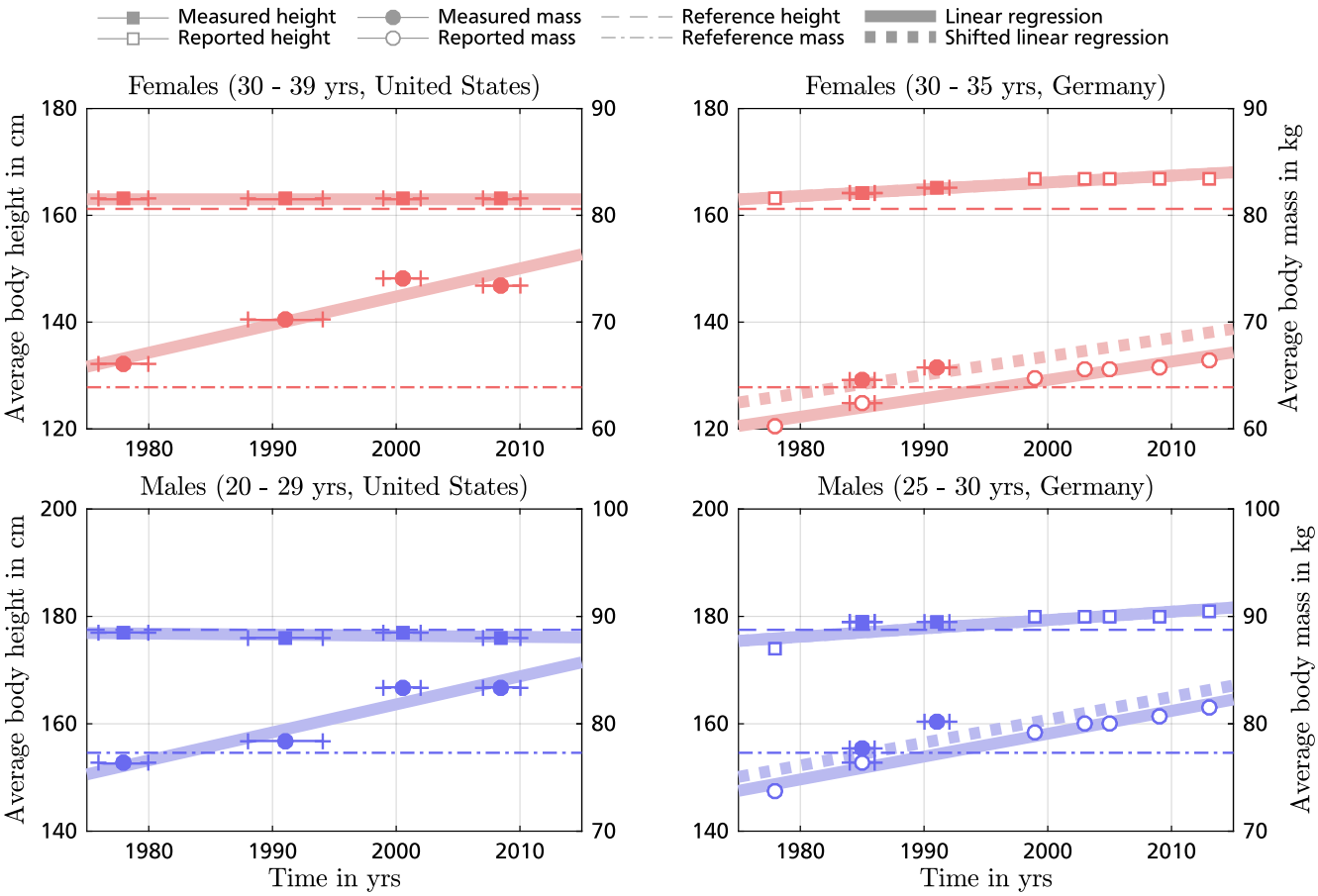

Figure 8.10.: Historical development of average body measures in the United States and Germany for females and males over the past forty years.

while Lephart et al. only found deviations of up to 0.3 % for all body segments in the determination of the center of mass and principal moments of inertia [134]. An additional aspect that potentially affects the estimation results is the age of the underlying measurement data. McConville et al. and Young et al. conducted their measurements in the late 1970s and selected the subjects in accordance with the average body height and mass of the general United States adult population at that time. The historical development of the average body height and mass in the United States and Germany for females and males in a comparable age range over the past forty years is presented in Figure 8.10. The average data for the United States contains measured values over different time periods and has been adopted from the National Center for Health Statistics [85, 160]. The average data for Germany is a mix of self-reported and measured values taken from reports of the Federal Statistics Office and the Robert Koch Institute [216, 217, 218, 219, 220, 221, 187, 188]. In order to visualize the basic trend, a linear regression has been applied which is indicated by the thick red and blue lines. Due to the difference between self-reported and measured values, the linear regressions for Germany were shifted by a constant offset that was derived from one data point with measured and self-reported values. The two linear regressions coincide for the body height but notable differ for the body mass. The dashed and dot-dashed lines mark the original reference values in the measurement data by McConville et al. and Young et al. While the body height for both genders remained rather constant in the United States or only marginally increased in Germany, the body mass constantly grew in both countries. For this reason, the reference height is still generally

valid but the reference mass is considerably lower than the present average value. Since the regression model represents a fixed relation between the individual anthropometric parameters, an application of the model on present Caucasian subjects with an appropriate age supposes an even distribution of the additional body mass on all body segments with a consistent body shape. This presumption is rather unrealistic and therefore causes additional uncertainties in the estimation process. Furthermore, the regression model was only established for the right body side with assuming symmetry. Hence, probable differences between a dominant and non-dominant arm or leg cannot be considered. Other potential constraints of the uncertainty and sensitivity analysis comprise the lack of covariances in the measurement data which enforces a neglect of possible correlations between the measurands and the unknown effect of the assumptions made by Dumas et al. with regard to the rotation matrices for the male subjects. Despite the described limitations, the comprehensive regression model provided by Dumas et al. is currently one of the best choices for the estimation of anthropometric parameters. The described uncertainty and sensitivity analysis together with the revised regression parameters give new insights into the relation between the involved uncertainty sources and enable improved estimation results.

8.6 Conclusion

Uncertainties in body segment lengths and regression parameters for anthropometric parameter estimation have a direct influence on the kinematic and dynamic properties of the biomechanical model. The presented uncertainty and sensitivity analysis provides a systematic investigation of uncertainty propagation and apportionment in all regression parameters of a comprehensive regression model and personalized anthropometric parameters which are exemplarily evaluated for the thigh segment. The investigation is based on statistical properties reported in literature as well as the previously obtained results for the uncertainty quantification in biomechanical measurements and the uncertainty analysis for joint center estimation. The examined regression model covers the most relevant body segments for a biomechanical simulation of human locomotion and does not apply restrictive assumptions on the inertial parameters. The results of the uncertainty analysis indicate comparatively high variances in the regression parameters for the body segments of the torso and rather small variations in the regression parameters for arms and legs, whereas the results of the sensitivity analysis show that the uncertainties of the estimated anthropometric parameters for the thigh segments of the actual subjects almost exclusively arise from the variability in the associated regression parameters. Based on the found uncertainties, revised regression parameters have been derived from the respective distributions. These findings provide reasonable statistical models for the uncertainty and sensitivity analysis of the inverse dynamics simulation but also reveal essential limitations in existing regression models for anthropometric parameter estimation.

9 Uncertainty and Sensitivity Analysis of Motion Dynamics Simulations

The actual inverse dynamics simulation is the final step in the estimation of joint forces and torques resulting from a particular human motion. Within the simulation, the obtained joint trajectories and measured ground reaction forces are applied to a biomechanical model of the human locomotor system that is defined by the estimated joint center locations and anthropometric parameters. Due to these dependencies, the simulation results are potentially affected by several uncertainty sources in the preceding steps. The relevant uncertainty sources and the propagation of the individual uncertainties in the inverse dynamics procedure are illustrated in Figure 9.1.

The inverse dynamics simulation considered in this thesis focuses on the joint torques of hip, knee and ankle joint in a walking, running and kicking a ball motion performed by a female and male subject. In order to evaluate the overall uncertainty of the simulation results and understand the influences of the involved uncertainty sources, a comprehensive uncertainty and sensitivity analysis oriented towards the inverse dynamics procedure has been conducted with

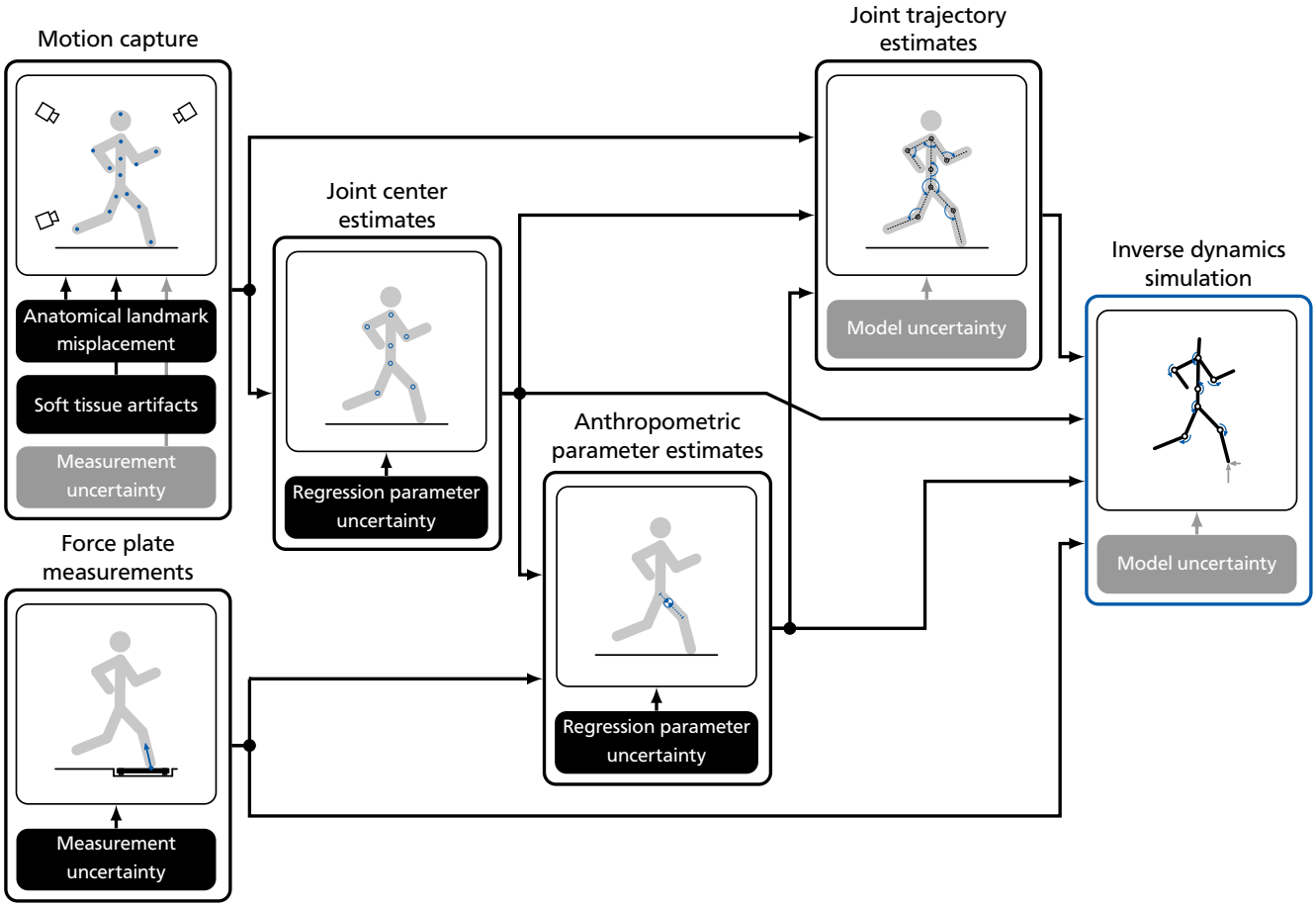

Figure 9.1.: Uncertainty propagation in the inverse dynamics simulation that is based on biomechanical measurements as well as joint center, anthropometric parameter and joint trajectory estimation.

incorporating all previously determined uncertainties. This approach ensures a systematic and consecutive assessment of uncertainty propagation and apportionment regarding the sequential nature of the procedure and existing dependencies between the involved uncertainty sources. The uncertainty quantification in biomechanical measurements presented in Chapter 6 showed that anatomic landmark misplacement, soft tissue artifacts as well as measurement uncertainties of the instrumented treadmill can have an essential impact on the measurement results. By contrast, the expectable measurement errors in motion capture are rather negligible and therefore excluded from the uncertainty and sensitivity analysis. The subsequent evaluation of regression models in joint center and anthropometric parameter estimation described in Chapter 7 and 8 revealed a considerable dispersion in the associated regression parameters which potentially affects the kinematic and dynamic properties of the biomechanical model. Moreover, model uncertainties which might arise from an inadequate representation of the human locomotor system can impair all steps that involve kinematics or dynamics simulations. Since a general evaluation for this type of uncertainty is complicated by missing reference data, the influence of model uncertainties is minimized by applying generally accepted modeling approaches. Model uncertainties are hence not included in the uncertainty and sensitivity analysis. In the overview shown in Figure 9.1, all uncertainty sources that are considered in the uncertainty and sensitivity analysis are indicated by a black box.

9.1 Related Work

Several studies have evaluated uncertainty propagation and apportionment caused by individual or multiple uncertainty sources in biomechanical dynamics simulations. As described in Chapter 4, the applied approaches can be divided into local and global sensitivity analysis methods. Local methods are computationally efficient but cannot explore the whole input space. Global methods can become computationally expensive but are more robust and allow to cover the whole input space.

Most of the studies that evaluated sensitivities in biomechanical dynamics simulations applied local methods. For example, Silva and Ambrósio [208] as well as Riemer et al. [181] investigated uncertainties and sensitivities in estimated joint torques for walking. Silva and Ambrósio considered deviations in body segment masses, anatomical landmarks and force plate measurements, whereas Riemer et al. regarded variations in motion capture data, force plate measurements as well as joint center, joint trajectory and anthropometric parameter estimation. In both studies, the respective biomechanical measurements and model parameters were perturbed in two discrete steps and the sensitivity was approximated by a finite difference quotient. With this method, Silva and Ambrósio found a high sensitivity to the center of pressure location and a rather small influence of uncertainties in anthropometric parameters and joint trajectories. Riemer et al. applied a small and a large set of deviations and observed variations of up to 232.0 % in the obtained joint torques. The magnitudes in more distal joints were smaller and the uncertainties in joint trajectories and anthropometric parameters were identified as the main contributors in uncertainty propagation. Pàmies-Vilà et al. individually analyzed the influence of uncertainties in anthropometric parameters, joint trajectories and force plate measurements on estimated joint torques for a walking motion [166]. For the deviations in the anthropometric parameters, a Gaussian distribution was assumed and the joint torques were computed for one thousand samples and a three-sigma interval of 5.0 %, 10.0 %

and 15.0 %. The other uncertainties were evaluated for two different optimization parameters in joint trajectories estimation and two different signal offsets in force plate measurements. The comparison of the individual results revealed rather high sensitivities to variances in joint trajectories and force plate measurements, while the impact of deviations in the anthropometric parameters was almost negligible. Wessling et al. examined the effect of perturbated anthropometric parameters on estimated joint torques and muscle forces in walking by varying the mass, center of mass and inertia tensor of the left thigh, shank and foot segments [237]. The respective parameters were adjusted individually as well as for different combinations of two parameters in a range from 60.0 % to 140.0 % of the reference value. A finite difference quotient was applied to approximate the corresponding sensitivities. The results indicated rather small effects on the joint torques but showed quite large variations in the muscle forces. These variations mainly resulted from slight changes in the initial conditions of the optimization problem that was applied for the muscle force estimation.

Comparatively few studies used global methods for the evaluation of sensitivities in biomechanical dynamics simulations. Reinbolt et al. evaluated how deviations in joint center and anthropometric parameter estimation affect the results of an inverse dynamics simulation for a synthetic walking motion [178]. In a Monte Carlo simulation with five thousand trials, the previously determined joint center and anthropometric parameter estimates were altered together or separately within 25.0 %, 50.0 %, 75.0 % and 100.0 % of predefined bounds with assuming a uniform distribution. The variations in the joint centers were found to have a significant effect on the estimated joint torques, while the influence of the varied anthropometric parameters was rather low. Nguyen and Reynolds used a Monte Carlo simulation to investigate the impact of variations in anthropometric parameter estimates obtained from different groups of regression models on estimated joint torques in walking [155]. The variations were modeled as independent Gaussian distributions with adopting the corresponding means and standard deviations from literature. For each group of regression models, a Monte Carlo simulation with two thousand trials based on Latin hypercube sampling was conducted. The results indicated that the variations in anthropometric parameters only have a small effect on the estimated joint torques in the stance phase. For the swing phase, the influence was slightly larger but not much greater than the inter-trial variability. Valente et al. evaluated the sensitivity of estimated joint trajectories, joint torques and muscle forces to uncertainties due to anatomical landmark misplacement, soft tissue artifacts as well as variability in joint center, anthropometric and muscle parameters for a walking motion [227]. A subject-specific biomechanical model of the lower limbs was created from magnetic resonance imaging and the required anatomical landmarks were identified with a virtual palpation procedure. The uncertainties of this procedure were experimentally determined with five examiners. The locations of the anatomical landmarks affected the calculation of reference frames, anthropometric parameters and joint centers. For muscle-tendon geometry as well as the anatomical landmark identification, independent Gaussian distributions were assumed, whereas uncertainties in maximum muscle tensions were presumed to follow independent uniform distributions. A Monte Carlo simulation with five hundred trials based on Latin hypercube sampling was applied to estimate the sensitivities with a correlation analysis. The found effects of the considered uncertainties were considerably smaller than in previous studies. The standard deviations reached 1.0 ° in the joint positions and 1.4 Nm in the joint torques. These results could have been caused by quite low uncertainties in the virtual palpation procedure, where the standard deviation did not exceed

4.2 mm for all anatomical landmarks. Myers et al. investigated the influence of variations in anatomical landmarks misplacement, soft tissue artifacts as well as anthropometric and muscle parameters on estimated joint trajectories, joint torques and muscle forces in walking [153]. All uncertainties were assumed to follow independent Gaussian distributions with means and standard deviations reported in literature. The sensitivities were calculated with a correlation analysis based on a Monte Carlo simulation with three thousand trials. The combined impact of all uncertainties resulted in average 90 % confidence intervals ranging from 2.7 ° to 6.4 ° in joint positions, 2.7 Nm to 8.1 Nm in joint torques and 35.8 N to 130.8 N in muscle forces. Soft tissue artifacts were identified as the main contributor to uncertainty propagation.

All of these studies assessed uncertainties and sensitivities for walking motions mainly performed by male subjects. A comparison between the results is rather difficult because each investigation considered a different set of uncertainty sources and applied different assumptions for the uncertainties of simulation inputs which also led to partially inconsistent conclusions. The uncertainties were modeled by discrete deviations, uniform distributions or Gaussian distributions with neglecting possible correlations. These limitations potentially reduce validity and applicability for the validation of biomechanical simulations. In addition, uncertainties and sensitivities for female subjects as well as other motion tasks might differ considerably from the core findings obtained for walking with male subjects.

9.2 Contribution

The presented uncertainty and sensitivity analysis evaluates uncertainty propagation and apportionment for joint torques in hip, knee and ankle joints and three different motion tasks performed by a female and male subject. The motion tasks cover repetitive and ballistic whole-body motions at different speeds and with varying motion sequences. The considered uncertainty sources comprise anatomical landmark misplacement, soft tissue artifacts and measurement uncertainties in force plate measurements as well as variations in regression parameters for joint center and anthropometric parameter estimation. The applied statistical models for the regarded uncertainties were derived from experimental investigations with the actual subjects and measurement systems or from comprehensive simulation studies based on reasonable statistical properties reported in literature. In contrast to previous studies, possible correlations among uncertain simulation inputs and model parameters are considered in all steps of the inverse dynamics procedure. The identified uncertainties allow to assess the credibility and accuracy of the simulation results in this and similar biomechanical simulations. The corresponding sensitivities enable to recognize uncertainty sources with particularly high influence. This information provides novel insights to improve the quality of biomechanical measurements and model parameter estimation and facilitates the validation of biomechanical simulations.

9.3 Uncertainty and Sensitivity Analysis

The uncertainty and sensitivity analysis has been performed for the repetitive motion tasks straight walking at 1.5 m/s and straight running at 3.0 m/s as well as the ballistic motion task kicking a ball performed by a healthy female subject (27 yrs, 161 cm, 57 kg) and healthy male subject (32 yrs, 179 cm, 85 kg). The inverse dynamics simulation was applied for one arbitrary

selected event per motion task. In the walking and running trials, this event is the gait cycle starting with the tenth heel strike of the right foot, while the fifth kick was selected in the kicking a ball trial. The examined joint torques in the inverse dynamics simulation comprise hip, knee and ankle torques about the local z-axes of the right leg. If hip abduction and rotation remain small which is the case for walking and running, leg motions about the local z-axes are approximately congruent with the sagittal plane. Details on the biomechanical measurements including the measurement protocol and data processing are provided in Chapter 5.

For the analysis, the modeling and simulation framework described in Chapter 3 and the uncertainty and sensitivity framework described in Chapter 4 have been applied by incorporating the determined statistical models for anatomical landmark misplacement, soft tissue artifacts and the measurement uncertainty of the instrumented treadmill presented in Chapter 6 as well as the regression parameters in joint center and anthropometric parameter estimation presented in Chapter 7 and 8. In anatomical landmark misplacement, the uncertainties obtained in the reproducibility experiments which denote the inter-examiner precision were used. To reduce the computation time, only anatomical landmarks on pelvis, thigh, shank and foot segments were perturbed and the three-dimensional sampling points of the surrounding skin surface were not considered. For the joint center estimation, spatial positions of the involved anatomical landmarks were calculated by averaging the motion capture data over four seconds during the initial idle time of the particular motion task. The length of the head segment was approximated by subtracting the vertical coordinate of the estimated lower neck joint from the measured body height. The measurement uncertainty for the body height was assumed to follow a Gaussian distribution with a standard deviation of 5.0 mm. For the wobbling mass parameters including mass ratio, natural frequency and damping coefficient, a Gaussian distribution with a standard deviation of 10 % relative to the reported reference value was presumed. The filtered ground reaction forces were filtered once more using a fourth order zero-lag low-pass filter with a cut-off frequency of 20 Hz. A spline interpolation was used to normalize each marker trajectory in time relative to the length of the motion sequence. Each normalized marker trajectory contained 101 frames describing the percentage of the motion sequence ranging from 0 % to 100 % with a constant sampling time. To improve the stability of the proportional-derivative control approach that calculated the joint forces and torques in the base joint, the joint trajectories and ground reaction forces were sampled up to 301 frames for the actual hybrid dynamics simulation. Subsequently, the resulting joint torques were sampled back down to 101 frames. For the integration in the hybrid dynamics simulation, a trapezoidal rule approach was implemented. Due to the relatively low mass of the used ball, the interactions during ball impact and the ball mass are neglected in the biomechanical dynamics simulations of the kicking motion. Also, the mass of the measurement equipment including markers and electrodes was neglected.

In each trial of the Monte Carlo simulation, a sample of the considered uncertainties was drawn from the specified distributions and applied to the inverse dynamics procedure. The uncertainty of the resulting joint torques in each frame was modeled by an appropriate Johnson distribution and sensitivities were rated through the first-order and total-effect sensitivity indices. In rare cases, the hybrid dynamics simulation became unstable which was detected through excessive amplitudes and first-order derivatives in the estimated joint torques. Simulation results of unstable trials were excluded from the uncertainty and sensitivity analysis. Each run of the inverse dynamics procedure had a computation time of about five seconds due to the rather slow forward kinematics simulation with ADOL-C integration for the extended Kalman

smoother. Therefore, the maximum number of trials in the Monte Carlo simulation was restricted to 60,000 trials for the uncertainty analysis which equivalents to 30,000 trials for the sensitivity analysis and a computation time of about eight days for each motion task and subject on the parallel computing cluster presented in Chapter 4. In addition, the threshold limit was set to $5 \cdot 10^{-4}$ for uncertainty convergence and $5 \cdot 10^{-3}$ for sensitivity convergence. The individual batches comprised 500 trials. In total, the sensitivity analysis had 255 input variables and 303 output variables.

9.4 Results

All Monte Carlo simulations executed the maximum number of 60,000 trials without reaching the specified convergence limits. Nevertheless, it is assumed that the convergence reached a sufficient level for a fundamental evaluation since the changes in the most relevant sensitivity indices for all motion tasks were less than 2.0 % in the last trial. The number of failed trials was below 0.5 % for all motion tasks. In order to facilitate a comparison between the female and male subject, the joint torques τ in hip, knee and ankle joints have been divided by a multiplication of body height (BH), body mass (BM) and gravity (g) yielding the relative torque $\hat{\tau}$. The relative deviation $\hat{\epsilon}_{95}$ is specified as the difference between the median value and the limit value of the 95 % probability interval. Sensitivity is given by the sensitivity indices S that equal to the normalized first-order indices, where all first-order indices were set to zero that had a vanishing total-effect index after rounding to four decimal places. The individual sensitivities have been grouped into seven categories which contain related uncertainty sources, i.e.,

- body measurements (BOM),
- force plate measurements (FOM)
- regression parameters for anthropometric parameter estimation (ANP)
- regression parameters for joint center estimation (JOC),
- anatomical landmark identification (ALI),
- wobbling mass parameters (WOM) and
- soft tissue artifacts (STA),

where the body measurements category contains uncertainties in body mass and body height.

Table 9.1.: Summary statistics of the uncertainty analysis in the walking motion performed by the female subject with the relative deviation $\hat{\epsilon}_{95}$ given in percent.

	Stance phase			**Swing phase**		
Joint	$\lvert\hat{\epsilon}\rvert_{95,\max}$	$\lvert\hat{\epsilon}\rvert_{95,\min}$	$\lvert\hat{\epsilon}\rvert_{95,\text{avg}}$	$\lvert\hat{\epsilon}\rvert_{95,\max}$	$\lvert\hat{\epsilon}\rvert_{95,\min}$	$\lvert\hat{\epsilon}\rvert_{95,\text{avg}}$
HJ	4.6703	0.6765	2.8623	2.3189	0.6003	1.2478
KJ	3.2117	0.2490	2.1024	0.6502	0.1083	0.2891
AJ	3.1572	0.0982	1.8271	0.0114	0.0016	0.0041

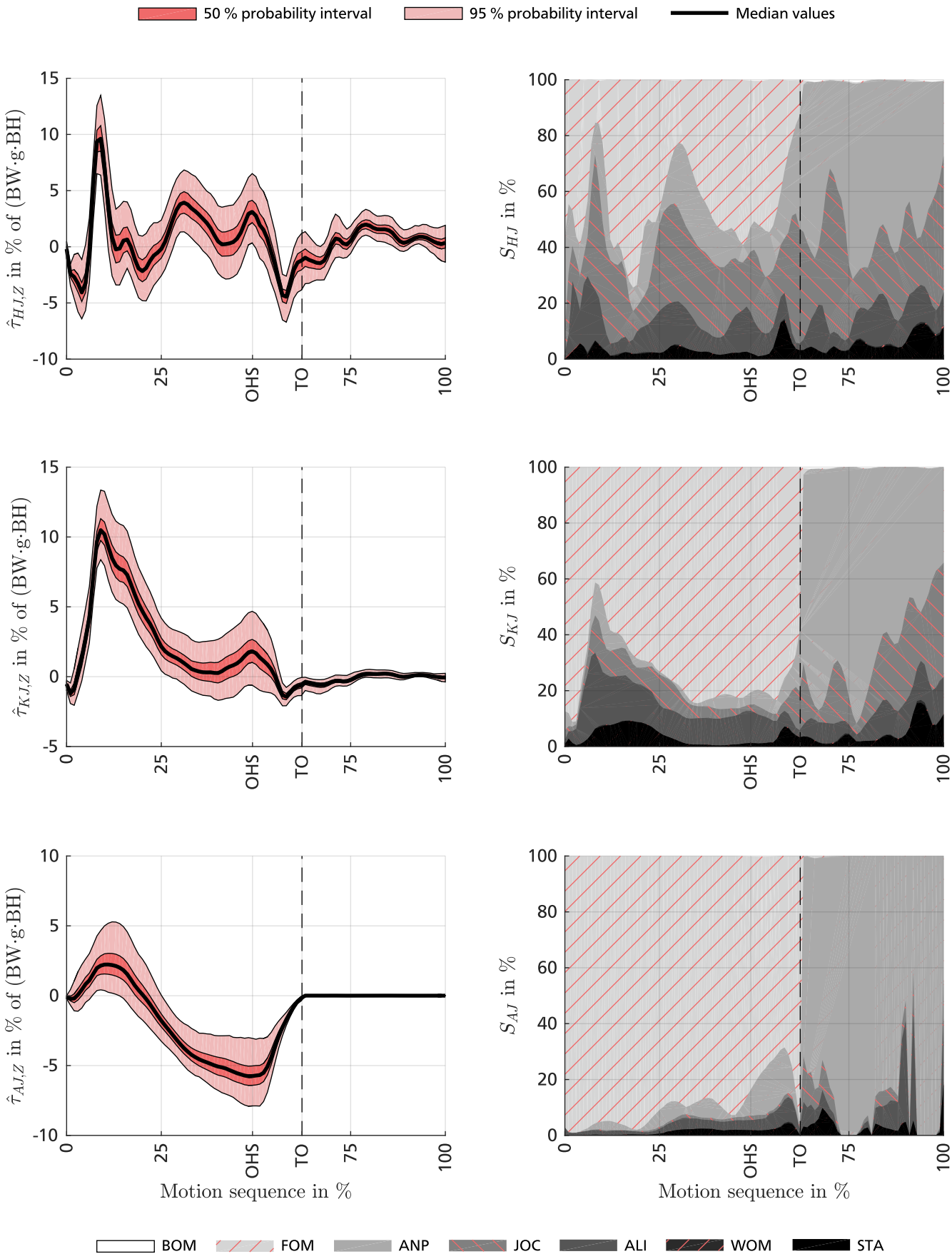

Figure 9.2.: Results of the uncertainty and sensitivity analysis in the walking motion performed by the female subject with the relative joint torques $\hat{\tau}$ and sensitivity indices S.

9.4.1 Walking

The results of the uncertainty and sensitivity analysis for the walking motion are presented in Figure 9.2 for the female subject and Figure 9.3 for the male subject. The dashed black line divides the motion sequence at toe off (TO) in stance and swing phase. Following the structure of a box plot, the bold black line in the left diagrams shows the median value, whereas the colored areas describe probability intervals of 50 % and 95 % for the individual Johnson distributions in each frame. The maximum, minimum and average values of the relative deviation for stance and swing phase in each joint are listed in Table 9.1 for the female subject and Table 9.2 for the male subject.

The fundamental shapes of the relative joint torques shown in the left diagrams are quite similar for both subjects. The largest peak torque occurs in the knee joint with reaching 94.4 Nm in median for the female subject and 143.7 Nm in median for the male subject. The negative peak torques in the ankle joint near the opposite heel strike (OHS) that initialize the push off motion are comparatively small with -51.9 Nm in median for the female subject and -92.8 Nm in median for the male subject. Regarding the uncertainty, there is a clear difference between the stance and swing phase. While there is an essential dispersion during the stance phase in all joints, the variance in knee and ankle joints is much lower during the swing phase. For the hip joint, the contrast between stance and swing phase is rather small. This finding is supported by the averaged relative deviations. The deviations also indicate that the relative uncertainty is higher for the female subject in the stance phase, while it is greater for the male subject in the swing phase. During the stance phase, the maximum deviation which can be regarded as an upper bound for the uncertainty reaches 42.0 Nm for the female subject and 80.5 Nm for the male subject. The maximum deviation in the swing phase amounts to 20.9 Nm for the female subject and 54.4 Nm for the male subject. In both phases, the uncertainty is higher for more proximal joints.

The clear difference between the two phases is also evident in the results of the sensitivity analysis presented as continuously stacked bar graphs in the right diagrams. During the stance phase, the uncertainties of the force plate measurements have the greatest impact on all joint torques for both subjects. Particularly, the variation of the center of pressure in the x-axis is by far greatest contributor. In the hip and knee joints, the share of the center of pressure is smaller and also uncertainties in anatomical landmark identification as well as the regression parameters for joint center and anthropometric parameters estimation have a considerable in-

Table 9.2.: Summary statistics of the uncertainty analysis in the walking motion performed by the male subject with the relative deviation $\hat{\epsilon}_{95}$ given in percent.

	Stance phase			**Swing phase**		
Joint	$\lvert\hat{\epsilon}\rvert_{95,\max}$	$\lvert\hat{\epsilon}\rvert_{95,\min}$	$\lvert\hat{\epsilon}\rvert_{95,\text{avg}}$	$\lvert\hat{\epsilon}\rvert_{95,\max}$	$\lvert\hat{\epsilon}\rvert_{95,\min}$	$\lvert\hat{\epsilon}\rvert_{95,\text{avg}}$
HJ	5.3906	0.5657	2.7364	3.6450	0.9763	1.8562
KJ	3.0404	0.2132	1.7323	0.9286	0.2328	0.4821
AJ	2.8029	0.0852	1.6588	0.0238	0.0031	0.0095

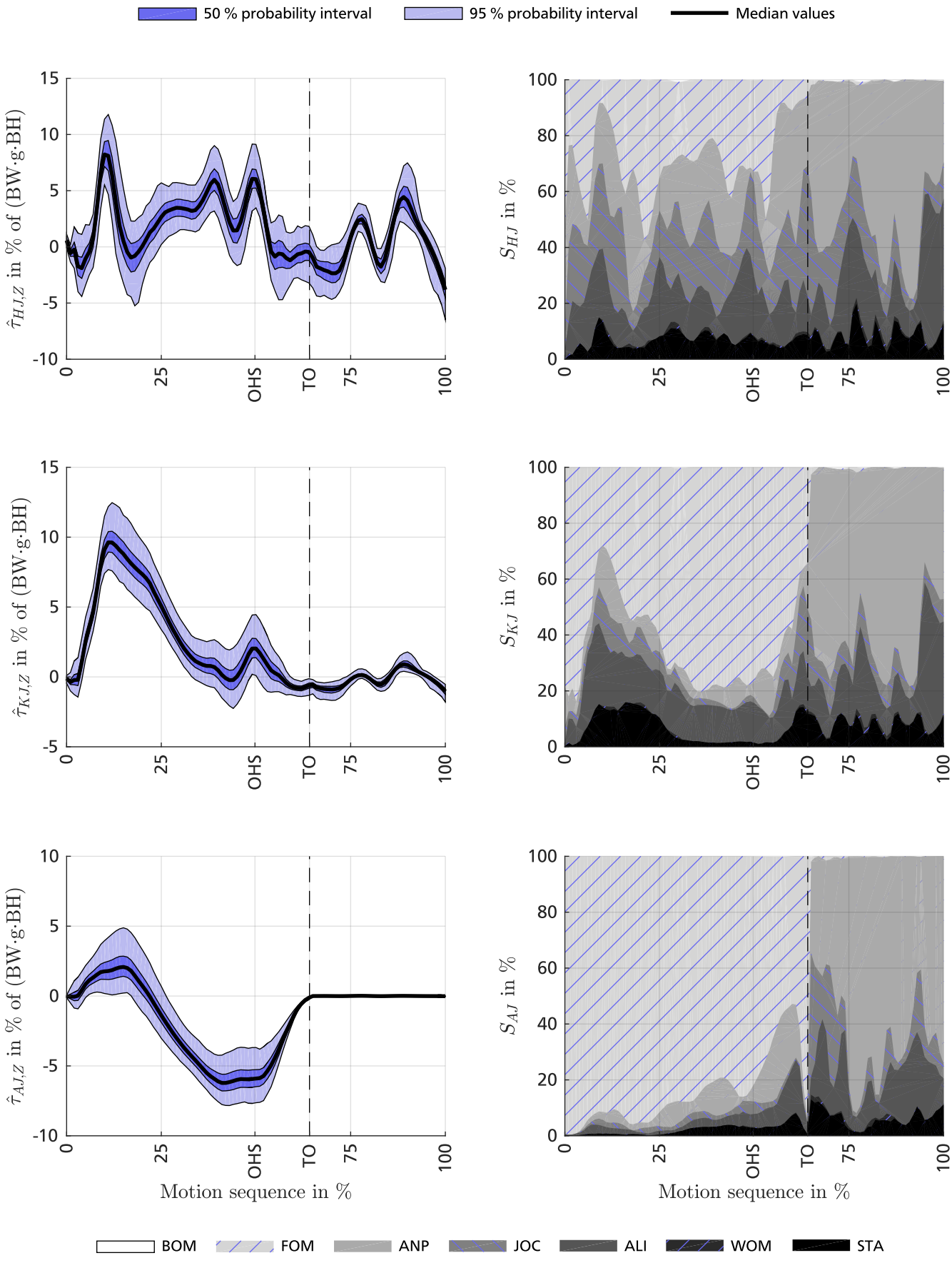

Figure 9.3.: Results of the uncertainty and sensitivity analysis in the walking motion performed by the male subject with the relative joint torques $\hat{\tau}$ and sensitivity indices S.

fluence. The hip joint torque is notably sensitive to the regression parameter for hip joint center estimation in the x-axis, while the variability of the knee joint torque is eminently affected by anatomical landmark misplacement in the MFC and LFC landmarks. In the swing phase, the ground reaction forces act on the other foot and therefore the impact abruptly disappears. Instead, uncertainties in anthropometric parameter estimation have the greatest share in all joints for both subjects. The main contributors are the regression parameters for the segment masses in thigh, shank and foot. Because the joint torque and the associated uncertainty in the ankle joint are very small during the swing phase, the respective sensitivities are of little relevance. Similar to the stance phase, the regression parameter for hip joint center estimation in the x-axis has a considerable influence on the hip joint torque. In contrast to the male subject, the estimated knee joint torque of the female subject is particularly sensitive to regression parameters for hip and knee joint estimation. Soft tissue artifacts only have a minor effect in both phases, whereas uncertainties in the body measurements and wobbling mass parameters are completely irrelevant.

9.4.2 Running

The results of the uncertainty and sensitivity analysis for the running motion are presented in Figure 9.4 for the female subject and Figure 9.5 for the male subject. The dashed black line divides the motion sequence at toe off (TO) in stance and swing phase. Following the structure of a box plot, the bold black line in the left diagrams shows the median value, whereas the colored areas describe probability intervals of 50 % and 95 % for the individual Johnson distributions in each frame. The maximum, minimum and average values of the relative deviation for stance and swing phase in each joint are listed in Table 9.3 for the female subject and Table 9.4 for the male subject.

The shapes of the relative joint torques for both subjects shown in the left diagrams have some distinctive differences in the hip joint, whereas knee and ankle joint torques are rather similar. The three peaks during the first 25 % of the motion sequence in the hip joint torque of the male subject coincide with changes in the hip joint acceleration. This difference between the subjects is also adumbrated in the joint position trajectories presented in Chapter 5. The largest peak torques are found in the knee joint with reaching 135.6 Nm in median for the female subject and 250.6 Nm in median for the male subject. The negative peak torques in the ankle joint that initialize the push off motion account to -99.6 Nm in median for the female subject and -176.7 Nm in median for the male subject. Regarding the uncertainty, the clear difference

Table 9.3.: Summary statistics of the uncertainty analysis in the running motion performed by the female subject with the relative deviation $\hat{\epsilon}_{95}$ given in percent.

	Stance phase			**Swing phase**		
Joint	$\lvert\hat{\epsilon}\rvert_{95,\max}$	$\lvert\hat{\epsilon}\rvert_{95,\min}$	$\lvert\hat{\epsilon}\rvert_{95,\text{avg}}$	$\lvert\hat{\epsilon}\rvert_{95,\max}$	$\lvert\hat{\epsilon}\rvert_{95,\min}$	$\lvert\hat{\epsilon}\rvert_{95,\text{avg}}$
HJ	8.2095	0.4376	4.7296	4.6884	1.1732	2.2507
KJ	5.6930	0.2687	3.1601	0.9768	0.1301	0.4109
AJ	5.6393	0.0937	2.8585	0.2388	0.0032	0.0065

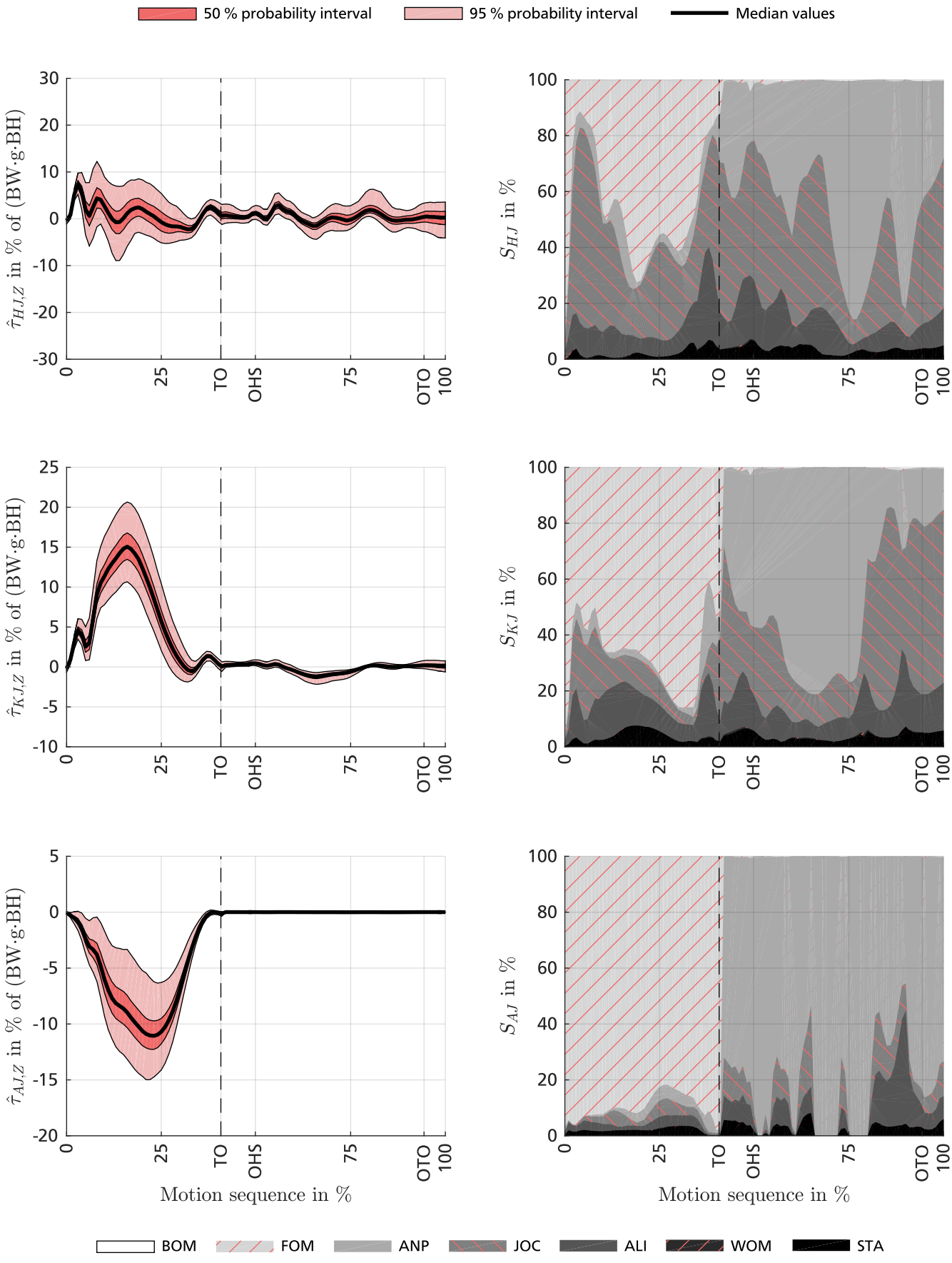

Figure 9.4.: Results of the uncertainty and sensitivity analysis in the running motion performed by the female subject with the relative joint torques $\hat{\tau}$ and sensitivity indices S.

between the stance and swing phase, especially in knee and ankle joints, is also evident for the running motion. There is a substantial dispersion during the stance phase in all joints, while the variations are much lower during the swing phase which is also supported by the averaged relative deviations. These deviations indicate again that the relative uncertainty is greater for the female subject in the stance phase, while it is higher for the male subject in the swing phase. During the stance phase, the maximum deviation which can be considered as an upper bound for the uncertainty reaches 73.9 Nm for the female subject and 175.7 Nm for the male subject. In the swing phase, the maximum deviation amounts to 42.2 Nm for the female subject and 88.9 Nm for the male subject. Similar to the walking motion, the uncertainty is higher for more proximal joints.

The results of the sensitivity analysis presented as continuously stacked bar graphs in the right diagrams also reflect the clear difference between the two phases. In the stance phase, the uncertainties of the force plate measurements have the greatest influence on all joint torques for both subjects, where the variability of the center of pressure in the x-axis again has the greatest share. Besides the center of pressure, the hip and knee joint torques are furthermore sensitive to uncertainties in anatomical landmark identification as well as the regression parameters for joint center and anthropometric parameters estimation. The three remarkable peaks regarding the uncertainties of anthropometric parameters marked by white stars in the bar graph for the hip joint of the male subject correspond to the peaks in hip joint acceleration. The effect mainly involves the regression parameters for the segment masses in shank and foot. This observation indicates that variations in inertial parameters become more important for motions with high accelerations. In addition, the variance of the hip joint torque for both subjects is particularly affected by the regression parameter for hip joint center estimation in the x-axis. The uncertainty of the knee joint torque is notably sensitive to variations in the regression parameter for knee joint estimation as well as anatomical landmark misplacement in the MFC and LFC landmarks. The swing phase in the running motion is initiated by the double float phase where no foot is in contact with the ground. As a consequence, the impact of the ground reaction forces abruptly disappears in the swing phase and the uncertainties in anthropometric parameter and joint center estimation have the greatest share in all joints for both subjects. The regression parameters for the segment masses in thigh, shank and foot as well as for hip joint center estimation in the x-axis are the main contributors. Similar to the walking motion, the joint torque and the associated uncertainty in the ankle joint are very small during the swing phase and the respective sensitivities have no actual relevance. Soft tissue artifacts are present

Table 9.4.: Summary statistics of the uncertainty analysis in the running motion performed by the male subject with the relative deviation $\hat{\epsilon}_{95}$ given in percent.

	Stance phase			Swing phase		
Joint	$\lvert\hat{\epsilon}\rvert_{95,\max}$	$\lvert\hat{\epsilon}\rvert_{95,\min}$	$\lvert\hat{\epsilon}\rvert_{95,\text{avg}}$	$\lvert\hat{\epsilon}\rvert_{95,\max}$	$\lvert\hat{\epsilon}\rvert_{95,\min}$	$\lvert\hat{\epsilon}\rvert_{95,\text{avg}}$
HJ	11.7686	0.3150	4.5113	5.9564	1.1840	2.9181
KJ	4.7686	0.2229	2.5666	2.0734	0.3407	0.6376
AJ	4.5514	0.1012	2.0847	0.2691	0.0045	0.0128

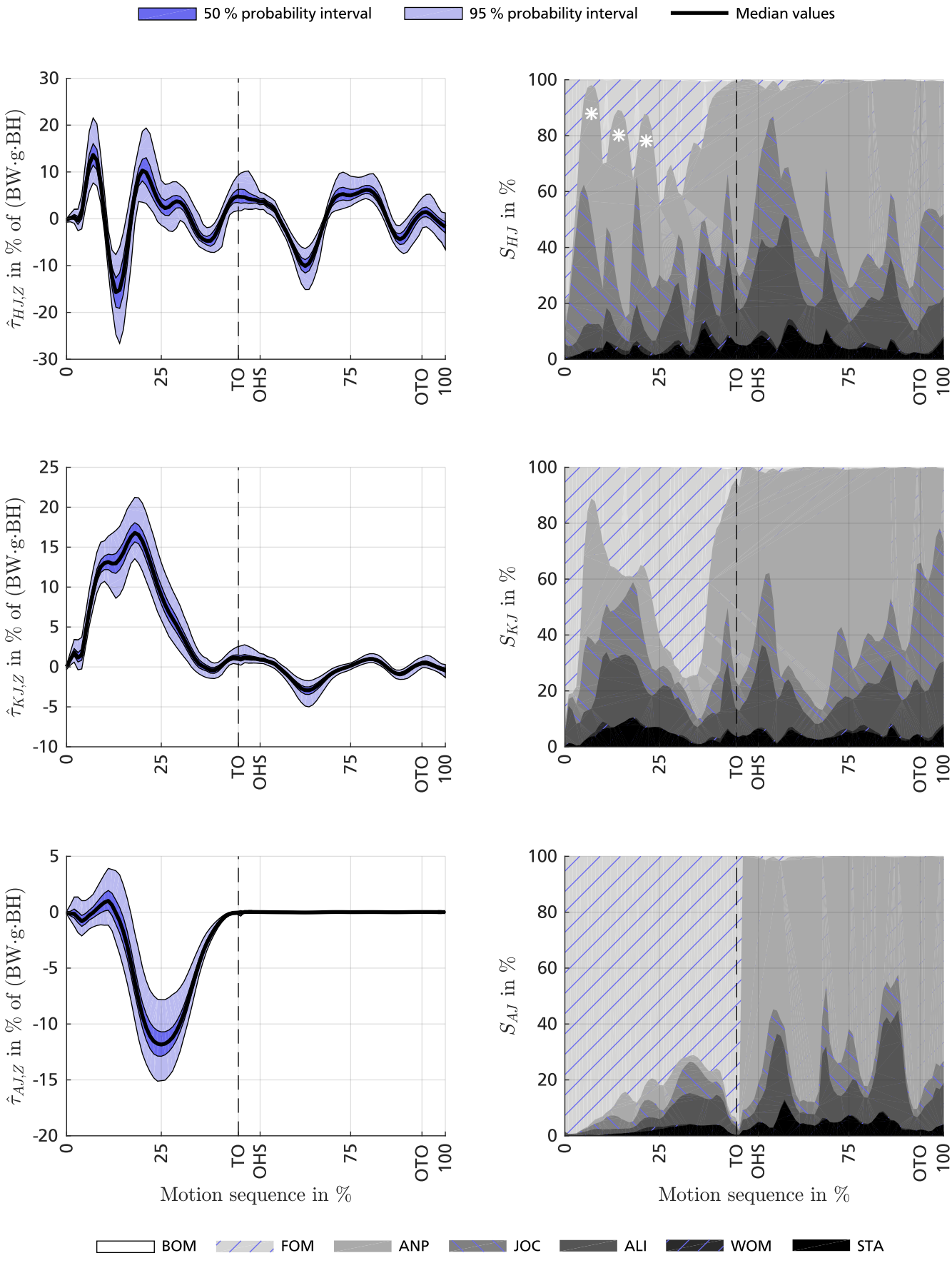

Figure 9.5.: Results of the uncertainty and sensitivity analysis in the running motion performed by the male subject with the relative joint torques $\hat{\tau}$ and sensitivity indices S.

in both phases but have no significant effect, while uncertainties in the body measurements and wobbling mass parameters are again completely irrelevant.

9.4.3 Kicking a Ball

The results of the uncertainty and sensitivity analysis for the kicking a ball motion are presented in Figure 9.6 for the female subject and Figure 9.7 for the male subject. The dashed black line divides the motion sequence at the reversal point of the hip joint position trajectory after the kick in a forward swing and backward swing phase. Following the structure of a box plot, the bold black line in the left diagrams shows the median value, whereas the colored areas describe probability intervals of 50 % and 95 % for the individual Johnson distributions in each frame. The maximum, minimum and average values of the relative deviation for both phases and each joint are listed in Table 9.5 for the female subject and Table 9.6 for the male subject.

In opposite to walking and running, the kicking a ball motion does not involve any change between a stance and swing phase. The considered right leg is never in contact with the ground but performs a fast and powerful swing forward ensued by the ball impact (BI) and follow through as well as the rather slow swing back. For this reason, the motion sequence is partitioned into a forward swing and backward swing phase. The shapes of the relative joint torques for both subjects shown in the left diagrams are quite different which suggests fairly individual kicking techniques as also evident from the joint position trajectories presented in Chapter 5. Whereas the joint torques of the female subject are rather flat beside the small peaks in ankle joint around the ball impact, the joint torques of the male subject have some distinct peaks near the ball impact and the reversal point. The three peaks in the ankle joint coincide with three peaks in ankle joint acceleration. The swing motion is mainly performed by the hip joint resulting in the largest peak torques of up to 49.1 Nm in median for the female subject and 130.4 Nm in median for the male subject. The motions and joint torques in the ankle joint are relatively small, where the peak torques reach 0.356 Nm in median for the female subject and 1.115 Nm in median for the male subject. This observation implies a small influence of the actual ball impact and justifies the neglect of the ball mass in the dynamics simulation. Regarding the uncertainty, the difference between the two phases is rather marginal for hip and knee joints but clearly distinct in the ankle joint which is also indicated by the averaged relative deviations. The relative uncertainty is greater for the male subject in all joints and both phases. During the swing forward phase, the maximum deviation which can be considered as an upper bound for the uncertainty is 30.9 Nm for the female subject and 110.6 Nm for the male subject. In the swing back phase,

Table 9.5.: Summary statistics of the uncertainty analysis in the kicking a ball motion performed by the female subject with the relative deviation $\hat{\epsilon}_{95}$ given in percent.

	Swing forward phase			**Swing back phase**		
Joint	$\lvert\hat{\epsilon}\rvert_{95,\max}$	$\lvert\hat{\epsilon}\rvert_{95,\min}$	$\lvert\hat{\epsilon}\rvert_{95,\text{avg}}$	$\lvert\hat{\epsilon}\rvert_{95,\max}$	$\lvert\hat{\epsilon}\rvert_{95,\min}$	$\lvert\hat{\epsilon}\rvert_{95,\text{avg}}$
HJ	3.4353	0.4726	1.7681	2.8595	0.5632	1.4442
KJ	0.7329	0.1007	0.3220	0.7169	0.1290	0.3010
AJ	0.0554	0.0025	0.0105	0.0090	0.0010	0.0029

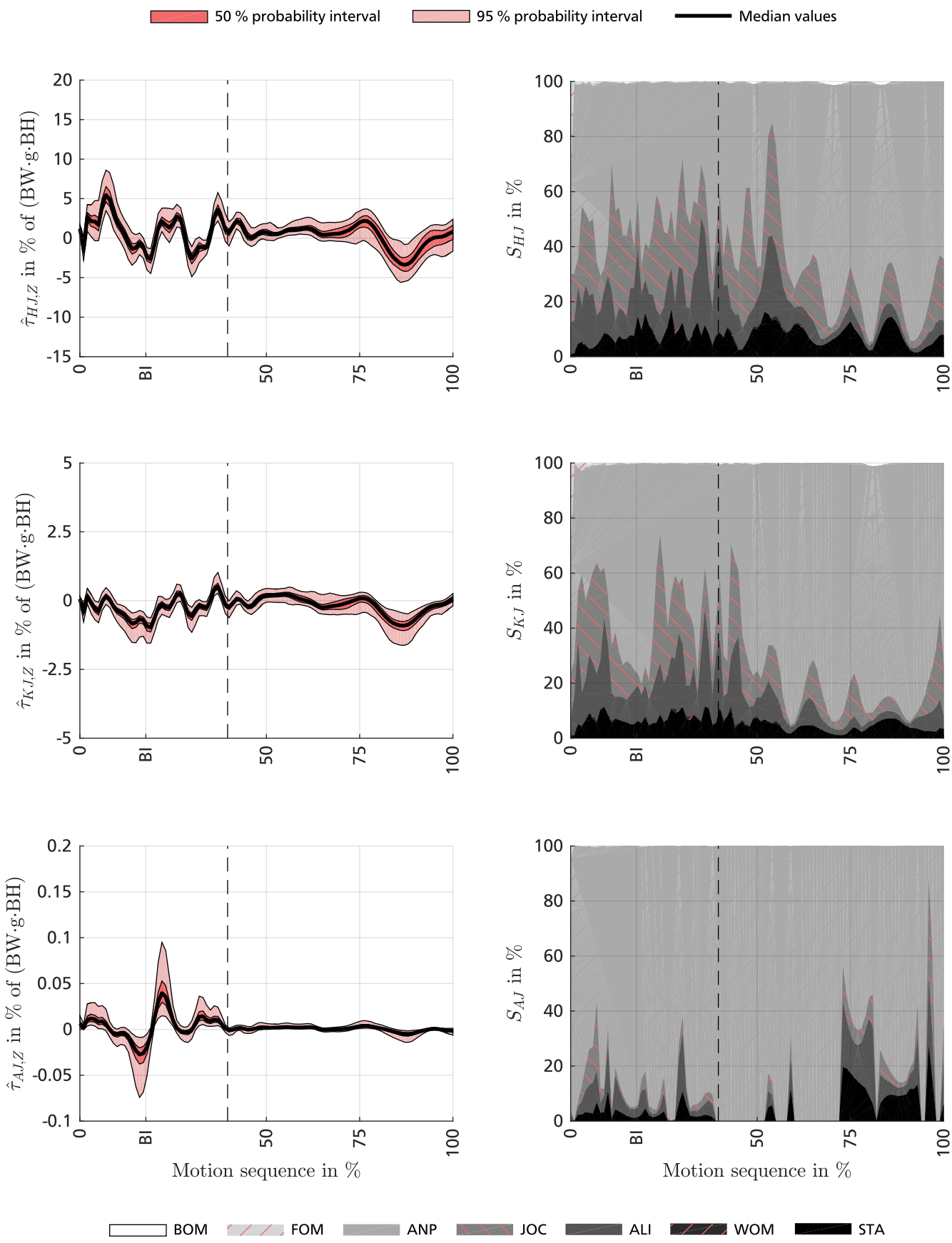

Figure 9.6.: Results of the uncertainty and sensitivity analysis for kicking a ball performed by the female subject with the relative joint torques $\hat{\tau}$ and sensitivity indices S.

the maximum deviation reaches 25.7 Nm for the female subject and 149.4 Nm for the male subject. Similar to the walking and running motions, the uncertainty is higher for more proximal joints.

The results of the sensitivity analysis presented as continuously stacked bar graphs in the right diagrams confirm the essential resemblance between swing forward and swing back phase. As in the swing phases of the walking and running motions, the uncertainties in the regression parameters for anthropometric parameter and joint center estimation as well as anatomical landmark identification have the greatest influence. Particularly, the regression parameters for the segment masses in thigh, shank and foot as well as for hip joint center estimation in the x-axis and knee joint center estimation are the main contributors in the hip and knee joints. For the ankle joint, variations in the regression parameters for the inertial parameters of the foot segment including the moments and products of inertia about the z- and y-axis as well as the segment mass have the largest impact. With regard to anatomical landmark misplacement, the hip and knee joint torques are furthermore sensitive to uncertainties in the MFC and LFC landmarks, while the ankle joint torque of the male subject is affected by a variability in the CAL and MT5 landmarks. The three peaks pertaining to the uncertainties of anthropometric parameters marked by white stars in the bar graph for the ankle joint of the male subject correspond to the peaks in ankle joint acceleration. Also in the bar graph for the ankle joint of the female subject, two smaller peaks of this type can be found near the ball impact. These observations yet again suggest that variations in inertial parameters have a higher share for motions with high accelerations. Soft tissue artifacts are present in both phases and have a slightly larger effect than in the other motion tasks. Uncertainties in the body measurements and wobbling mass parameters are again completely insignificant.

9.5 Discussion

The uncertainty analysis reveals substantial uncertainties in the joint torque estimates of hip, knee and ankle joint for both subjects in the considered motion tasks. There is a clear difference between phases involving ground reaction forces and phases with pure swing motions. For the walking and running motions, the joint torques exhibit much greater uncertainties during the stance phase than in the swing phase, where larger joint torques also induced larger uncertainties. The observed upper bounds for the deviations relative to the multiplication of body height, body mass and gravity reach 4.7 % for the female subject and 5.4 % for the male subject in the walking motion as well as 8.2 % for the female subject and 11.8 % for the male subject in the

Table 9.6.: Summary statistics of the uncertainty analysis in the kicking a ball motion performed by the male subject with the relative deviation $\hat{\epsilon}_{95}$ given in percent.

	Swing forward phase			**Swing back phase**		
Joint	$\lvert\hat{\epsilon}\rvert_{95,\max}$	$\lvert\hat{\epsilon}\rvert_{95,\min}$	$\lvert\hat{\epsilon}\rvert_{95,\text{avg}}$	$\lvert\hat{\epsilon}\rvert_{95,\max}$	$\lvert\hat{\epsilon}\rvert_{95,\min}$	$\lvert\hat{\epsilon}\rvert_{95,\text{avg}}$
HJ	7.4076	0.3213	2.3957	10.0083	0.9401	2.6316
KJ	1.7308	0.0844	0.5854	1.9890	0.2095	0.6838
AJ	0.1136	0.0028	0.0179	0.0219	0.0017	0.0072

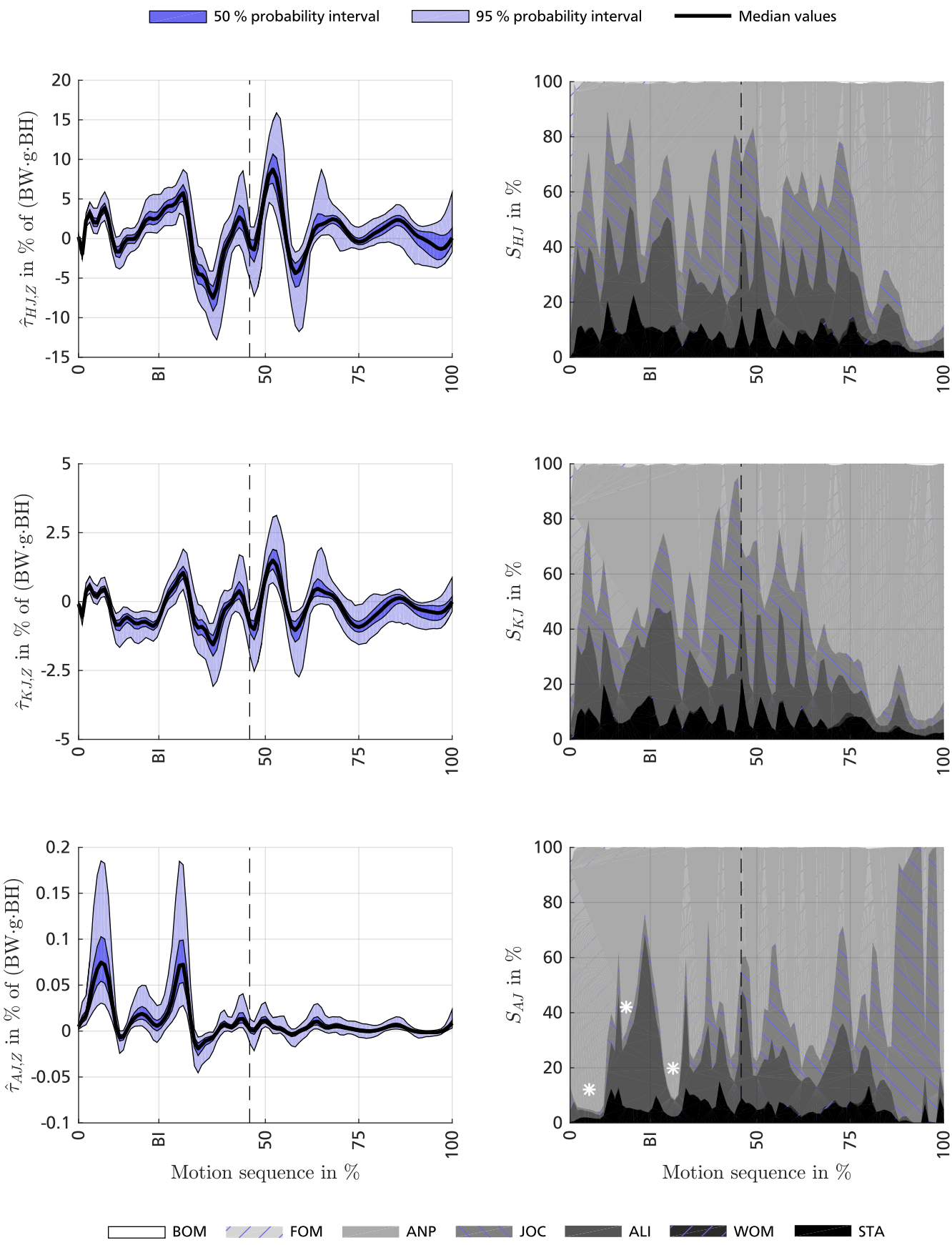

Figure 9.7.: Results of the uncertainty and sensitivity analysis for kicking a ball performed by the male subject with the relative joint torques $\hat{\tau}$ and sensitivity indices S.

running motion. The uncertainties in the kicking a ball motion vary for both subjects due to rather individual kicking techniques. The observed upper bounds for the relative deviations are 3.3 % for the female subject and 10.0 % for the male subject. A notable difference between the swing forward and swing back phases is only evident for the ankle joint. Deviations of these magnitudes in joint torque estimates can have a significant impact on derived scientific conclusions, engineering designs and clinical decisions. Especially, quantitative evaluations of the uncertain joint torques such as a subsequent estimation of muscle forces or the dimensioning of actuation concepts for assistive devices are affected by the potential discrepancies.

The clear difference between phases with and without ground contact is also evident in the results of the sensitivity analysis. During stance phase, the variations of the force plate measurements exhibit the greatest influence on the observed joint torque uncertainties, while the variances in the regression parameters for anthropometric parameter estimation have the highest share in swing phase. The by far largest contributors in the individual phases are the variability of the center of pressure in the x-axis as well as the variation of the regression parameters for the segment masses in thigh, shank and foot. Particular acceleration peaks in the running and kicking a ball motions indicated an increased sensitivity to uncertainties in inertial parameters for motion tasks with higher accelerations. With varying extent, the uncertainties of the hip and knee joint torques are also notably sensitive to variances of the regression parameters in joint center estimation as well as anatomical landmark misplacement. The involved regression parameters and anatomical landmarks are all exclusively related to the joints and body segments of the considered right leg. Soft tissue artifacts are present in both phases but only have a minor effect. This finding demonstrates the capability and efficiency of the extended Kalman smoother since soft tissue artifacts are usually regarded as one of the most relevant uncertainty sources, e.g. [98, 130]. In all motion tasks, variations in the body measurements and wobbling mass parameters do not have any significant share in the joint torque uncertainties. The order of the identified sensitivities is mostly identical for both subjects. In this context, it is important to note that small sensitivities for specific input variables or model parameters do not also imply a reduced importance for the inverse dynamics simulation. A low sensitivity index just means that the particular input variable or model parameter can change within the specified uncertainty distribution without having a substantial impact on the simulation results. In summary, well-calibrated force plates, improved regression models for anthropometric parameter and joint center estimation as well as a careful identification of the involved anatomical landmarks are recognized as the most important prerequisites for more accurate inverse dynamics simulations in human motion analysis.

The comparison between the female and male subject indicates a larger uncertainty for the female subject during the stance phase, while the uncertainty is higher for the male subject during the swing phase which also includes the kicking a ball motion. This observation could result from a different impact of the variations in the center of pressure as the greatest contributor to joint torque uncertainties in the stance phase. The joint torques and hence also the involved uncertainties of the male subject are commonly greater due to a larger body mass and longer body segments in the legs. This relation between body measurements and observed uncertainties is nonlinear and cannot be fully compensated with a normalization by body mass and body height. For this reason, the absolute and relative uncertainties can be expected to be generally higher for the male subject. During the stance phase, the magnitudes of the variations in the center of pressure measurements are the same for both subjects. Because of the shorter female

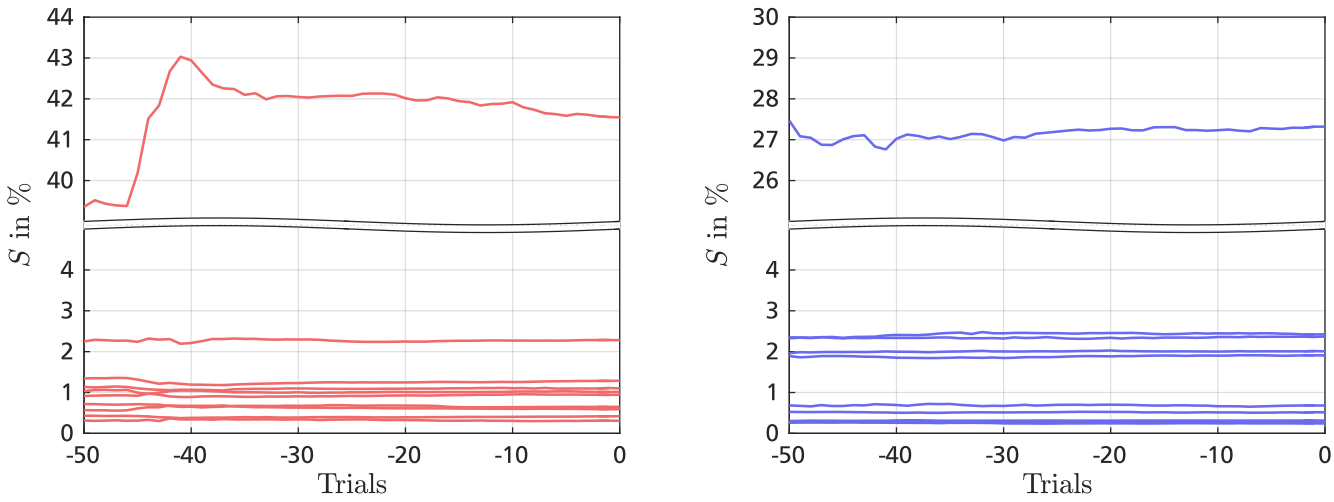

Figure 9.8.: Progress of the ten most relevant sensitivity indices S in the walking motion over the last fifty trials for the female subject (left) and male subject (right).

foot segment, the impact of a particular variation is comparatively greater and therefore leads to higher variances in the joint torques. This effect could exceed the fundamentally higher uncertainties in the male subject and cause the different results for phases with and without ground contact.

Furthermore, the results show that the variances in proximal joints are generally greater than in more distal joints. This finding directly follows from the characteristic propagation of forces in an open kinematic chain. Starting with the most distal body segment, external and internal forces as well as the associated uncertainties are recursively accumulated for the following more proximal body segments. In this way, the uncertainties continuously increase in proximal direction and are reflected in the corresponding joint torques.

A potential limitation of the presented uncertainty and sensitivity analysis for the walking motion is the existent difference between the found peak torques and torque apportionment compared to reported reference values in literature. For example, the averaged measurements with twenty-one female and male subjects (25.4 yrs, 173.0 cm, 70.9 kg) for walking at 1.6 m/s provided by Lipfert [136] yield a peak torque of 62.2 Nm in the knee joint and -108.7 Nm in the ankle joint. The found median peak torques in the knee joint are considerably larger with 94.4 Nm for the female subject and 143.7 Nm for the male subject, whereas the negative median peak torques in the ankle joint only reach -51.9 Nm for the female subject and -92.8 Nm for the male subject. Since the measurements by Lipfert were also taken on an instrumented treadmill but with the subjects wearing athletic footwear, these differences could be an indication for deviations from the regular gait pattern during barefoot walking on an instrumented treadmill. A further reason could be the individual characteristic of a single gait cycle performed by a single subject as against an averaged gait cycle over several steps and different subjects. In any case, the presented results are not based on an entirely typical gait cycle for a walking motion. Another possible restriction is the termination of the Monte Carlo simulation after 60,000 trials before the specified convergence was reached. Ongoing changes in the estimated sensitivity indices imply that the input space has not been fully covered and significant fluctuations cannot be excluded. Nevertheless, it is reasonable to assume a good approximation of the actual uncertainties and sensitivities after the applied number of trials. Figure 9.8 exemplarily shows

the progress of the ten in average most important sensitivity indices in the walking motion over the last fifty trials for the female and male subject. The sensitivity index with the highest value refers to the center of pressure in the x-axis. Nearly all of the relevant sensitivity indices reached a stable value and did not change considerably. Only the most relevant sensitivity index for the female subject performed a step of about 3.5 % and slowly decreased over the last trials. This example shows that the expectable fluctuations in the important sensitivity indices are rather small and the fundamental relations are represented by the obtained results. For future uncertainty and sensitivity analyses, the computation time might be drastically decreased by reducing the number of input variables. Since model parameters of the head, arms and the left leg had no substantial influence on the joint torque uncertainties, the related input variables could at least temporarily be neglected in further studies. Also, the computation time of the forward kinematics simulation with ADOL-C integration has potential for improvements.

It should be noted that the described uncertainty and sensitivity analysis primarily reflects uncertainty propagation and apportionment for the specific biomechanical measurements and the particular uncertainties of the applied measurement systems and data processing approaches. On one hand, most of the involved uncertainty sources are generally valid like the variations in the regression parameters for anthropometric parameter and joint center estimation or the anatomical landmark misplacement. On the other hand, some uncertainty sources depend on the actual measurement systems like the in this particular case highly critical variances of the force plate measurements with the instrumented treadmill. For this reason, the reported results do not represent a universal evaluation but rather provide a realistic example for the impact of uncertainties in a typical inverse dynamics simulation procedure. The core findings apply to this and similar biomechanical simulations and allow to evaluate the credibility and accuracy.

9.6 Conclusion

The presented uncertainty and sensitivity analysis provides an evaluation of the uncertainty propagation and apportionment for joint torques of hip, knee and ankle joints in a walking, running and kicking a ball motion performed by a female and male subject. All relevant uncertainty sources in biomechanical measurements and model parameter estimation have been incorporated into the investigation regarding potential correlations among the individual input variables. The obtained results reveal substantial uncertainties in the joint torque estimates for both subjects in the considered motion tasks. In general, higher joint torques also induced larger uncertainties. A clear difference between phases involving ground reaction forces and phases with pure swing motions has been found. The joint torque uncertainty is much greater during the stance phase than in the swing phase. Variations in the measured center of pressure and the regression parameters for anthropometric parameter estimation have been identified as the main contributors in the respective phases. Additionally, variances in the regression parameters for joint center estimation as well as anatomical landmark misplacement were found to have a considerable share with varying extent. Observed distinctions between the female and male subject can be mainly ascribed to differences in segment lengths and body mass or individual motion patterns. The presented findings apply to this and similar biomechanical simulations and give new insights into the uncertainty propagation and apportionment in the inverse dynamics simulation procedure. Based on the obtained results, adequate measures for a sustainable qual-

ity management can be derived that improve the quality of biomechanical measurements as well as model parameter estimation and facilitates the validation of biomechanical simulations.

10 Complementary Work towards Design Methodologies for Assistive Devices

Biomechanical simulations of human motions provide a versatile and powerful instrument for the design and analysis of assistive devices like prostheses or orthoses. Assistive devices for lower limbs support people with amputation or musculoskeletal diseases to restore and improve locomotion abilities. The acceptance and usability of such a technical system strongly depend on the user's ability to control and utilize the device but also to incorporate it into everyday routine locomotion. Ideally, the user regards the device as part of his own body which provides a customized, familiar and predictable behavior with autonomously supporting versatile locomotion [144]. This goal touches research questions in engineering and psychology and has been studied in an interdisciplinary group of mechanical engineers, computer scientists and psychologists in order to investigate user-centered design methodologies towards a seamless integration of assistive devices into the user's body schema [244]. The described approaches and results originate from a close collaboration with Philipp Beckerle and Stephan Rinderknecht from the Institute for Mechatronic Systems in Mechanical Engineering at Technische Universität Darmstadt, Germany, Tim Schürmann and Joachim Vogt from the Work and Engineering Psychology Group at Technische Universität Darmstadt, Germany as well as Oliver Christ from the Institute Humans in Complex Systems at Fachhochschule Nordwestschweiz, Switzerland.

A fundamental concept in the investigation of design methodologies for assistive devices is the Prosthesis-User-in-the-Loop simulator that has been developed and continuously refined to facilitate the design and optimization of lower limb prostheses considering user experience and assessment [51, 243]. The primary objective of this simulator, presented in Figure 10.1, is to provide a holistic simulation of human gait with different prostheses to the participating user. Therefore, the mechanical behavior and interactions of a simulated prosthesis as well as visual and acoustic impressions of the environment are reproduced while the user

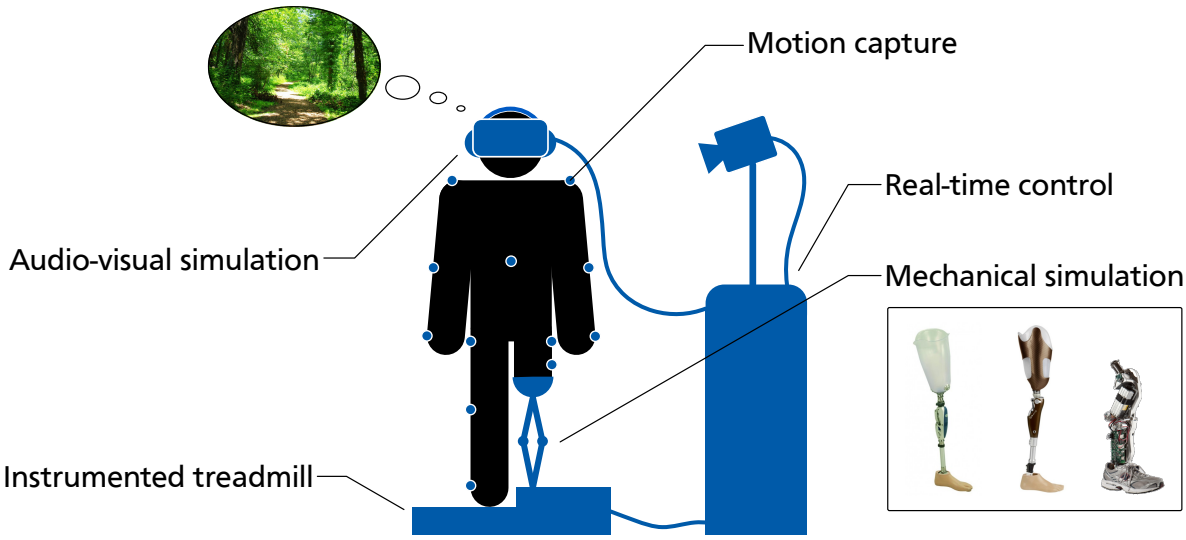

Figure 10.1.: Schematic diagram of the Prosthesis-User-in-the-Loop simulator with different types of lower limb prostheses adapted from Otto Bock and Vanderbilt University.

walks on an instrumented treadmill. A real-time control system coordinates the mechanical and audio-visual simulation based on motion capture data and ground reaction force measurements [243]. This approach supports a novel user-centered design methodology for the development of future prostheses or the analysis and optimization of existing devices by involving the users directly into the design process. The user's experiences and assessments can be determined and translated into technical design criteria by psychological methods such as psychometric questionnaires, test designs and statistical evaluation. Because the simulator does not require a hardware realization of the simulated prosthesis, users can be incorporated in fundamental research as well as the whole development process. Regarding the seamless integration into the user's body schema, the simultaneous mechanical and audio-visual simulation provides a high potential to analyze and manipulate the user's perception during everyday routine locomotion [51].

A summary of research results on central aspects in the development and evaluation of the Prosthesis-User-in-the-Loop simulator including appropriate actuation concepts for the simulator but also the simulated assistive devices, suitable approaches for mechanical and audio-visual simulation as well as relevant mechanisms and factors influencing body schema integration is provided in the remainder.

10.1 Actuation Concepts

Serial elastic actuator concepts are a promising approach to ensure inherent safety and energy efficiency in technical systems that involve close human-machine interaction like assistive devices or the presented simulator [133, 229]. Incorporated passive elastic elements reduce force peaks due to collisions or abrupt motions and have the ability to store and release energy. An additional possibility to adjust the properties of the elastic elements can further improve the performance capability as it allows to match the natural frequency of the actuator to the fundamental frequency of the desired trajectory [27]. In order to provide such a variable elastic actuator with a compact and customizable configuration, the Variable Torsion Stiffness actuator has been developed and evaluated with regard to biomechanical and medical applications [202, 203]. The actuator can adjust the stiffness of a torsional elastic element by varying the effective length via a relocatable counter bearing. This functional concept allows to impress custom stiffness characteristics or set the stiffness for power-optimal operation. To improve stiffness adaptation, systematic deviations caused by variations in material and geometry of the elastic element as well as friction in the drive train were analyzed and compensated based on experimental evaluations [24]. A nonlinear position control approach applying feedback linearization in combination with a power-optimized stiffness control was developed and evaluated to ensure an accurate and energy-efficient tracking performance for periodic motions [27]. The energy consumption is reduced by exploiting the system dynamics considering resonance and anti-resonance characteristics with tuning the stiffness according to the current system state and joint trajectory [25].

In order to investigate the impact of parallel elastic elements, a serial-parallel elastic actuation concept for an active ankle prosthesis was designed and assessed with biomechanical simulation results of human walking motions [35]. An advanced operational strategy allows to store energy in the stance phase which is released during push off to support the electrical drive. The

parallel elasticity generates up to 25 % of the required ankle torque and helps to save energy and weight due to reduced power requirements for the applied electrical drive. On the basis of this result, a systematic investigation with regard to power consumption was performed for actuator concepts with serial and parallel elasticities [26]. The results indicate that actuators with exclusive serial or parallel elasticity can minimize power consumption when the stiffness is tuned to the natural dynamics. Actuators which combine both types of elasticities do not provide further advantages regarding power consumption but might allow a more versatile stiffness adjustment. Inspired by these findings, a novel methodology for the design and optimization of elastically actuated lower limb prostheses was presented and exemplarily implemented for an active knee prosthesis [28]. This methodology incorporates actuator inertia and the inertial parameters of the prosthesis in the design process. In the first phase, the prosthesis and its elastic actuator are designed and optimized with respect to power consumption or peak power based on biomechanical simulation results obtained from healthy subjects. The designed prosthesis is implemented in a biomechanical inverse dynamics simulation by substituting the inertial properties of one leg with those of the prosthesis. In the second phase, another stiffness optimization is performed by applying the inverse dynamics simulation to revise the elastic actuator. The evaluation of the active knee prosthesis revealed a reduction of peak power by about 10 % for walking and over 30 % for running.

10.2 Mechanical Simulation

The mechanical simulation has to replicate the biomechanical interactions between the residual leg and the simulated assistive device during human gait. This task is very challenging and requires a complex mechatronic hardware and a sophisticated control strategy. In order to demonstrate the general feasibility, a reduced simulator concept for ankle motions in sagittal plane was designed and dimensioned with biomechanical simulation results for walking motions [22]. The ankle joint of healthy subjects is mechanically locked by an orthosis shoe to induce a temporary disability. The simulator restores the impaired ankle motion by controlling position and orientation of the orthosis shoe in one rotational and two translational dimensions with respect to the gait phase. An essential aspect of the control of the simulator and the study of factors for body schema integration is the imitation of postural movements. To investigate the influence of visual, tactile and proprioceptive feedback on the integration of artificial limbs, the body-proximal robot Int^{2}Bot was developed and built [21, 23]. The robot models the functionality and appearance of a human leg with thigh, shank and foot and imitates squatting motions. The movements of the robot are controlled by a computed torque control approach with friction compensation based on information acquired from a sensor orthosis with inertial measurement units worn by a subject or a depth camera. For the generation of the desired joint trajectories, several inverse kinematics approaches were evaluated and systematically compared [200]. The extended Kalman filter achieves the best overall performance in the estimation of the knee and ankle joint positions. In reference to the rubber hand illusion [36], experimental evaluations with the robot are performed by covering the human leg, while the movements of the robotic leg can be seen in a mirror [48]. Preliminary studies with five healthy subjects and an increasing visual delay indicate high values for perceived agency, whereas ownership and location are rated rather low irrespective of the visual delay.

Besides the actuation and control of the mechanical simulation, the characteristics of biomechanical interactions at the interface between the residual limb and simulator influence the experience of the user. The involved dynamic effects in the socket have been analyzed in simulation and experimentally. The simulative study applied a subject-specific inverse dynamics simulation and biomechanical measurements of healthy subjects to approximate forces and torques in sagittal plane for different residual limb lengths in walking and running motions [245]. The experimental study applied a novel measuring approach for detecting relative movements between the residual limb and the socket of a prosthesis as well as the occurring forces and torques during a walking motion at different velocities [157]. The relative movements were determined by applying motion capture techniques and a special socket with cavities for reflective markers. Forces and torques were measured with a custom-build measuring adapter that was incorporated into the prosthesis. The results based on measurements with one amputee show considerable relative movements for slow, self-selected and fast walking speeds and reveal the causal relation for relative movements in sagittal plane.

10.3 Audio-visual Simulation

In order to enable a holistic perceptional illusion of walking with the simulated prosthesis, the audio-visual simulation is supposed to complement the mechanical simulation by providing a visual impression of the environment and assistive device as well as the corresponding audible soundscape with respect to the performed locomotion. By simulating for example a walk through a park, the user should experience the scenic attractions when looking around, his own body and the simulated prosthesis when looking down and possible acoustic stimuli like step sounds, birds in the trees or technical noise of the simulated prosthesis. This approach allows to test different everyday situations with fading out the distracting laboratory environment and adjusting relevant mechanisms and factors for body schema integration [51].

Recent developments in three-dimensional computer graphics and head-mounted displays enable the use of virtual reality for implementing such a holistic perceptional illusion based on biomechanical kinematics simulations in combination with a personalized virtual avatar which gives the user a sensation of being part of the simulated scene [51, 243]. The desired focus on immersion requires to create a connection between the user and the virtual environment but also between the user and his virtual avatar. Synchronizing the body movement of the user and his avatar is a crucial step to improve the feeling of presence by enhancing the experience of agency and body ownership over the avatar [43, 51]. Several modern consumer products provide cheap and highly integrated sensors for tracking human motion and could potentially replace sophisticated and expensive professional motion capture systems. Depth cameras like the KINECT (Microsoft, USA) or XTION PRO (Asus, Taiwan) are a prominent product class that allows to extract body segment motions based on a stream of depth images. In a pilot study, the impact of temporal delay in depth cameras between the performed and simulated motion with regard to the perceptional illusion was assessed [50]. The results reveal considerable delays especially in fast motions which constrain the experience of agency. In order to avoid these delays in the simulation of realistic lower limb motions, a real-time step detection was developed that uses the integrated sensors of the head-mounted display OCULUS RIFT (Oculus VR, USA) for discriminating left and right steps and estimating the current walking speed [43]. This information enables to animate the virtual avatar by triggering and scaling predefined leg trajectories.

Results of a comparison between four different step detection approaches with two healthy subjects show that a position-based step detector can recognize more than 92 % of the steps in a walking trial. In a following study, the step detection was used to investigate the influence of step sounds and a natural soundscape on the feeling of presence [122]. Thirty-six healthy subjects rated the virtual experience with and without sounds in various combinations. The results indicate a significantly higher rating of presence and realism for simulations including a natural soundscape, whereas step sounds do not improve the feeling of presence.

10.4 Body Schema Integration

The rubber hand illusion is a psychological paradigm that shows how the body schema of healthy subjects can be manipulated and shifted towards an artificial limb [36]. This cognitive effect is a promising starting point for the investigation of body schema integration with regard to assistive devices. In the experimental evaluation of the rubber hand illusion, a subject sees a rubber hand which is stimulated by a brush, while the real hand is hidden but stimulated synchronously. After a certain time, this process can induce a feeling of ownership over the rubber hand which is attributed to a multisensory integration of visual, tactile and proprioceptive information. In order to transfer the induced illusion to human motions with prostheses or orthoses, a systematic literature research has been performed to find relevant maintaining factors [48]. The analyzed studies indicate that the tactile information can be replaced by movements, where active and voluntary movements might additionally evoke a feeling of agency. Both sensations can help to improve body schema integration of assistive devices by moving the induced illusion from the hand to the leg [20].

An important requirement for user-centered development is an assessment of the user's needs and appropriate influencing factors. For gathering data with practical relevance, a questionnaire regarding satisfaction, usability, appearance, functionality and handling of the prosthesis in different situations was created. Sixty-five amputees completed the questionnaire. In a first evaluation, the fit of the shaft and a natural gait pattern were identified as important factors for satisfaction and body schema integration [248]. A second evaluation found dissatisfaction for different motor functions accompanied by a feeling of social exclusion [49]. Problems during changes in walking speed impair the feeling of security, whereas appearance, usability and functional features affect general satisfaction. Based on these results, a design methodology that allows to translate the identified factors to the functional design of prosthetic devices was developed [20]. By applying a quality function deployment approach, the psychological factors are connected to technical criteria which enables a consideration of satisfaction, feeling of security and body schema integration in the development process. A detailed description of the design methodology is provided by Beckerle [18, 19].

11 Conclusion

Biomechanical simulations of human motion dynamics have the potential to facilitate scientific research and clinical applications in medicine, rehabilitation, robotics and sports. Simulation-based approaches allow to estimate many crucial variables like joint forces and torques or muscle forces that cannot be measured in classical experiment-based approaches. The credibility and accuracy of simulation results strongly depend on the applied biomechanical model of the human locomotor system as well as the available biomechanical measurements. This thesis contributes to the field of human biomechanics by analyzing uncertainty and sensitivity in human motion dynamics simulations. Based on the important class of inverse dynamics simulations, the impact of common uncertainty sources has been systematically investigated for selected joint torques of the lower limbs in the three representative motion tasks walking, running and kicking a ball performed by a female and a male subject. The uncertainty and sensitivity analysis considered dispersion in the acquisition of biomechanical measurements, estimation of model parameters and realization of dynamics simulations with a parallel assessment of uncertainty propagation and apportionment for both genders. The approach guarantees a systematic evaluation of uncertainty and sensitivity regarding the sequential nature of the inverse dynamics simulation and existing dependencies between the involved uncertainty sources.

11.1 Contributions

This thesis makes several contributions towards more credible and accurate human motion dynamics simulations which are summarized in the following paragraphs.

Efficient Computational Frameworks

In order to enable a fast but adequate assessment of uncertainty propagation and apportionment, efficient computational frameworks for biomechanical modeling and simulation as well as uncertainty and sensitivity analysis have been presented in Chapter 3 and 4. High computational efficiency is a crucial requirement for the application of probabilistic methods as these approaches require a large number of repetitive simulation trials. The modeling and simulation framework provides a detailed three-dimensional biomechanical model of the human locomotor system and efficient algorithms for kinematics and dynamics simulations based on a lightweight and powerful multibody systems library. The low computational demand of the multibody systems library ensures fast execution times and a reduced memory consumption. The application of a comprehensive regression model for anthropometric parameters allows to personalize the model parameters to individual subjects. In contrast to other modeling approaches, soft tissue dynamics are considered by incorporating a wobbling mass model and the model parameters include all relevant dynamic properties without imposing restrictive assumptions on the center of mass or inertia tensor. This comprehensive modeling provides a more detailed representation of the actual dynamics in the human locomotor system. The uncertainty and sensitivity framework augments existing approaches in biomechanical studies by applying advanced statistical

models and considering possible correlations among uncertain simulation inputs and model parameters. By using a global analysis based on Monte Carlo simulation along with a parametric multivariate distribution system that covers the entire permissible skewness-kurtosis region, the exploration of the whole input space and a consideration of nonlinearities in the biomechanical model as well as interactions in the input variables are ensured. The preservation of these inherent characteristics avoids oversimplification and yields more realistic results. In contrast to conventional approaches based on Latin hypercube sampling, the quasi-random sampling strategy and the iterative implementation considerably decrease the required memory consumption and enable a flexible control over the number of random trials. Instead of running a predefined and fixed number of random trials, the simulation can be adjustably terminated after reaching a specified convergence limit which effectively saves computational time with assuring reliable simulation results. This combination of two powerful computational frameworks is the first of its kind to provide a comprehensive biomechanical model for various human motions together with an appropriate uncertainty and sensitivity analysis that covers different classes of probability distributions and considers potential correlations. These features make both computational frameworks unique and provide a sound basis for future research in modeling and simulation of human motion dynamics.

Comprehensive Biomechanical Measurements

The comprehensive HuMoD database with biomechanical measurements for various human motions performed by a female and male subject has been presented in Chapter 5. The database contains high-quality measurement data from a three-dimensional motion capture system, an instrumented treadmill and an electromyographical measurement system for eight different motion tasks representing typical repetitive and goal-oriented motions. For joint trajectory estimation, an extended Kalman smoother approach has been described which reduces the influence of soft tissue artifacts and ensures smooth joint trajectories and consistent spatial motion data. Besides the raw measurement data, estimates for anthropometric parameters, joint center locations and joint trajectories as well as the source code of the applied computational scripts and a detailed documentation have been provided and published for open data and open source use.

In preparation for the uncertainty and sensitivity analysis, a systematic evaluation of important uncertainty sources in motion capture and force plate measurements has been presented and discussed in Chapter 6. The evaluation yields statistical models for anatomical landmark misplacement, soft tissue artifacts and measurements errors for both measurement systems. Anatomical landmark misplacement and the measurement errors were assessed based on experimental investigations with the actual subjects and measurement systems which ensures compatibility with the collected biomechanical measurements. In contrast to previous studies, potential correlations between the individual measurands are considered and incorporated into the statistical models. The impact of soft tissue artifacts in combination with the extended Kalman smoother was evaluated based on a computational model presented in literature and an exemplary uncertainty analysis.

The results show that anatomic landmark misplacement, soft tissue artifacts as well as measurement uncertainties of the instrumented treadmill considerably impair biomechanical measurements, whereas measurement uncertainties of the motion capture system are rather negligible.

The principal standard deviations in anatomical landmark identification reached up to 28.1 mm for repetitive trials with different examiners and 17.0 mm for repetitive trials with one examiner. Despite the application of the extended Kalman smoother, the imposed soft tissue artifacts caused standard deviations of up to 2.5 ° in the leg joints. The measurement uncertainty of the applied instrumented treadmill resulted in standard deviations ranging from 3.149 N to 3.961 N for ground reaction forces and from 10.8 mm to 18.2 mm for the center of pressure. Uncertainties of these magnitudes substantially affect the tracking of body segments and the estimation of ground reaction forces which can have a significant impact on derived model parameters and simulation results.

Uncertainty and Sensitivity Analysis of Model Parameter Estimation

An extensive uncertainty analysis of joint center estimation as well as a comprehensive uncertainty and sensitivity analysis of anthropometric parameter estimation have been described in Chapter 7 and 8. The variance in common regression parameters for the estimation of joint center locations in female and male subjects was assessed by exploiting statistical properties of anatomical landmarks provided in literature in combination with a Kriging interpolation approach. By incorporating the found uncertainties for joint center estimation and biomechanical measurements as well as additional statistical properties reported in literature, the variation of widely used regression parameters for the estimation of anthropometric parameters was evaluated for female and male subjects. The results indicate substantial variances in most of the considered joints and body segments and provide representative statistical models as well as a sound basis for refined regression parameters. The found relative standard deviations of the regression parameters with respect to the provided reference values reach up to 296.3 % for joint center estimation and 67,254.9 % for anthropometric parameter estimation. Such high uncertainties considerably influence the accuracy of the obtained model parameters and affect the personalization of the biomechanical model. In order to improve anthropometric parameter estimation, a revised set of regression parameters was derived from the found probability distributions. The anthropometric parameters for the right thigh segment of the actual subjects determined with this set coincide quite well with the found median values of the probability distributions and have a maximum deviation of 2.1 % for the female subject and 2.8 % for the male subject. In contrast, the anthropometric parameters calculated with the original reference values exhibit deviations of up to 519.4 % for the female subject and 189.3 % for the male subject. These results indicate a clear improvement in the estimation results regarding the expectable uncertainties. Nevertheless, a general problem for the applicability and validity of the applied regression models is the age of the underlying measurement data. Since most of the relevant measurements were performed in the 1980s or before, an application on present subjects causes additional uncertainties in the estimation process. Together with the revealed uncertainties, this fact emphasizes that updated regression models based on contemporary measurement data are necessary to further improve model parameter estimation.

Uncertainty and Sensitivity Analysis of Joint Torque Estimation

In order to evaluate the propagation of individual uncertainty sources, a comprehensive uncertainty and sensitivity analysis for joint torque estimates in hip, knee and ankle joints has been presented in Chapter 9 with incorporating all previously determined uncertainties. In contrast

to previous studies, the performed analysis regards both genders and three different motion tasks. In addition, the systematic assessment of the involved uncertainty sources and the consequent consideration of possible correlations among uncertain simulation inputs and model parameters improves the significance of the obtained results. The uncertainty analysis reveals crucial deviations in all joints at different phases of the motion sequence and establishes causal relations between joint kinematics and the found dispersion. The observed upper bounds for the deviations reach up to 80.6 Nm in the walking motion, 176.1 Nm in the running motion and 149.3 Nm in the kicking motion. A clear difference between phases involving ground reaction forces and phases with pure swing motions has been found, where the joint torque uncertainty is much greater during phases with ground contact. Variations in the measured center of pressure and the regression parameters for anthropometric parameter estimation have been identified as the most relevant uncertainty sources. But also variances in the regression parameters for joint center estimation as well as anatomical landmark misplacement have a considerable share with varying extent. Observed distinctions between the female and male subject mainly originate from differences in segment lengths and body mass or individual motion patterns. The presented results show that especially uncertainties in force plate measurements and anthropometric parameter estimates have a significant influence on the simulation results. Deviations of 50.0 % or more with regard to the estimated median value demonstrate the large variability. Such uncertainties substantially affect the results of biomechanical and medical investigations but can also lead to an inappropriate dimensioning of critical components in assistive devices like load-bearing structures or actuation concepts. In conclusion, an adequate calibration of the applied force plates or instrumented treadmill as well as refined regression models for anthropometric parameter and joint center estimation are the most important requirements for more accurate human motion dynamics simulations. In addition, a careful identification of the involved anatomical landmarks helps to further improve the simulation results.

Biomechanical Simulations for the Design and Analysis of Assistive Devices

A number of complementary research topics regarding a user-centered design methodology for active assistive devices based on biomechanical simulations of human motions have been investigated. A summary of the obtained results has been provided in Chapter 10. The presented Prosthesis-User-in-the-Loop simulator is a novel approach towards a seamless integration of assistive devices into the body schema. By imitating the mechanical behavior of a simulated prosthesis as well as visual and acoustic impressions of the environment, the concept enables a holistic simulation of human gait with different assistive devices. This approach allows to study important technical criteria but also influential psychological factors at the same time. In the presented investigations, a particular focus was put on the analysis and implementation of serial elastic actuator concepts that ensure inherent safety and energy efficiency as well as the development of a personalized audio-visual simulation with respect to relevant psychological factors. Regarding the actuator concepts, a novel serial elastic actuator with variable stiffness and a compact and customizable configuration has been developed. Furthermore, a new methodology for the design and optimization of elastically actuated lower limb prostheses based on biomechanical dynamics simulations was presented and exemplarily implemented for an active knee prosthesis. The evaluation revealed a reduction of peak power by about 10 % for walking and over 30 % for running. Concerning the audio-visual simulation, different factors for improving the feeling of presence and body ownership in a virtual simulation environment have

been studied. A good temporal synchronization of the actual and simulated motions as well as the integration of a natural soundscape led to significantly higher ratings for presence and realism. These results provide an initial basis for the investigation of body schema integration with regard to assistive devices.

11.2 Outlook

While the contributions of this thesis provide a comprehensive evaluation of uncertainties and sensitivities in the inverse dynamics procedure, further research is required to investigate the impact of uncertainty propagation on subsequent applications like muscle force estimation or the development of assistive devices. In particular, the derivation of personalized model parameters for macroscopic muscle models might be affected by significant uncertainties which impair the results of a static optimization. For the development of prostheses or orthoses, variations in estimated joint torques have to be considered in the dimensioning of constructive components and actuator concepts. The identified uncertainties give a reasonable point of reference for the expectable variations. In the long term, the presented findings suggest that adequate measures for a sustainable quality management are necessary to improve the quality of biomechanical measurements as well as model parameter estimation and to facilitate the validation of biomechanical simulations.

The results of the uncertainty and sensitivity analysis indicate that variances in force plate measurements but also anthropometric parameter and joint center estimates have the greatest impact on the obtained joint torques. While measurement errors of force plates or instrumented treadmills can be reduced by consistent and routine calibration procedures, anthropometric parameters and joint center locations are typically calculated with simplified regression models based on outdated and incomplete databases of human body measurements which have been recorded for very specific populations.

Recent developments in three-dimensional scanner technology potentially facilitate and simplify the generation of personalized volume models that can be applied for the computation of individual model parameters or refined regression models. This approach also allows to take currently disregarded populations like young, elderly and disabled people into account. In combination with modern medical imaging, additional details like personalized wobbling mass models could be incorporated. The computational frameworks presented in this thesis can be easily adapted to evaluate improved or enhanced regression models as well as other motion tasks or joint torques. In that respect, the provided statistical models and revised regression parameters provide a suitable basis and reference.

A Appendix

A.1 Hierarchical Model Tree

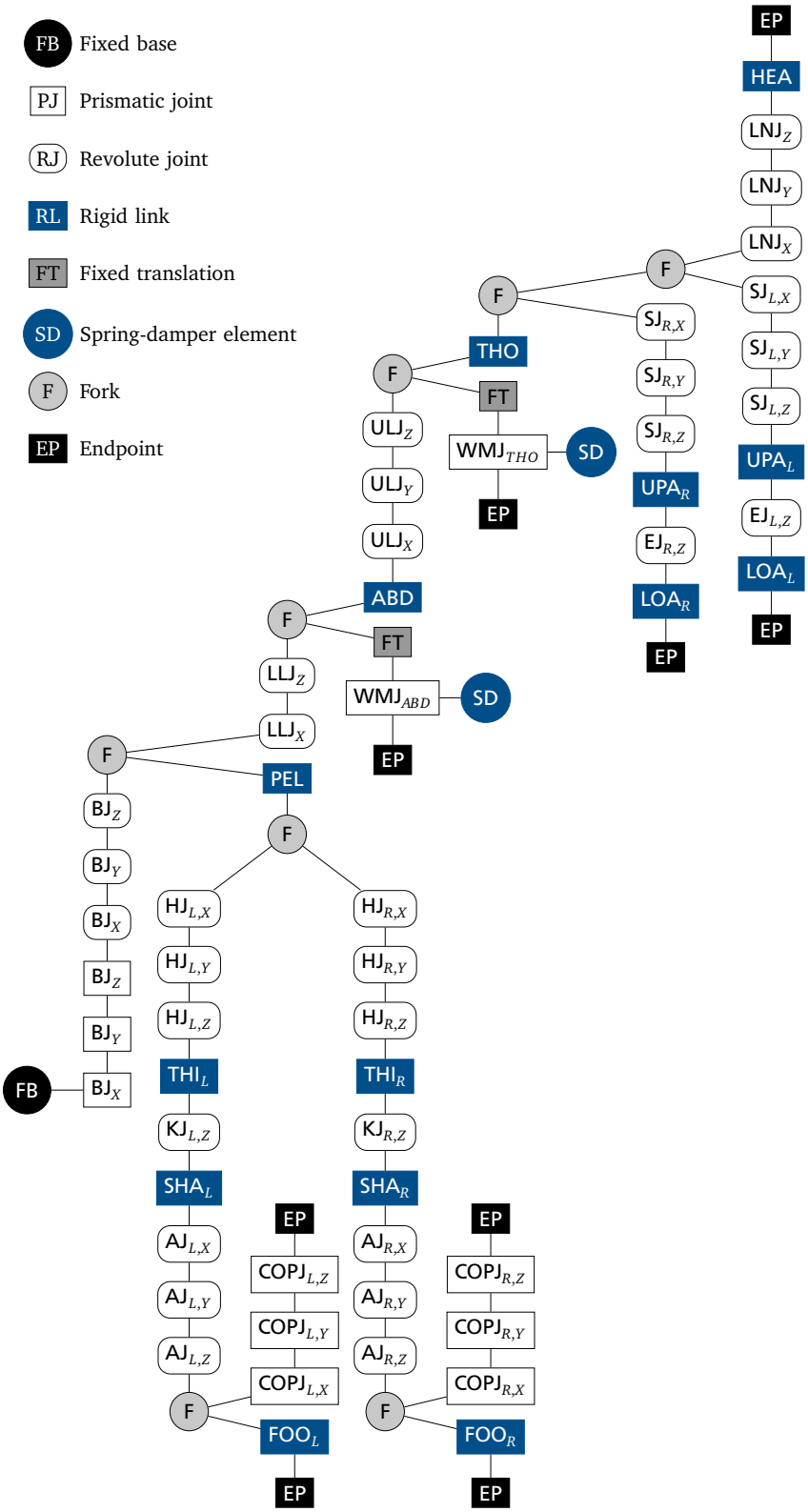

GLA	**Glabella**: Undepressed skin surface point obtained by palpating the most forward projection of the forehead in the midline at the level of the brow ridges [177].
TRA_L, TRA_R	**Left and right tragion**: Undepressed skin surface point obtained by palpating the most anterior margin of the cartilaginous notch just superior to the tragus of the ear located at the upper edge of the external auditory meatus [177].
SUP	**Suprasternale**: Undepressed skin surface point at the superior margin of the jugular notch of the manubrium on the midline of the sternum [177].
C7	**7th cervical vertebra**: Depressed skin surface point at the most posterior aspect of the spinous process of the 7th cervical vertebra [177].
T8	**8th thoracic vertebra**: Depressed skin surface point at the most posterior aspect of the spinous process of the 8th thoracic vertebra [177].
T12	**12th thoracic vertebra**: Depressed skin surface point at the most posterior aspect of the spinous process of the 12th thoracic vertebra [177].
ACR_L, ACR_R	**Left and right acromion**: Undepressed skin surface point obtained by palpating the most anterior portion of the lateral margin of the acromial process of the scapula [177].
LHC_L, LHC_R	**Left and right lateral humeral epicondyle**: Undepressed skin surface point at the most lateral aspect of the humeral epicondyle [177].
WRI_L, WRI_R	**Left and right wrist**: Undepressed skin surface point on the dorsal surface of the wrist midway between the radial and ulnar styloid processes [177].
US_L, US_R	**Left and right ulnar styloid**: The most distal point on the ulna [145].
RS_L, RS_R	**Left and right radial styloid**: The point at the distal tip of the radius [145].
$ASIS_L$, $ASIS_R$	**Left and right anterior-superior iliac spine**: Depressed skin surface point at the anterior-superior iliac spine. Located by palpating proximally on the midline of the anterior thigh surface until the anterior prominence of the iliac spine is reached [177].
$PSIS_L$, $PSIS_R$	**Left and right posterior-superior iliac spine**: Depressed skin surface point at the posterior-superior iliac spine. This landmark is located by palpating posteriorly along the margin of the iliac spine until the most posterior prominence is located, adjacent to the sacrum [177].
PS	**Pubic symphysis**: Depressed skin surface point at the anterior margin of the pubic symphysis, located by the subject by palpating inferiorly on the midline of the abdomen until reaching the pubis. The subject is instructed to rock his or her fingers around the lower margin of the symphysis to locate the most anterior point [177].

GTR_L, GTR_R **Left and right greater trochanter**: Undepressed skin surface point at the most lateral prominent of the upper femur [247].

LFC_L, LFC_R **Left and right lateral femoral epicondyle**: Undepressed skin surface point at the most lateral aspect of the lateral femoral epicondyle [177].

MFC_L, MFC_R **Left and right medial femoral epicondyle**: Undepressed skin surface point at the most medial aspect of the medial femoral epicondyle [247].

LM_L, LM_R **Left and right lateral malleolus**: Undepressed skin surface point at the most lateral aspect of the malleolus of the fibula [177].

MM_L, MM_R **Left and right medial malleolus**: Undepressed skin surface point at the most medial aspect of the malleolus of the tibia [247].

SPH_L, SPH_R **Left and right sphyrion**: The most distal point on the medial side of the tibia [145].

CAL_L, CAL_R **Left and right calcaneus**: Undepressed skin surface point at the most posterior prominent of the calcaneus [247].

$MT2_L$, $MT2_R$ **Left and right 2nd metatarsal head**: Undepressed skin surface point above the distal head of the 2nd metatarsal [247].

$MT5_L$, $MT5_R$ **Left and right 5th metatarsal head**: Undepressed skin surface point above the distal head of the 5th metatarsal [247].

HAL_L, HAL_R **Left and right hallux**: The anterior point of the 1st digit of each foot [247].

A.3 Abbreviations for Skeletal Muscles

SOL_L, SOL_R **Left and right soleus muscle**: Plantar flexion of the ankle joint [105].

TIA_L, TIA_R **Left and right tibialis anterior muscle**: Dorsiflexion of the ankle joint and assistance in inversion of the foot [105].

GLS_L, GLS_R **Left and right gastrocnemius lateralis muscle**: Flexion of the ankle joint and assist in flexion of the knee joint [105].

VSL_L, VSL_R **Left and right vastus lateralis muscle**: Extension of the knee joint [105].

RCF_L, RCF_R **Left and right rectus femoris muscle**: Extension of the knee joint and flexion of the hip joint [105].

BCF_L, BCF_R **Left and right biceps femoris muscle**: Flexion and lateral rotation of the knee joint. The long head also extends and assists in lateral rotation of the hip joint [105].

GLX_L, GLX_R **Left and right gluteus maximus muscle**: Extends, laterally rotates and lower fibers assist in adduction of the hip joint. The upper fibers assist in adduction. Through its insertion into the iliotibial tract, helps to stabilize the knee in extension [105].

A.4 Normal Vectors for Reflective Markers

GLA The normal vector is parallel to the line connecting the midpoint between the TRA markers with the GLA marker.

TRA The normal vector is parallel to the line connecting the TRA markers.

SUP, C7 The normal vector is parallel to the line connecting the C7 and SUP markers.

T8 The normal vector is parallel to the vector sum of the normal vectors specified for the SUP, C7 and T12 markers.

T12 The normal vector is parallel to the line connecting the T8 and T12 markers rotated by 0.5π rad about the line connecting the ACR markers.

ACR The normal vector is perpendicular to the normal vector specified for the SUP and C7 markers and the line connecting the ACR markers.

LHC The normal vector is perpendicular to the lines connecting the WRI and LHC markers as well as the estimated shoulder joint center and LHC marker.

ASIS, PSIS The normal vector is parallel to the line connecting the midpoint between the ASIS markers with the midpoint between the PSIS markers.

PS The normal vector is parallel to the line connecting the midpoint between the PSIS markers with the PS marker.

GTR The normal vector is parallel to the line connecting the GTR markers.

LFC, MFC The normal vector is parallel to the line connecting the LFC and MFC markers.

LM, MM The normal vector is parallel to the line connecting the LM and MM markers.

CAL The normal vector is parallel to the line connecting the CAL and MT2 markers

MT2, MT5, HAL The normal vector is perpendicular to the lines connecting the CAL and MT5 markers as well as the MT2 and MT5 markers.

A.5 Segment Reference Frames

HEA The y-axis is assumed to be perpendicular to the plane containing the GLA, TRA_L and TRA_R markers pointing distally. The z-axis is perpendicular to the y-axis and the line connecting the lower neck joint and the GLA marker pointing right. The x-axis is the line perpendicular to the y- and z-axis pointing anteriorly. The origin is the LNJ [66].

THO The y-axis is given by the connection of ULJ and LNJ pointing superior. The z-axis is perpendicular to the y-axis and the line connecting the C7 and SUP markers pointing right. The x-axis is the line perpendicular to the y- and z-axes pointing anteriorly. The origin is the LNJ [68].

ABD The y-axis is given by the connection of LLJ and ULJ pointing superior. The z-axis is perpendicular to the y-axis and the line connecting the C7 and SUP markers pointing right. The x-axis is the line perpendicular to the y- and z-axis pointing anteriorly. The origin is the ULJ [68].

UPA The y-axis is given by the connection of SJ and EJ pointing proximally. The x-axis is perpendicular to the y-axis and the line connecting EJ and the LHC marker pointing anteriorly. The z-axis is the line perpendicular to the x- and y-axes pointing right. The origin is the SJ [66].

LOA The y-axis is given by the connection of the WRI marker and EJ pointing proximally. The x-axis is perpendicular to the y-axis and the line connecting EJ and the LHC marker pointing anteriorly. The z-axis is the line perpendicular to the x- and y-axes pointing right. The origin is the EJ [66].

PEL The z-axis is given by the connection of the $ASIS_L$ and $ASIS_R$ markers pointing right. The x-axis is given by the line connecting the midpoint of the $ASIS_L$ and $ASIS_R$ markers with the midpoint of the $PSIS_L$ and $PSIS_R$ markers pointing anteriorly. The y-axis is the line perpendicular to the x- and z-axes pointing superior. The origin is the LLJ [66].

THI The x-axis is perpendicular to the plane containing the HJ as well as MFC and LFC markers pointing anteriorly. The y-axis is given by the line connection HJ and KJ joints pointing proximally. The z-axis is the line perpendicular to the x- and y-axes pointing right. The origin is the HJ [66].

SHA The x-axis is perpendicular to the plane containing the KJ as well as the MM and LM markers pointing anteriorly. The y-axis is given by the line connecting KJ and AJ pointing proximally. The z-axis is the line perpendicular to the x- and y-axes pointing right. The origin is the KJ [66].

FOO The x-axis is given by the connection of the CAL marker with the point defined by adding three-quarters of the distance between the MT2 and MT5 markers to the location of the MT5 marker in medial direction and points in anterior direction. The y-axis is perpendicular to the plantar aspect of the foot approximated by the plane containing the CAL, MT2 and MT5 markers pointing proximally. The z-axis is the line perpendicular to the x- and y-axes pointing right. The origin is the AJ [66].

A.6 Parameters of the Extended Kalman Smoother

Diagonal elements of the process covariance matrix $\mathbf{\Sigma}_w$ and measurement covariance matrix $\mathbf{\Sigma}_v$ for the extended Kalman smoother. All other elements are set to zero.

	$\text{diag}(\mathbf{\Sigma}_w)$			$\text{diag}(\mathbf{\Sigma}_v)$	
	Female	Male		Female	Male
LNJ_X	$1.0 \cdot 18000.0$	$1.0 \cdot 18000.0$	GLA	$1.0 \cdot 0.5665^2$	$1.0 \cdot 0.65958^2$
LNJ_Y	$1.0 \cdot 18000.0$	$1.0 \cdot 18000.0$	TRA_L	$1.0 \cdot 0.5665^2$	$1.0 \cdot 0.65958^2$
LNJ_Z	$1.0 \cdot 18000.0$	$1.0 \cdot 18000.0$	TRA_R	$1.0 \cdot 0.5665^2$	$1.0 \cdot 0.65958^2$
$\text{SJ}_{L,X}$	$1.0 \cdot 18000.0$	$1.0 \cdot 18000.0$	SUP	$1.0 \cdot 0.5665^2$	$1.0 \cdot 0.65958^2$
$\text{SJ}_{L,Y}$	$1.0 \cdot 18000.0$	$1.0 \cdot 18000.0$	ACR_L	$2.0 \cdot 0.5665^2$	$2.0 \cdot 0.65958^2$
$\text{SJ}_{L,Z}$	$1.0 \cdot 18000.0$	$1.0 \cdot 18000.0$	ACR_R	$2.0 \cdot 0.5665^2$	$2.0 \cdot 0.65958^2$
$\text{SJ}_{R,X}$	$1.0 \cdot 18000.0$	$1.0 \cdot 18000.0$	C7	$1.0 \cdot 0.5665^2$	$1.0 \cdot 0.65958^2$
$\text{SJ}_{R,Y}$	$1.0 \cdot 18000.0$	$1.0 \cdot 18000.0$	T8	$1.0 \cdot 0.5665^2$	$1.0 \cdot 0.65958^2$
$\text{SJ}_{R,Z}$	$1.0 \cdot 18000.0$	$1.0 \cdot 18000.0$	T12	$1.0 \cdot 0.5665^2$	$1.0 \cdot 0.65958^2$
$\text{EJ}_{L,Z}$	$1.0 \cdot 18000.0$	$1.0 \cdot 18000.0$	LHC_L	$1.0 \cdot 0.5665^2$	$1.0 \cdot 0.65958^2$
$\text{EJ}_{R,Z}$	$1.0 \cdot 18000.0$	$1.0 \cdot 18000.0$	LHC_R	$1.0 \cdot 0.5665^2$	$1.0 \cdot 0.65958^2$
ULJ_X	$1.0 \cdot 18000.0$	$1.0 \cdot 18000.0$	WRI_L	$1.0 \cdot 0.5665^2$	$1.0 \cdot 0.65958^2$
ULJ_Y	$1.0 \cdot 18000.0$	$1.0 \cdot 18000.0$	WRI_R	$1.0 \cdot 0.5665^2$	$1.0 \cdot 0.65958^2$
ULJ_Z	$1.0 \cdot 18000.0$	$1.0 \cdot 18000.0$	ASIS_L	$1.0 \cdot 0.5665^2$	$1.0 \cdot 0.65958^2$
LLJ_X	$1.0 \cdot 18000.0$	$1.0 \cdot 18000.0$	ASIS_R	$1.0 \cdot 0.5665^2$	$1.0 \cdot 0.65958^2$
LLJ_Y	$1.0 \cdot 18000.0$	$1.0 \cdot 18000.0$	PSIS_L	$1.0 \cdot 0.5665^2$	$1.0 \cdot 0.65958^2$
LLJ_Z	$1.0 \cdot 18000.0$	$1.0 \cdot 18000.0$	PSIS_R	$1.0 \cdot 0.5665^2$	$1.0 \cdot 0.65958^2$
$\text{HJ}_{L,X}$	$1.0 \cdot 18000.0$	$1.0 \cdot 18000.0$	PS	$1.0 \cdot 0.5665^2$	$1.0 \cdot 0.65958^2$
$\text{HJ}_{L,Y}$	$1.0 \cdot 18000.0$	$1.0 \cdot 18000.0$	GTR_L	$2.0 \cdot 0.5665^2$	$2.0 \cdot 0.65958^2$
$\text{HJ}_{L,Z}$	$1.0 \cdot 18000.0$	$1.0 \cdot 18000.0$	GTR_R	$2.0 \cdot 0.5665^2$	$2.0 \cdot 0.65958^2$
$\text{HJ}_{R,X}$	$1.0 \cdot 18000.0$	$1.0 \cdot 18000.0$	LFC_L	$0.7 \cdot 0.5665^2$	$0.7 \cdot 0.65958^2$
$\text{HJ}_{R,Y}$	$1.0 \cdot 18000.0$	$1.0 \cdot 18000.0$	LFC_R	$0.7 \cdot 0.5665^2$	$0.7 \cdot 0.65958^2$
$\text{HJ}_{R,Z}$	$1.0 \cdot 18000.0$	$1.0 \cdot 18000.0$	MFC_L	$0.7 \cdot 0.5665^2$	$0.7 \cdot 0.65958^2$
$\text{KJ}_{L,Z}$	$3.0 \cdot 18000.0$	$3.0 \cdot 18000.0$	MFC_R	$0.7 \cdot 0.5665^2$	$0.7 \cdot 0.65958^2$
$\text{KJ}_{R,Z}$	$3.0 \cdot 18000.0$	$3.0 \cdot 18000.0$	LM_L	$0.5 \cdot 0.5665^2$	$0.5 \cdot 0.65958^2$
$\text{AJ}_{L,X}$	$3.0 \cdot 18000.0$	$3.0 \cdot 18000.0$	LM_R	$0.5 \cdot 0.5665^2$	$0.5 \cdot 0.65958^2$
$\text{AJ}_{L,Y}$	$3.0 \cdot 18000.0$	$3.0 \cdot 18000.0$	MM_L	$0.5 \cdot 0.5665^2$	$0.5 \cdot 0.65958^2$
$\text{AJ}_{L,Z}$	$3.0 \cdot 18000.0$	$3.0 \cdot 18000.0$	MM_R	$0.5 \cdot 0.5665^2$	$0.5 \cdot 0.65958^2$
$\text{AJ}_{R,X}$	$3.0 \cdot 18000.0$	$3.0 \cdot 18000.0$	CAL_L	$0.1 \cdot 0.5665^2$	$0.1 \cdot 0.65958^2$
$\text{AJ}_{R,Y}$	$3.0 \cdot 18000.0$	$3.0 \cdot 18000.0$	CAL_R	$0.1 \cdot 0.5665^2$	$0.1 \cdot 0.65958^2$
$\text{AJ}_{R,Z}$	$3.0 \cdot 18000.0$	$3.0 \cdot 18000.0$	MT2_L	$0.1 \cdot 0.5665^2$	$0.1 \cdot 0.65958^2$
			MT2_R	$0.1 \cdot 0.5665^2$	$0.1 \cdot 0.65958^2$
			MT5_L	$0.1 \cdot 0.5665^2$	$0.1 \cdot 0.65958^2$
			MT5_R	$0.1 \cdot 0.5665^2$	$0.1 \cdot 0.65958^2$

A.7 Covariance Matrices for Anatomical Landmark Misplacement

Elements of the symmetrical covariance matrices for reproducibility and repeatability of the female subject given in millimeters squared.

	Reproducibility						Repeatability					
	$\Sigma_{X,X}$	$\Sigma_{Y,Y}$	$\Sigma_{Z,Z}$	$\Sigma_{X,Y}$	$\Sigma_{X,Z}$	$\Sigma_{Y,Z}$	$\Sigma_{X,X}$	$\Sigma_{Y,Y}$	$\Sigma_{Z,Z}$	$\Sigma_{X,Y}$	$\Sigma_{X,Z}$	$\Sigma_{Y,Z}$
GLA	3.48	10.61	2.79	3.75	0.16	0.30	0.35	0.75	0.67	0.16	−0.03	−0.16
TRA_L	20.12	10.77	3.48	−10.29	0.38	−0.30	0.27	0.15	0.09	−0.03	0.04	−0.01
TRA_R	20.64	8.84	3.70	−7.99	1.69	−0.84	1.53	1.72	0.43	0.97	0.01	0.07
SUP	4.72	5.96	10.11	−2.64	−2.52	3.82	1.02	1.20	0.97	−0.73	−0.44	0.48
ACR_L	120.59	126.03	200.45	−27.36	−1.71	75.09	5.44	1.25	2.00	−0.68	−1.16	0.43
ACR_R	138.92	110.23	150.11	−32.53	12.12	−49.38	4.23	1.30	3.27	0.38	−1.88	−0.63
C7	14.15	21.71	11.15	11.31	−2.07	−2.88	0.38	0.38	3.14	0.00	−0.07	−0.05
T8	29.73	190.76	24.53	−32.22	−1.67	9.23	0.60	0.88	4.35	−0.03	0.09	−0.65
T12	129.42	577.22	75.93	−165.72	3.43	−10.52	10.69	69.00	10.62	−10.22	0.93	−6.45
LHC_L	4.48	15.07	2.75	1.24	−0.24	0.67	0.84	3.41	0.55	0.27	−0.06	−0.02
LHC_R	34.83	37.72	9.85	−20.46	−1.77	1.07	1.62	1.72	0.60	1.08	0.45	0.47
WRI_L	11.64	13.93	7.29	−3.83	−3.67	4.15	0.33	0.25	0.30	0.04	−0.18	−0.02
WRI_R	6.98	5.23	1.99	−2.87	0.48	−0.76	0.59	0.64	0.15	0.41	0.04	0.01
$ASIS_L$	10.79	26.10	6.71	−11.84	3.99	−7.05	1.75	3.56	1.84	−1.62	1.05	−1.59
$ASIS_R$	14.87	16.72	18.64	−10.69	−11.67	12.40	0.46	1.42	0.95	0.11	−0.22	−0.59
$PSIS_L$	83.03	204.95	356.66	18.86	−12.50	−124.00	2.48	5.99	6.35	0.95	0.69	1.95
$PSIS_R$	57.06	156.30	177.79	19.43	4.79	74.73	2.79	4.02	14.60	1.05	−2.60	−4.07
PS	0.98	4.30	1.99	0.31	−0.11	−0.86	0.59	3.50	1.11	0.22	−0.07	−0.86
GTR_L	402.98	474.41	240.42	−28.28	36.01	70.56	19.44	44.41	11.63	−8.96	2.03	3.71
GTR_R	122.90	183.39	77.61	−7.53	2.17	−40.50	34.58	31.09	7.65	−24.23	−1.40	0.58
LFC_L	89.60	157.13	30.54	77.62	8.85	9.38	6.52	3.74	1.99	1.67	1.28	0.31
LFC_R	115.14	227.71	60.40	65.89	−13.75	9.01	6.08	8.68	3.54	−0.49	−0.92	0.71
MFC_L	30.64	23.60	8.76	16.70	−4.48	−1.38	5.62	17.00	5.60	0.53	−0.53	5.09
MFC_R	19.16	9.69	10.84	1.92	8.51	0.11	2.54	7.74	2.41	−0.14	0.57	−1.75
LM_L	1.96	3.31	0.95	−0.70	0.06	−0.33	0.76	0.67	1.29	−0.30	−0.66	0.39
LM_R	3.10	2.82	1.81	−0.31	0.53	0.35	1.28	1.30	2.05	−0.17	0.84	0.01
MM_L	1.46	1.07	0.38	−0.66	0.19	−0.13	1.85	0.49	1.07	−0.32	−1.04	0.23
MM_R	5.00	9.01	1.83	−5.10	−1.01	1.49	0.13	0.12	0.07	−0.06	0.05	−0.03
CAL_L	4.86	31.93	13.08	−1.35	−0.76	14.83	0.49	3.39	0.76	−0.13	−0.03	0.63
CAL_R	5.60	42.46	7.35	3.04	−0.64	−7.86	0.58	4.42	0.67	0.16	0.02	0.05
$MT2_L$	11.17	2.48	2.54	−2.77	1.90	−0.58	0.42	0.24	0.59	−0.06	−0.05	0.01
$MT2_R$	8.84	1.95	1.32	−2.40	−0.09	0.05	1.65	0.68	1.13	−0.34	0.14	−0.09
$MT5_L$	6.44	1.53	2.62	−0.42	−1.58	0.53	0.55	0.35	0.59	−0.03	−0.05	0.15
$MT5_R$	1.19	0.46	1.13	0.42	−0.88	−0.40	0.51	0.58	1.48	0.24	−0.44	−0.62
HAL_L	1.85	1.94	1.09	−1.39	−0.88	0.89	0.12	0.22	0.23	−0.06	0.03	−0.06
HAL_R	1.41	1.43	0.64	−1.02	0.21	−0.19	0.04	0.05	0.25	−0.00	−0.00	0.03

Elements of the symmetrical covariance matrices for reproducibility and repeatability of the male subject given in millimeters squared.

	Reproducibility						Repeatability					
	$\Sigma_{X,X}$	$\Sigma_{Y,Y}$	$\Sigma_{Z,Z}$	$\Sigma_{X,Y}$	$\Sigma_{X,Z}$	$\Sigma_{Y,Z}$	$\Sigma_{X,X}$	$\Sigma_{Y,Y}$	$\Sigma_{Z,Z}$	$\Sigma_{X,Y}$	$\Sigma_{X,Z}$	$\Sigma_{Y,Z}$
GLA	3.66	16.78	3.19	4.20	−0.31	−1.09	0.13	0.43	0.39	0.09	−0.06	−0.26
TRA_L	49.80	30.95	12.56	−16.10	0.55	−0.23	0.99	1.03	0.44	0.22	−0.03	0.08
TRA_R	21.34	27.78	8.16	−9.55	1.37	−2.33	3.31	1.32	0.73	0.40	−0.09	0.09
SUP	3.24	5.81	8.91	−1.68	−1.36	2.88	1.84	3.06	5.58	−1.16	1.49	−2.45
ACR_L	114.91	80.30	164.82	−21.25	−22.77	49.05	3.71	2.72	10.17	−0.03	0.29	2.20
ACR_R	129.60	94.95	180.67	−20.48	−0.53	−43.34	13.75	3.71	6.61	−0.43	−2.40	−0.85
C7	3.84	5.17	10.27	1.48	−0.65	−1.84	22.59	32.83	6.73	21.02	1.09	1.45
T8	108.17	475.31	101.88	−117.99	2.27	−16.82	0.36	1.01	0.61	−0.14	−0.05	−0.02
T12	58.94	187.35	30.69	−70.83	−4.56	8.16	5.13	31.77	4.63	−5.36	−0.18	0.97
LHC_L	24.04	37.43	8.06	−20.11	−3.33	3.23	1.86	4.07	1.33	0.80	−0.54	−0.85
LHC_R	73.31	84.84	30.06	−24.30	6.91	−0.96	3.53	4.42	2.15	−0.45	0.55	0.36
WRI_L	23.10	13.40	7.32	4.74	1.15	2.41	1.06	2.01	0.93	−0.71	−0.48	0.83
WRI_R	10.32	4.46	2.93	−0.65	−0.37	−0.79	2.70	2.57	1.45	0.35	0.33	−0.30
$ASIS_L$	14.62	40.36	16.31	−9.14	6.22	−8.05	4.32	6.92	4.21	0.17	1.40	0.32
$ASIS_R$	12.11	54.44	17.00	1.12	−3.30	−8.60	11.02	11.92	10.64	−0.42	−4.70	0.04
$PSIS_L$	38.03	99.77	230.70	4.48	−3.68	−100.28	39.99	280.42	50.64	25.37	5.61	40.53
$PSIS_R$	30.04	74.38	198.45	4.54	7.74	83.74	34.24	279.46	35.71	11.97	0.42	13.71
PS	3.02	13.30	2.45	−3.65	−0.61	1.90	3.39	14.23	2.18	−4.20	−0.06	0.29
GTR_L	101.13	104.25	49.44	−14.91	1.67	12.38	28.80	26.26	14.71	2.42	4.79	3.33
GTR_R	343.09	576.49	115.37	−306.55	7.13	9.29	38.23	18.66	8.55	−11.14	−2.26	−0.23
LFC_L	18.31	65.01	12.88	8.58	3.21	1.55	34.78	90.03	15.85	38.56	6.59	11.80
LFC_R	59.46	175.98	29.55	65.28	−9.78	−17.36	25.35	62.86	13.06	21.18	−4.98	−6.14
MFC_L	131.80	114.46	32.35	87.43	−16.75	−11.46	4.23	6.05	1.68	3.50	−0.98	−0.90
MFC_R	33.98	69.51	14.48	32.81	6.09	7.04	4.22	3.68	2.92	0.66	1.45	−0.08
LM_L	5.61	2.09	1.13	1.40	−0.70	−0.19	2.51	3.01	1.67	−0.04	−0.52	0.36
LM_R	3.60	3.41	2.77	0.13	1.36	0.16	1.13	3.04	1.19	0.20	0.36	0.07
MM_L	6.64	7.63	3.07	1.23	−0.15	−0.46	11.40	4.31	3.38	2.70	−3.28	−1.00
MM_R	1.08	5.77	0.84	0.30	0.07	0.15	2.19	1.40	0.88	−0.43	0.59	−0.15
CAL_L	6.24	25.50	13.64	−0.51	−0.78	5.97	0.50	3.60	1.00	−0.01	−0.00	1.15
CAL_R	7.40	20.75	16.42	−0.42	0.89	−4.18	3.36	20.83	9.54	0.83	−0.46	−10.18
$MT2_L$	6.72	1.34	2.36	−1.24	2.32	−0.50	0.45	0.18	0.63	−0.05	−0.21	0.04
$MT2_R$	15.43	3.70	5.25	−3.04	1.83	−0.40	0.33	0.15	0.56	−0.05	−0.17	0.05
$MT5_L$	3.17	1.77	3.57	−0.53	−1.17	1.14	1.61	0.37	0.84	−0.29	−0.80	0.21
$MT5_R$	12.18	4.74	7.10	4.61	−6.35	−3.30	1.84	0.37	0.44	0.32	−0.30	−0.11
HAL_L	2.48	1.70	0.84	−1.52	−0.78	0.59	0.11	0.14	0.47	−0.03	−0.01	−0.02
HAL_R	2.75	2.06	1.13	−1.76	1.08	−0.90	0.08	0.11	0.11	−0.05	−0.03	0.04

A.8 Uncertainty of Regression Parameter for Joint Center Estimation

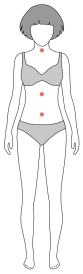

Female
torso joints

Probability density
Median value
Mean value
Reference value

Johnson distribution type
and coefficients

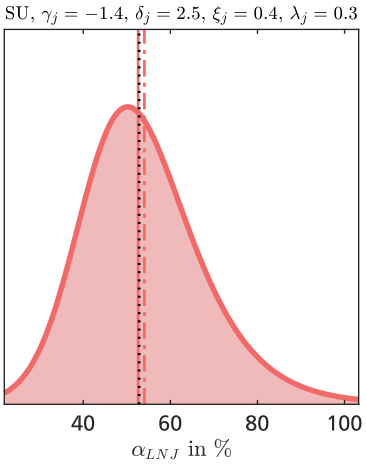

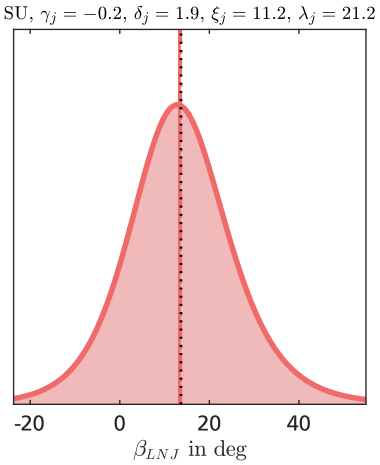

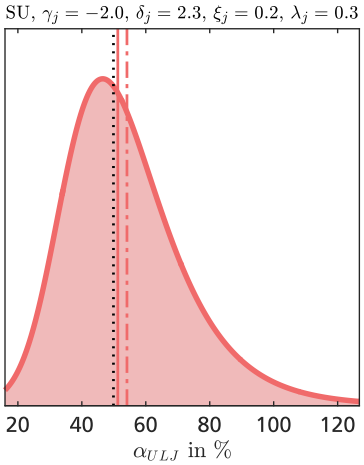

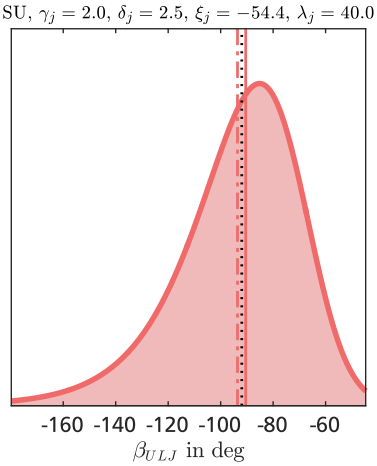

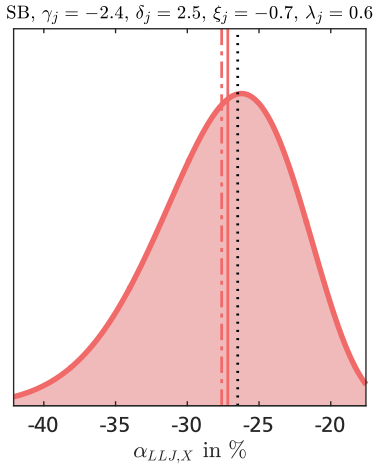

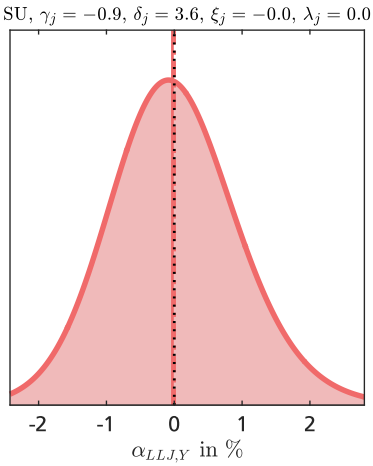

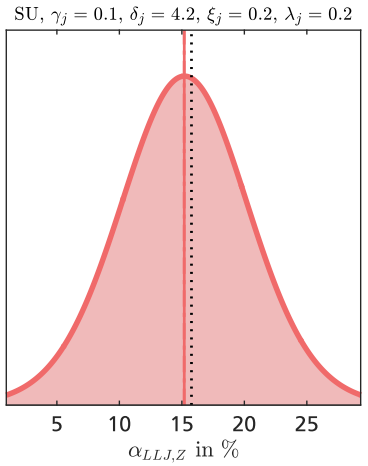

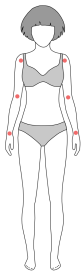

Female arm joints

Probability density
Median value
Mean value
Reference value

Johnson distribution type and coefficients

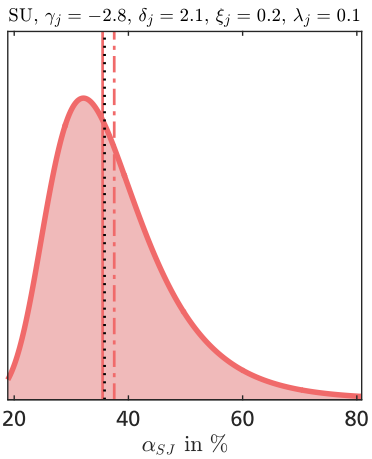

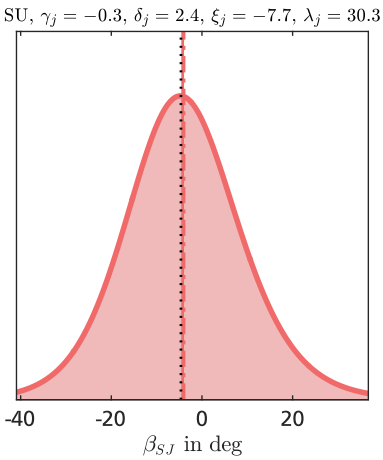

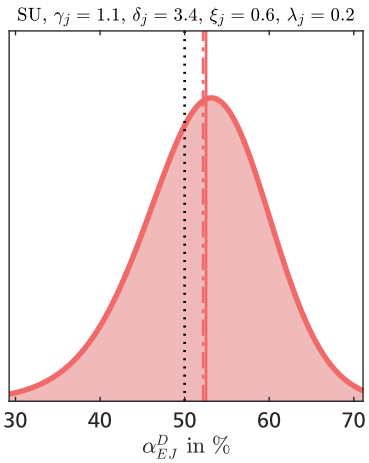

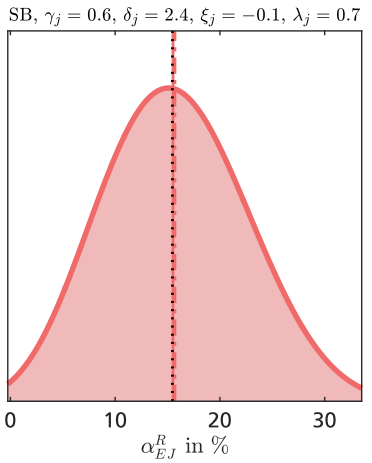

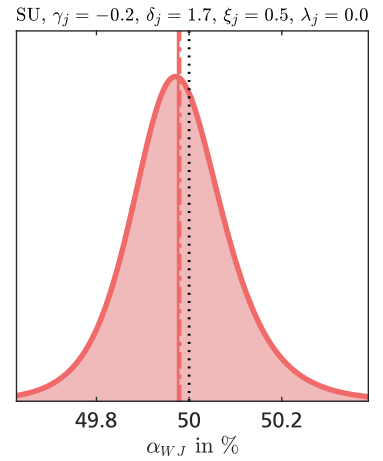

Copula covariance matrix for regression parameters of joint centers in the female torso and arm.

Σ_c	α_{LNJ}	β_{LNJ}	α_{ULJ}	β_{ULJ}	$\alpha_{LLJ,X}$	$\alpha_{LLJ,Y}$	$\alpha_{LLJ,Z}$	α_{SJ}	β_{SJ}	α^D_{EJ}	α^R_{EJ}	α_{WJ}
α_{LNJ}	0.0815	*	-	-	-	-	-	-	-	-	-	-
β_{LNJ}	0.0115	0.0359	-	-	-	-	-	-	-	-	-	-
α_{ULJ}	-	-	0.0835	*	-	-	-	-	-	-	-	-
β_{ULJ}	-	-	0.0000	0.0000	-	-	-	-	-	-	-	-
$\alpha_{LLJ,X}$	-	-	-	-	0.0825	*	*	-	-	-	-	-
$\alpha_{LLJ,Y}$	-	-	-	-	0.0015	0.0696	*	-	-	-	-	-
$\alpha_{LLJ,Z}$	-	-	-	-	-0.0084	-0.0004	0.0230	-	-	-	-	-
α_{SJ}	-	-	-	-	-	-	-	0.0832	*	*	*	*
β_{SJ}	-	-	-	-	-	-	-	0.0174	0.0403	*	*	*
α^D_{EJ}	-	-	-	-	-	-	-	-0.0004	0.0001	0.0007	*	*
α^R_{EJ}	-	-	-	-	-	-	-	-0.0046	0.0021	0.0002	0.0836	*
α_{WJ}	-	-	-	-	-	-	-	0.0061	0.0017	0.0007	-0.0026	0.0370

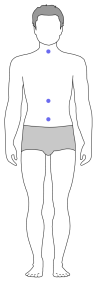

Male torso joints

Probability density
Median value
Mean value
Reference value

Johnson distribution type and coefficients

SU, $\gamma_j = -11.6$, $\delta_j = 6.8$, $\xi_j = -0.3$, $\lambda_j = 0.3$

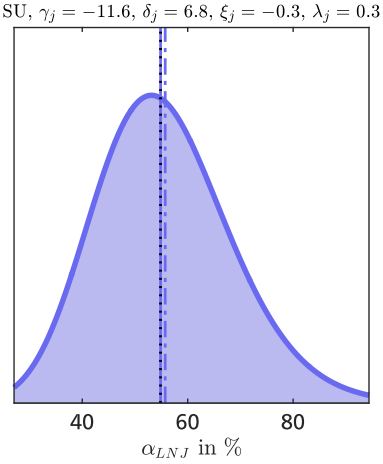

SU, $\gamma_j = -0.1$, $\delta_j = 2.2$, $\xi_j = 6.7$, $\lambda_j = 21.1$

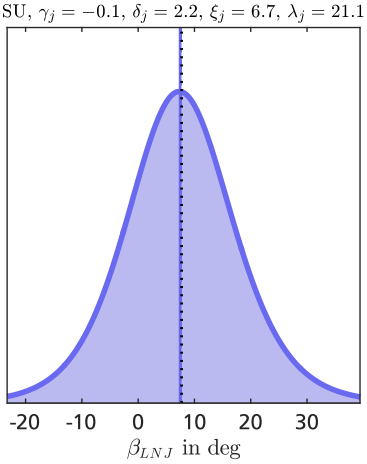

SU, $\gamma_j = -3.5$, $\delta_j = 2.9$, $\xi_j = 0.2$, $\lambda_j = 0.3$

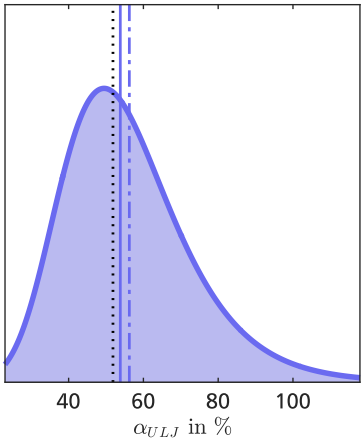

SU, $\gamma_j = 2.4$, $\delta_j = 3.0$, $\xi_j = -49.9$, $\lambda_j = 50.4$

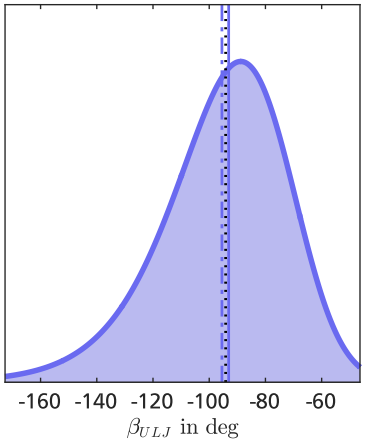

SB, $\gamma_j = -0.3$, $\delta_j = 2.2$, $\xi_j = -0.5$, $\lambda_j = 0.4$

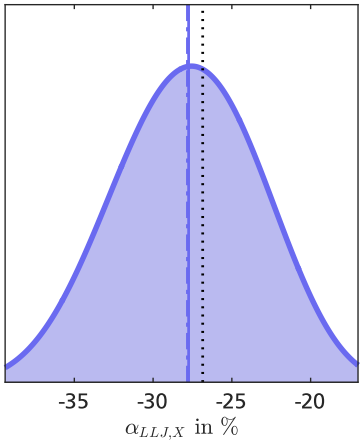

SU, $\gamma_j = -1.9$, $\delta_j = 5.7$, $\xi_j = -0.0$, $\lambda_j = 0.1$

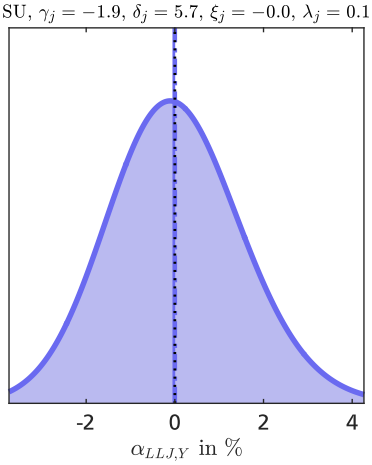

SB, $\gamma_j = 0.5$, $\delta_j = 2.9$, $\xi_j = -0.1$, $\lambda_j = 0.6$

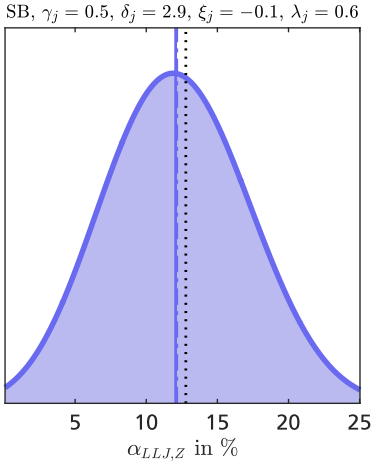

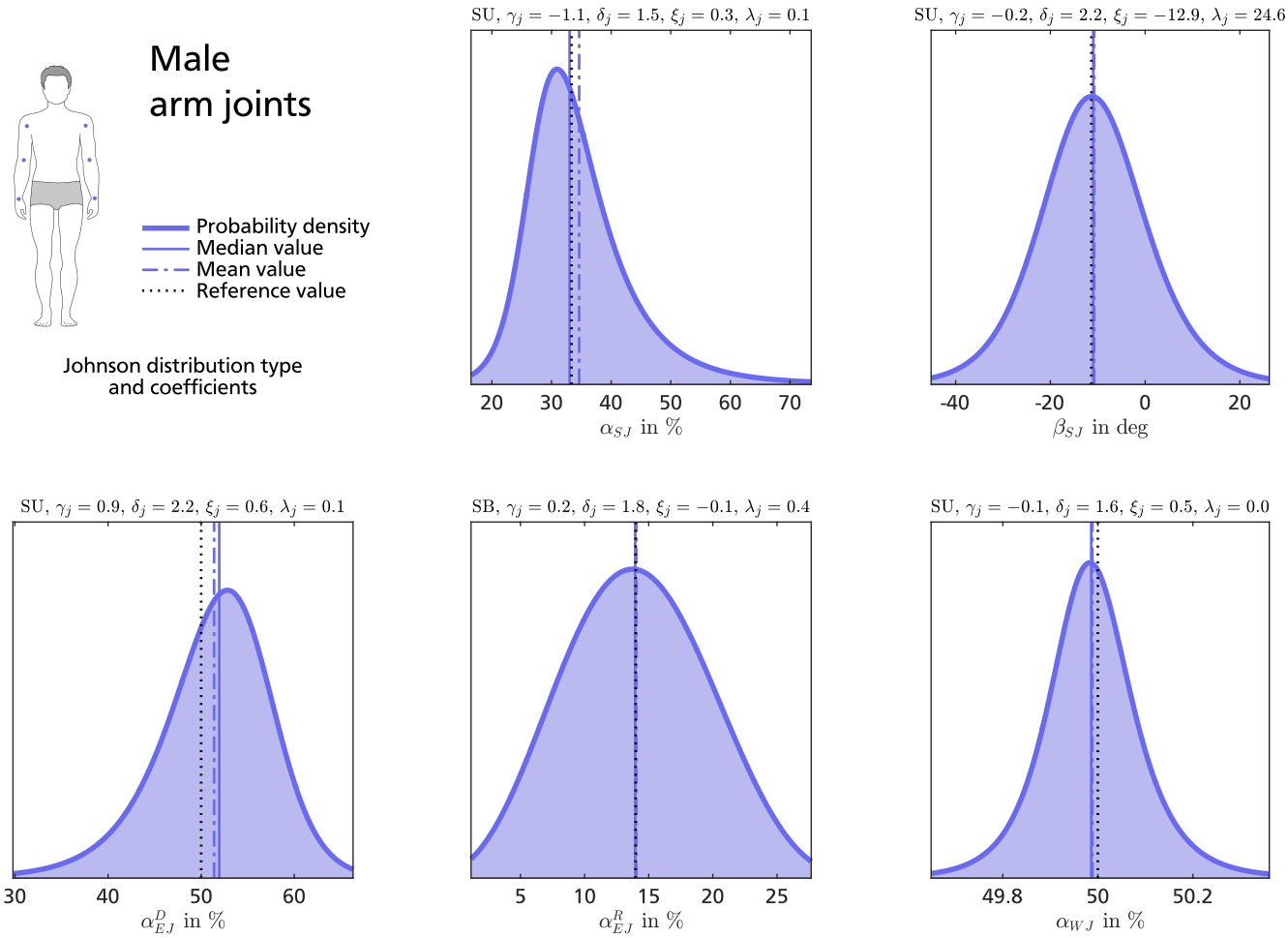

Copula covariance matrix for regression parameters of joint centers in the male torso and arm.

Σ_c	α_{LNJ}	β_{LNJ}	α_{ULJ}	β_{ULJ}	$\alpha_{LLJ,X}$	$\alpha_{LLJ,Y}$	$\alpha_{LLJ,Z}$	α_{SJ}	β_{SJ}	α^D_{EJ}	α^R_{EJ}	α_{WJ}
α_{LNJ}	0.0835	*	-	-	-	-	-	-	-	-	-	-
β_{LNJ}	0.0078	0.0311	-	-	-	-	-	-	-	-	-	-
α_{ULJ}	-	-	0.0831	*	-	-	-	-	-	-	-	-
β_{ULJ}	-	-	0.0000	0.0000	-	-	-	-	-	-	-	-
$\alpha_{LLJ,X}$	-	-	-	-	0.0833	*	*	-	-	-	-	-
$\alpha_{LLJ,Y}$	-	-	-	-	0.0001	0.0831	*	-	-	-	-	-
$\alpha_{LLJ,Z}$	-	-	-	-	-0.0189	-0.0002	0.0833	-	-	-	-	-
α_{SJ}	-	-	-	-	-	-	-	0.0781	*	*	*	*
β_{SJ}	-	-	-	-	-	-	-	0.0084	0.0353	*	*	*
α^D_{EJ}	-	-	-	-	-	-	-	-0.0002	0.0001	0.0016	*	*
α^R_{EJ}	-	-	-	-	-	-	-	-0.0024	0.0051	0.0015	0.0831	*
α_{WJ}	-	-	-	-	-	-	-	0.0045	0.0008	0.0015	0.0031	0.0322

A.9 Uncertainty of Regression Parameter for Anthropometric Parameter Estimation

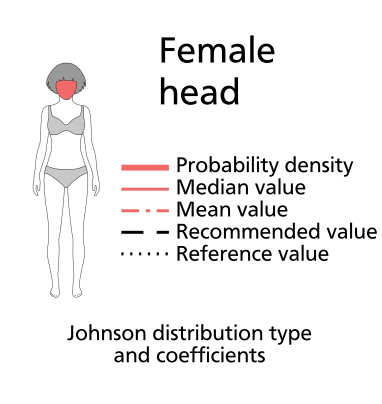

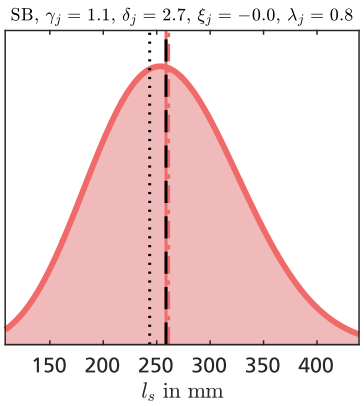

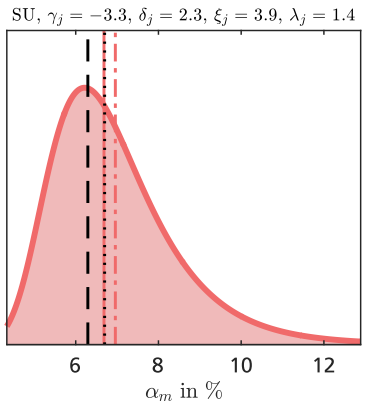

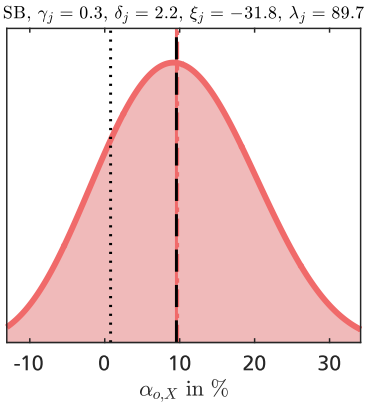

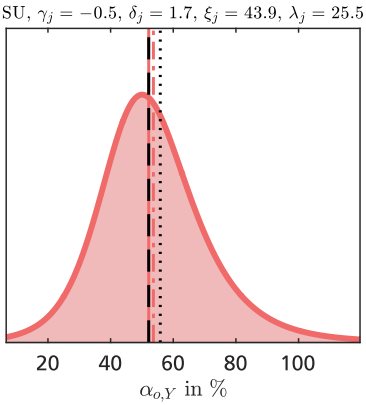

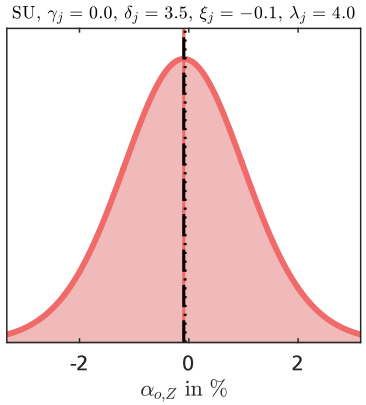

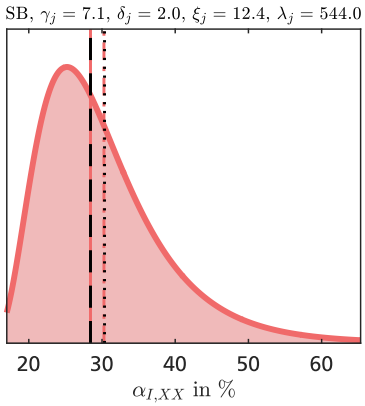

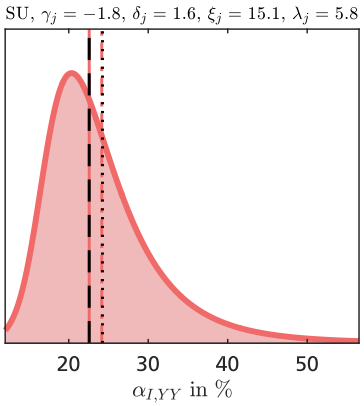

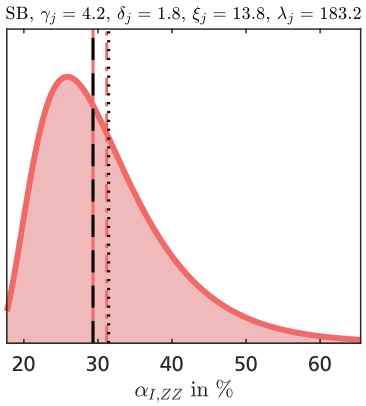

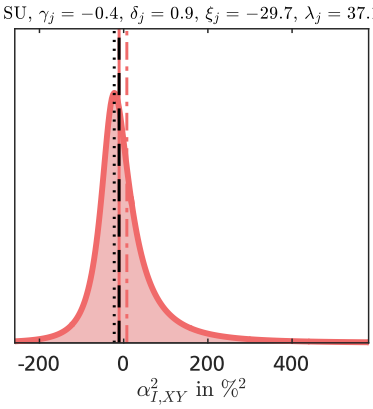

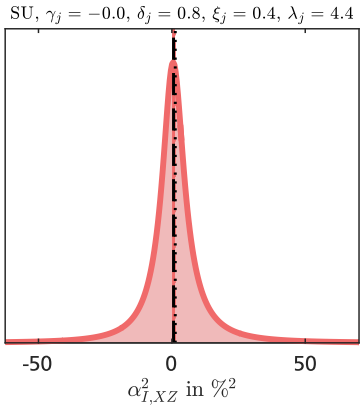

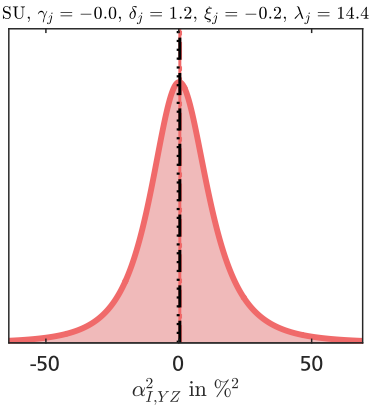

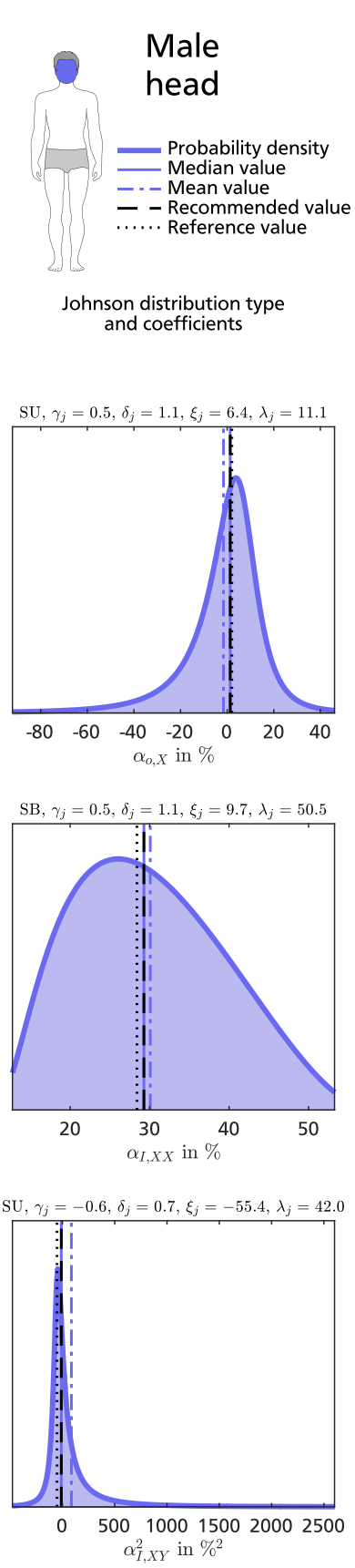
Male
head
Probability density
Median value
Mean value
Recommended value
Reference value
Johnson distribution type
and coefficients
SB, $\gamma_j = 6.0$, $\delta_j = 4.0$, $\xi_j = -0.3$, $\lambda_j = 3.4$
200 400 600
l_s in mm
SU, $\gamma_j = -2.8$, $\delta_j = 2.5$, $\xi_j = 4.3$, $\lambda_j = 1.8$
6 8 10
α_m in %
SU, $\gamma_j = 0.5$, $\delta_j = 1.1$, $\xi_j = 6.4$, $\lambda_j = 11.1$
-80 -60 -40 -20 0 20 40
$\alpha_{o,X}$ in %
SB, $\gamma_j = -0.1$, $\delta_j = 0.6$, $\xi_j = 14.9$, $\lambda_j = 78.6$
20 40 60 80
$\alpha_{o,Y}$ in %
SU, $\gamma_j = -0.0$, $\delta_j = 1.3$, $\xi_j = 0.1$, $\lambda_j = 1.3$
-4 -2 0 2 4
$\alpha_{o,Z}$ in %
SB, $\gamma_j = 0.5$, $\delta_j = 1.1$, $\xi_j = 9.7$, $\lambda_j = 50.5$
20 30 40 50
$\alpha_{I,XX}$ in %
SB, $\gamma_j = 3.2$, $\delta_j = 1.2$, $\xi_j = 7.5$, $\lambda_j = 161.8$
10 20 30 40 50 60
$\alpha_{I,YY}$ in %
SU, $\gamma_j = -1.5$, $\delta_j = 2.0$, $\xi_j = 19.5$, $\lambda_j = 15.1$
20 30 40 50 60 70
$\alpha_{I,ZZ}$ in %
SU, $\gamma_j = -0.6$, $\delta_j = 0.7$, $\xi_j = -55.4$, $\lambda_j = 42.0$
0 500 1000 1500 2000 2500
$\alpha^2_{I,XY}$ in %^{2}
SU, $\gamma_j = 0.2$, $\delta_j = 0.6$, $\xi_j = -1.1$, $\lambda_j = 4.4$
-200 -100 0 100
$\alpha^2_{I,XZ}$ in %^{2}
SU, $\gamma_j = -0.2$, $\delta_j = 0.9$, $\xi_j = 2.3$, $\lambda_j = 10.3$
-50 0 50 100
$\alpha^2_{I,YZ}$ in %^{2}

Copula covariance matrix for regression parameters of anthropometric parameters in the female head.

Σ_c	α_m	$\alpha_{o,X}$	$\alpha_{o,Y}$	$\alpha_{o,Z}$	$\alpha_{I,XX}$	$\alpha_{I,YY}$	$\alpha_{I,ZZ}$	$\alpha_{I,XY}$	$\alpha_{I,XZ}$	$\alpha_{I,YZ}$
α_m	0.0841	$*$	$*$	$*$	$*$	$*$	$*$	$*$	$*$	$*$
$\alpha_{o,X}$	0.0013	0.0839	$*$	$*$	$*$	$*$	$*$	$*$	$*$	$*$
$\alpha_{o,Y}$	-0.0007	-0.0424	0.0555	$*$	$*$	$*$	$*$	$*$	$*$	$*$
$\alpha_{o,Z}$	0.0006	-0.0019	0.0035	0.0262	$*$	$*$	$*$	$*$	$*$	$*$
$\alpha_{I,XX}$	-0.0020	-0.0122	0.0473	0.0050	0.0827	$*$	$*$	$*$	$*$	$*$
$\alpha_{I,YY}$	-0.0020	-0.0110	0.0449	0.0048	0.0782	0.0833	$*$	$*$	$*$	$*$
$\alpha_{I,ZZ}$	-0.0020	-0.0132	0.0476	0.0048	0.0790	0.0771	0.0821	$*$	$*$	$*$
$\alpha_{I,XY}$	0.0018	-0.0163	0.0245	0.0017	0.0271	0.0312	0.0315	0.0490	$*$	$*$
$\alpha_{I,XZ}$	-0.0007	-0.0030	0.0057	0.0019	0.0076	0.0083	0.0111	0.0053	0.0280	$*$
$\alpha_{I,YZ}$	-0.0005	-0.0004	0.0049	-0.0095	0.0100	0.0096	0.0104	0.0034	0.0018	0.0280

Copula covariance matrix for regression parameters of anthropometric parameters in the male head.

Σ_c	α_m	$\alpha_{o,X}$	$\alpha_{o,Y}$	$\alpha_{o,Z}$	$\alpha_{I,XX}$	$\alpha_{I,YY}$	$\alpha_{I,ZZ}$	$\alpha_{I,XY}$	$\alpha_{I,XZ}$	$\alpha_{I,YZ}$
α_m	0.0831	$*$	$*$	$*$	$*$	$*$	$*$	$*$	$*$	$*$
$\alpha_{o,X}$	0.0000	0.0101	$*$	$*$	$*$	$*$	$*$	$*$	$*$	$*$
$\alpha_{o,Y}$	-0.0002	-0.0027	0.0841	$*$	$*$	$*$	$*$	$*$	$*$	$*$
$\alpha_{o,Z}$	-0.0005	0.0001	-0.0034	0.0254	$*$	$*$	$*$	$*$	$*$	$*$
$\alpha_{I,XX}$	-0.0011	-0.0033	0.0664	0.0007	0.0815	$*$	$*$	$*$	$*$	$*$
$\alpha_{I,YY}$	-0.0029	-0.0048	-0.0092	0.0091	0.0251	0.0837	$*$	$*$	$*$	$*$
$\alpha_{I,ZZ}$	-0.0009	-0.0058	0.0517	0.0033	0.0726	0.0385	0.0750	$*$	$*$	$*$
$\alpha_{I,XY}$	0.0003	-0.0108	0.0008	0.0039	0.0178	0.0357	0.0285	0.0561	$*$	$*$
$\alpha_{I,XZ}$	0.0002	-0.0002	-0.0020	0.0042	0.0012	0.0072	0.0027	0.0033	0.0164	$*$
$\alpha_{I,YZ}$	-0.0005	-0.0012	0.0073	-0.0072	0.0147	0.0156	0.0158	0.0077	-0.0004	0.0367

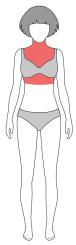

Female thorax

Probability density
Median value
Mean value
Recommended value
Reference value

Johnson distribution type and coefficients

SU, $\gamma_j = -8.7$, $\delta_j = 16.7$, $\xi_j = 0.1$, $\lambda_j = 0.4$

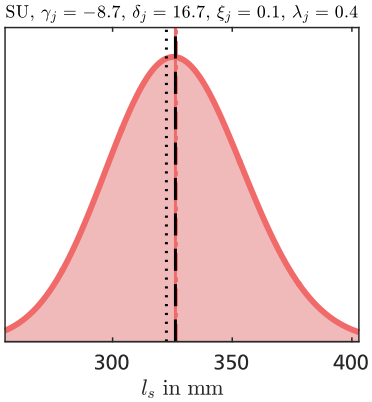

l_s in mm

SU, $\gamma_j = -1.7$, $\delta_j = 2.2$, $\xi_j = 16.2$, $\lambda_j = 12.5$

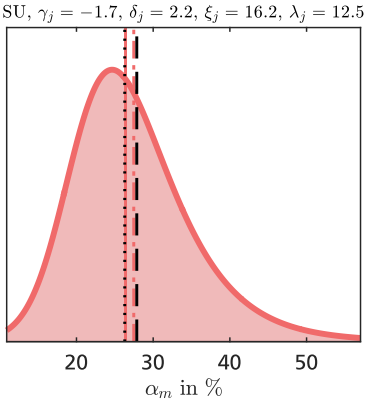

α_m in %

SB, $\gamma_j = 0.3$, $\delta_j = 1.0$, $\xi_j = -28.1$, $\lambda_j = 75.7$

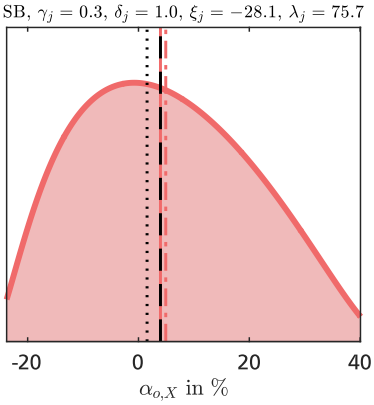

$\alpha_{o,X}$ in %

SB, $\gamma_j = -0.2$, $\delta_j = 1.8$, $\xi_j = -77.7$, $\lambda_j = 59.2$

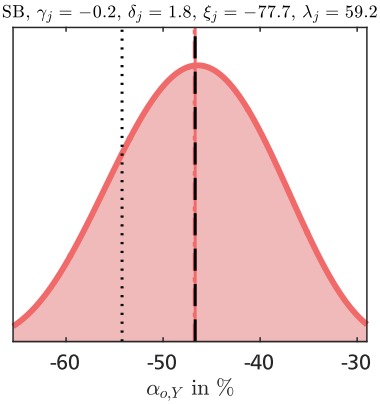

$\alpha_{o,Y}$ in %

SU, $\gamma_j = 0.1$, $\delta_j = 2.9$, $\xi_j = 0.2$, $\lambda_j = 2.5$

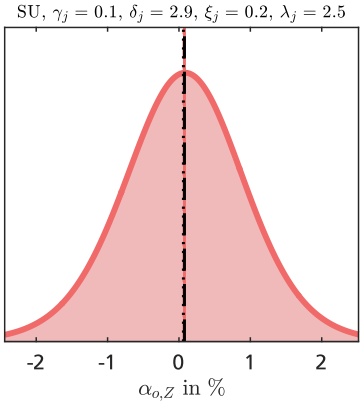

$\alpha_{o,Z}$ in %

SU, $\gamma_j = -6.2$, $\delta_j = 5.5$, $\xi_j = 3.5$, $\lambda_j = 24.0$

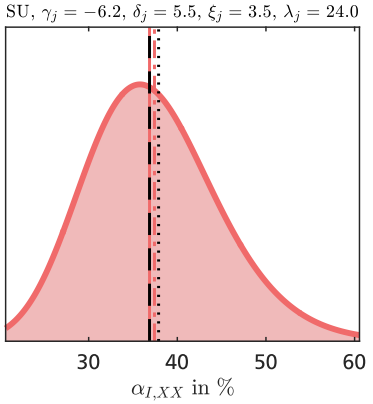

$\alpha_{I,XX}$ in %

SU, $\gamma_j = -1.0$, $\delta_j = 3.0$, $\xi_j = 25.8$, $\lambda_j = 18.6$

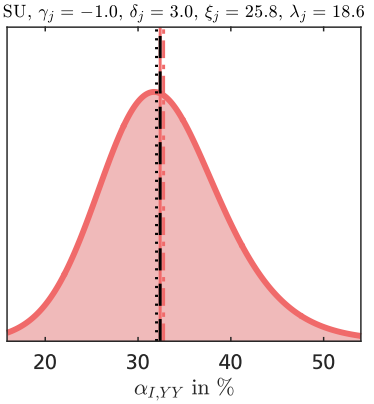

$\alpha_{I,YY}$ in %

SU, $\gamma_j = -0.2$, $\delta_j = 2.0$, $\xi_j = 31.8$, $\lambda_j = 13.5$

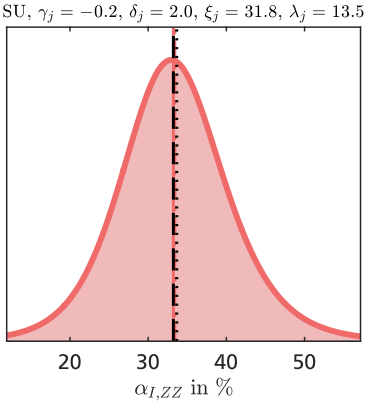

$\alpha_{I,ZZ}$ in %

SU, $\gamma_j = 0.5$, $\delta_j = 1.2$, $\xi_j = 11.6$, $\lambda_j = 190.3$

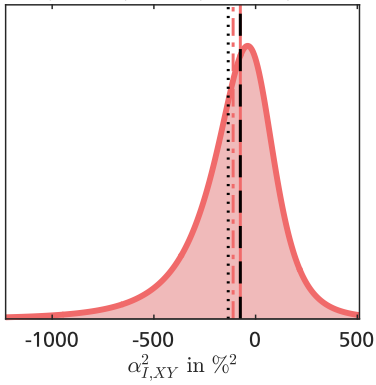

$\alpha^2_{I,XY}$ in %^{2}

SU, $\gamma_j = 0.2$, $\delta_j = 0.8$, $\xi_j = -1.6$, $\lambda_j = 19.4$

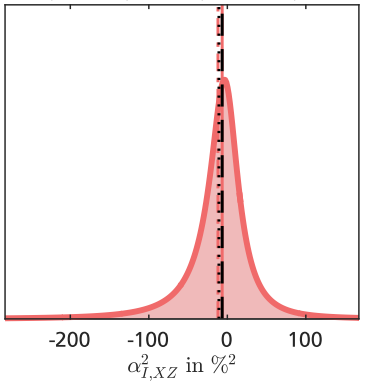

$\alpha^2_{I,XZ}$ in %^{2}

SU, $\gamma_j = -0.0$, $\delta_j = 0.8$, $\xi_j = 1.5$, $\lambda_j = 18.1$

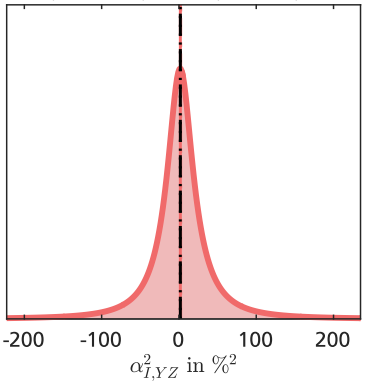

$\alpha^2_{I,YZ}$ in %^{2}

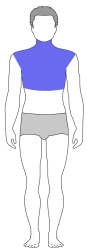

Male thorax

Probability density
Median value
Mean value
Recommended value
Reference value

Johnson distribution type and coefficients

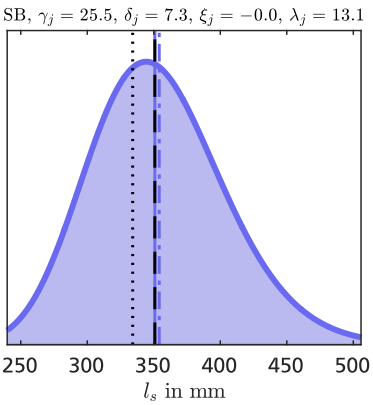

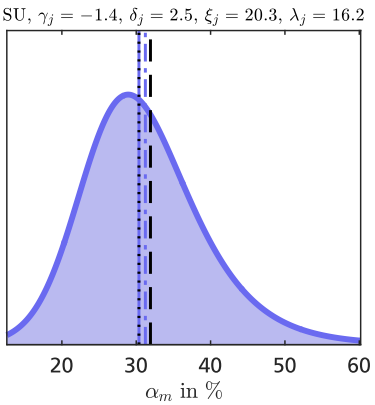

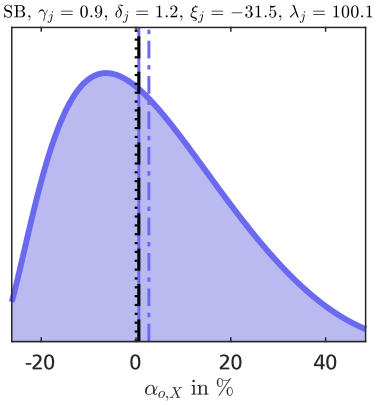

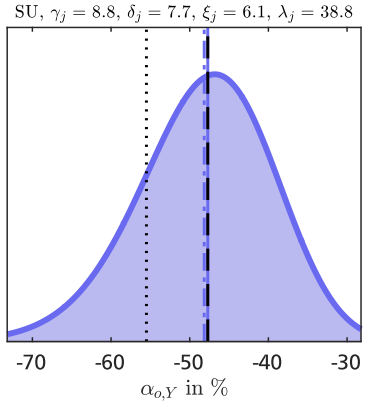

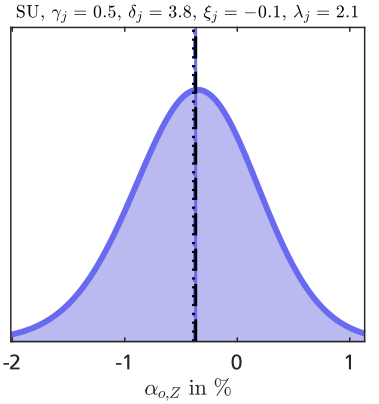

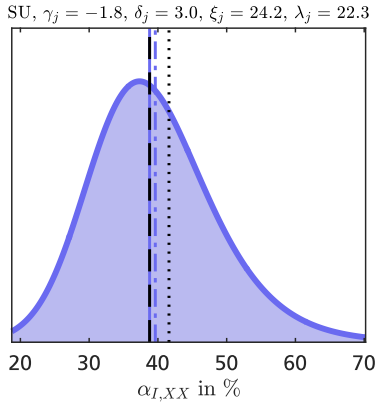

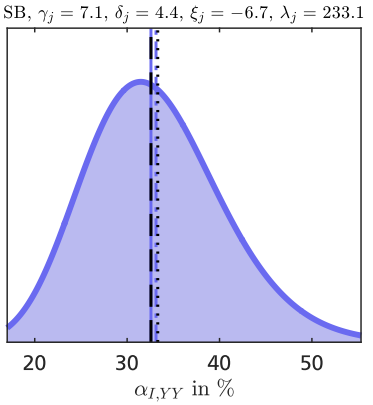

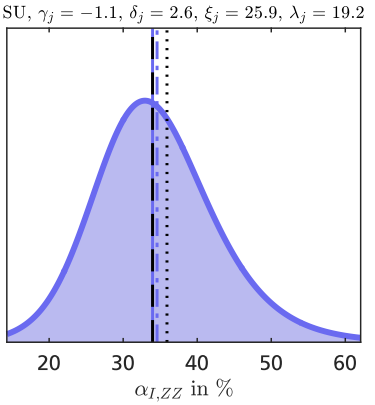

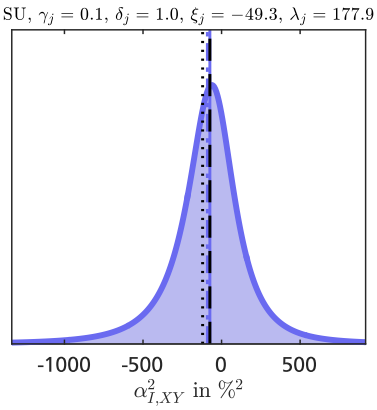

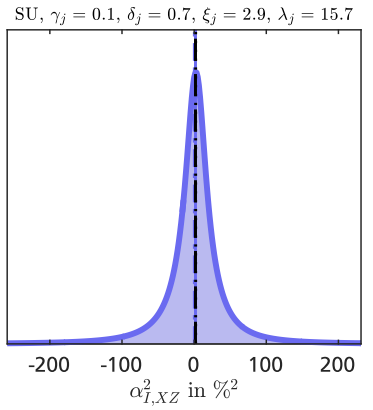

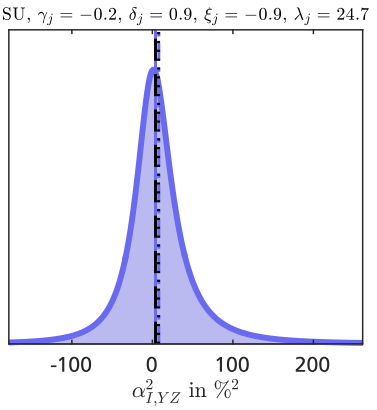

Copula covariance matrix for regression parameters of anthropometric parameters in the female thorax.

Σ_c	α_m	$\alpha_{o,X}$	$\alpha_{o,Y}$	$\alpha_{o,Z}$	$\alpha_{I,XX}$	$\alpha_{I,YY}$	$\alpha_{I,ZZ}$	$\alpha_{I,XY}$	$\alpha_{I,XZ}$	$\alpha_{I,YZ}$
α_m	0.0824	$*$	$*$	$*$	$*$	$*$	$*$	$*$	$*$	$*$
$\alpha_{o,X}$	0.0006	0.0820	$*$	$*$	$*$	$*$	$*$	$*$	$*$	$*$
$\alpha_{o,Y}$	0.0056	0.0090	0.0837	$*$	$*$	$*$	$*$	$*$	$*$	$*$
$\alpha_{o,Z}$	0.0008	-0.0004	-0.0020	0.0211	$*$	$*$	$*$	$*$	$*$	$*$
$\alpha_{I,XX}$	-0.0265	0.0089	-0.0164	0.0012	0.0829	$*$	$*$	$*$	$*$	$*$
$\alpha_{I,YY}$	-0.0269	-0.0069	-0.0128	0.0001	0.0441	0.0747	$*$	$*$	$*$	$*$
$\alpha_{I,ZZ}$	-0.0189	0.0009	-0.0101	0.0008	0.0232	0.0217	0.0366	$*$	$*$	$*$
$\alpha_{I,XY}$	-0.0013	0.0067	0.0041	-0.0003	0.0016	0.0017	0.0014	0.0067	$*$	$*$
$\alpha_{I,XZ}$	-0.0022	-0.0007	-0.0012	0.0005	-0.0016	0.0009	0.0035	0.0008	0.0168	$*$
$\alpha_{I,YZ}$	-0.0034	-0.0054	-0.0039	0.0001	0.0057	0.0049	0.0020	-0.0007	0.0011	0.0275

Copula covariance matrix for regression parameters of anthropometric parameters in the male thorax.

Σ_c	α_m	$\alpha_{o,X}$	$\alpha_{o,Y}$	$\alpha_{o,Z}$	$\alpha_{I,XX}$	$\alpha_{I,YY}$	$\alpha_{I,ZZ}$	$\alpha_{I,XY}$	$\alpha_{I,XZ}$	$\alpha_{I,YZ}$
α_m	0.0800	$*$	$*$	$*$	$*$	$*$	$*$	$*$	$*$	$*$
$\alpha_{o,X}$	-0.0010	0.0819	$*$	$*$	$*$	$*$	$*$	$*$	$*$	$*$
$\alpha_{o,Y}$	0.0000	0.0000	0.0008	$*$	$*$	$*$	$*$	$*$	$*$	$*$
$\alpha_{o,Z}$	-0.0002	0.0002	0.0000	0.0071	$*$	$*$	$*$	$*$	$*$	$*$
$\alpha_{I,XX}$	-0.0238	0.0094	-0.0004	-0.0003	0.0830	$*$	$*$	$*$	$*$	$*$
$\alpha_{I,YY}$	-0.0274	0.0011	-0.0003	-0.0004	0.0514	0.0827	$*$	$*$	$*$	$*$
$\alpha_{I,ZZ}$	-0.0228	0.0052	-0.0003	0.0002	0.0422	0.0424	0.0750	$*$	$*$	$*$
$\alpha_{I,XY}$	-0.0013	0.0218	0.0001	0.0003	0.0010	0.0028	0.0018	0.0183	$*$	$*$
$\alpha_{I,XZ}$	-0.0027	-0.0028	0.0000	-0.0004	0.0075	0.0027	0.0036	-0.0015	0.0242	$*$
$\alpha_{I,YZ}$	-0.0038	-0.0006	0.0000	-0.0001	0.0066	-0.0004	0.0156	-0.0005	0.0033	0.0356

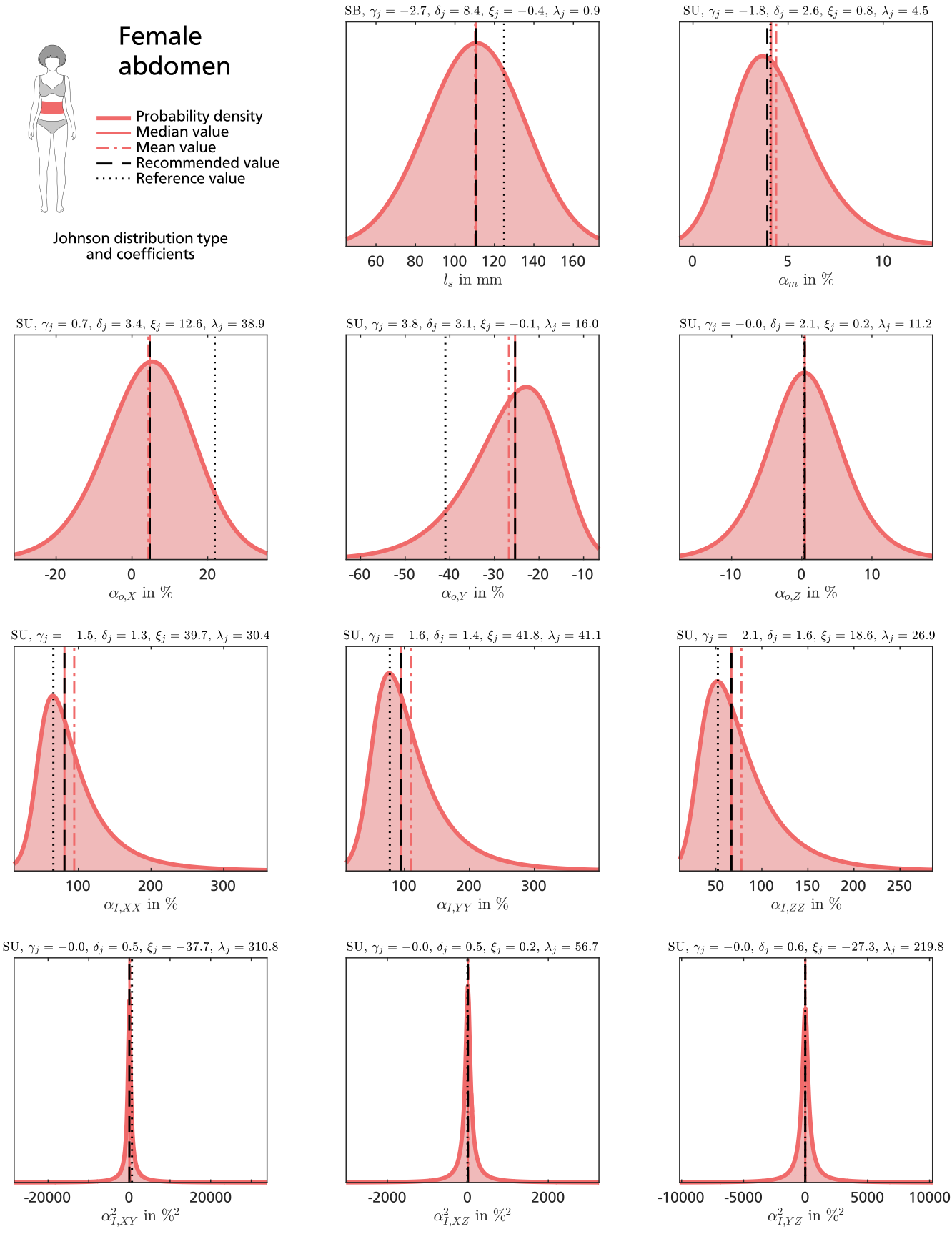
Female abdomen
Probability density
Median value
Mean value
Recommended value
Reference value
Johnson distribution type and coefficients
SB, $\gamma_j = -2.7$, $\delta_j = 8.4$, $\xi_j = -0.4$, $\lambda_j = 0.9$
60 80 100 120 140 160
l_s in mm
SU, $\gamma_j = -1.8$, $\delta_j = 2.6$, $\xi_j = 0.8$, $\lambda_j = 4.5$
0 5 10
α_m in %
SU, $\gamma_j = 0.7$, $\delta_j = 3.4$, $\xi_j = 12.6$, $\lambda_j = 38.9$
-20 0 20
$\alpha_{o,X}$ in %
SU, $\gamma_j = 3.8$, $\delta_j = 3.1$, $\xi_j = -0.1$, $\lambda_j = 16.0$
-60 -50 -40 -30 -20 -10
$\alpha_{o,Y}$ in %
SU, $\gamma_j = -0.0$, $\delta_j = 2.1$, $\xi_j = 0.2$, $\lambda_j = 11.2$
-10 0 10
$\alpha_{o,Z}$ in %
SU, $\gamma_j = -1.5$, $\delta_j = 1.3$, $\xi_j = 39.7$, $\lambda_j = 30.4$
100 200 300
$\alpha_{I,XX}$ in %
SU, $\gamma_j = -1.6$, $\delta_j = 1.4$, $\xi_j = 41.8$, $\lambda_j = 41.1$
100 200 300
$\alpha_{I,YY}$ in %
SU, $\gamma_j = -2.1$, $\delta_j = 1.6$, $\xi_j = 18.6$, $\lambda_j = 26.9$
50 100 150 200 250
$\alpha_{I,ZZ}$ in %
SU, $\gamma_j = -0.0$, $\delta_j = 0.5$, $\xi_j = -37.7$, $\lambda_j = 310.8$
-20000 0 20000
$\alpha^2_{I,XY}$ in %^{2}
SU, $\gamma_j = -0.0$, $\delta_j = 0.5$, $\xi_j = 0.2$, $\lambda_j = 56.7$
-2000 0 2000
$\alpha^2_{I,XZ}$ in %^{2}
SU, $\gamma_j = -0.0$, $\delta_j = 0.6$, $\xi_j = -27.3$, $\lambda_j = 219.8$
-10000 -5000 0 5000 10000
$\alpha^2_{I,YZ}$ in %^{2}

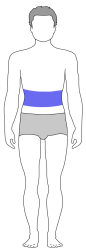

Male abdomen

Probability density
Median value
Mean value
Recommended value
Reference value

Johnson distribution type and coefficients

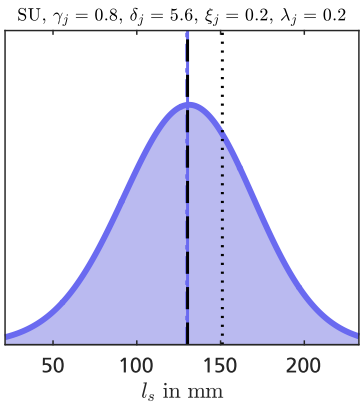

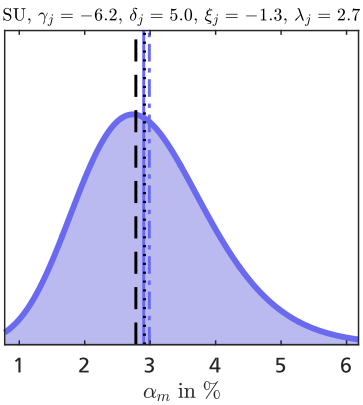

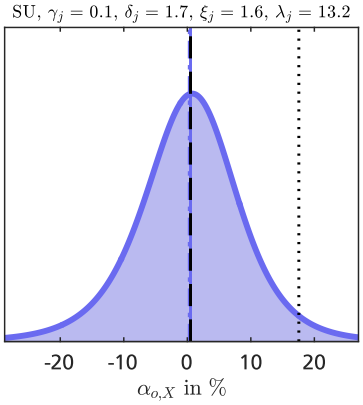

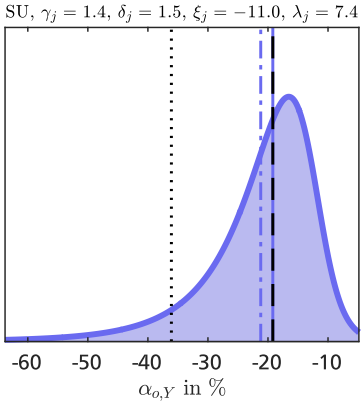

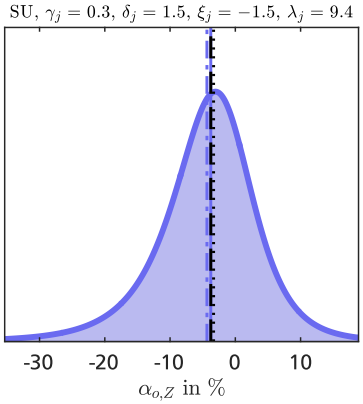

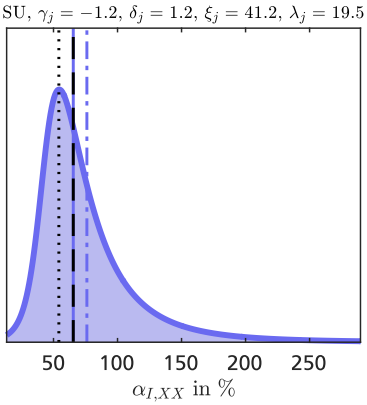

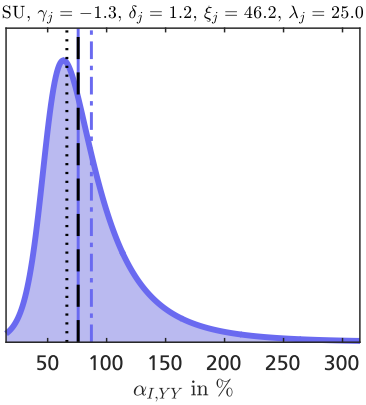

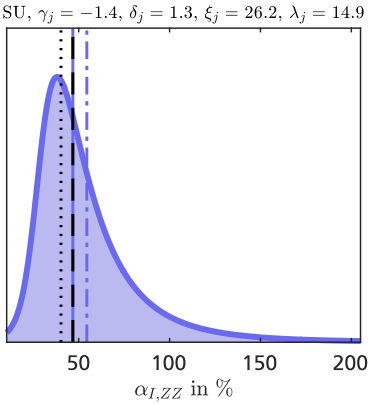

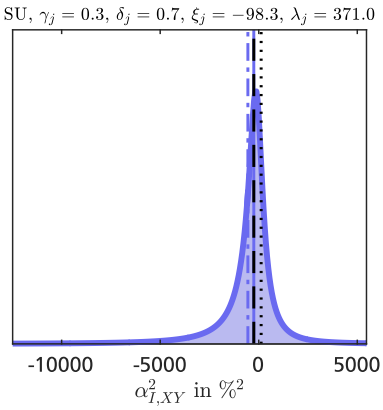

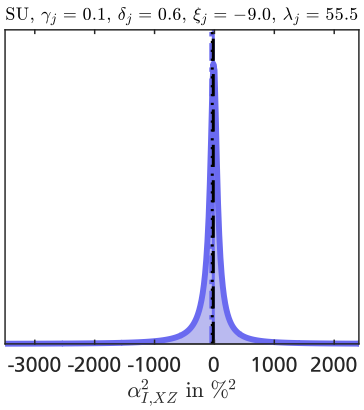

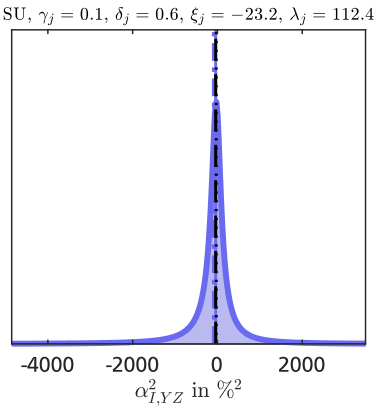

Copula covariance matrix for regression parameters of anthropometric parameters in the female abdomen.

Σ_c	α_m	$\alpha_{o,X}$	$\alpha_{o,Y}$	$\alpha_{o,Z}$	$\alpha_{I,XX}$	$\alpha_{I,YY}$	$\alpha_{I,ZZ}$	$\alpha_{I,XY}$	$\alpha_{I,XZ}$	$\alpha_{I,YZ}$
α_m	0.0828	$*$	$*$	$*$	$*$	$*$	$*$	$*$	$*$	$*$
$\alpha_{o,X}$	0.0003	0.0044	$*$	$*$	$*$	$*$	$*$	$*$	$*$	$*$
$\alpha_{o,Y}$	0.0000	0.0000	0.0000	$*$	$*$	$*$	$*$	$*$	$*$	$*$
$\alpha_{o,Z}$	0.0001	0.0000	0.0000	0.0282	$*$	$*$	$*$	$*$	$*$	$*$
$\alpha_{I,XX}$	-0.0451	0.0015	0.0000	0.0029	0.0811	$*$	$*$	$*$	$*$	$*$
$\alpha_{I,YY}$	-0.0440	0.0017	0.0000	0.0029	0.0561	0.0832	$*$	$*$	$*$	$*$
$\alpha_{I,ZZ}$	-0.0425	0.0010	0.0000	0.0033	0.0469	0.0456	0.0813	$*$	$*$	$*$
$\alpha_{I,XY}$	-0.0067	-0.0009	0.0000	0.0015	0.0107	0.0136	0.0091	0.0286	$*$	$*$
$\alpha_{I,XZ}$	-0.0084	0.0005	0.0000	0.0015	0.0120	0.0102	0.0073	0.0005	0.0278	$*$
$\alpha_{I,YZ}$	-0.0077	-0.0002	0.0000	0.0101	0.0101	0.0092	0.0141	0.0026	0.0021	0.0261

Copula covariance matrix for regression parameters of anthropometric parameters in the male abdomen.

Σ_c	α_m	$\alpha_{o,X}$	$\alpha_{o,Y}$	$\alpha_{o,Z}$	$\alpha_{I,XX}$	$\alpha_{I,YY}$	$\alpha_{I,ZZ}$	$\alpha_{I,XY}$	$\alpha_{I,XZ}$	$\alpha_{I,YZ}$
α_m	0.0834	$*$	$*$	$*$	$*$	$*$	$*$	$*$	$*$	$*$
$\alpha_{o,X}$	-0.0011	0.0195	$*$	$*$	$*$	$*$	$*$	$*$	$*$	$*$
$\alpha_{o,Y}$	-0.0001	0.0001	0.0001	$*$	$*$	$*$	$*$	$*$	$*$	$*$
$\alpha_{o,Z}$	0.0002	-0.0002	-0.0001	0.0120	$*$	$*$	$*$	$*$	$*$	$*$
$\alpha_{I,XX}$	-0.0274	0.0043	-0.0004	0.0019	0.0782	$*$	$*$	$*$	$*$	$*$
$\alpha_{I,YY}$	-0.0276	0.0037	-0.0005	0.0024	0.0618	0.0798	$*$	$*$	$*$	$*$
$\alpha_{I,ZZ}$	-0.0267	0.0049	-0.0004	0.0017	0.0570	0.0553	0.0801	$*$	$*$	$*$
$\alpha_{I,XY}$	-0.0006	0.0004	0.0000	-0.0003	0.0066	-0.0003	0.0049	0.0138	$*$	$*$
$\alpha_{I,XZ}$	-0.0035	0.0006	-0.0001	0.0001	0.0074	0.0080	0.0067	-0.0004	0.0206	$*$
$\alpha_{I,YZ}$	-0.0045	0.0007	-0.0001	0.0023	0.0089	0.0086	0.0112	0.0004	0.0013	0.0215

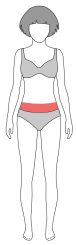

Female pelvis

Probability density
Median value
Mean value
Recommended value
Reference value

Johnson distribution type and coefficients

SU, $\gamma_j = -5.1$, $\delta_j = 7.0$, $\xi_j = 0.0$, $\lambda_j = 0.1$

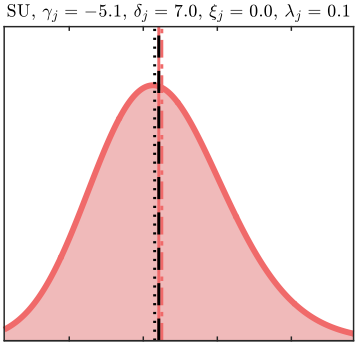

l_s in mm

SU, $\gamma_j = -1.7$, $\delta_j = 2.9$, $\xi_j = 6.3$, $\lambda_j = 13.7$

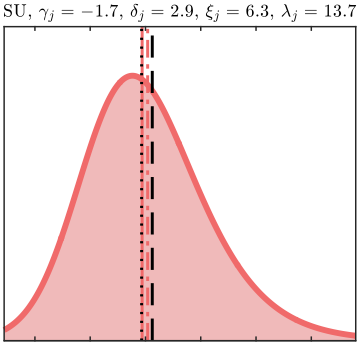

α_m in %

SU, $\gamma_j = 0.8$, $\delta_j = 3.3$, $\xi_j = 10.0$, $\lambda_j = 60.4$

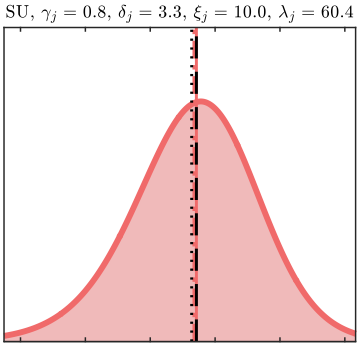

$\alpha_{o,X}$ in %

SB, $\gamma_j = -0.4$, $\delta_j = 1.2$, $\xi_j = -72.3$, $\lambda_j = 82.0$

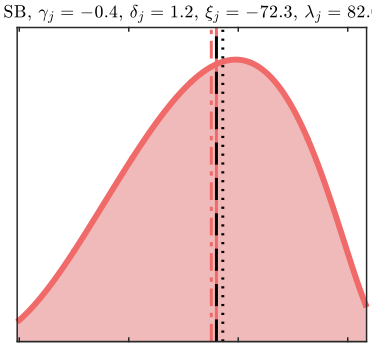

$\alpha_{o,Y}$ in %

SB, $\gamma_j = -21.3$, $\delta_j = 13.4$, $\xi_j = -956.0$, $\lambda_j = 1151.5$

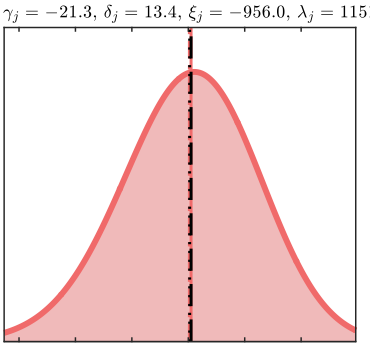

$\alpha_{o,Z}$ in %

SU, $\gamma_j = -1.0$, $\delta_j = 1.5$, $\xi_j = 70.3$, $\lambda_j = 35.5$

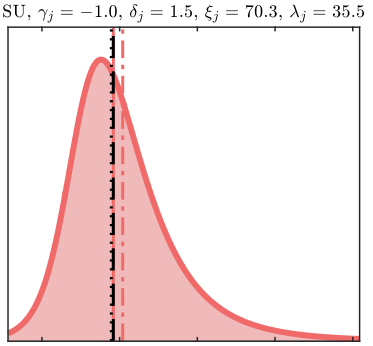

$\alpha_{I,XX}$ in %

SU, $\gamma_j = -1.3$, $\delta_j = 2.0$, $\xi_j = 66.3$, $\lambda_j = 55.2$

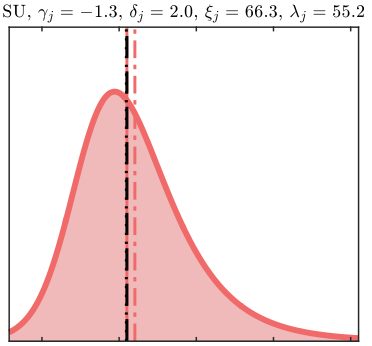

$\alpha_{I,YY}$ in %

SU, $\gamma_j = -1.6$, $\delta_j = 2.0$, $\xi_j = 41.4$, $\lambda_j = 45.0$

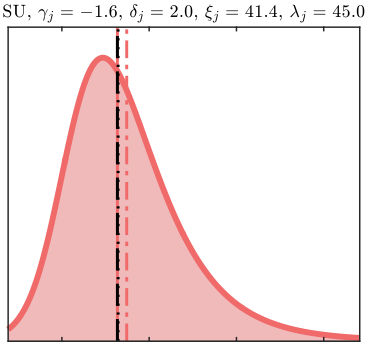

$\alpha_{I,ZZ}$ in %

SU, $\gamma_j = 0.4$, $\delta_j = 1.0$, $\xi_j = -115.5$, $\lambda_j = 2007.2$

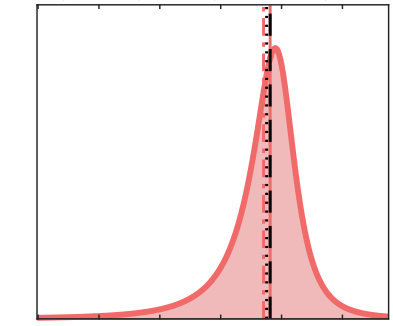

$\alpha^2_{I,XY}$ in %^{2}

SU, $\gamma_j = -0.0$, $\delta_j = 0.7$, $\xi_j = -19.9$, $\lambda_j = 165.4$

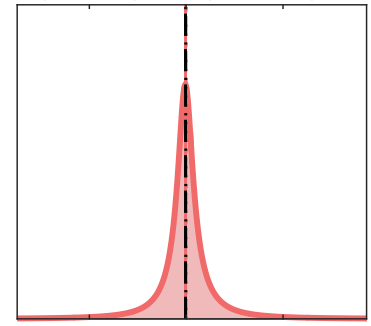

$\alpha^2_{I,XZ}$ in %^{2}

SU, $\gamma_j = -0.0$, $\delta_j = 0.7$, $\xi_j = -5.5$, $\lambda_j = 134.7$

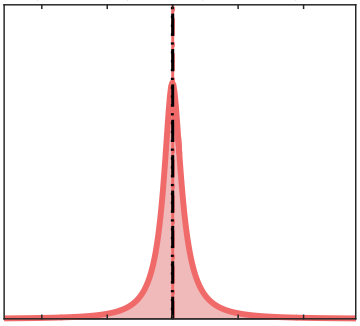

$\alpha^2_{I,YZ}$ in %^{2}

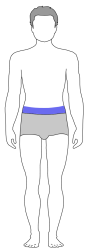

Male pelvis

Probability density
Median value
Mean value
Recommended value
Reference value

Johnson distribution type and coefficients

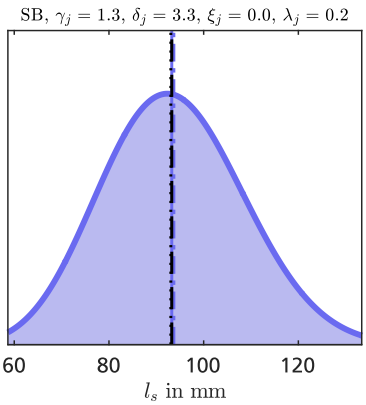

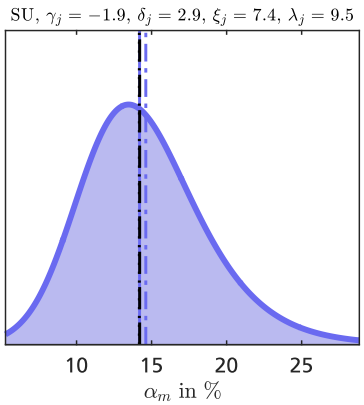

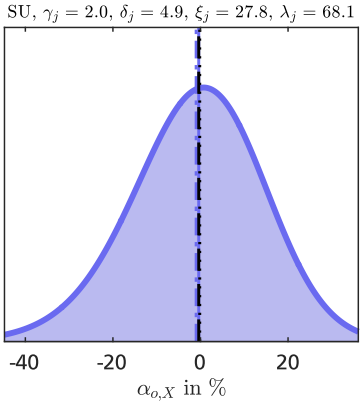

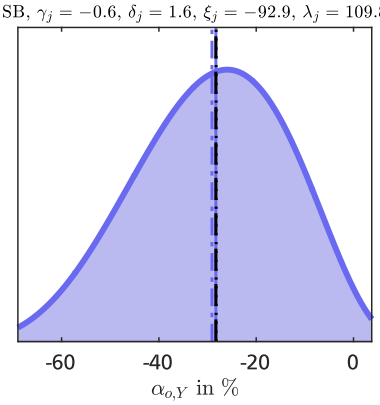

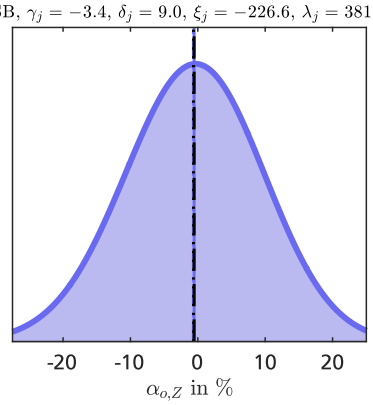

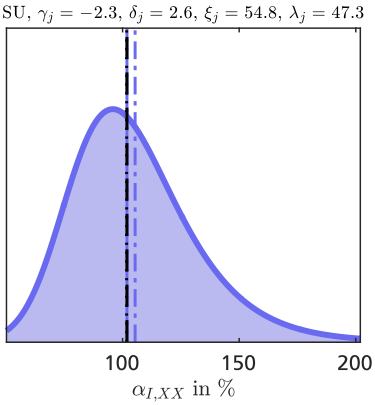

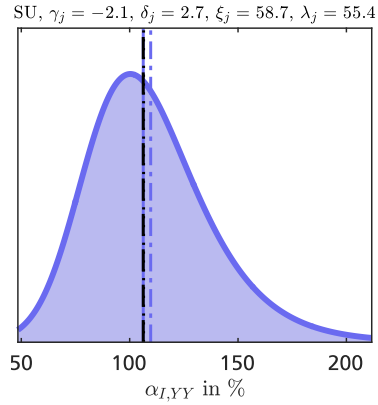

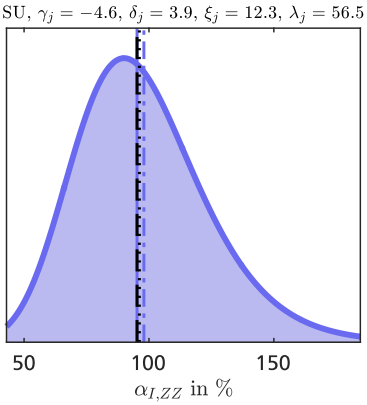

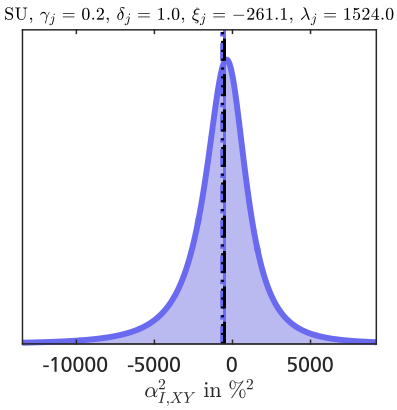

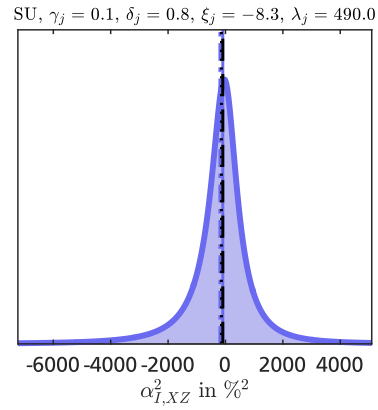

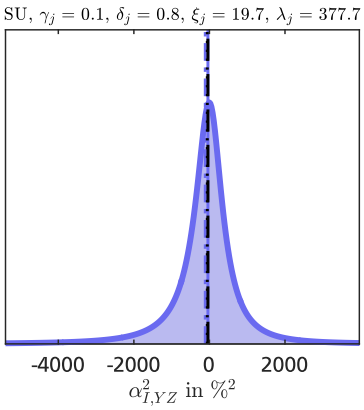

Copula covariance matrix for regression parameters of anthropometric parameters in the female pelvis.

Σ_c	α_m	$\alpha_{o,X}$	$\alpha_{o,Y}$	$\alpha_{o,Z}$	$\alpha_{I,XX}$	$\alpha_{I,YY}$	$\alpha_{I,ZZ}$	$\alpha_{I,XY}$	$\alpha_{I,XZ}$	$\alpha_{I,YZ}$
α_m	0.0826	$*$	$*$	$*$	$*$	$*$	$*$	$*$	$*$	$*$
$\alpha_{o,X}$	-0.0001	0.0493	$*$	$*$	$*$	$*$	$*$	$*$	$*$	$*$
$\alpha_{o,Y}$	-0.0001	0.0024	0.0027	$*$	$*$	$*$	$*$	$*$	$*$	$*$
$\alpha_{o,Z}$	0.0001	-0.0002	0.0010	0.0328	$*$	$*$	$*$	$*$	$*$	$*$
$\alpha_{I,XX}$	-0.0272	0.0079	-0.0007	0.0009	0.0831	$*$	$*$	$*$	$*$	$*$
$\alpha_{I,YY}$	-0.0244	0.0091	-0.0006	-0.0037	0.0604	0.0771	$*$	$*$	$*$	$*$
$\alpha_{I,ZZ}$	-0.0255	0.0079	-0.0009	0.0019	0.0698	0.0616	0.0805	$*$	$*$	$*$
$\alpha_{I,XY}$	-0.0022	-0.0132	-0.0012	-0.0001	0.0115	0.0061	0.0045	0.0197	$*$	$*$
$\alpha_{I,XZ}$	-0.0033	0.0046	0.0004	-0.0002	0.0130	0.0046	0.0012	0.0047	0.0227	$*$
$\alpha_{I,YZ}$	-0.0198	0.0050	-0.0013	-0.0093	0.0515	0.0481	0.0596	0.0054	-0.0032	0.0779

Copula covariance matrix for regression parameters of anthropometric parameters in the male pelvis.

Σ_c	α_m	$\alpha_{o,X}$	$\alpha_{o,Y}$	$\alpha_{o,Z}$	$\alpha_{I,XX}$	$\alpha_{I,YY}$	$\alpha_{I,ZZ}$	$\alpha_{I,XY}$	$\alpha_{I,XZ}$	$\alpha_{I,YZ}$
α_m	0.0828	$*$	$*$	$*$	$*$	$*$	$*$	$*$	$*$	$*$
$\alpha_{o,X}$	-0.0005	0.0591	$*$	$*$	$*$	$*$	$*$	$*$	$*$	$*$
$\alpha_{o,Y}$	0.0000	0.0005	0.0004	$*$	$*$	$*$	$*$	$*$	$*$	$*$
$\alpha_{o,Z}$	0.0006	0.0000	-0.0002	0.0288	$*$	$*$	$*$	$*$	$*$	$*$
$\alpha_{I,XX}$	-0.0246	0.0079	-0.0002	0.0096	0.0702	$*$	$*$	$*$	$*$	$*$
$\alpha_{I,YY}$	-0.0232	0.0041	-0.0004	0.0093	0.0442	0.0814	$*$	$*$	$*$	$*$
$\alpha_{I,ZZ}$	-0.0268	0.0088	-0.0002	0.0089	0.0580	0.0482	0.0840	$*$	$*$	$*$
$\alpha_{I,XY}$	-0.0063	-0.0260	-0.0003	0.0036	0.0179	0.0133	0.0144	0.0368	$*$	$*$
$\alpha_{I,XZ}$	-0.0011	0.0016	-0.0001	0.0002	-0.0034	0.0047	0.0186	-0.0018	0.0287	$*$
$\alpha_{I,YZ}$	-0.0023	0.0018	-0.0006	-0.0037	0.0185	0.0214	0.0293	0.0054	0.0102	0.0537

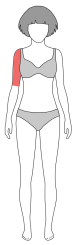

Female upper arm

Probability density
Median value
Mean value
Recommended value
Reference value

Johnson distribution type and coefficients

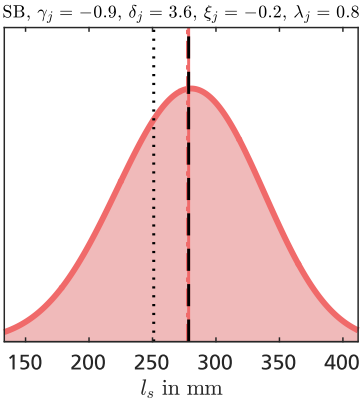

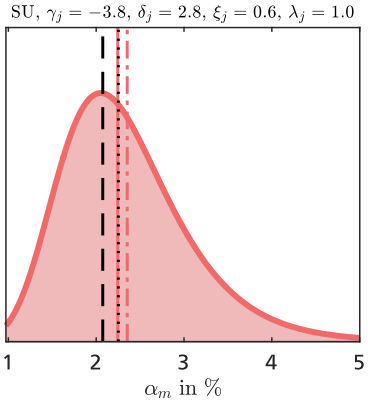

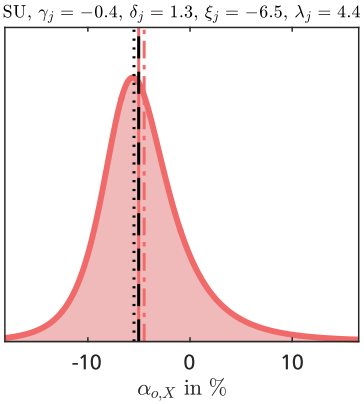

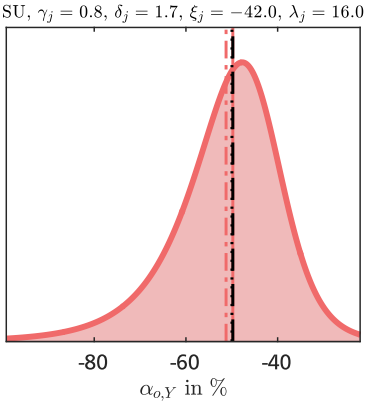

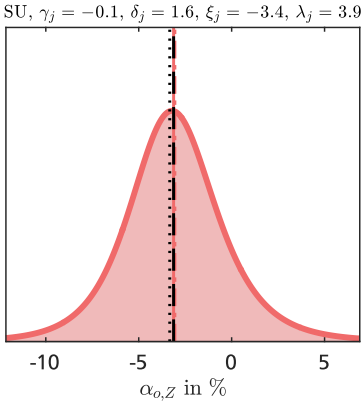

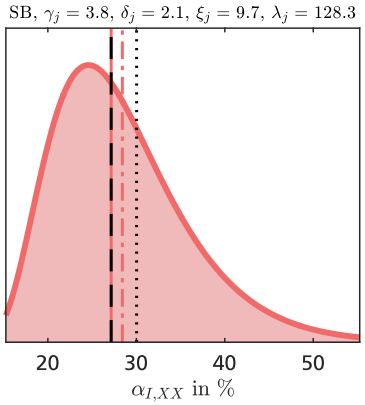

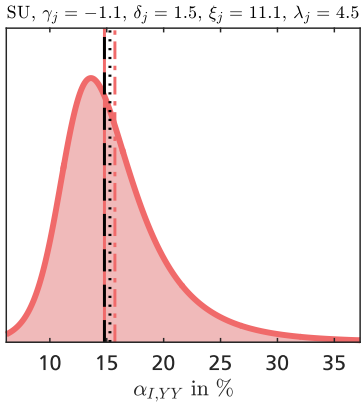

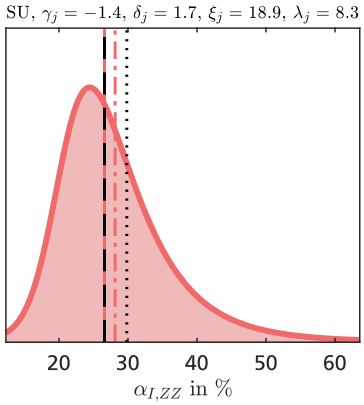

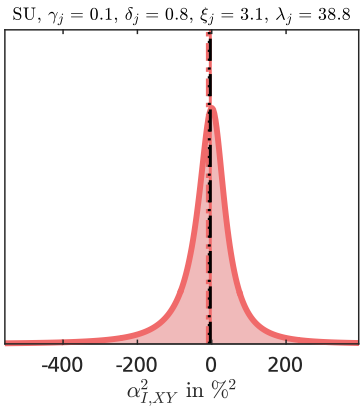

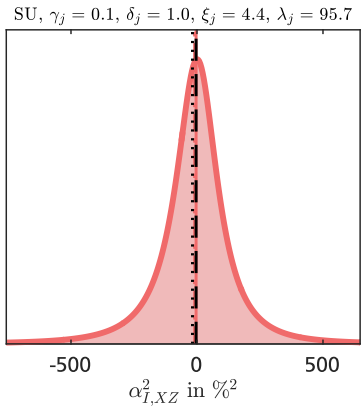

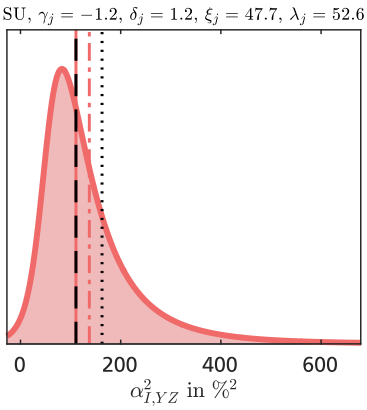

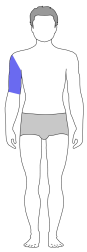

Male upper arm

Probability density
Median value
Mean value
Recommended value
Reference value

Johnson distribution type and coefficients

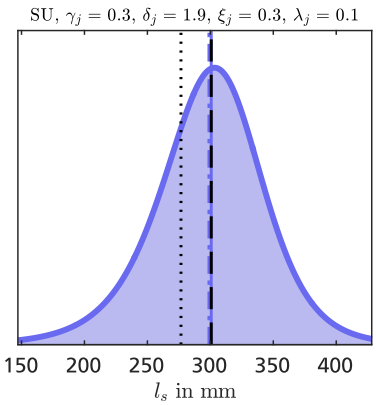

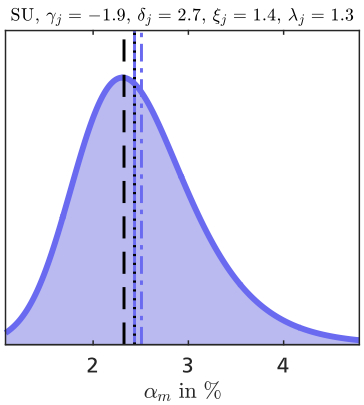

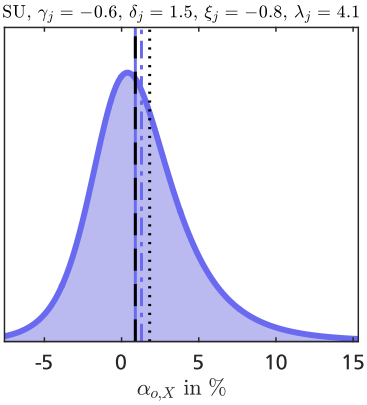

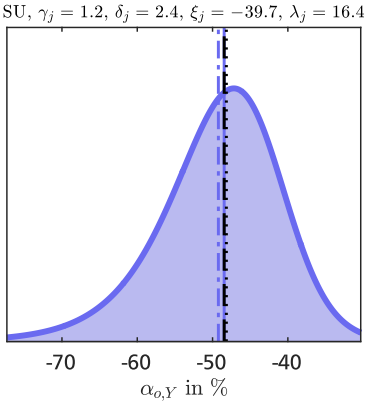

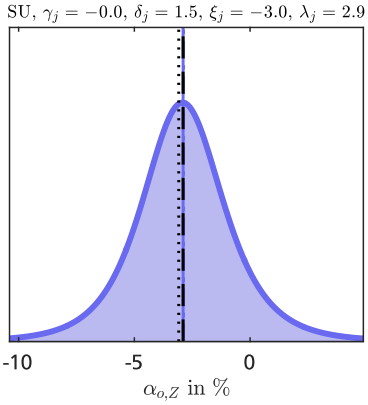

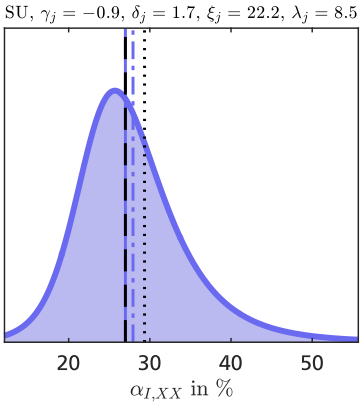

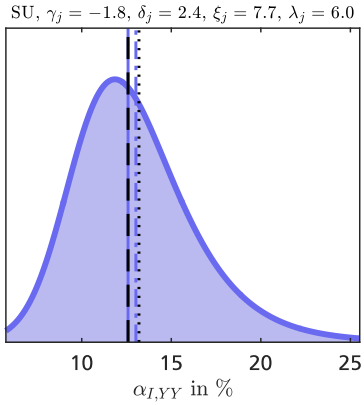

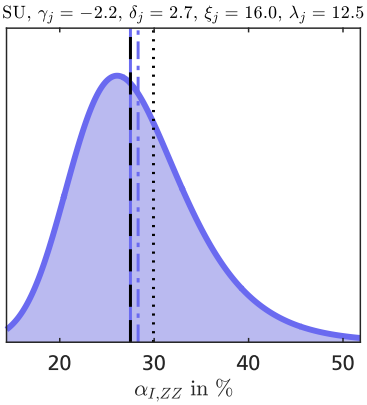

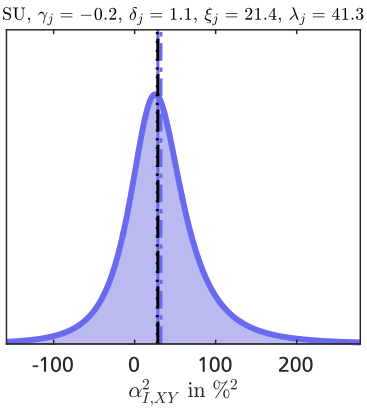

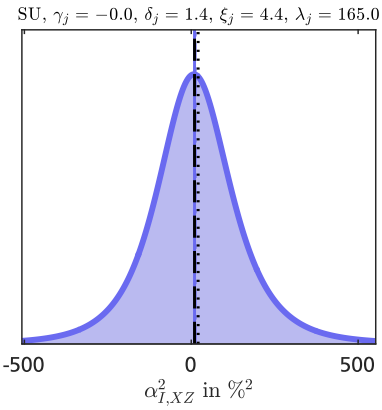

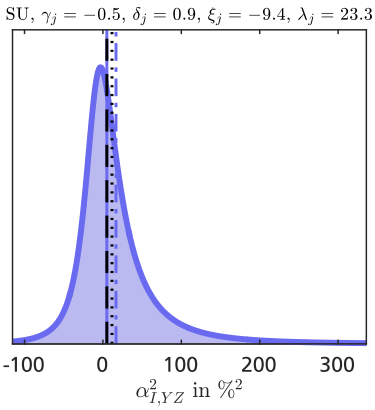

Copula covariance matrix for regression parameters of anthropometric parameters in the female upper arm.

Σ_c	α_m	$\alpha_{o,X}$	$\alpha_{o,Y}$	$\alpha_{o,Z}$	$\alpha_{I,XX}$	$\alpha_{I,YY}$	$\alpha_{I,ZZ}$	$\alpha_{I,XY}$	$\alpha_{I,XZ}$	$\alpha_{I,YZ}$
α_m	0.0841	$*$	$*$	$*$	$*$	$*$	$*$	$*$	$*$	$*$
$\alpha_{o,X}$	0.0009	0.0208	$*$	$*$	$*$	$*$	$*$	$*$	$*$	$*$
$\alpha_{o,Y}$	0.0003	-0.0015	0.0315	$*$	$*$	$*$	$*$	$*$	$*$	$*$
$\alpha_{o,Z}$	-0.0005	0.0095	0.0142	0.0551	$*$	$*$	$*$	$*$	$*$	$*$
$\alpha_{I,XX}$	-0.0288	0.0019	0.0221	0.0202	0.0832	$*$	$*$	$*$	$*$	$*$
$\alpha_{I,YY}$	-0.0261	0.0016	0.0255	0.0339	0.0652	0.0845	$*$	$*$	$*$	$*$
$\alpha_{I,ZZ}$	-0.0297	-0.0033	0.0214	0.0089	0.0615	0.0592	0.0820	$*$	$*$	$*$
$\alpha_{I,XY}$	-0.0138	-0.0137	0.0123	0.0026	0.0450	0.0335	0.0258	0.0665	$*$	$*$
$\alpha_{I,XZ}$	-0.0036	-0.0038	0.0048	0.0039	0.0018	0.0104	0.0192	-0.0071	0.0248	$*$
$\alpha_{I,YZ}$	0.0000	0.0000	0.0000	0.0000	-0.0001	-0.0001	-0.0001	0.0000	0.0000	0.0000

Copula covariance matrix for regression parameters of anthropometric parameters in the male upper arm.

Σ_c	α_m	$\alpha_{o,X}$	$\alpha_{o,Y}$	$\alpha_{o,Z}$	$\alpha_{I,XX}$	$\alpha_{I,YY}$	$\alpha_{I,ZZ}$	$\alpha_{I,XY}$	$\alpha_{I,XZ}$	$\alpha_{I,YZ}$
α_m	0.0824	$*$	$*$	$*$	$*$	$*$	$*$	$*$	$*$	$*$
$\alpha_{o,X}$	0.0009	0.0122	$*$	$*$	$*$	$*$	$*$	$*$	$*$	$*$
$\alpha_{o,Y}$	0.0004	-0.0008	0.0275	$*$	$*$	$*$	$*$	$*$	$*$	$*$
$\alpha_{o,Z}$	0.0006	-0.0055	0.0115	0.0423	$*$	$*$	$*$	$*$	$*$	$*$
$\alpha_{I,XX}$	-0.0198	-0.0010	0.0148	0.0080	0.0505	$*$	$*$	$*$	$*$	$*$
$\alpha_{I,YY}$	-0.0234	-0.0045	0.0230	0.0193	0.0361	0.0828	$*$	$*$	$*$	$*$
$\alpha_{I,ZZ}$	-0.0226	-0.0030	0.0196	0.0108	0.0347	0.0432	0.0823	$*$	$*$	$*$
$\alpha_{I,XY}$	-0.0126	-0.0139	0.0139	0.0194	0.0317	0.0437	0.0281	0.0834	$*$	$*$
$\alpha_{I,XZ}$	-0.0021	0.0000	0.0024	0.0033	0.0084	0.0062	-0.0017	0.0064	0.0281	$*$
$\alpha_{I,YZ}$	-0.0028	0.0033	-0.0017	-0.0127	0.0014	-0.0010	0.0015	-0.0036	0.0016	0.0141

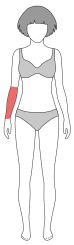

Female lower arm

Probability density
Median value
Mean value
Recommended value
Reference value

Johnson distribution type and coefficients

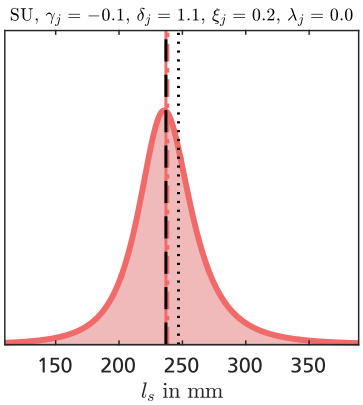

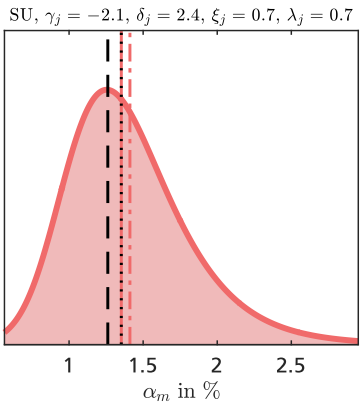

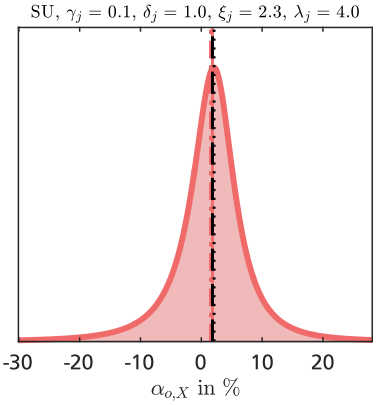

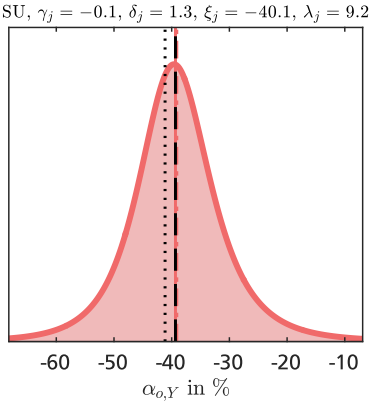

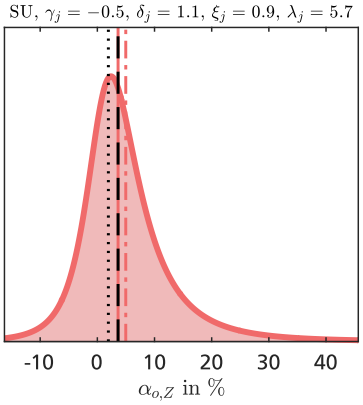

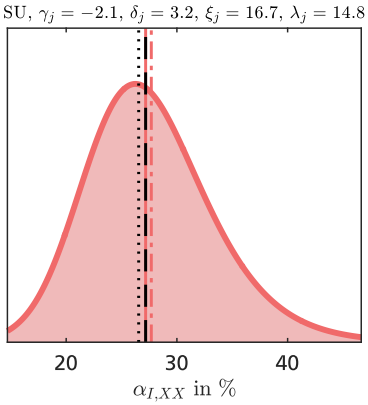

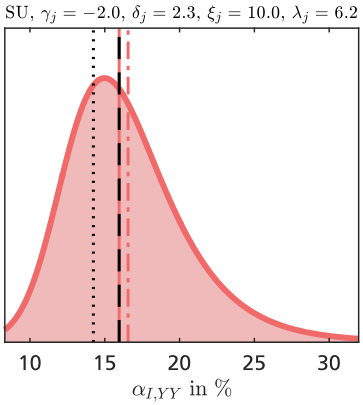

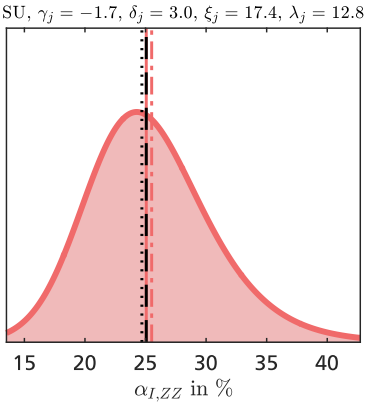

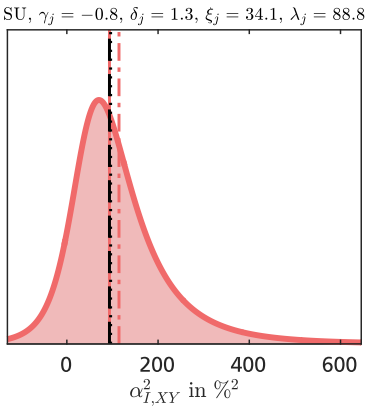

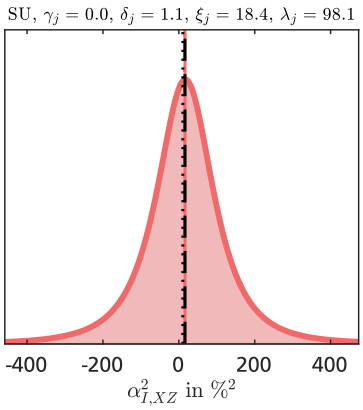

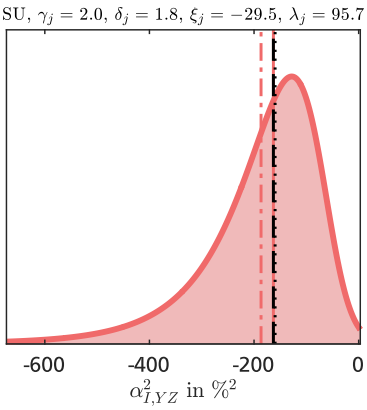

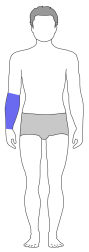

Male lower arm

Probability density
Median value
Mean value
Recommended value
Reference value

Johnson distribution type and coefficients

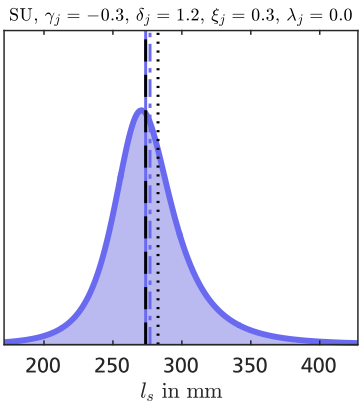

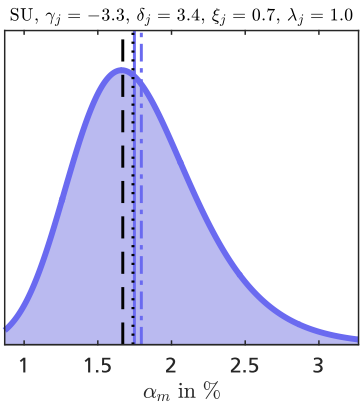

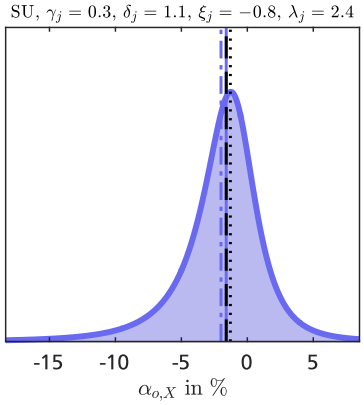

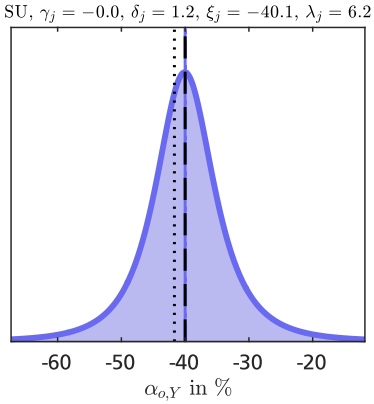

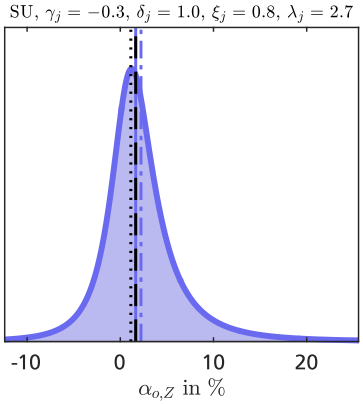

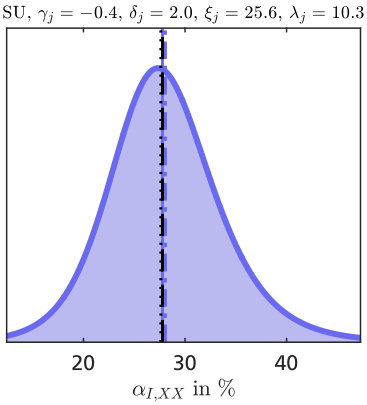

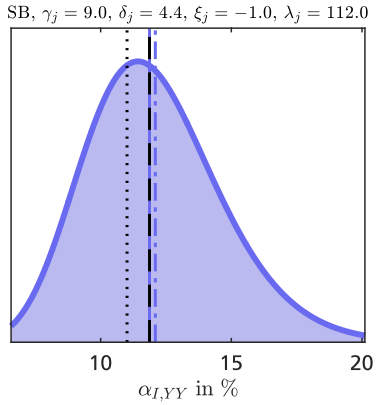

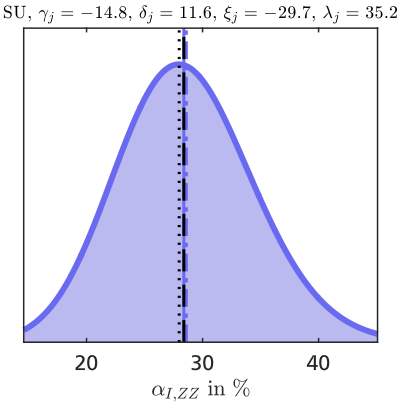

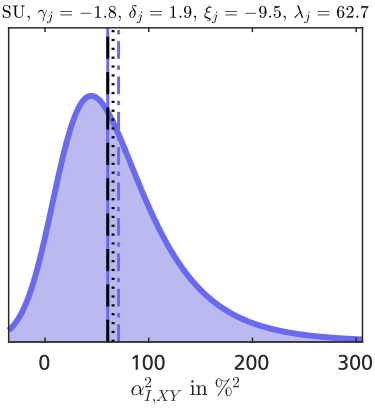

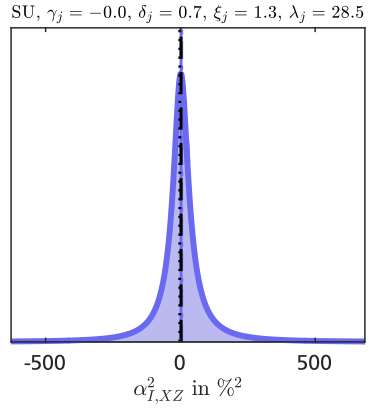

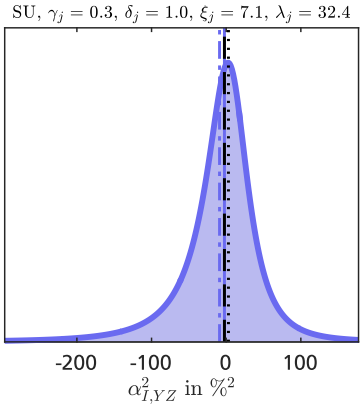

Copula covariance matrix for regression parameters of anthropometric parameters in the female lower arm.

Σ_c	α_m	$\alpha_{o,X}$	$\alpha_{o,Y}$	$\alpha_{o,Z}$	$\alpha_{I,XX}$	$\alpha_{I,YY}$	$\alpha_{I,ZZ}$	$\alpha_{I,XY}$	$\alpha_{I,XZ}$	$\alpha_{I,YZ}$
α_m	0.0822	$*$	$*$	$*$	$*$	$*$	$*$	$*$	$*$	$*$
$\alpha_{o,X}$	0.0018	0.0829	$*$	$*$	$*$	$*$	$*$	$*$	$*$	$*$
$\alpha_{o,Y}$	0.0007	-0.0016	0.0518	$*$	$*$	$*$	$*$	$*$	$*$	$*$
$\alpha_{o,Z}$	0.0001	0.0000	0.0026	0.0138	$*$	$*$	$*$	$*$	$*$	$*$
$\alpha_{I,XX}$	-0.0162	0.0103	0.0015	0.0013	0.0462	$*$	$*$	$*$	$*$	$*$
$\alpha_{I,YY}$	-0.0219	-0.0065	0.0067	0.0015	0.0203	0.0826	$*$	$*$	$*$	$*$
$\alpha_{I,ZZ}$	-0.0199	0.0074	0.0046	0.0010	0.0276	0.0460	0.0649	$*$	$*$	$*$
$\alpha_{I,XY}$	-0.0066	-0.0184	0.0063	0.0007	0.0084	0.0415	0.0184	0.0760	$*$	$*$
$\alpha_{I,XZ}$	-0.0069	-0.0104	0.0031	0.0010	0.0249	0.0203	-0.0042	0.0470	0.0746	$*$
$\alpha_{I,YZ}$	0.0006	-0.0017	-0.0003	0.0000	-0.0008	-0.0004	-0.0035	0.0021	0.0035	0.0015

Copula covariance matrix for regression parameters of anthropometric parameters in the male lower arm.

Σ_c	α_m	$\alpha_{o,X}$	$\alpha_{o,Y}$	$\alpha_{o,Z}$	$\alpha_{I,XX}$	$\alpha_{I,YY}$	$\alpha_{I,ZZ}$	$\alpha_{I,XY}$	$\alpha_{I,XZ}$	$\alpha_{I,YZ}$
α_m	0.0824	$*$	$*$	$*$	$*$	$*$	$*$	$*$	$*$	$*$
$\alpha_{o,X}$	0.0002	0.0472	$*$	$*$	$*$	$*$	$*$	$*$	$*$	$*$
$\alpha_{o,Y}$	0.0000	0.0000	0.0000	$*$	$*$	$*$	$*$	$*$	$*$	$*$
$\alpha_{o,Z}$	0.0020	0.0008	0.0000	0.0823	$*$	$*$	$*$	$*$	$*$	$*$
$\alpha_{I,XX}$	-0.0240	0.0021	0.0000	0.0044	0.0842	$*$	$*$	$*$	$*$	$*$
$\alpha_{I,YY}$	-0.0245	0.0031	0.0000	0.0056	0.0314	0.0744	$*$	$*$	$*$	$*$
$\alpha_{I,ZZ}$	-0.0249	0.0033	0.0000	0.0056	0.0328	0.0380	0.0829	$*$	$*$	$*$
$\alpha_{I,XY}$	-0.0079	0.0008	0.0000	0.0051	0.0307	0.0205	0.0181	0.0829	$*$	$*$
$\alpha_{I,XZ}$	-0.0043	-0.0016	0.0000	0.0025	0.0424	0.0083	-0.0142	0.0301	0.0579	$*$
$\alpha_{I,YZ}$	0.0118	-0.0008	0.0000	0.0036	-0.0081	-0.0117	-0.0526	0.0041	0.0216	0.0835

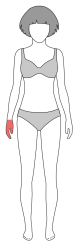

Female hand

Probability density
Median value
Mean value
Recommended value
Reference value

Johnson distribution type and coefficients

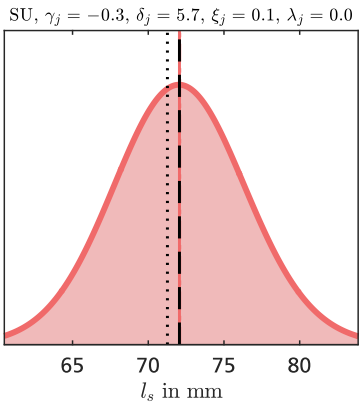

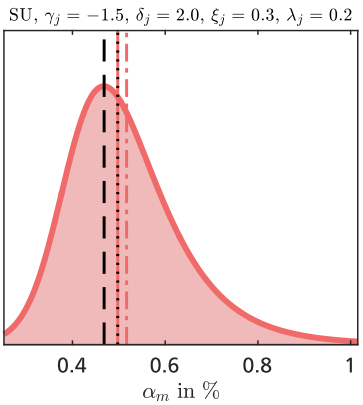

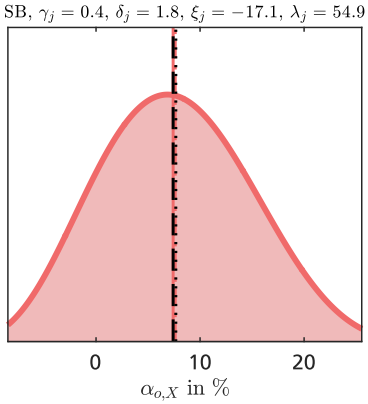

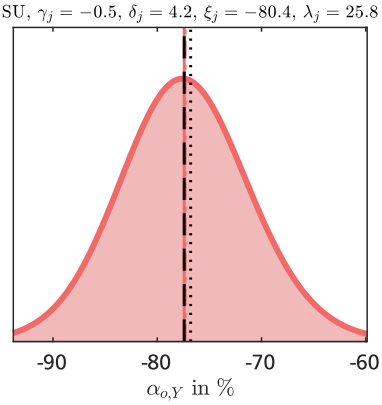

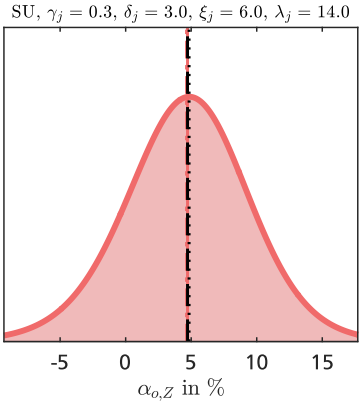

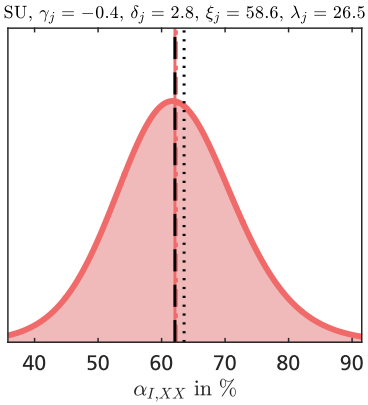

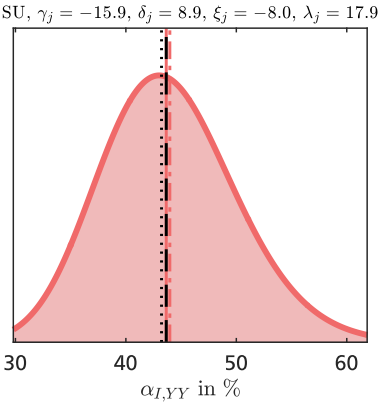

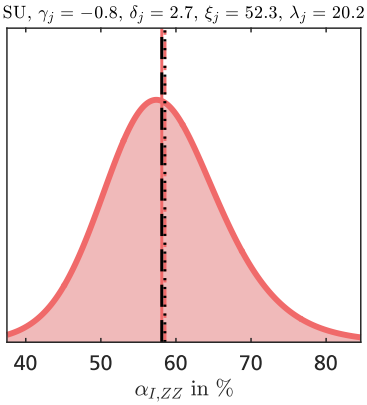

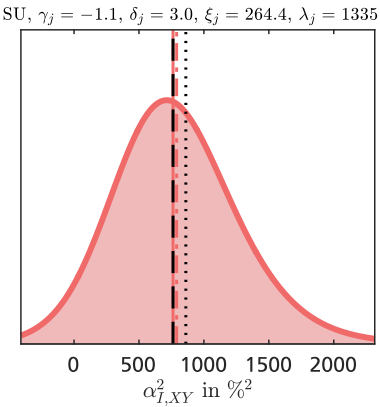

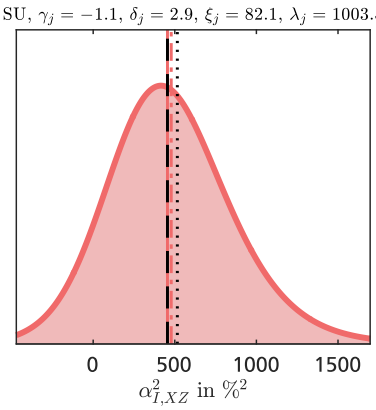

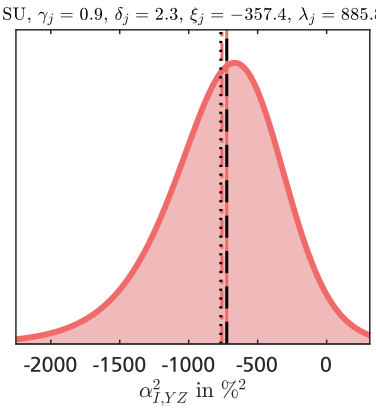

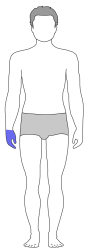

Male hand

Probability density
Median value
Mean value
Recommended value
Reference value

Johnson distribution type and coefficients

SB, $\gamma_j = -0.6$, $\delta_j = 5.8$, $\xi_j = 0.0$, $\lambda_j = 0.1$

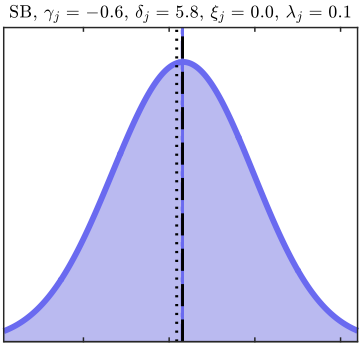

l_s in mm

SU, $\gamma_j = -1.4$, $\delta_j = 2.2$, $\xi_j = 0.5$, $\lambda_j = 0.2$

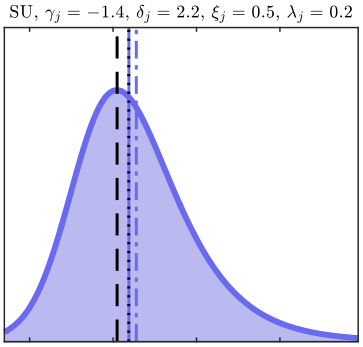

α_m in %

SU, $\gamma_j = -0.4$, $\delta_j = 15.6$, $\xi_j = 6.9$, $\lambda_j = 50.7$

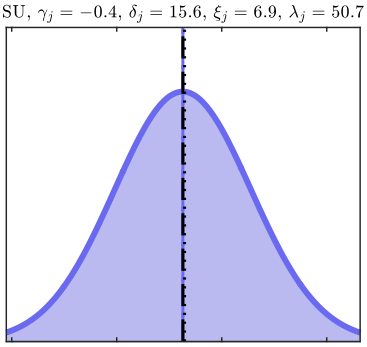

$\alpha_{o,X}$ in %

SU, $\gamma_j = 3.4$, $\delta_j = 6.8$, $\xi_j = -75.8$, $\lambda_j = 15.1$

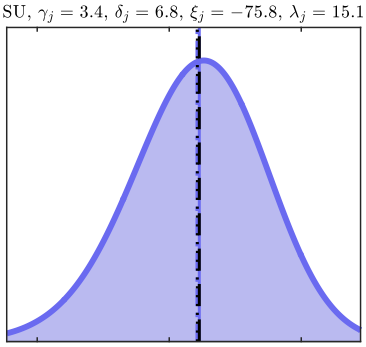

$\alpha_{o,Y}$ in %

SB, $\gamma_j = -0.0$, $\delta_j = 1.4$, $\xi_j = 0.6$, $\lambda_j = 13.3$

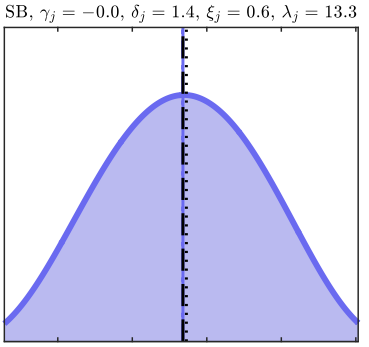

$\alpha_{o,Z}$ in %

SU, $\gamma_j = -13.0$, $\delta_j = 12.9$, $\xi_j = -26.1$, $\lambda_j = 73.3$

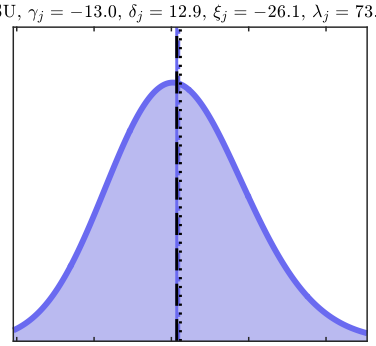

$\alpha_{I,XX}$ in %

SU, $\gamma_j = -1.0$, $\delta_j = 3.3$, $\xi_j = 33.1$, $\lambda_j = 15.6$

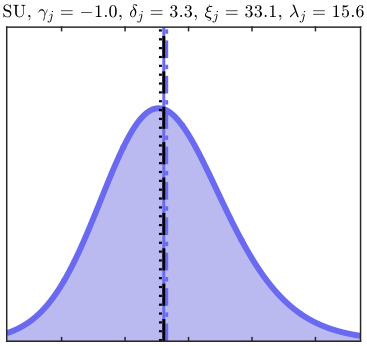

$\alpha_{I,YY}$ in %

SB, $\gamma_j = 5.6$, $\delta_j = 5.6$, $\xi_j = -4.9$, $\lambda_j = 224.2$

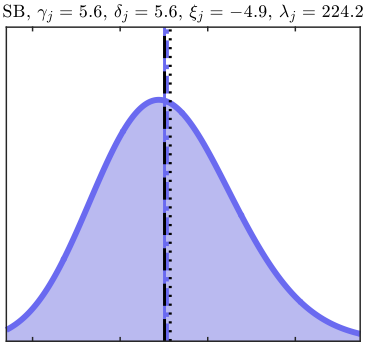

$\alpha_{I,ZZ}$ in %

SB, $\gamma_j = 1.9$, $\delta_j = 2.0$, $\xi_j = -416.1$, $\lambda_j = 3052.8$

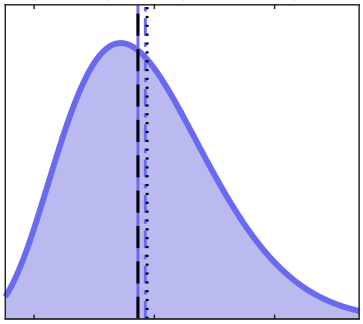

$\alpha^2_{I,XY}$ in %^{2}

SU, $\gamma_j = -0.6$, $\delta_j = 1.5$, $\xi_j = 82.3$, $\lambda_j = 332.4$

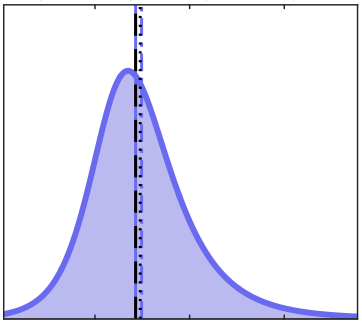

$\alpha^2_{I,XZ}$ in %^{2}

SB, $\gamma_j = -5.0$, $\delta_j = 2.7$, $\xi_j = -5518.6$, $\lambda_j = 5967.3$

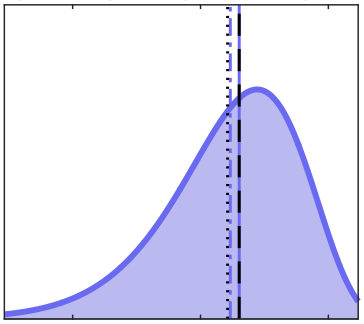

$\alpha^2_{I,YZ}$ in %^{2}

Copula covariance matrix for regression parameters of anthropometric parameters in the female hand.

Σ_c	α_m	$\alpha_{o,X}$	$\alpha_{o,Y}$	$\alpha_{o,Z}$	$\alpha_{I,XX}$	$\alpha_{I,YY}$	$\alpha_{I,ZZ}$	$\alpha_{I,XY}$	$\alpha_{I,XZ}$	$\alpha_{I,YZ}$
α_m	0.0834	$*$	$*$	$*$	$*$	$*$	$*$	$*$	$*$	$*$
$\alpha_{o,X}$	0.0004	0.0022	$*$	$*$	$*$	$*$	$*$	$*$	$*$	$*$
$\alpha_{o,Y}$	0.0015	0.0008	0.0822	$*$	$*$	$*$	$*$	$*$	$*$	$*$
$\alpha_{o,Z}$	-0.0005	-0.0004	-0.0032	0.0709	$*$	$*$	$*$	$*$	$*$	$*$
$\alpha_{I,XX}$	-0.0357	-0.0015	0.0037	-0.0004	0.0733	$*$	$*$	$*$	$*$	$*$
$\alpha_{I,YY}$	-0.0340	-0.0015	0.0042	0.0016	0.0573	0.0801	$*$	$*$	$*$	$*$
$\alpha_{I,ZZ}$	-0.0297	-0.0015	0.0023	-0.0002	0.0377	0.0360	0.0823	$*$	$*$	$*$
$\alpha_{I,XY}$	-0.0023	-0.0002	0.0000	-0.0002	0.0048	-0.0055	0.0023	0.0100	$*$	$*$
$\alpha_{I,XZ}$	-0.0039	-0.0003	0.0007	-0.0003	0.0064	0.0059	0.0039	0.0004	0.0276	$*$
$\alpha_{I,YZ}$	-0.0047	-0.0003	0.0010	0.0010	0.0066	0.0091	0.0039	0.0001	0.0083	0.0282

Copula covariance matrix for regression parameters of anthropometric parameters in the male hand.

Σ_c	α_m	$\alpha_{o,X}$	$\alpha_{o,Y}$	$\alpha_{o,Z}$	$\alpha_{I,XX}$	$\alpha_{I,YY}$	$\alpha_{I,ZZ}$	$\alpha_{I,XY}$	$\alpha_{I,XZ}$	$\alpha_{I,YZ}$
α_m	0.0829	$*$	$*$	$*$	$*$	$*$	$*$	$*$	$*$	$*$
$\alpha_{o,X}$	0.0000	0.0000	$*$	$*$	$*$	$*$	$*$	$*$	$*$	$*$
$\alpha_{o,Y}$	0.0030	0.0000	0.0828	$*$	$*$	$*$	$*$	$*$	$*$	$*$
$\alpha_{o,Z}$	0.0017	0.0000	-0.0024	0.0831	$*$	$*$	$*$	$*$	$*$	$*$
$\alpha_{I,XX}$	-0.0313	0.0000	0.0055	-0.0019	0.0828	$*$	$*$	$*$	$*$	$*$
$\alpha_{I,YY}$	-0.0304	0.0000	0.0030	-0.0008	0.0639	0.0818	$*$	$*$	$*$	$*$
$\alpha_{I,ZZ}$	-0.0266	0.0000	0.0031	-0.0015	0.0504	0.0457	0.0825	$*$	$*$	$*$
$\alpha_{I,XY}$	-0.0003	0.0000	0.0017	-0.0013	0.0081	-0.0076	0.0043	0.0188	$*$	$*$
$\alpha_{I,XZ}$	-0.0013	0.0000	-0.0004	0.0011	-0.0032	0.0021	0.0115	-0.0024	0.0197	$*$
$\alpha_{I,YZ}$	-0.0020	0.0000	0.0004	-0.0002	0.0012	0.0049	0.0096	-0.0028	0.0080	0.0204

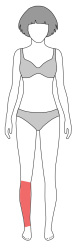

Female shank

Probability density
Median value
Mean value
Recommended value
Reference value

Johnson distribution type and coefficients

SU, $\gamma_j = -0.5$, $\delta_j = 1.9$, $\xi_j = 0.4$, $\lambda_j = 0.1$

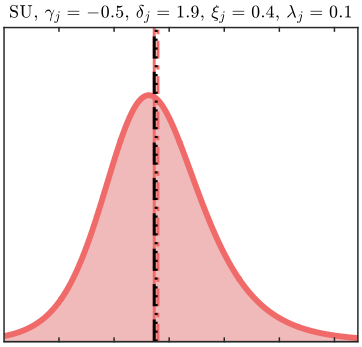

l_s in mm

SU, $\gamma_j = -3.7$, $\delta_j = 2.9$, $\xi_j = 1.3$, $\lambda_j = 2.0$

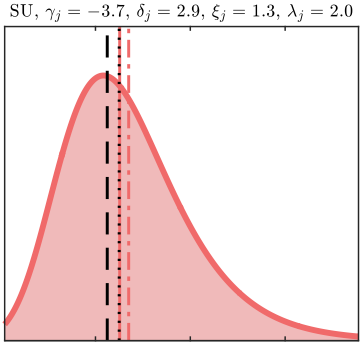

α_m in %

SU, $\gamma_j = -0.2$, $\delta_j = 2.5$, $\xi_j = -5.2$, $\lambda_j = 8.8$

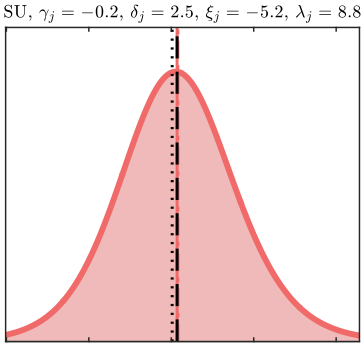

$\alpha_{o,X}$ in %

SU, $\gamma_j = -0.3$, $\delta_j = 1.8$, $\xi_j = -43.0$, $\lambda_j = 13.4$

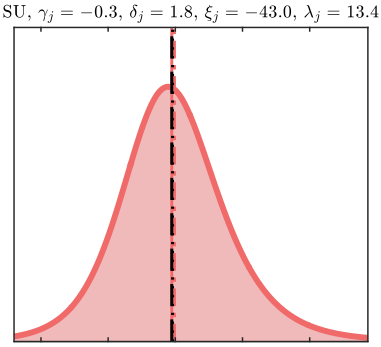

$\alpha_{o,Y}$ in %

SU, $\gamma_j = -0.6$, $\delta_j = 1.1$, $\xi_j = 2.7$, $\lambda_j = 3.5$

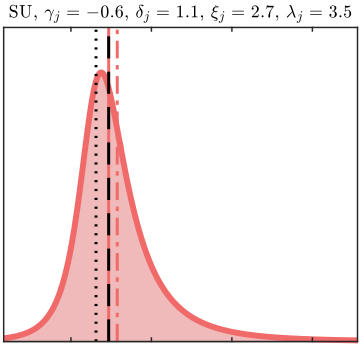

$\alpha_{o,Z}$ in %

SU, $\gamma_j = -6.6$, $\delta_j = 4.2$, $\xi_j = 5.3$, $\lambda_j = 9.5$

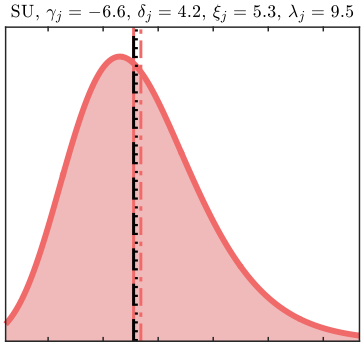

$\alpha_{I,XX}$ in %

SU, $\gamma_j = -3.7$, $\delta_j = 3.1$, $\xi_j = 4.5$, $\lambda_j = 4.5$

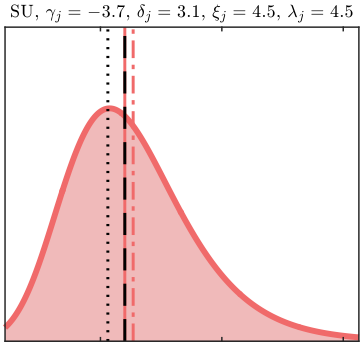

$\alpha_{I,YY}$ in %

SU, $\gamma_j = -4.5$, $\delta_j = 4.5$, $\xi_j = 7.9$, $\lambda_j = 16.9$

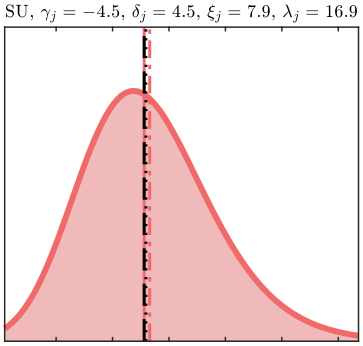

$\alpha_{I,ZZ}$ in %

SU, $\gamma_j = -0.3$, $\delta_j = 1.8$, $\xi_j = -11.2$, $\lambda_j = 93.3$

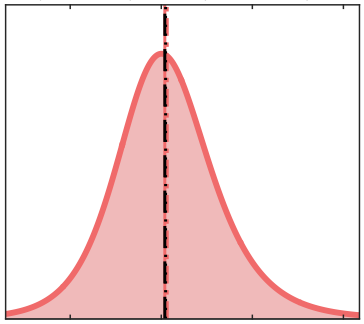

$\alpha^2_{I,XY}$ in %^{2}

SU, $\gamma_j = 0.0$, $\delta_j = 0.8$, $\xi_j = 3.3$, $\lambda_j = 47.3$

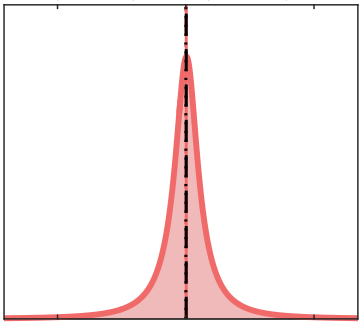

$\alpha^2_{I,XZ}$ in %^{2}

SU, $\gamma_j = 0.5$, $\delta_j = 0.9$, $\xi_j = 23.5$, $\lambda_j = 29.2$

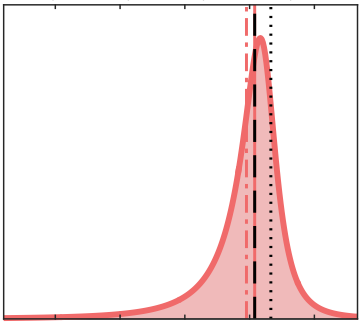

$\alpha^2_{I,YZ}$ in %^{2}

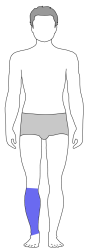

Male shank

Probability density
Median value
Mean value
Recommended value
Reference value

Johnson distribution type and coefficients

SU, $\gamma_j = -0.3$, $\delta_j = 2.2$, $\xi_j = 0.4$, $\lambda_j = 0.1$

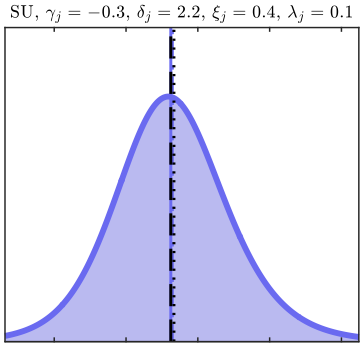

l_s in mm

SU, $\gamma_j = -3.3$, $\delta_j = 3.4$, $\xi_j = 2.0$, $\lambda_j = 2.5$

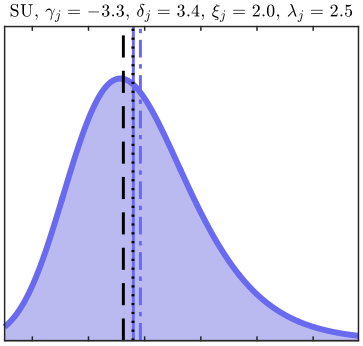

α_m in %

SU, $\gamma_j = -1.4$, $\delta_j = 2.5$, $\xi_j = -8.3$, $\lambda_j = 5.3$

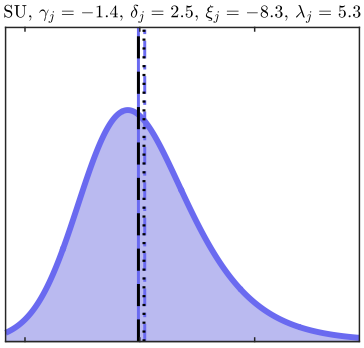

$\alpha_{o,X}$ in %

SU, $\gamma_j = -0.5$, $\delta_j = 1.9$, $\xi_j = -43.2$, $\lambda_j = 9.4$

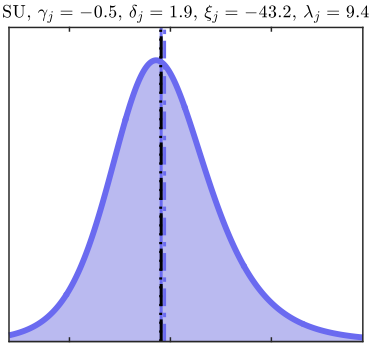

$\alpha_{o,Y}$ in %

SU, $\gamma_j = -0.8$, $\delta_j = 1.1$, $\xi_j = 0.2$, $\lambda_j = 2.6$

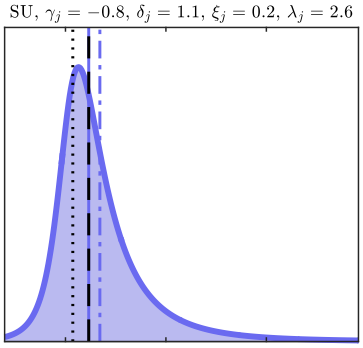

$\alpha_{o,Z}$ in %

SU, $\gamma_j = -1.1$, $\delta_j = 3.4$, $\xi_j = 22.3$, $\lambda_j = 17.1$

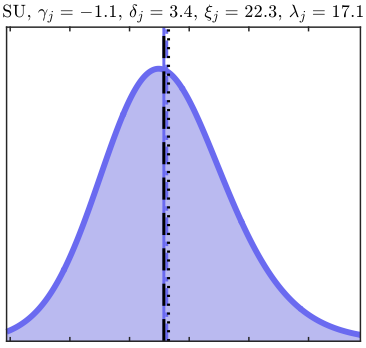

$\alpha_{I,XX}$ in %

SU, $\gamma_j = -1.2$, $\delta_j = 2.3$, $\xi_j = 8.1$, $\lambda_j = 3.5$

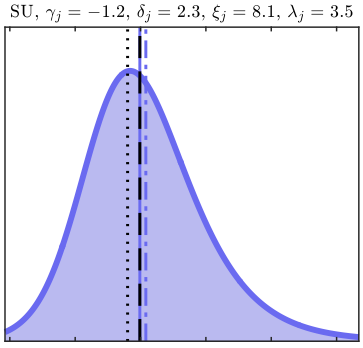

$\alpha_{I,YY}$ in %

SU, $\gamma_j = -0.6$, $\delta_j = 2.3$, $\xi_j = 24.9$, $\lambda_j = 11.2$

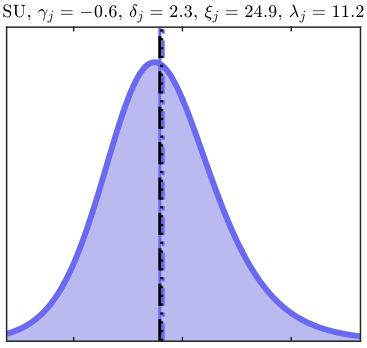

$\alpha_{I,ZZ}$ in %

SU, $\gamma_j = -1.2$, $\delta_j = 3.7$, $\xi_j = -58.2$, $\lambda_j = 157.5$

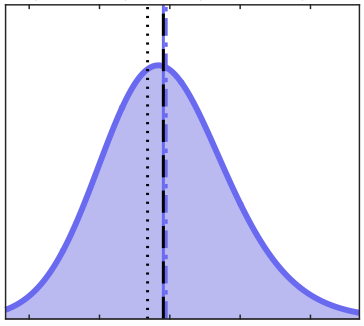

$\alpha^2_{I,XY}$ in %^{2}

SU, $\gamma_j = -0.0$, $\delta_j = 0.8$, $\xi_j = -3.9$, $\lambda_j = 53.3$

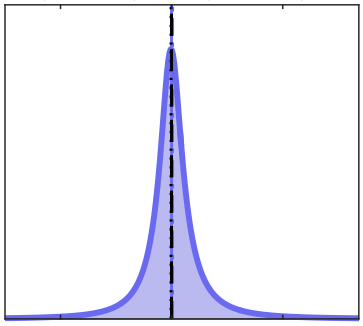

$\alpha^2_{I,XZ}$ in %^{2}

SU, $\gamma_j = 0.5$, $\delta_j = 1.1$, $\xi_j = 12.5$, $\lambda_j = 30.2$

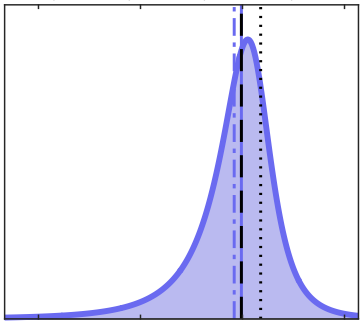

$\alpha^2_{I,YZ}$ in %^{2}

Copula covariance matrix for regression parameters of anthropometric parameters in the female shank.

Σ_c	α_m	$\alpha_{o,X}$	$\alpha_{o,Y}$	$\alpha_{o,Z}$	$\alpha_{I,XX}$	$\alpha_{I,YY}$	$\alpha_{I,ZZ}$	$\alpha_{I,XY}$	$\alpha_{I,XZ}$	$\alpha_{I,YZ}$
α_m	0.0836	$*$	$*$	$*$	$*$	$*$	$*$	$*$	$*$	$*$
$\alpha_{o,X}$	-0.0012	0.0356	$*$	$*$	$*$	$*$	$*$	$*$	$*$	$*$
$\alpha_{o,Y}$	0.0021	-0.0020	0.0436	$*$	$*$	$*$	$*$	$*$	$*$	$*$
$\alpha_{o,Z}$	0.0000	-0.0034	0.0111	0.0560	$*$	$*$	$*$	$*$	$*$	$*$
$\alpha_{I,XX}$	-0.0267	-0.0042	0.0296	0.0111	0.0837	$*$	$*$	$*$	$*$	$*$
$\alpha_{I,YY}$	-0.0237	-0.0013	0.0204	0.0190	0.0468	0.0822	$*$	$*$	$*$	$*$
$\alpha_{I,ZZ}$	-0.0258	-0.0054	0.0290	0.0113	0.0654	0.0460	0.0825	$*$	$*$	$*$
$\alpha_{I,XY}$	-0.0002	-0.0197	-0.0002	0.0184	0.0062	0.0093	0.0052	0.0412	$*$	$*$
$\alpha_{I,XZ}$	-0.0016	-0.0001	0.0008	0.0012	0.0042	0.0020	0.0039	0.0002	0.0260	$*$
$\alpha_{I,YZ}$	-0.0017	-0.0014	-0.0001	-0.0096	0.0040	0.0012	0.0058	-0.0008	0.0002	0.0085

Copula covariance matrix for regression parameters of anthropometric parameters in the male shank.

Σ_c	α_m	$\alpha_{o,X}$	$\alpha_{o,Y}$	$\alpha_{o,Z}$	$\alpha_{I,XX}$	$\alpha_{I,YY}$	$\alpha_{I,ZZ}$	$\alpha_{I,XY}$	$\alpha_{I,XZ}$	$\alpha_{I,YZ}$
α_m	0.0837	$*$	$*$	$*$	$*$	$*$	$*$	$*$	$*$	$*$
$\alpha_{o,X}$	0.0003	0.0808	$*$	$*$	$*$	$*$	$*$	$*$	$*$	$*$
$\alpha_{o,Y}$	-0.0006	-0.0108	0.0509	$*$	$*$	$*$	$*$	$*$	$*$	$*$
$\alpha_{o,Z}$	-0.0007	-0.0311	0.0098	0.0670	$*$	$*$	$*$	$*$	$*$	$*$
$\alpha_{I,XX}$	-0.0227	-0.0091	0.0263	0.0071	0.0776	$*$	$*$	$*$	$*$	$*$
$\alpha_{I,YY}$	-0.0253	-0.0094	0.0242	0.0167	0.0371	0.0778	$*$	$*$	$*$	$*$
$\alpha_{I,ZZ}$	-0.0209	-0.0080	0.0225	0.0061	0.0420	0.0321	0.0590	$*$	$*$	$*$
$\alpha_{I,XY}$	0.0007	-0.0587	-0.0028	0.0393	-0.0054	0.0034	-0.0012	0.0767	$*$	$*$
$\alpha_{I,XZ}$	-0.0047	-0.0055	0.0028	0.0042	0.0004	0.0045	0.0067	0.0064	0.0291	$*$
$\alpha_{I,YZ}$	-0.0013	-0.0017	-0.0012	-0.0088	0.0015	-0.0006	0.0025	0.0011	0.0019	0.0082

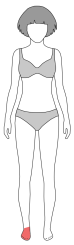

Female foot

Probability density
Median value
Mean value
Recommended value
Reference value

Johnson distribution type and coefficients

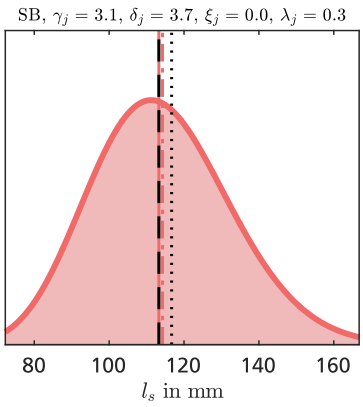

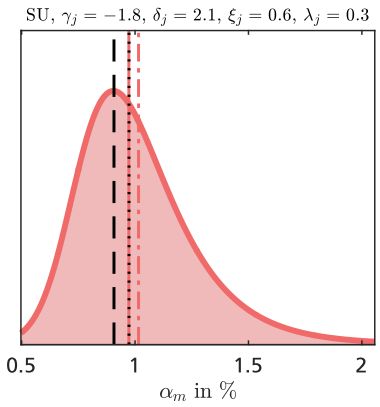

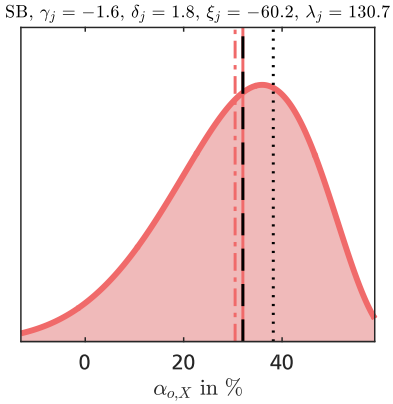

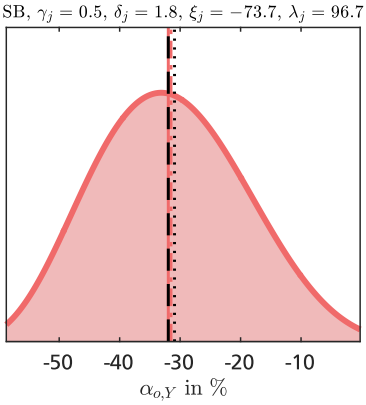

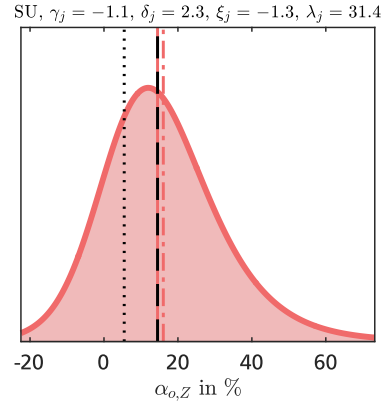

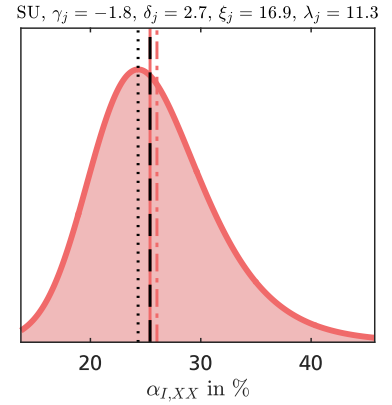

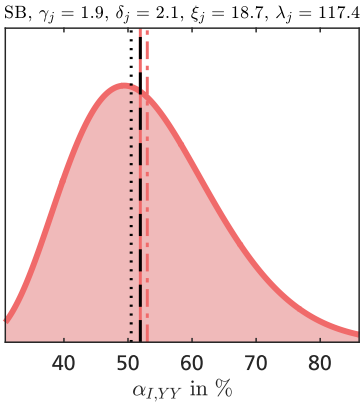

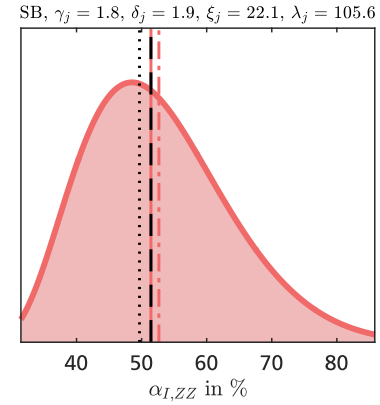

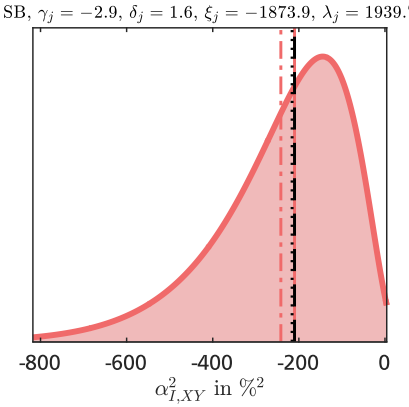

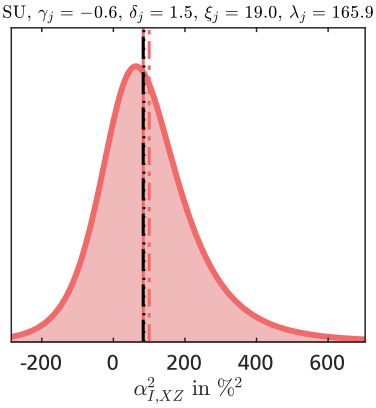

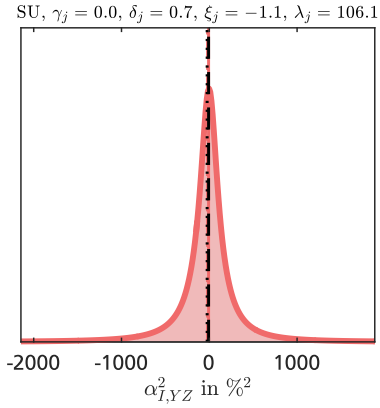

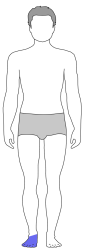

Male foot

Probability density
Median value
Mean value
Recommended value
Reference value

Johnson distribution type and coefficients

SB, $\gamma_j = -0.1$, $\delta_j = 1.1$, $\xi_j = 0.1$, $\lambda_j = 0.1$

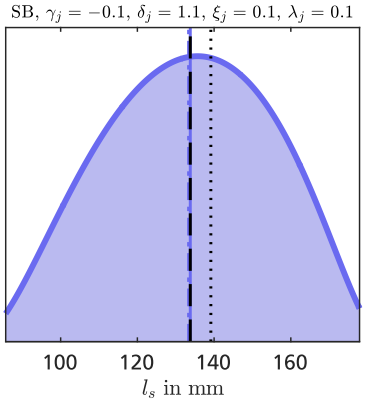

SU, $\gamma_j = -1.1$, $\delta_j = 1.9$, $\xi_j = 0.9$, $\lambda_j = 0.4$

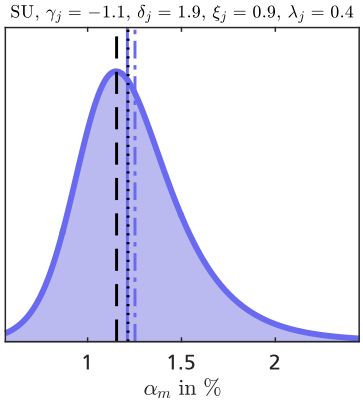

SB, $\gamma_j = -2.2$, $\delta_j = 1.5$, $\xi_j = -34.2$, $\lambda_j = 98.1$

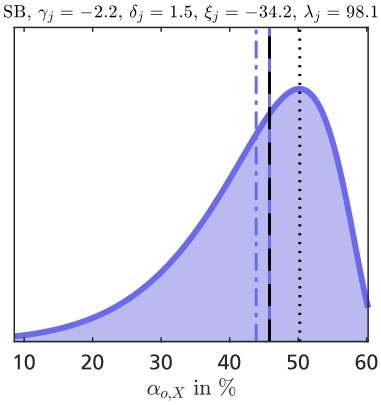

SB, $\gamma_j = 0.0$, $\delta_j = 1.0$, $\xi_j = -54.6$, $\lambda_j = 61.9$

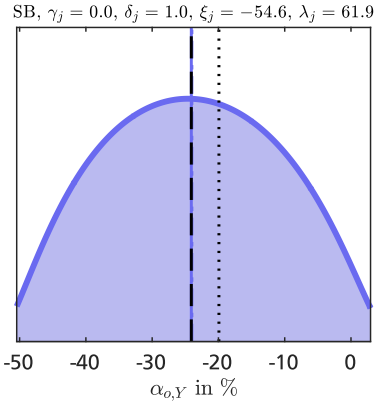

SU, $\gamma_j = -1.5$, $\delta_j = 1.4$, $\xi_j = -1.7$, $\lambda_j = 8.5$

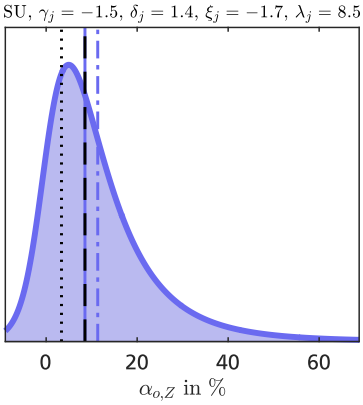

SB, $\gamma_j = 1.7$, $\delta_j = 1.7$, $\xi_j = 11.2$, $\lambda_j = 46.2$

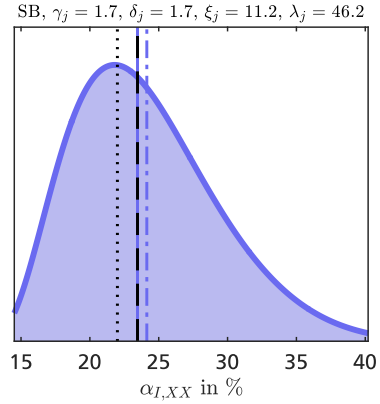

SB, $\gamma_j = 12.4$, $\delta_j = 4.6$, $\xi_j = -8.8$, $\lambda_j = 954.0$

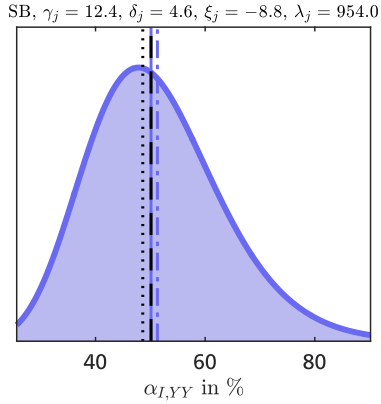

SB, $\gamma_j = 3.1$, $\delta_j = 2.3$, $\xi_j = 15.6$, $\lambda_j = 169.3$

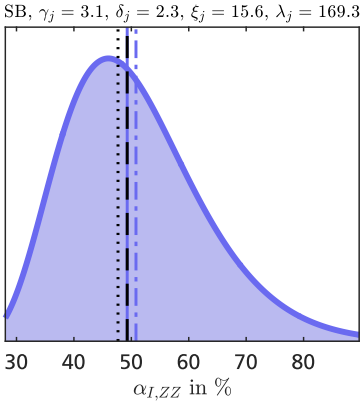

SU, $\gamma_j = -2.2$, $\delta_j = 1.9$, $\xi_j = 21.9$, $\lambda_j = 168.4$

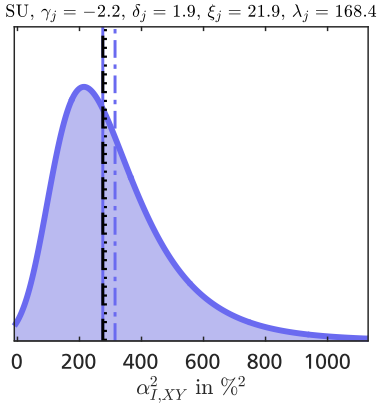

SU, $\gamma_j = 3.7$, $\delta_j = 2.1$, $\xi_j = 81.4$, $\lambda_j = 71.7$

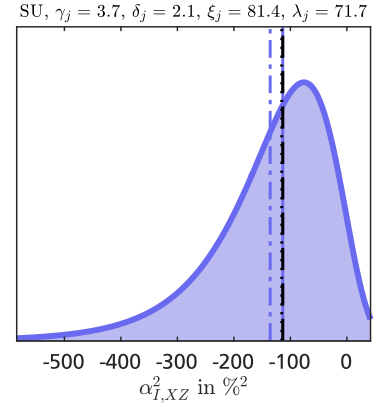

SU, $\gamma_j = 0.1$, $\delta_j = 0.6$, $\xi_j = 12.6$, $\lambda_j = 55.5$

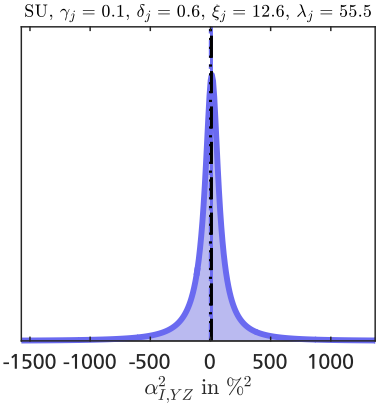

Copula covariance matrix for regression parameters of anthropometric parameters in the female foot.

Σ_c	α_m	$\alpha_{o,X}$	$\alpha_{o,Y}$	$\alpha_{o,Z}$	$\alpha_{I,XX}$	$\alpha_{I,YY}$	$\alpha_{I,ZZ}$	$\alpha_{I,XY}$	$\alpha_{I,XZ}$	$\alpha_{I,YZ}$
α_m	0.0835	$*$	$*$	$*$	$*$	$*$	$*$	$*$	$*$	$*$
$\alpha_{o,X}$	-0.0003	0.0829	$*$	$*$	$*$	$*$	$*$	$*$	$*$	$*$
$\alpha_{o,Y}$	-0.0007	0.0326	0.0825	$*$	$*$	$*$	$*$	$*$	$*$	$*$
$\alpha_{o,Z}$	0.0010	-0.0364	-0.0063	0.0767	$*$	$*$	$*$	$*$	$*$	$*$
$\alpha_{I,XX}$	-0.0167	-0.0449	-0.0013	0.0126	0.0847	$*$	$*$	$*$	$*$	$*$
$\alpha_{I,YY}$	-0.0166	-0.0462	-0.0013	0.0111	0.0622	0.0837	$*$	$*$	$*$	$*$
$\alpha_{I,ZZ}$	-0.0166	-0.0454	-0.0007	0.0113	0.0603	0.0651	0.0827	$*$	$*$	$*$
$\alpha_{I,XY}$	0.0117	0.0263	-0.0001	-0.0057	-0.0376	-0.0562	-0.0384	0.0847	$*$	$*$
$\alpha_{I,XZ}$	-0.0038	-0.0131	-0.0016	0.0036	0.0176	0.0213	0.0199	-0.0126	0.0563	$*$
$\alpha_{I,YZ}$	-0.0010	-0.0019	0.0019	0.0003	0.0030	-0.0043	0.0114	0.0092	0.0026	0.0246

Copula covariance matrix for regression parameters of anthropometric parameters in the male foot.

Σ_c	α_m	$\alpha_{o,X}$	$\alpha_{o,Y}$	$\alpha_{o,Z}$	$\alpha_{I,XX}$	$\alpha_{I,YY}$	$\alpha_{I,ZZ}$	$\alpha_{I,XY}$	$\alpha_{I,XZ}$	$\alpha_{I,YZ}$
α_m	0.0756	$*$	$*$	$*$	$*$	$*$	$*$	$*$	$*$	$*$
$\alpha_{o,X}$	0.0000	0.0852	$*$	$*$	$*$	$*$	$*$	$*$	$*$	$*$
$\alpha_{o,Y}$	0.0003	0.0338	0.0841	$*$	$*$	$*$	$*$	$*$	$*$	$*$
$\alpha_{o,Z}$	0.0026	-0.0122	-0.0265	0.0792	$*$	$*$	$*$	$*$	$*$	$*$
$\alpha_{I,XX}$	-0.0187	-0.0541	-0.0095	-0.0052	0.0832	$*$	$*$	$*$	$*$	$*$
$\alpha_{I,YY}$	-0.0184	-0.0501	-0.0090	-0.0051	0.0628	0.0828	$*$	$*$	$*$	$*$
$\alpha_{I,ZZ}$	-0.0172	-0.0489	-0.0083	-0.0059	0.0562	0.0542	0.0831	$*$	$*$	$*$
$\alpha_{I,XY}$	-0.0145	-0.0375	-0.0091	-0.0038	0.0497	0.0680	0.0378	0.0814	$*$	$*$
$\alpha_{I,XZ}$	0.0000	0.0000	0.0000	0.0000	0.0000	0.0000	0.0000	0.0000	0.0000	$*$
$\alpha_{I,YZ}$	-0.0016	-0.0034	0.0004	-0.0013	0.0028	-0.0054	0.0153	-0.0095	0.0000	0.0241

Acknowledgments

This thesis was written during my time as a research associate at the Simulation, Systems Optimization and Robotics Group in the Department of Computer Science of Technische Universität Darmstadt. Parts of my research have been funded by the Deutsche Forschungsgemeinschaft (DFG) and the Forum für interdisziplinäre Forschung (FiF) of Technische Universität Darmstadt.

I would like to express my gratitude to my supervisor and first examiner Prof. Dr. Oskar von Stryk for providing me with patient guidance, valuable support and great creative freedom. The very encouraging and fruitful discussions with him helped me to focus my research and shape this thesis. Likewise, I want to thank Prof. Dr. André Seyfarth for agreeing to become my second examiner and allowing me to perform the biomechanical measurements that formed the basis for my research in his laboratory. His advice on various aspects of human biomechanics and the always supportive comments contributed immensely to the scientific outcome of this thesis.

I wish to acknowledge the support and help given by my former and current colleagues at the Simulation, Systems Optimization and Robotics Group. Special thanks go to Jérôme Kirchhoff and Marie Schumacher for the countless but always enlightening whiteboard sessions. Those open discussions helped me a lot to improve my research and make substantial progress. I am also particularly grateful for the assistance given by the staff of the Locomotion Laboratory during the biomechanical measurements. Especially, Dr. Martin Grimmer and Christian Schumacher provided me with very valuable support and helpful advice regarding the measurement equipment. My special thanks are extended to Markus Hessinger and Jürgen Hielscher from the Institute of Electromechanical Design for allowing me to use their highly accurate force-torque sensor during my reference measurements and assisting me in the preparation of the experimental setup.

I would like to express further gratitude to Dr.-Ing. Philipp Beckerle and Prof. Dr.-Ing. Stephan Rinderknecht as well as Tim Schürmann, Dr. Oliver Christ and Prof. Dr. Joachim Vogt for the very productive and pleasant collaboration. Particularly, I want to thank Dr.-Ing. Philipp Beckerle for the always motivating discussions and for reviewing parts of the manuscript.

Most of all, I wish to thank my family for their constant support, I could not have finished the work on this thesis without them. I am especially grateful for the endless patience of my wife Anna, her warm words of encouragement that motivated me to keep up and her thorough review of the manuscript.

Bibliography

[1] M. Ackermann. *Dynamics and Energetics of Walking with Prostheses*. Phd, Universität Stuttgart, 2007.

[2] E. J. Alexander and T. P. Andriacchi. Correcting for deformation in skin-based marker systems. *Journal of Biomechanics*, 34(3):355–61, 2001.

[3] N. Alexander and H. Schwameder. Lower limb joint forces during walking on the level and slopes at different inclinations. *Gait & Posture*, 45(1):137–142, 2016.

[4] R. M. Alexander. Mechanics of bipedal locomotion. In P. S. Davies and N. Sunderland, editors, *Perspectives in experimental biology*, pages 493–504. Pergamon Press, first edition, 1976.

[5] T. Alkjaer, E. B. Simonsen, and P. Dyhre-Poulsen. Comparison of inverse dynamics calculated by two- and three-dimensional models during walking. *Gait & Posture*, 13(2):73–77, 2001.

[6] S. Almosnino, T. Kajaks, and P. A. Costigan. The free moment in walking and its change with foot rotation angle. *Sports Medicine, Arthroscopy, Rehabilitation, Therapy & Technology*, 1(1):19–27, 2009.

[7] N. Alnu'man. *Advanced Simulation of an Adaptive Lower Limb Prosthesis*. Phd, Technische Universität Darmstadt, 2010.

[8] F. J. Alonso, J. M. del Castillo, and P. Pintado. Motion data processing and wobbling mass modelling in the inverse dynamics of skeletal models. *Mechanism and Machine Theory*, 42(9):1153–1169, 2007.

[9] F. Alton, L. Baldey, S. Caplan, and M. C. Morrissey. A kinematic comparison of overground and treadmill walking. *Clinical Biomechanics*, 13(6):434–440, 1998.

[10] M. S. Andersen, S. Mellon, G. Grammatopoulos, and H. S. Gill. Evaluation of the accuracy of three popular regression equations for hip joint centre estimation using computerised tomography measurements for metal-on-metal hip resurfacing arthroplasty patients. *Gait & Posture*, 38(4):1044–1047, 2013.

[11] A. E. Anderson, B. J. Ellis, and J. A. Weiss. Verification, Validation and Sensitivity Studies in Computational Biomechanics. *Computer Methods in Biomechanics and Biomedical Engineering*, 10(3):1171–184, 2012.

[12] D. E. Anderson, M. L. Madigan, and M. A. Nussbaum. Maximum voluntary joint torque as a function of joint angle and angular velocity: Model development and application to the lower limb. *Journal of Biomechanics*, 40(14):3105–3113, 2007.

[13] A. S. Arnold and S. L. Delp. Computer modeling of gait abnormalities in cerebral palsy: application to treatment planning. *Theoretical Issues in Ergonomics Science*, 6(3-4):305–312, 2005.

[14] E. M. Arnold, S. R. Hamner, A. Seth, M. Millard, and S. L. Delp. How muscle fiber lengths and velocities affect muscle force generation as humans walk and run at different speeds. *Journal of Experimental Biology*, 216(1):2150–2160, 2013.

[15] G. A. Ateshian and M. H. Friedman. Integrative biomechanics: A paradigm for clinical applications of fundamental mechanics. *Journal of Biomechanics*, 42(10):1444–1451, 2009.

[16] S. K. Au, P. Bonato, and H. M. Herr. An EMG-position controlled system for an active ankle-foot prosthesis: An initial experimental study. In *Proceedings of the IEEE International Conference on Rehabilitation Robotics*, pages 375–379, 2005.

[17] K. Ayusawa, G. Venture, and Y. Nakamura. Real-time Implementation of Physically Consistent Identification of Human Body Segments. In *Proceedings of the IEEE International Conference on Robotics and Automation*, pages 6282–6287, 2011.

[18] P. Beckerle. *Human-machine-centered design and actuation of lower limb prosthetic systems*. Phd, Technische Universität Darmstadt, 2014.

[19] P. Beckerle, O. Christ, T. Schürmann, J. Vogt, O. von Stryk, and S. Rinderknecht. A human-machine-centered design method for (powered) lower limb prosthetics. *Robotics and Autonomous Systems*, accepted, 2017.

[20] P. Beckerle, O. Christ, M. Windrich, S. Rinderknecht, J. Vogt, and J. Wojtusch. A Methodological Approach to Integrate Psychological Factors to Lower Limb Prosthetic Functional Design. In *Proceedings of the ISPO 2013 World Congress*, page 185, Hyderabad, 2013.

[21] P. Beckerle, O. Christ, J. Wojtusch, J. Schuy, K. Wolff, S. Rinderknecht, J. Vogt, and O. von Stryk. Design and control of a robot for the assessment of psychological factors in prosthetic development. In *Proceedings of the IEEE International Conference on Systems, Man, and Cybernetics*, pages 1485–1490, Seoul, 2012.

[22] P. Beckerle, L. Lahnstein, J. Wojtusch, S. Rinderknecht, and O. von Stryk. Conception and Design of a Hardware Simulator for Restoring Lost Biomechanical Function. In *Proceedings of the IEEE International Conference on Systems, Man, and Cybernetics*, pages 1906–1911, Manchester, 2013.

[23] P. Beckerle, F. Schültje, J. Wojtusch, and O. Christ. Implementation, Control and User-Feedback of the Int^{2}Bot for the Investigation of Lower Limb Body Schema Integration. In *Proceedings of the IEEE International Symposium on Robot and Human Interactive Communication*, pages 704–709, Edinburgh, 2014.

[24] P. Beckerle, F. Stuhlenmiller, J. Schuy, J. Wojtusch, S. Rinderknecht, and O. von Stryk. Friction Compensation and Stiffness Evaluation on a Variable Torsion Stiffness. In *Proceedings of the International Symposium on Adaptive Motion of Animals and Machines*, pages 64–65, Darmstadt, 2013.

[25] P. Beckerle, J. Wojtusch, S. Rinderknecht, and O. von Stryk. Mechanical Influences on the Design of Actuators with Variable Stiffness. In *Proceedings of the International Symposium on Adaptive Motion of Animals and Machines*, pages 66–67, Darmstadt, 2013.

[26] P. Beckerle, J. Wojtusch, S. Rinderknecht, and O. von Stryk. Analysis of System Dynamic Influences in Robotic Actuators with Variable Stiffness. *Smart Structures and Systems*, 13(4):711–730, 2014.

[27] P. Beckerle, J. Wojtusch, J. Schuy, B. Strah, S. Rinderknecht, and O. von Stryk. Power-optimized Stiffness and Nonlinear Position Control of an Actuator with Variable Torsion Stiffness. In *Proceedings of the International Conference on Advanced Intelligent Mechatronics*, pages 387–392, Wollongong, 2013.

[28] P. Beckerle, J. Wojtusch, A. Seyfarth, O. von Stryk, and S. Rinderknecht. Analyzing and Considering Inertial Effects in Powered Lower Limb Prosthetic Design. In *Proceedings of the IEEE International Conference on Rehabilitation Robotics*, pages 325–330, Singapore, 2015.

[29] A. L. Bell, D. R. Pedersen, and R. A. Brand. A Comparison of the Accuracy of Several Hip Center Location Prediction Methods. *Journal of Biomechanics*, 23(6):617–621, 1990.

[30] D. L. Benoit, D. K. Ramsey, M. Lamontagne, L. Xu, P. Wretenberg, and P. Renström. Effect of skin movement artifact on knee kinematics during gait and cutting motions measured in vivo. *Gait & Posture*, 24(2):152–164, 2006.

[31] E. V. Billis, N. E. Foster, and C. C. Wright. Reproducibility and repeatability: Errors of three groups of physiotherapists in locating spinal levels by palpation. *Manual Therapy*, 8(4):223–232, 2003.

[32] R. Blickhan. The spring-mass model for running and hopping. *Journal of Biomechanics*, 22(11-12):1217–1227, 1989.

[33] M. F. Bobbert. Possibilities and limitations of musculoskeletal modelling and optimization in sports and rehabilitation. In *Keynote at the Joint Conference on Motor Control and Learning, Biomechanics and Training*, Darmstadt, 2016.

[34] M. F. Bobbert, J. C. L. Richard, and D. A. Kistemaker. Humans make near-optimal adjustments of control to initial body configuration in vertical squat jumping. *Neuroscience*, 237:232–42, 2013.

[35] S. Böker, P. Beckerle, J. Wojtusch, and S. Rinderknecht. A Novel Design Approach and Operational Strategy for an Active Ankle-Foot Prosthesis. In *Proceedings of the International Symposium on Adaptive Motion of Animals and Machines*, pages 26–28, Darmstadt, 2013.

[36] M. Botvinick and J. Cohen. Rubber hands 'feel' touch that eyes see. *Nature*, 391(1):756, 1998.

[37] V. Camomilla, A. Cereatti, G. Vannozzi, and A. Cappozzo. An optimized protocol for hip joint centre determination using the functional method. *Journal of Biomechanics*, 39(6):1096–106, 2006.

[38] F. Campolongo, J. Cariboni, and A. Saltelli. An effective screening design for sensitivity analysis of large models. *Environmental Modelling and Software*, 22(10):1509–1518, 2007.

[39] A. Cappozzo, U. Della Croce, A. Leardini, and L. Chiari. Human movement analysis using stereophotogrammetry. Part 1: theoretical background. *Gait & Posture*, 21(2):186–96, 2005.

[40] V. Carbone, R. Fluit, P. Pellikaan, M. M. van der Krogt, D. Janssen, M. Damsgaard, L. Vigneron, T. Feilkas, H. F. J. M. Koopman, and N. Verdonschot. TLEM 2.0 – A comprehensive musculoskeletal geometry dataset for subject-specific modeling of lower extremity. *Journal of Biomechanics*, 48(5):734–741, 2015.

[41] V. Carbone, M. M. van der Krogt, H. F. J. M. Koopman, and N. Verdonschot. Sensitivity of subject-specific models to Hill muscle-tendon model parameters in simulations of gait. *Journal of Biomechanics*, 49(9):1953–1960, 2016.

[42] M. C. Carson, M. Harrington, E. Thompson, J. J. O'Connor, and T. N. Theologis. Kinematic analysis of a multi-segment foot model for research and clinical applications: A repeatability analysis. *Journal of Biomechanics*, 34(10):1299–1307, 2001.

[43] P. Caserman, P. Krabbe, J. Wojtusch, and O. von Stryk. Real-Time Step Detection Using the Integrated Sensors of a Head-Mounted Display. In *Proceedings of the IEEE International Conference on Systems, Man, and Cybernetics*, pages 003510–003515, Budapest, 2016.

[44] A. Cedraro, A. Cappello, and L. Chiari. A portable system for in-situ re-calibration of force platforms: Experimental validation. *Gait & Posture*, 29(3):449–453, 2009.

[45] Y. Chen, A. Wiesel, Y. C. Eldar, and A. O. Hero. Shrinkage algorithms for MMSE covariance estimation. *IEEE Transactions on Signal Processing*, 58(10):5016–5029, 2010.

[46] L. Chèze, B. J. Fregly, and J. Dimnet. A solidification procedure to facilitate kinematic analyses based on video system data. *Journal of Biomechanics*, 28(7):879–884, 1995.

[47] L. Chiari, U. Della Croce, A. Leardini, and A. Cappozzo. Human movement analysis using stereophotogrammetry. Part 2: instrumental errors. *Gait & Posture*, 21(2):197–211, 2005.

[48] O. Christ, P. Beckerle, J. Preller, M. Jokisch, S. Rinderknecht, J. Wojtusch, O. von Stryk, and J. Vogt. The rubber hand illusion: Maintaining factors and a new perspective in rehabilitation and biomedical engineering? *Biomedical Engineering*, 57(S1):846–849, 2012.

[49] O. Christ, M. Jokisch, J. Preller, P. Beckerle, J. Wojtusch, S. Rinderknecht, O. von Stryk, and J. Vogt. User-Centered Prosthetic Development: Comprehension of Amputees' Needs. *Biomedical Engineering*, 57(S1):1098–1101, 2012.

[50] O. Christ, J. Wojtusch, and P. Beckerle. Robotic Mirroring of Movements in the Lower Limbs: Signal Delay of a Consumer Device Sensor. In *Proceedings of the Meeting of the Society of Applied Neurosciences*, page 96, Utrecht, 2014.

[51] O. Christ, J. Wojtusch, P. Beckerle, K. Wolff, J. Vogt, O. von Stryk, and S. Rinderknecht. Prosthesis-User-in-the-Loop: User-centered design parameters and visual simulation. In *Proceedings of the International Conference of the IEEE Engineering in Medicine and Biology Society*, pages 1929–1932, San Diego, 2012.

[52] C. E. Clauser, J. T. McConville, and J. W. Young. Weight, volume and center of mass of segments of the human body. Technical report, US Air Force, Dayton, 1969.

[53] S. H. Collins, P. G. Adamczyk, D. P. Ferris, and A. D. Kuo. A simple method for calibrating force plates and force treadmills using an instrumented pole. *Gait & Posture*, 29(1):59–64, 2009.

[54] S. H. Collins, P. G. Adamczyk, and A. D. Kuo. Dynamic arm swinging in human walking. *Proceedings of the Royal Society of London Series B: Biological Science*, 276(1673):3679–88, 2009.

[55] R. I. Cukier, H. B. Levine, and K. E. Shuler. Nonlinear sensitivity analysis of multiparameter model systems. *Journal of Computational Physics*, 26(1):1–42, 1978.

[56] R. B. Davis, S. Õunpuu, D. Tyburski, and J. R. Gage. A gait analysis data collection and reduction technique. *Human Movement Science*, 10(5):575–587, 1991.

[57] F. de Groote, T. de Laet, I. Jonkers, and J. de Schutter. Kalman smoothing improves the estimation of joint kinematics and kinetics in marker-based human gait analysis. *Journal of Biomechanics*, 41(16):3390–3398, 2008.

[58] P. de Leva. Adjustments to Zatsiorsky-Seluyanov's segment inertia parameters. *Journal of Biomechanics*, 29(9):1223–1230, 1996.

[59] U. Della Croce and A. Cappozzo. A spot check for estimating stereophotogrammetric errors. *Medical & Biological Engineering & Computing*, 38(3):260–266, 2000.

[60] U. Della Croce, A. Cappozzo, and D. C. Kerrigan. Pelvis and lower limb anatomical landmark calibration precision and its propagation to bone geometry and joint angles. *Medical & Biological Engineering & Computing*, 37(2):155–161, 1999.

[61] U. Della Croce, A. Leardini, L. Chiari, and A. Cappozzo. Human movement analysis using stereophotogrammetry. Part 4: assessment of anatomical landmark misplacement and its effects on joint kinematics. *Gait & Posture*, 21(2):226–37, 2005.

[62] S. L. Delp, F. C. Anderson, A. S. Arnold, P. Loan, A. Habib, C. John, E. Guendelman, and D. G. Thelen. OpenSim: Open-Source Software to Create and Analyze Dynamic Simulations of Movement. *IEEE Transactions on Biomedical Engineering*, 54(11):1940–1950, 2007.

[63] W. T. Dempster. Space Requirements of the Seated Operator. Technical report, United States Air Force, 1955.

[64] C. R. Dickerson, D. B. Chaffin, and R. E. Hughes. A mathematical musculoskeletal shoulder model for proactive ergonomic analysis. *Computer Methods in Biomechanics and Biomedical Engineering*, 10(6):389–400, 2007.

[65] R. Dumas and L. Chèze. Soft tissue artifact compensation by linear 3D interpolation and approximation methods. *Journal of Biomechanics*, 42(13):2214–2217, 2009.

[66] R. Dumas, L. Chèze, and J.-P. Verriest. Adjustments to McConville et al. and Young et al. body segment inertial parameters. *Journal of Biomechanics*, 40(3):543–553, 2007.

[67] R. Dumas, L. Chèze, and J.-P. Verriest. Corrigendum to "Adjustments to McConville et al. and Young et al. body segment inertial parameters". *Journal of Biomechanics*, 40(7):1651–1652, 2007.

[68] R. Dumas, T. Robert, L. Chèze, and J.-P. Verriest. Thorax and abdomen body segment inertial parameters adjusted from McConville et al. and Young et al. *International Biomechanics*, 2(1):113–118, 2015.

[69] R. Dumas and J. Wojtusch. Estimation of the Body Segment Inertial Parameters for the Rigid Body Biomechanical Models used in Motion Analysis. In B. Müller and S. I. Wolf, editors, *Handbook of Human Motion*. Springer, first edition, 2017.

[70] T. Dupré, K. R. L. Mortensen, F. G. Lysdal, J. Funken, R. Müller, M. Braun, H. Krahl, U. Kersting, and W. Potthast. Hip Joint Load and Muscle Stress in Soccer Inside Passing. In *Proceedings of the International Conference on Biomechanics in Sports*, pages 565–568, Tsukuba, 2016.

[71] J. L. Durkin, J. J. Dowling, and D. M. Andrews. The measurement of body segment inertial parameters using dual energy X-ray absorptiometry. *Journal of Biomechanics*, 35(12):1575–80, 2002.

[72] Y. Ehara, H. Fujimoto, S. Miyazaki, M. Mochimaru, S. Tanaka, and S. Yamamoto. Comparison of the performance of 3D camera systems II. *Gait & Posture*, 5(3):251–255, 1997.

[73] Y. Ehara, H. Fujimoto, S. Miyazaki, S. Tanaka, and S. Yamamoto. Comparison of the performance of 3D camera systems. *Gait & Posture*, 3(3):166–169, 1995.

[74] B. C. Elliott, J. A. Alderson, and E. R. Denver. System and modelling errors in motion analysis: Implications for the measurement of the elbow angle in cricket bowling. *Journal of Biomechanics*, 40(12):2679–2685, 2007.

[75] J. Englsberger, P. Kozłowski, C. Ott, and A. Albu-Schäffer. Biologically Inspired Deadbeat Control for Running: From Human Analysis to Humanoid Control and Back. *IEEE Transactions on Robotics*, 32(4):854–867, 2016.

[76] J. Eschweiler, J.-P. Stromps, M. Fischer, F. Schick, B. Rath, N. Pallua, and K. Radermacher. Development of a biomechanical model of the wrist joint for patient-specific model guided surgical therapy planning. *Journal of Engineering in Medicine*, 230(4):310–325, 2016.

[77] A. Faller and M. Schünke. *The Human Body - An Introduction to Structure and Function*. Georg Thieme Verlag, first edition, 2004.

[78] S. D. Farahani, W. Bertucci, M. S. Andersen, M. de Zee, and J. Rasmussen. Prediction of crank torque and pedal angle profiles during pedaling movements by biomechanical optimization. *Structural and Multidisciplinary Optimization*, 51(1):251–266, 2015.

[79] R. Featherstone. The Calculation of Robot Dynamics Using Articulated-Body Inertias. *The International Journal of Robotics Research*, 2(1):13–30, 1983.

[80] R. Featherstone. *Rigid Body Dynamics Algorithms*. Springer, first edition, 2008.

[81] D. P. Ferris and C. L. Lewis. Robotic lower limb exoskeletons using proportional myoelectric control. In *Proceedings of the International Conference of the IEEE Engineering in Medicine and Biology Society*, volume 2009, pages 2119–2124, 2009.

[82] N. P. Fey, G. K. Klute, and R. R. Neptune. Optimization of Prosthetic Foot Stiffness to Reduce Metabolic Cost and Intact Knee Loading During Below-Knee Amputee Walking: A Theoretical Study. *Journal of Biomechanical Engineering*, 134(11):111005–1–111005–10, 2012.

[83] B. J. Fregly, T. F. Besier, D. G. Lloyd, S. L. Delp, S. A. Banks, M. G. Pandy, and D. D. D'Lima. Grand challenge competition to predict in vivo knee loads. *Journal of Orthopaedic Research*, 30(4):503–513, 2012.

[84] M. Friedmann, J. Wojtusch, and O. von Stryk. A modular and efficient approach to computational modeling and sensitivity analysis of robot and human motion dynamics. *Proceedings in Applied Mathematics and Mechanics*, 12(1):85–86, 2012.

[85] C. D. Fryar, Q. Gu, and C. L. Ogden. Anthropometric Reference Data for Children and Adults: United States, 2007-2010. 2012.

[86] J. R. Full and D. E. Koditschek. Templates and anchors: Neuromechanical hypotheses of legged locomotion on land. *Journal of Experimental Biology*, 1999.

[87] G. Furness, M. P. Reilly, and S. Kuchi. An evaluation of ultrasound imaging for identification of lumbar intervertebral level. *Anaesthesia*, 57(3):277–280, 2002.

[88] I. C. Gadotti and D. Magee. Validity of surface markers placement on the cervical spine for craniocervical posture assessment. *Manual Therapy*, 18(3):243–247, 2013.

[89] B. Gao and N. Zheng. Investigation of soft tissue movement during level walking: Translations and rotations of skin markers. *Journal of Biomechanics*, 41(15):3189–3195, 2008.

[90] F. George and K. M. Ramachandran. Estimation of parameters of Johnson's system of distributions. *Journal of Modern Applied Statistical Methods*, 10(2):494–504, 2011.

[91] H. Geyer and H. M. Herr. A Muscle-Reflex Model That Encodes Principles of Legged Mechanics Produces Human Walking Dynamics and Muscle Activities. *IEEE Transactions on Neural Systems and Rehabilitation Engineering*, 18(3):263–273, 2010.

[92] H. Geyer, A. Seyfarth, and R. Blickhan. Compliant leg behaviour explains basic dynamics of walking and running. *Proceedings of the Royal Society of London Series B: Biological Science*, 273(1603):2861–2867, 2006.

[93] M. Grimmer, M. Eslamy, S. Gliech, and A. Seyfarth. A comparison of parallel-and series-elastic elements in an actuator for mimicking human ankle joint in walking and running. In *Proceedings of the IEEE International Conference on Robotics and Automation*, pages 2463–2470. IEEE, 2012.

[94] M. Grimmer, M. Holgate, R. Holgate, A. Boehler, J. Ward, K. Hollander, T. Sugar, and A. Seyfarth. A powered prosthetic ankle joint for walking and running. *BioMedical Engineering OnLine*, 15(3):286–301, 2016.

[95] M. Grimmer and A. Seyfarth. Stiffness Adjustment of a Series Elastic Actuator in an Ankle-foot Prosthesis for Walking and Running: The Trade-off between Energy and Peak Power Optimization. In *Proceedings of the IEEE International Conference on Robotics and Automation*, pages 1439–1444, Shanghai, 2011.

[96] K. Gruber, H. Ruder, J. Denoth, and K. Schneider. A comparative study of impact dynamics: wobbling mass model versus rigid body models. *Journal of Biomechanics*, 31(5):439–44, 1998.

[97] M. Günther. *Computersimulationen zur Synthetisierung des muskulär erzeugten menschlichen Gehens unter Verwendung eines biomechanischen Mehrkörpermodells*. Phd, Eberhard-Karls-Universität, 1997.

[98] M. Günther, V. A. Sholukha, D. Keßler, V. Wank, and R. Blickhan. Dealing with skin motion and wobbling masses in inverse dynamics. *Journal of Mechanics in Medicine and Biology*, 3(3):309–335, 2003.

[99] D. F. B. Haeufle, S. Grimmer, and A. Seyfarth. The role of intrinsic muscle properties for stable hopping–stability is achieved by the force-velocity relation. *Bioinspiration & Biomimetics*, 5(1):16004, 2010.

[100] D. M. Hamby. A review of techniques for parameter sensitivity analysis of environmental models. *Environmental Monitoring and Assessment*, 32(2):135–154, 1994.

[101] J. C. Harlick, S. Milosavljevic, and P. D. Milburn. Palpation identification of spinous processes in the lumbar spine. *Manual Therapy*, 12(1):56–62, 2007.

[102] M. E. Harrington, A. B. Zavatsky, S. E. M. Lawson, Z. Yuan, and T. N. Theologis. Prediction of the hip joint centre in adults, children, and patients with cerebral palsy based on magnetic resonance imaging. *Journal of Biomechanics*, 40(3):595–602, 2007.

[103] H. Hatze. A mathematical model for the computational determination of parameter values of anthropomorphic segments. *Journal of Biomechanics*, 13(10):833–843, 1980.

[104] A. Henze. *Dreidimensionale biomechanische Modellierung und die Entwicklung eines Reglers zur Simulation zweibeinigen Gehens*. Phd, Eberhard-Karls-Universität, 2002.

[105] H. J. Hermens, B. Freriks, C. Disselhorst-Klug, and R. Günter. Development of recommendations for SEMG sensors and sensor placement procedures. *Journal of Electromyography and Kinesiology*, 10(5):361–374, 2000.

[106] J. L. Hicks, T. K. Uchida, A. Seth, A. Rajagopal, and S. L. Delp. Is my model good enough? Best practices for verification and validation of musculoskeletal models and simulations of human movement. *Journal of Biomechanical Engineering*, 137(2):1–24, 2015.

[107] A. V. Hill. The heat of shortening and the dynamic constants of muscle. *Proceedings of the Royal Society of London Series B: Biological Science*, 1938.

[108] I. D. Hill. Algorithm AS 100: Normal-Johnson and Johnson-Normal Transformations. *Journal of the Royal Society. Series C (Applied Statistics)*, 25(2):190–192, 1976.

[109] I. D. Hill, R. Hill, and R. L. Holder. Algorithm AS 99: Fitting Johnson Curves by Moments. *Journal of the Royal Society. Series C (Applied Statistics)*, 25(2):180–189, 1976.

[110] L. J. Holmberg and A. M. Lund. A musculoskeletal full-body simulation of cross-country skiing. *Journal of Sports Engineering and Technology*, 222(1):11–22, 2008.

[111] U. Holmgren and K. Waling. Inter-examiner reliability of four static palpation tests used for assessing pelvic dysfunction. *Manual Therapy*, 13(1):50–56, 2008.

[112] H. J. Hsieh, T. W. Lu, S. C. Chen, C. M. Chang, and C. Hung. A new device for in situ static and dynamic calibration of force platforms. *Gait & Posture*, 33(4):701–705, 2011.

[113] A. F. Huxley. Muscle structure and theories of contraction. *Progress in Biophysics and Biophysical Chemistry*, 7(1):257–318, 1957.

[114] H. Huxley and J. Hanson. Changes in the Cross-Striations of Muscle during Contraction and Stretch and their Structural Interpretation. *Nature*, 22(173):973–976, 1954.

[115] R. L. Iman, J. M. Davenport, and D. K. Zeigler. Latin hypercube sampling (program user's guide). 1980.

[116] ISO 5725-1. Accuracy (trueness and precision) of measurement methods and results - Part 1: General principles and definitions. Standard, International Organization for Standardization (ISO), Geneva, 1994.

[117] M. Jackson, É. Sylvestre, J. Bleau, P. Allard, and M. Begon. Estimating optimal shoulder immobilization postures following surgical repair of massive rotator cuff tears. *Journal of Biomechanics*, 46(1):179–182, 2013.

[118] N. L. Johnson. Systems of Frequency Curves Generated by Methods of Translation. *Biometrika*, 36(1/2):149–176, 1949.

[119] Joint Committee for Guides in Metrology. Evaluation of measurement data - Guide to the expression of uncertainty in measurement. 2008.

[120] Joint Committee for Guides in Metrology. Evaluation of measurement data - Supplement 1 - Propagation of distributions using a Monte Carlo method. 2008.

[121] Joint Committee for Guides in Metrology. Evaluation of measurement data - Supplement 2 - Extension to any number of output quantities. 2011.

[122] A. C. Kern, W. Ellermeier, and J. Wojtusch. Noise-Cancelling, Steps and Soundscapes — The Effect of Auditory Stimulation on Presence in Virtual Realities while Walking. In *Proceedings of the ACM Conference on Virtual Reality Software and Technology*, pages 87–90, Munich, 2016.

[123] J. Kilby, N. R. Heneghan, and M. Maybury. Manual palpation of lumbo-pelvic landmarks: A validity study. *Manual Therapy*, 17(3):259–262, 2012.

[124] H. W. Kim, Y. J. Ko, W. I. Rhee, J. S. Lee, J. E. Lim, S. J. Lee, S. Im, and J. I. Lee. Interexaminer Reliability and Accuracy of Posterior Superior Iliac Spine and Iliac Crest Palpation for Spinal Level Estimations. *Journal of Manipulative and Physiological Therapeutics*, 30(5):386–389, 2007.

[125] P. Klein and P. Sommerfeld. *Biomechanik der menschlichen Gelenke*. Elsevier, first edition, 2004.

[126] P. Konrad. *The ABC of EMG*. Noraxon Inc., first edition, 2006.

[127] S. Kucherenko, D. Albrecht, and A. Saltelli. Exploring multi-dimensional spaces: A Comparison of Latin Hypercube and Quasi Monte Carlo Sampling Techniques. Preprint, arXiv:1505.02350 [stat.AP], 2015.

[128] S. Kucherenko, S. Tarantola, and P. Annoni. Estimation of global sensitivity indices for models with dependent variables. *Computer Physics Communications*, 183(4):937–946, 2012.

[129] A. Leardini, A. Cappozzo, F. Catani, S. Toksvig-Larsen, A. Petitto, V. Sforza, G. Cassanelli, and S. Giannini. Validation of a functional method for the estimation of hip joint centre location. *Journal of Biomechanics*, 32(1):99–103, 1999.

[130] A. Leardini, L. Chiari, U. Della Croce, and A. Cappozzo. Human movement analysis using stereophotogrammetry. Part 3. Soft tissue artifact assessment and compensation. *Gait & Posture*, 21(2):212–225, 2005.

[131] A. Leardini, J. J. O'Connor, F. Catani, and S. Giannini. A geometric model of the human ankle joint. *Journal of Biomechanics*, 32(6):585–591, 1999.

[132] L.-F. Lee, M. S. Narayanan, S. Kannan, F. Mendel, and V. N. Krovi. Case Studies of Musculoskeletal-Simulation-Based Rehabilitation Program Evaluation. *IEEE Transactions on Robotics*, 25(3):634–638, 2009.

[133] T. Lens. *Physical Human-Robot Interaction with a Lightweight, Elastic Tendon Driven Robotic Arm: Modeling, Control, and Safety Analysis*. Phd, Technische Universität Darmstadt, 2012.

[134] S. A. Lephart, J. H. Bolte, and C. B. Albery. The Effect of Variable and Uniform Densities on the Inertial Properties of Cadaver Segments, a Comparison of Frozen and Thawed Densities, and Segment Densities Related to Endomorphy and Ectomorphy. *Journal of Sports*, 1(2):119–136, 2014.

[135] A. Lewis, C. Stewart, N. Postans, and J. Trevelyan. Development of an instrumented pole test for use as a gait laboratory quality check. *Gait & Posture*, 26(2):317–322, 2007.

[136] S. W. Lipfert. *Kinematic and dynamic similarities between walking and running*. Phd, Friedrich-Schiller-Universität, 2010.

[137] S. W. Lipfert, M. Günther, D. Renjewski, and A. Seyfarth. Impulsive ankle push-off powers leg swing in human walking. *The Journal of Experimental Biology*, 217(1):1218–1228, 2014.

[138] H. Liu, C. Holt, and S. Evans. Accuracy and repeatability of an optical motion analysis system for measuring small deformations of biological tissues. *Journal of Biomechanics*, 40(1):210–214, 2007.

[139] W. Liu and B. M. Nigg. A mechanical model to determine the influence of masses and mass distribution on the impact force during running. *Journal of Biomechanics*, 33(2):219–224, 2000.

[140] J. Y. S. Luh, M. W. Walker, and R. P. C. Paul. On-Line Computational Scheme for Mechanical Manipulators. *Journal of Dynamic Systems, Measurement, and Control*, 102(2):69, 1980.

[141] K. Manal, I. McClay Davis, B. Galinat, and S. Stanhope. The accuracy of estimating proximal tibial translation during natural cadence walking: Bone vs. skin mounted targets. *Clinical Biomechanics*, 18(2):126–131, 2003.

[142] C. Mandery, Ö. Terlemez, M. Do, N. Vahrenkamp, and T. Asfour. The KIT whole-body human motion database. In *International Conference on Advanced Robotics*, pages 329–336, Istanbul, 2015.

[143] J. Matoušek. On the L2-discrepancy for Anchored Boxes. *Journal of Complexity*, 14(4):527–556, 1998.

[144] Á. Mayer, K. Kudar, K. Bretz, and J. Tihanyi. Body schema and body awareness of amputees. *Prosthetics and Orthotics International*, 32(3):363–382, 2008.

[145] J. T. McConville, T. D. Churchill, I. Kaleps, C. E. Clauser, and J. Cuzzi. Anthropometric Relationships of Body and Body Segment Moments of Inertia. Technical report, Aerospace Medical Research Laboratory, Dayton, 1980.

[146] J. T. McConville and C. E. Clauser. Anthropometric Assessment of the Mass Distribution Characteristics of the Living Human Body. *Proceedings of the Human Factors and Ergonomics Society Annual Meeting*, 20(16):379–383, 1976.

[147] N. Metropolis and S. M. Unam. The Monte Carlo Method. *Journal of the American Statistical Association*, 44(247):335–341, 1949.

[148] C. S. Moriguchi, L. Carnaz, L. C. C. B. Silva, L. E. B. Salasar, R. L. Carregaro, T. de Oliveira Sato, and H. J. C. G. Coury. Reliability of intra- and inter-rater palpation discrepancy and estimation of its effects on joint angle measurements. *Manual Therapy*, 14(3):299–305, 2009.

[149] M. D. Morris. Factorial Sampling Plans for Preliminary Computational Experiments. *Technometrics*, 33(2):161–174, 1991.

[150] V. C. Mow and R. Huiskes. *Basic Orthopaedic Biomechanics & Mechano-Biology*. Lippincott Williams & Wilkins, third edition, 2005.

[151] M. Müller, T. Röder, M. Clausen, B. Eberhardt, B. Krüger, and A. Weber. Documentation Mocap Database HDM05. Technical report, Universität Bonn, 2007.

[152] M. P. Murray. Gait as a total pattern of movement. *American Journal of Physical Medicine*, 46(1):290–333, 1967.

[153] C. A. Myers, K. B. Shelburne, P. J. Laz, and B. S. Davidson. A Probabilistic Approach to Quantify the Impact of Uncertainty Propagation in Musculoskeletal Simulations. *Annals of Biomedical Engineering*, 43(5):1098–1111, 2015.

[154] M. Nakashima, S. Maeda, T. Miwa, and H. Ichikawa. Optimizing simulation of the arm stroke in crawl swimming considering muscle strength characteristics of athlete swimmers. *Journal of Biomechanical Science and Engineering*, 7(2):102–117, 2012.

[155] T. C. Nguyen and K. J. Reynolds. The effect of variability in body segment parameters on joint moment using Monte Carlo simulations. *Gait & Posture*, 39(1):346–353, 2014.

[156] B. M. Nigg and W. Herzog. *Biomechanics of the Musculo-skeletal System*. Wiley, second edition, 1999.

[157] V. Noll, J. Wojtusch, J. Schuy, M. Grimmer, P. Beckerle, and S. Rinderknecht. Measurement of Biomechanical Interactions at the Stump-Socket Interface in Lower Limb Prostheses. In *Proceedings of the International Conference of the IEEE Engineering in Medicine and Biology Society*, pages 5517–5520, Milan, 2015.

[158] T. F. Novacheck. The biomechanics of running. *Gait & Posture*, 7(1):77–95, 1998.

[159] F. Ofli, R. Chaudhry, G. Kurillo, R. Vidal, and R. Bajcsy. Berkeley MHAD: A comprehensive Multimodal Human Action Database. In *IEEE Workshop on Applications of Computer Vision*, pages 53–60, Clearwater, 2013.

[160] C. L. Ogden, C. D. Fryar, M. D. Carroll, and K. M. Flegal. Mean body weight, height, and body mass index, United States 1960-2002. 2004.

[161] C. O'Haire and P. Gibbons. Inter-examiner and intra-examiner agreement for assessing sacroiliac anatomical landmarks using palpation and observation: pilot study. *Manual Therapy*, 5(1):13–20, 2000.

[162] S. T. Osis, B. A. Hettinga, S. Macdonald, and R. Ferber. Effects of simulated marker placement deviations on running kinematics and evaluation of a morphometric-based placement feedback method. *PLoS ONE*, 11(1), 2016.

[163] M. T. G. Pain and J. H. Challis. Wobbling mass influence on impact ground reaction forces: A simulation model sensitivity analysis. *Journal of Applied Biomechanics*, 20(3):309–316, 2004.

[164] R. Pàmies-Vilà. *Application of Multibody Dynamics Techniques to the Analysis of Human Gait*. Phd, Universitst Politècnica de Catalunya, 2012.

[165] R. Pàmies-Vilà, J. M. Font-llagunes, J. Cuadrado, and F. J. Alonso. Influence of Input Data Errors on the Inverse Dynamics Analysis of Human Locomotion. In *Proceedings of the Joint International Conference on Multibody System Dynamics*, pages 186–195, Lappeenranta, 2010.

[166] R. Pàmies-Vilà, J. M. Font-Llagunes, J. Cuadrado, and F. J. Alonso. Analysis of different uncertainties in the inverse dynamic analysis of human gait. *Mechanism and Machine Theory*, 58(1):153–164, 2012.

[167] R. Pàmies-Vilà, O. Pätkau, A. Dòria-Cerezo, and J. M. Font-Llagunes. Influence of the controller design on the accuracy of a forward dynamic simulation of human gait. *Mechanism and Machine Theory*, 107:123–138, 2017.

[168] J. Park, S. M. Ebert, M. P. Reed, and J. J. Hallman. Development of an Optimization Method for Locating the Pelvis in an Automobile Seat. In *Proceedings of the International Conference on Applied Human Factors and Ergonomics*, pages 3447–3453, Las Vegas, 2015.

[169] A. Peters, B. Galna, M. Sangeux, M. Morris, and R. Baker. Quantification of soft tissue artifact in lower limb human motion analysis: a systematic review. *Gait & Posture*, 31(1):1–8, 2010.

[170] S. J. Piazza and P. R. Cavanagh. Measurement of the screw-home motion of the knee is sensitive to errors in axis alignment. *Journal of Biomechanics*, 33(8):1029–1034, 2000.

[171] J. A. I. Prinold, C. Mazzà, R. Di Marco, I. Hannah, C. Malattia, S. Magni-Manzoni, M. Petrarca, A. B. Ronchetti, L. Tanturri de Horatio, E. H. P. van Dijkhuizen, S. Wesarg, and M. Viceconti. A Patient-Specific Foot Model for the Estimate of Ankle Joint Forces in Patients with Juvenile Idiopathic Arthritis. *Annals of Biomedical Engineering*, 44(1):247–257, 2016.

[172] S. G. Psycharakis and S. Miller. Estimation of Errors in Force Platform Data. *Research Quarterly for Exercise and Sport*, 77(4):514–518, 2006.

[173] M. Rabuffetti, G. Baroni, M. Ferrarin, G. Ferrigno, and A. Pedotti. Self-marking of anatomical landmarks for on-orbit experimental motion analysis compared to expert direct-marking. *Human Movement Science*, 21(4):439–455, 2002.

[174] A. Rajagopal, C. Dembia, M. DeMers, D. Delp, J. Hicks, and S. Delp. Full body musculoskeletal model for muscle-driven simulation of human gait. *IEEE Transactions on Biomedical Engineering*, 63(10):2068–2079, 2016.

[175] G. Rao, D. Amarantini, E. Berton, and D. Favier. Influence of body segments' parameters estimation models on inverse dynamics solutions during gait. *Journal of Biomechanics*, 39(8):1531–1536, 2006.

[176] J. Rasmussen, V. Vondrak, M. Damsgaard, M. de Zee, S. T. Christensen, and Z. Dostal. The AnyBody Project – Computer Analysis of the Human Body. In *International Congress of Biomechanics - Biomechanics of Man*, pages 270–274, Čejkovice, 2002.

[177] M. P. Reed, M. A. Manary, and L. W. Schneider. Methods for Measuring and Representing Automobile Occupant Posture. Technical Report 724, The Engineering Society For Advanced Mobility Land Sea Air and Space (SAE), Detroit, 1999.

[178] J. A. Reinbolt, R. T. Haftka, T. L. Chmielewski, and B. J. Fregly. Are Patient-Specific Joint and Inertial Parameters Necessary for Accurate Inverse Dynamics Analyses of Gait? *IEEE Transactions on Biomedical Engineering*, 54(5):782–793, 2007.

[179] H. M. Reynolds, C. C. Snow, and J. W. Young. Spatial Geometry of the Human Pelvis. Technical report, FAA Civil Aeromedical Institute, Oklahoma City, 1982.

[180] J. G. Richards. The measurement of human motion: A comparison of commercially available systems. *Human Movement Science*, 18(5):589–602, 1999.

[181] R. Riemer, E. T. Hsiao-Wecksler, and X. Zhang. Uncertainties in inverse dynamics solutions: A comprehensive analysis and an application to gait. *Gait & Posture*, 27(4):578–88, 2008.

[182] P. O. Riley, G. Paolini, U. Della Croce, K. W. Paylo, and D. C. Kerrigan. A kinematic and kinetic comparison of overground and treadmill walking in healthy subjects. *Gait & Posture*, 26(1):17–24, 2006.

[183] D. H. Robbins. Anthropometric Specifications for Mid-sized Male Dummies - Volume 2. Technical report, University of Michigan Transportation Research Institute, Ann Arbor, 1983.

[184] D. H. Robbins. Anthropometric Specifications for Small Female and Large Male Dummies - Volume 3. Technical report, University of Michigan Transportation Research Institute, Ann Arbor, 1983.

[185] T. Robert, L. Chèze, R. Dumas, and J.-P. Verriest. Joint forces and moments calculation for a 3D whole body model during complex movement. In *Proceedings of the International Symposium on the 3-D Analysis of Human Movement*, pages 1–4, Valenciennes, 2006.

[186] T. Robert, L. Chèze, R. Dumas, and J.-P. Verriest. Validation of net joint loads calculated by inverse dynamics in case of complex movements: Application to balance recovery movements. *Journal of Biomechanics*, 40(11):2450–2456, 2007.

[187] Robert Koch Institut. Gesundheitssurvey Ost/West 1990-1992. 1992.

[188] Robert Koch Institut. Nationaler Untersuchungssurvey der DHP 1984-1986. 1993.

[189] R. Robinson, H. S. Robinson, G. Bjørke, and A. Kvale. Reliability and validity of a palpation technique for identifying the spinous processes of C7 and L5. *Manual Therapy*, 14(4):409–414, 2009.

[190] A. Rouhandeh, C. Joslin, Z. Qu, and Y. Ono. Soft-tissue artefact assessment and compensation in hip joint kinematics using motion capture data and ultrasound depth measurements. In *IEEE International Conference on Biomedical Engineering and Systems*, pages 4342–4345, Prague, 2014.

[191] A. Saltelli. Making best use of model evaluations to compute sensitivity indices. *Computer Physics Communications*, 145(2):280–297, 2002.

[192] A. Saltelli, P. Annoni, I. Azzini, F. Campolongo, M. Ratto, and S. Tarantola. Variance based sensitivity analysis of model output. Design and estimator for the total sensitivity index. *Computer Physics Communications*, 181(2):259–270, 2010.

[193] A. Saltelli, A. Ratto, T. Andres, F. Campolongo, J. Cariboni, D. Gatelli, M. Saisana, and S. Tarantola. *Global Sensitivity Analisys. The Primer*. Wiley, first edition, 2008.

[194] A. Saltelli, S. Tarantola, F. Campolongo, and M. Ratto. *Sensitivity Analysis in Practice: A Guide to Assessing Scientific Models*. Wiley, first edition, 2004.

[195] M. Sangeux, F. Marin, F. Charleux, L. Dürselen, and M. C. Ho Ba Tho. Quantification of the 3D relative movement of external marker sets vs. bones based on magnetic resonance imaging. *Clinical Biomechanics*, 21(9):984–991, 2006.

[196] M. Sangeux, A. Peters, and R. Baker. Hip joint centre localization: Evaluation on normal subjects in the context of gait analysis. *Gait & Posture*, 34(3):324–328, 2011.

[197] L. W. Schneider, D. H. Robbins, M. A. Pflüg, and R. G. Snyder. Development of Anthropometrically Based Design Specifications for an Advanced Anthropometric Dummy Family - Volume 1. Technical report, University of Michigan Transportation Research Institute, Ann Arbor, 1983.

[198] D. Scholz, C. Maufroy, S. Kurowski, K. Radkhah, and O. von Stryk. Simulation and Experimental Evaluation of the Contribution of Biarticular Gastrocnemius Structure to Joint Synchronization in Human-Inspired Three-Segmented Elastic Legs. In *Proceedings of the International Conference on Simulation, Modeling and Programming for Autonomous Robots*, pages 251–260, Tsukuba, 2012.

[199] C. Schölzel and P. Friederichs. Multivariate non-normally distributed random variables in climate research - Introduction to the copula approach. *Nonlinear Processes in Geophysics*, 15(5):761–772, 2008.

[200] F. Schültje, P. Beckerle, M. Grimmer, J. Wojtusch, and S. Rinderknecht. Comparison of Trajectory Generation Methods for a Human-Robot Interface based on Motion Tracking in the Int²Bot. In *Proceedings of the IEEE International Symposium on Robot and Human Interactive Communication*, pages 710–715, Edinburgh, 2014.

[201] G. Schultz and K. D. Mombaur. Modeling and Optimal Control of Human-Like Running. *IEEE/ASME Transactions on Mechatronics*, 15(5):783–792, 2010.

[202] J. Schuy, P. Beckerle, J. Faber, J. Wojtusch, S. Rinderknecht, and O. von Stryk. Dimensioning and evaluation of the elastic element in a Variable Torsion Stiffness actuator. In *Proceedings of the International Conference on Advanced Intelligent Mechatronics*, pages 1786–1791, Wellbeing, 2013.

[203] J. Schuy, P. Beckerle, J. Wojtusch, S. Rinderknecht, and O. von Stryk. Conception and evaluation of a novel variable torsion stiffness for biomechanical applications. In *Proceedings of the IEEE RAS/EMBS International Conference on Biomedical Robotics and Biomechatronics*, pages 713–718, Rome, 2012.

[204] M. H. Schwartz and A. Rozumalski. A new method for estimating joint parameters from motion data. *Journal of Biomechanics*, 38(1):107–116, 2005.

[205] G. K. Seidel, D. M. Marchinda, M. Dijkers, and R. W. Soutas-Little. Hip joint center location from palpable bony landmarks - A cadaver study. *Journal of Biomechanics*, 28(8):995–998, 1995.

[206] R. E. Shannon. *Systems Simulation: The Art and Science*. Prentice Hall, first edition, 1975.

[207] B. Siciliano, L. Sciavicco, L. Villani, and G. Oriolo. *Robotics: Modelling, Planning and Control*. Springer, first edition, 2008.

[208] M. P. T. Silva and J. A. C. Ambrósio. Sensitivity of the results produced by the inverse dynamic analysis of a human stride to perturbed input data. *Gait & Posture*, 19(1):35–49, 2004.

[209] A. Sklar. Fonctions de répartition à n dimensions et leurs marges. *Publications de l'Institut de Statistique de L'Université de Paris*, 8(1):229–231, 1959.

[210] L. H. Sloot, H. Houdijk, and J. Harlaar. A comprehensive protocol to test instrumented treadmills. *Medical Engineering and Physics*, 37(6):610–616, 2015.

[211] R. G. Snyder, D. B. Chaffin, and R. K. Schutz. Link System of the Human Torso. Technical report, Air Force Aerospace Medical Research Laboratory, Dayton, 1972.

[212] I. M. Sobol'. On the distribution of points in a cube and the approximate evaluation of integrals. *USSR Computational Mathematics and Mathematical Physics*, 7(4):86–112, 1967.

[213] M. Sreenivasa, C. J. Chamorro, D. Gonzalez-Alvarado, O. Rettig, and S. Wolf. Patient-specific bone geometry and segment inertia from MRI images for model-based analysis of pathological gait. *Journal of Biomechanics*, 49(9):1918–1925, 2016.

[214] R. Stagni, S. Fantozzi, A. Cappello, and A. Leardini. Quantification of soft tissue artefact in motion analysis by combining 3D fluoroscopy and stereophotogrammetry: A study on two subjects. *Clinical Biomechanics*, 20(3):320–329, 2005.

[215] R. Stagni, A. Leardini, A. Cappozzo, M. Grazia Benedetti, and A. Cappello. Effects of hip joint centre mislocation on gait analysis results. *Journal of Biomechanics*, 33(11):1479–1487, 2000.

[216] Statistisches Bundesamt. Mikrozensus - Körpermaße der Bevölkerung 1978. 1978.

[217] Statistisches Bundesamt. Mikrozensus - Körpermaße der Bevölkerung 1999. 2001.

[218] Statistisches Bundesamt. Mikrozensus - Körpermaße der Bevölkerung 2003. 2004.

[219] Statistisches Bundesamt. Mikrozensus - Körpermaße der Bevölkerung 2005. 2006.

[220] Statistisches Bundesamt. Mikrozensus - Körpermaße der Bevölkerung 2009. 2010.

[221] Statistisches Bundesamt. Mikrozensus - Körpermaße der Bevölkerung 2013. 2014.

[222] L. M. Stelzer. *Forward Dynamics Simulation and Optimization of Walking Robots and Humans*. Phd, Technische Universität Darmstadt, 2007.

[223] I. Südhoff, S. van Driessche, S. Laporte, J. A. de Guise, and W. Skalli. Comparing three attachment systems used to determine knee kinematics during gait. *Gait & Posture*, 25(4):533–543, 2007.

[224] S. Tarantola, D. Gatelli, and T. A. Mara. Random balance designs for the estimation of first order sensitivity indices. *Reliability Engineering and System Safety*, 91(6):717–727, 2006.

[225] N. Thatte and H. Geyer. Toward Balance Recovery With Leg Prostheses Using Neuromuscular Model Control. *IEEE Transactions on Biomedical Engineering*, 63(5):904–913, 2016.

[226] F. Trochu. A contouring program based on dual kriging interpolation. *Engineering with Computers*, 9(1):160–177, 1993.

[227] G. Valente, L. Pitto, D. Testi, A. Seth, S. L. Delp, R. Stagni, M. Viceconti, and F. Taddei. Are subject-specific musculoskeletal models robust to the uncertainties in parameter identification? *PLoS ONE*, 9(11):1–10, 2014.

[228] A. J. van den Bogert, T. Geijtenbeek, O. Even-Zohar, F. Steenbrink, and E. C. Hardin. A real-time system for biomechanical analysis of human movement and muscle function. *Medical & Biological Engineering & Computing*, 51(10):1069–1077, 2013.

[229] R. van Ham, T. G. Sugar, B. Vanderborght, K. W. Hollander, and D. Lefeber. Compliant Actuator Designs. *IEEE Robotics & Automation Magazine*, 16(3):81–94, 2009.

[230] C. L. Vaughan. Kistler Force Plate Formulae. Technical report, University of Cape Town, 1999.

[231] G. Venture, K. Ayusawa, and Y. Nakamura. Optimal estimation of human body segments dynamics using realtime visual feedback. In *Proceedings of the IEEE/RSJ International Conference on Intelligent Robots and Systems*, pages 1627–1632, St. Louis, 2009.

[232] D. Villeger, A. Costes, B. Watier, and P. Moretto. An algorithm to decompose ground reaction forces and moments from a single force platform in walking gait. *Medical Engineering and Physics*, 36(11):1530–1535, 2014.

[233] R. von Schwerin. *MultiBody System SIMulation*. Springer, first edition, 1999.

[234] M. W. Walker and D. E. Orin. Efficient Dynamic Computer Simulation of Robotic Mechanisms. *Journal of Dynamic Systems, Measurement, and Control*, 104(3):205, 1982.

[235] A. Walther and A. Griewank. Getting started with ADOL-C. In *Combinatorial Scientific Computing*, chapter 7, pages 181–202. Chapman-Hall CRC Computational Science, first edition, 2012.

[236] H. Weisberg. *Central Tendency and Variability*. SAGE, second edition, 1992.

[237] M. Wesseling, F. de Groote, and I. Jonkers. The effect of perturbing body segment parameters on calculated joint moments and muscle forces during gait. *Journal of Biomechanics*, 47(2):596–601, 2014.

[238] R. E. Wheeler. Quantile Estimators of Johnson Curve Parameters. *Biometrika*, 67(3):725–728, 1980.

[239] M. W. Whittle. *Gait Analysis - An Introduction*. Butterworth-Heinemann, fourth edition, 2007.

[240] M. Windolf, N. Götzen, and M. Morlock. Systematic accuracy and precision analysis of video motion capturing systems-exemplified on the Vicon-460 system. *Journal of Biomechanics*, 41(12):2776–2780, 2008.

[241] D. A. Winter. Kinematic and kinetic patterns in human gait: Variability and compensating effects. *Human Movement Science*, 3(1-2):51–76, 1984.

[242] D. A. Winter. *Biomechanics and Motor Control of Human Movement*. John Wiley & Sons, fourth edition, 2009.

[243] J. Wojtusch, P. Beckerle, O. Christ, K. Wolff, O. von Stryk, S. Rinderknecht, and J. Vogt. Prosthesis-User-in-the-Loop: A user-specific biomechanical modeling and simulation environment. In *Proceedings of the International Conference of the IEEE Engineering in Medicine and Biology Society*, pages 4181–4184, San Diego, 2012.

[244] J. Wojtusch, P. Beckerle, T. Schürmann, M. Schumacher, O. Christ, A. Seyfarth, S. Rinderknecht, J. Vogt, and O. von Stryk. Towards Seamless Integration of Active Assistive Devices into the User's Body Schema. In *Proceedings of the Cybathlon Symposium*, page 32, Zurich, 2016.

[245] J. Wojtusch, P. Beckerle, and O. von Stryk. A Biomechanical Model for the Estimation of Dynamic Interactions at the Transfemoral Socket Interface. In *Proceedings of the ISPO 2013 World Congress*, page 228, Hyderabad, 2013.

[246] J. Wojtusch, J. Kunz, and O. von Stryk. MBSlib - An Efficient Multibody Systems Library for Kinematics and Dynamics Simulation, Optimization and Sensitivity Analysis. *IEEE Robotics and Automation Letters*, 1(2):954–960, 2016.

[247] J. Wojtusch and O. von Stryk. HuMoD - A Versatile and Open Database for the Investigation, Modeling and Simulation of Human Motion Dynamics on Actuation Level. In *Proceedings of the IEEE-RAS International Conference on Humanoid Robots*, pages 74–79, Seoul, 2015.

[248] K. Wolff, P. Beckerle, J. Wojtusch, and O. Christ. Nutzerfreundliche, energieeffiziente, aktive Beinprothesen: Eine neue Entwicklungsmethodik bindet Prothesennutzer ganzheitlich ein. *Orthopädie Technik*, 12(5):76–79, 2012.

[249] G. Wu and P. R. Cavanagh. ISB Recommendations for Standardization in the Reporting of Kinematic Data. *Journal of Biomechanics*, 28(10):1257–1261, 1995.

[250] G. Wu, S. Siegler, P. Allard, C. Kirtley, A. Leardini, D. Rosenbaum, M. Whittle, D. D. D'Lima, L. Cristofolini, H. Witte, O. Schmid, and I. Stokes. ISB Recommendation on Definitions of Joint Coordinate System of Various Joints for the Reporting of Human Joint Motion - Part I: Ankle, Hip and Spine. *Journal of Biomechanics*, 35(4):543–548, 2002.

[251] G. Wu, F. C. T. van der Helm, H. E. J. Veeger, M. Makhsous, P. van Roy, C. Anglin, J. Nagels, A. R. Karduna, K. McQuade, X. Wang, F. W. Werner, and B. Buchholz. ISB Recommendation on Definitions of Joint Coordinate Systems of Various Joints for the Reporting of Human Joint Motion Part II: Shoulder, Elbow, Wrist and Hand. *Journal of Biomechanics*, 38(5):981–992, 2005.

[252] G. T. Yamaguchi and F. E. Zajac. A planar model of the knee joint to characterize the knee extensor mechanism. *Journal of Biomechanics*, 22(1):1–10, 1989.

[253] M. R. Yeadon. The Simulation of Aerial Movement - A Mathematical Inertia Model of the Human Body. *Journal of Biomechanics*, 23(1):67–74, 1990.

[254] M. R. Yeadon and M. Morlock. The Appropriate Use of Regression Equations Inertia for the Estimation of Segmental Parameters. *Journal of Biomechanics*, 22(617):683–689, 1989.

[255] J. W. Young, R. F. Chandler, C. C. Snow, K. M. Robinette, G. F. Zehner, and M. S. Lofberg. Anthropometric and mass distribution characteristics of the adult female. Technical report, FAA Civil Aeromedical Institute, Oklahoma City, 1983.

[256] B. M. Yu, K. V. Shenoy, and M. Sahani. Derivation of Extended Kalman Filtering and Smoothing Equations. Technical report, Stanford University, 2004.

[257] B. M. Yu, K. V. Shenoy, and M. Sahani. Derivation of Kalman Filtering and Smoothing Equations. Technical report, Stanford University, 2004.

[258] A. A. Zadpoor, A. A. Nikooyan, and A. R. Arshi. A model-based parametric study of impact force during running. *Journal of Biomechanics*, 40(9):2012–2021, 2007.

[259] V. M. Zatsiorsky. *Kinematics of Human Motion*. Human Kinetics, first edition, 1998.

[260] V. M. Zatsiorsky. *Kinetics of Human Motion*. Human Kinetics, first edition, 2002.

[261] V. M. Zatsiorsky, V. N. Seluyanov, and L. G. Chugunova. Methods of determining mass-inertial characteristics of human body segments. In G. G. Chernyi and S. A. Regirer, editors, *Contemporary Problems of Biomechanics*, pages 272–291. CRC Press, first edition, 1990.

Publications

Book Chapters

R. Dumas and J. Wojtusch. Estimation of the Body Segment Inertial Parameters for the Rigid Body Biomechanical Models used in Motion Analysis. In B. Müller and S. I. Wolf, editors, *Handbook of Human Motion*. Springer, first edition, 2017.

Journal Papers

J. Wojtusch, J. Kunz, and O. von Stryk. MBSlib - An Efficient Multibody Systems Library for Kinematics and Dynamics Simulation, Optimization and Sensitivity Analysis. *IEEE Robotics and Automation Letters*, 1(2):954–960, 2016.

P. Beckerle, J. Wojtusch, S. Rinderknecht, and O. von Stryk. Analysis of System Dynamic Influences in Robotic Actuators with Variable Stiffness. *Smart Structures and Systems*, 13(4):711–730, 2014.

O. Christ, M. Jokisch, J. Preller, P. Beckerle, J. Wojtusch, S. Rinderknecht, O. von Stryk, and J. Vogt. User-Centered Prosthetic Development: Comprehension of Amputees' Needs. *Biomedical Engineering*, 57(S1):1098–1101, 2012.

O. Christ, P. Beckerle, J. Preller, M. Jokisch, S. Rinderknecht, J. Wojtusch, O. von Stryk, and J. Vogt. The rubber hand illusion: Maintaining factors and a new perspective in rehabilitation and biomedical engineering? *Biomedical Engineering*, 57(S1):846–849, 2012.

K. Wolff, P. Beckerle, J. Wojtusch, and O. Christ. Nutzerfreundliche, energieeffiziente, aktive Beinprothesen: Eine neue Entwicklungsmethodik bindet Prothesennutzer ganzheitlich ein. *Orthopädie Technik*, 12(5):76–79, 2012.

H. Mochizuki, J. Wojtusch, S. Takahashi, and H. Nakamura. Design of Distributed Control System Using Reconfiguration Method. *IEICE Technical Report on Reliability*, 108(125):25–28, 2008.

Conference Papers

P. Caserman, P. Krabbe, J. Wojtusch, and O. von Stryk. Real-Time Step Detection Using the Integrated Sensors of a Head-Mounted Display. In *Proceedings of the IEEE International Conference on Systems, Man, and Cybernetics*, pages 003510–003515, Budapest, 2016.

A. C. Kern, W. Ellermeier, and J. Wojtusch. Noise-Cancelling, Steps and Soundscapes — The Effect of Auditory Stimulation on Presence in Virtual Realities while Walking. In *Proceedings of the ACM Conference on Virtual Reality Software and Technology*, pages 87–90, Munich, 2016.

P. Beckerle, J. Wojtusch, A. Seyfarth, O. von Stryk, and S. Rinderknecht. Analyzing and Considering Inertial Effects in Powered Lower Limb Prosthetic Design. In *Proceedings of the IEEE International Conference on Rehabilitation Robotics*, pages 325–330, Singapore, 2015.

V. Noll, J. Wojtusch, J. Schuy, M. Grimmer, P. Beckerle, and S. Rinderknecht. Measurement of Biomechanical Interactions at the Stump-Socket Interface in Lower Limb Prostheses. In *Proceedings of the International Conference of the IEEE Engineering in Medicine and Biology Society*, pages 5517–5520, Milan, 2015.

J. Wojtusch and O. von Stryk. HuMoD - A Versatile and Open Database for the Investigation, Modeling and Simulation of Human Motion Dynamics on Actuation Level. In *Proceedings of the IEEE-RAS International Conference on Humanoid Robots*, pages 74–79, Seoul, 2015.

P. Beckerle, F. Schültje, J. Wojtusch, and O. Christ. Implementation, Control and User-Feedback of the Int²Bot for the Investigation of Lower Limb Body Schema Integration. In *Proceedings of the IEEE International Symposium on Robot and Human Interactive Communication*, pages 704–709, Edinburgh, 2014.

O. Christ, J. Wojtusch, and P. Beckerle. Robotic Mirroring of Movements in the Lower Limbs: Signal Delay of a Consumer Device Sensor. In *Proceedings of the Meeting of the Society of Applied Neurosciences*, page 96, Utrecht, 2014.

F. Schültje, P. Beckerle, M. Grimmer, J. Wojtusch, and S. Rinderknecht. Comparison of Trajectory Generation Methods for a Human-Robot Interface based on Motion Tracking in the Int²Bot. In *Proceedings of the IEEE International Symposium on Robot and Human Interactive Communication*, pages 710–715, Edinburgh, 2014.

P. Beckerle, J. Wojtusch, J. Schuy, B. Strah, S. Rinderknecht, and O. von Stryk. Power-optimized Stiffness and Nonlinear Position Control of an Actuator with Variable Torsion Stiffness. In *Proceedings of the International Conference on Advanced Intelligent Mechatronics*, pages 387–392, Wollongong, 2013.

P. Beckerle, J. Wojtusch, S. Rinderknecht, and O. von Stryk. Mechanical Influences on the Design of Actuators with Variable Stiffness. In *Proceedings of the International Symposium on Adaptive Motion of Animals and Machines*, pages 66–67, Darmstadt, 2013.

P. Beckerle, F. Stuhlenmiller, J. Schuy, J. Wojtusch, S. Rinderknecht, and O. von Stryk. Friction Compensation and Stiffness Evaluation on a Variable Torsion Stiffness. In *Proceedings of the International Symposium on Adaptive Motion of Animals and Machines*, pages 64–65, Darmstadt, 2013.

P. Beckerle, L. Lahnstein, J. Wojtusch, S. Rinderknecht, and O. von Stryk. Conception and Design of a Hardware Simulator for Restoring Lost Biomechanical Function. In *Proceedings of the IEEE International Conference on Systems, Man, and Cybernetics*, pages 1906–1911, Manchester, 2013.

S. Böker, P. Beckerle, J. Wojtusch, and S. Rinderknecht. A Novel Design Approach and Operational Strategy for an Active Ankle-Foot Prosthesis. In *Proceedings of the International Symposium on Adaptive Motion of Animals and Machines*, pages 26–28, Darmstadt, 2013.

J. Schuy, P. Beckerle, J. Faber, J. Wojtusch, S. Rinderknecht, and O. von Stryk. Dimensioning and evaluation of the elastic element in a Variable Torsion Stiffness actuator. In *Proceedings of the International Conference on Advanced Intelligent Mechatronics*, pages 1786–1791, Wellbeing, 2013.

P. Beckerle, O. Christ, J. Wojtusch, J. Schuy, K. Wolff, S. Rinderknecht, J. Vogt, and O. von Stryk. Design and control of a robot for the assessment of psychological factors in prosthetic development. In *Proceedings of the IEEE International Conference on Systems, Man, and Cybernetics*, pages 1485–1490, Seoul, 2012.

O. Christ, J. Wojtusch, P. Beckerle, K. Wolff, J. Vogt, O. von Stryk, and S. Rinderknecht. Prosthesis-User-in-the-Loop: User-centered design parameters and visual simulation. In *Proceedings of the International Conference of the IEEE Engineering in Medicine and Biology Society*, pages 1929–1932, San Diego, 2012.

M. Friedmann, J. Wojtusch, and O. von Stryk. A modular and efficient approach to computational modeling and sensitivity analysis of robot and human motion dynamics. *Proceedings in Applied Mathematics and Mechanics*, 12(1):85–86, 2012.

J. Schuy, P. Beckerle, J. Wojtusch, S. Rinderknecht, and O. von Stryk. Conception and evaluation of a novel variable torsion stiffness for biomechanical applications. In *Proceedings of the IEEE RAS/EMBS International Conference on Biomedical Robotics and Biomechatronics*, pages 713–718, Rome, 2012.

J. Wojtusch, P. Beckerle, O. Christ, K. Wolff, O. von Stryk, S. Rinderknecht, and J. Vogt. Prosthesis-User-in-the-Loop: A user-specific biomechanical modeling and simulation environment. In *Proceedings of the International Conference of the IEEE Engineering in Medicine and Biology Society*, pages 4181–4184, San Diego, 2012.

J. Wojtusch, H. Mochizuki, S. Takahashi, H. Nakamura, and R. Nordmann. The Concept and Implementation of the PROTEUS System. In *Electronics, Information and Systems Conference Papers*, pages 717–721, Hakodate, 2008.

Workshop Papers

J. Wojtusch, P. Beckerle, T. Schürmann, M. Schumacher, O. Christ, A. Seyfarth, S. Rinderknecht, J. Vogt, and O. von Stryk. Towards Seamless Integration of Active Assistive Devices into the User's Body Schema. In *Proceedings of the Cybathlon Symposium*, page 32, Zurich, 2016.

P. Beckerle, O. Christ, M. Windrich, S. Rinderknecht, J. Vogt, and J. Wojtusch. A Methodological Approach to Integrate Psychological Factors to Lower Limb Prosthetic Functional Design. In *Proceedings of the ISPO 2013 World Congress*, page 185, Hyderabad, 2013.

J. Wojtusch, P. Beckerle, and O. von Stryk. A Biomechanical Model for the Estimation of Dynamic Interactions at the Transfemoral Socket Interface. In *Proceedings of the ISPO 2013 World Congress*, page 228, Hyderabad, 2013.

J. Wojtusch and J. Kunz. MBSlib (multibody systems library), 2016. http://www.sim.informatik.tu-darmstadt.de/mbslib/ (accessed on 2017-04-15).

J. Wojtusch. HuMoD (biomechanical measurements database), 2015. http://www.sim.informatik.tu-darmstadt.de/humod/ (accessed on 2017-04-15).

Wissenschaftlicher Werdegang[1]

2002	Allgemeine Hochschulreife
2004 - 2011	Studium der Mechatronik am Fachbereich Elektrotechnik und Informationstechnik der Technischen Universität Darmstadt
2007 - 2008	Stipendium der Japan Student Service Organization am Fachbereich Computer Science der Nihon University
2011	Abschluss mit Erlagung des akademischen Grades eines Diplom-Ingenieurs
2011 - 2017	Wissenschaftlicher Mitarbeiter und Doktorand am Fachbereich Informatik der Technischen Universität Darmstadt
2017	Disputation zur Erlangung des akademischen Grades eines Doktor-Ingenieurs
seit 2017	Wissenschaftlicher Mitarbeiter beim Europäischen Raumflugkontrollzentrum

Erklärung[2]

Hiermit erkläre ich, dass ich die vorliegende Arbeit, mit Ausnahme der ausdrücklich genannten Hilfsmittel, selbständig verfasst habe.

[1] gemäß § 20 Abs. 3 der Promotionsordnung der Technischen Universität Darmstadt
[2] gemäß § 9 Abs. 1 der Promotionsordnung der Technischen Universität Darmstadt